Uncertainty and sensitivity analysis of aspects of the neutronics of a prismatic block-type HTGR

SF Sihlangu


orcid.org/0000-0001-9962-6924

Thesis submitted in fulfilment of the requirements for the degree *Doctor of Philosophy in Nuclear Engineering* at the North-West University

Promoter:	Dr V V Naicker
Co-promoter:	Dr J Hou
Co-promoter:	Mr F Reitsma

November 2019

DECLARATION

I Sinenhlanhla F. Sihlangu hereby that declare this thesis entitled: "*Uncertainty and sensitivity analysis of aspects of the neutronics of a prismatic block-type HTGR*" submitted to the North-West University is in compliance with the requirements set for the degree of "*Doctor of Philosophy in Nuclear Engineering"*

I further declare that this thesis is my own work, has been text-edited in accordance with the requirements and has not been submitted to any other university for any other degree.

_____ _____

Sinenhlanhla F. Sihlangu Date

To my father, Musa Langa and my mother, Bongiwe Sihlangu

ACKNOWLEDGEMENTS

First and foremost, I am grateful to God for providing me with the strength and perseverance to complete this project.

I extend my gratitude to my supervisor Dr Naicker for her guidance, her time and her assistance throughout the course of this study.

I am very grateful to my co-supervisors, Dr Hou and Mr Reitsma for their assistance.

Financial support is provided by the DST Research Chair in Nuclear Engineering and is highly appreciated.

I dedicate this thesis to my late father. Thank you for always being there Dad, I would not have made it this far if it wasn't for you, thank you for your love, support and protection. I also dedicate this thesis to my mother. Thank you Mom for your love, support and constant encouragement. I am grateful to my sister Noma and a special thank you to my baby sister Mandy. I love you all so much.

I am also thankful to my loved ones for their support and encouragement.

ABSTRACT

The International Atomic Energy Agency (IAEA) Coordinated Research Project (CRP) on High Temperature Gas-cooled Reactors (HTGR) Uncertainty Analysis in Modelling (UAM) has been established aiming to study uncertainty propagation in HTGR modelling. One of the research outcomes of this CRP is to calculate sensitivity coefficients and to propagate uncertainties for the MHTGR-350 using various sensitivity and uncertainty methods. This CRP was launched due to a shift towards Best Estimate Plus Uncertainty (BEPU) methods for safety analysis rather than the conservative methods. It is imperative in BEPU analysis that a parameter and its confidence limits lie within the safety margins. SCALE has a suite of uncertainty codes that allow quantification of uncertainties. These codes include Sampler and CE TSUNAMI-3D, which are chosen because they have the capability to accommodate the double heterogeneity of HTGRs. The large graphite quantities and hexagonal geometry for the prismatic designs should be taken into consideration when selecting analysis codes for HTGRs.

One of the methods used in this study is the CLUTCH approach available in the CE TSUNAMI-3D module in SCALE 6.2. It is a continuous energy based method that is capable of accommodating the double heterogeneity of the TRISO coated particles contained in the HTGR fuel. In this study, results of the sensitivity and uncertainty analysis of the fresh fuel compact and fresh fuel block specified in CRP Exercise I are presented. In using the CLUTCH method, the weighting function $F^*(\vec{r})$ must be specified in terms of spatial meshes and converged before the sensitivity coefficients can be calculated. Effort has been made in developing the methodology to ensure the convergence of this function by monitoring the uncertainty of $F^*(\vec{r})$ tallies and the relative standard deviation of $k_{\inf}$ due to cross section covariance data. In addition, the sensitivity of $k_{\inf}$ to some of the parameters used in the KENO-VI calculation contributing to the uncertainty has also been studied. The resulting optimized CE TSUNAMI models are compared to the resulting optimized Sampler/NEWT and optimized Sampler/KENO-VI models.

In the 350 MW Modular High Temperature Gas-Cooled Reactor (MHTGR-350), not only is the fuel double heterogeneous but so are the lumped burnable poisons (LBP). The first level of heterogeneity is the coated particles in a graphite matrix and the second level of heterogeneity is the fuel element. The LBP are composed of BISO particles and the fuel is composed of TRISO particles. In this study, an investigation is conducted for the different methods to model coated particles using KENO-VI and NEWT. KENO-VI is a Monte Carlo critical transport code in SCALE and NEWT is a multigroup discreet ordinates transport code. Both codes are part of the SCALE package. The most efficient way of modelling BISO and TRISO particles is established in SCALE and its impact on the $k_{\inf}$ is investigated. The fuel TRISO particles are modelled in continuous

energy (CE) and the sensitivity of packing and randomization on k_{inf} is investigated. Jiggling of coated particles is shown to have an insignificant effect on k_{inf} and on the uncertainty propagated due to nuclear data uncertainty.

In the multi-group (MG) treatment, coated particles are modelled with the doublehet function in SCALE. The doublehet function is only designed for particles that contain fuel, LBP BISO particles could therefore not be modelled. Hence a method called the LBP Trace method is developed to model the LBP coated particles using the doublehet function. The change in the macroscopic absorption cross section that would be passed to a nodal core calculation were found to be less than 1.4%. Furthermore, the LBP Trace method also showed small changes in the nuclear data uncertainty when compared to the conventional case. Finally, it was found that the multiplication factor changed by 1500 pcm compared to the conventional (homogenized) case, when using the LBP Trace method.

The MHTGR-350 benchmark is validated by performing the same calculations on an experimental reactor that is neutronically similar. Two reactors are said to be neutronically similar if they have the same sensitivity profiles. In this case the HTTR is chosen. Neutronic similarities are observed for the HTTR and MHTGR-350 fuel block and fuel compact systems. The HTTR is a very complex reactor and was modelled using NWURCS; this verifies NWURCS capability to model the prismatic HTGRs. The HTTR and MHTGR-350 fuel pin and fuel block are compared in terms of multiplication factors, relative standard deviation due to nuclear data uncertainty and the top six contributors to nuclear data uncertainty.

The uncertainty in the multiplication factor for the MHTGR-350 and HTTR systems is very sensitive to the ^{235}U $(\bar{\nu})$ / ^{235}U $(\bar{\nu})$ contribution, hence it is always the first ranked contribution. Comparison of the critical, subcritical and supercritical benchmark HTTR core models showed good comparability between the critical and subcritical HTTR, although insertion of control rods increased the c-graphite elastic / c-graphite elastic contribution. When control rods are fully inserted the c-graphite elastic / c-graphite elastic contribution ranks first and ^{235}U $(\bar{\nu})$ / ^{235}U $(\bar{\nu})$ contribution ranks second. Insertion of the control rods also causes a spike in the ^{235}U (χ) / ^{235}U (χ) contribution.

KEYWORDS: *Uncertainty Analysis, Sensitivity Analysis, HTGR, HTTR, MHTGR, NWURCS*

TABLE OF CONTENTS

LIST OF TABLES

LIST OF FIGURES

ABBREVIATIONS

1D	One Dimensional
2D	Two Dimensional
3D	Three Dimensional
AMPX	Automation for MUG, POPOP4 and XLACS
BEPU	Best Estimate Plus Uncertainty
BISO	Bistructural Isotropic
BONAMI	Bondarenko AMPX Interpolator
BP	Burnable Poison
CE	Continuous Energy
CENTRM	Continuous Energy Transport Module
CMFD	Coarse-Mesh Finite-Difference acceleration
CLUTCH	Contribution-Linked Eigen value sensitivity/Uncertainty estimation via Track length importance characterization
CP	Coated Particle
CPU	Central Processing Unit
CR	Control Rods
CRP	Coordinated Research Project
CSAS	Criticality Safety Analysis Sequence
CZP	Cold Zero Power
DBRC	Doppler Broadening Rejection Correction
ESC	Extended Step-Characterization
FHH	Fuel Handling Hole
Fortran	Formula Translation
GEN-IV	Generation IV
GRS	Global Research Safety
HFP	Hot Full Power
HTGR	High Temperature Gas Cooled Reactor
HTTR	High Temperature Test Reactor
IAEA	International Atomic Energy Agency
IFP	Iterated Fission Probability
INET	Institute for New and Nuclear Technology
INL	Idaho National Laboratory
IRPhEP	International Reactor Physics Experiment Evaluation Project
JAERI	Japan Atomic Energy Research Institute
KAERI	Korea Atomic Energy Research Institute
LBP	Lumped Burnable Poison
LWR	Light Water Reactor
MCNP	Monte Carlo N-Particle Transport Code
McCARD	Monte Carlo Code for Advanced Reactor Design and analysis
MG	Multi-Group
MHTGR	Modular High Temperature Reactor
NEA	Nuclear Energy Agency
NESTLE	Nodal Eigenvalue, Steady-State, Transient, Le Vore Evaluator
NEWT	New ESC-based Weighting Transport
NGNP	Next Generation Nuclear Plant
NPG	Neutrons Per Generation
NPP	Nuclear Power Plant
NSK	Number of Skipped Generations
NWURCS	North West University Reactor Code Suite.
OECD	Organization for Economic Cooperation and Development
ORIGEN	Oak Ridge Isotope Generation
pcm	Per cent mille

PMC	Produce Multigroup Cross sections
RAM	Random Access Memory
RPV	Reactor Pressure Vessel
RSICC	Radiation Safety Information Computational Canter
SA	Sensitivity Analysis
SCALE	Standardized Computer Analyses for Licensing Evaluation
TRISO	Tristructural Isotropic
TRITON	Transport Rigor Implemented with Time-dependent Operation for Neutronic depletion
TSUNAMI	Tools for Sensitivity and Uncertainty Analysis Methodology Implementation
UA	Uncertainty Analysis
UAM	Uncertainty Analysis in Modelling
UQ	Uncertainty Quantification
USA	United States of America
VHTRC	Very High Temperature Reactor Core Assembly
XS	Cross Section
XSProc	Cross Section Processing

SYMBOLS

χ	Energy distribution of fission neutrons
γ	Gamma rays released in a radiative capture reaction
k_{eff}	Neutron multiplication factor for a finite system
k_{inf}	Neutron multiplication factor for an infinite system
$\bar{\nu}$	Mean number of neutrons emitted per fission
Σ_x	Macroscopic cross section for reaction x

SCALE PARAMETERS

CFP	Number of latent generations
$CMFD$	Enables Coarse-Mesh Finite-Difference acceleration
DBH	Upper energy cut-off for the DBRC method
DBL	Lower energy cut-off for the DBRC method
DBR	Enables or disables the DBRC
$Epseigen$	Convergence criterion for k_{eff}
$Epsilon$	Sets spatial and eigenvalue criteria to the same value
$Epsinner$	Spatial convergence criterion for inner iterations
$Epsouter$	Spatial convergence criterion for outer iterations
FRE	Enables or disables free gas treatment
GEN	Total number of generations
$grid$	Number of mesh points used to discretize
$Inners$	Maximum number of inner iterations
ISN	Order of angular quadrature
$Mesh$	3D Spatial mesh spatial mesh that covers all fissionable regions
N	Total number of samples
NPG	Total number of neutrons per generation
$Outers$	Maximum number of outer iterations
P_n	Order for scattering in a mixture
SCT	Number of discrete scattering angles
$Sides$	Number of sides of the polygon used to model a cylinder
SIG	SIGMA or standard deviation
Sn	Order of the Sn level quadrature set
SZF	Spatial mesh factor
TTL	Temperature tolerance
UUM	Use of unionized parameters
$xycmfd$	Specifies the same number of fine-mesh cells per coarse mesh cell in the x and y direction.

CHAPTER 1: INTRODUCTION

1.1 The concept of uncertainty analysis and sensitivity analysis

Any measured value contains an uncertainty which is as a result of the tools used to acquire the result. A result without an uncertainty has limited use. In computer simulations uncertainties arise from assumptions, modelling, simplifications, methodology and tools. All of these uncertainties combine and have an effect on the output. The reliability of simulation results depends on a realistic estimation of uncertainties and the absence of uncertainty propagation in any result limits its usefulness.

A sensitivity analysis differs from uncertainty since it attempts to determine the effect that a minor change in input values causes in the output values (Pusa, 2012). Sensitivity analysis plays a role in ranking the various sources of uncertainty and error in the results of the core analyses. Uncertainty analysis attempts to determine the change in the output values from an entire set of possible outcomes, together with associated probabilities of occurrence (Loucks and Van Beek, 2005). Both sensitivity and uncertainty analyses are crucial to address cost, safety and licensing needs and should be applied to all aspects of multiphysics simulations (Strydom et al, 2015).

1.2 Coordinated research project on HTGR

In nuclear safety research there exist two popular methods for licensing and safety analysis, i.e. the traditional conservative methods as well the Best Estimate Plus Uncertainty (BEPU) methods. The conservative methods rely on the use of conservative codes, making conservative assumptions on plant data, system performance and system availability as well as making use of initial and boundary conditions. These methods render results that are biased. The BEPU methods aim to reduce the level of conservatism in safety assessment calculations. These BEPU methods are vastly replacing conservative methods for safety analysis and nuclear power plant licensing. BEPU methods are based on best estimate computer codes, conservative assumptions and realistic (with uncertainty) initial and boundary conditions (Menzel et al, 2018).

BEPU methods have the aim of providing the analyst with the safety margins according to the latest best estimate codes as well as the identification of uncertainties associated with the use of these best estimate codes (Menzel et al, 2018). Best estimate calculations of safety parameters were first allowed rather than conservative code models in the 1980s under Title 10, Part 50, Section 46 (10 CFR 50.46) of the United States Code of Federal Regulations under the condition that uncertainties are quantified and qualified (Strydom, 2012).

The increasing need for BEPU predictions with their confidence bounds requires an in-depth knowledge of sensitivity analysis and uncertainty analysis. Specifically, in terms of HTGRs, this has led to a launch of the International Atomic Energy Agency (IAEA) Coordinated Research Project (CRP) on High Temperature Gas Reactor (HTGR) Uncertainty Analysis in Modelling (UAM), on which this work is based and forms a part of.

The IAEA CRP on HTGRs (Strydom et al, 2015) follows from the Organization for Economic Corporation and Development (OECD) CRP on Light Water Reactors (LWR) (Ivanov, et al, 2013). The objective of the CRP on HTGRs is to determine the uncertainty in HTGR calculations at all stages of coupled reactor physics/ thermal hydraulic and depletion calculations. This objective is achieved by performing a full chain of uncertainty propagation from basic data and engineering uncertainties and across different scales and physics phenomena (Strydom et al, 2015). There is a need to study uncertainty analysis and sensitivity analysis of HTGRs since they have their own peculiarities, which include large graphite content, double heterogeneity (coated particles and fuel compacts) and high temperatures which require their own specialized techniques that differ from LWRs. Two benchmark problems are defined, one is the pebble-bed design of the HTGR and the other is prismatic design of the HTGR. The pebble-bed benchmark is a 250-MW modular pebble-bed design. The prismatic HTGR is the focus of this work and this design is the General Atomics Modular High Temperature Gas-Cooled Reactor (MHTGR-350).

The CRP is divided into four phases. Phase I focuses on local neutronics and local thermal-hydraulics, Phase II on global stand-alone modelling, Phase III on design calculations, and finally, Phase IV on safety calculations. In Phase I, there are four exercises (Exercise I-1 to Exercise I-4), of which the first two are:

Exercise I-1: Cell Physics: Derivation of the multi-group microscopic cross section libraries.

Exercise I-2: Local Physics: Derivation of the few-group macroscopic cross section libraries.

Exercise I-1 defines the homogeneous and heterogeneous fuel compact and Exercise I-2 defines the heterogeneous single fuel block. The lattice (cell and local) physics calculations are used to generate nodal parameters for the full-core simulation (Canuti et al, 2012). The nodal parameters are affected by uncertainties and in lattice physics these uncertainties are:

- uncertainties due to nuclear data;
- uncertainties associated with methods and modelling approximations used in lattice physics codes;
- multigroup cross section uncertainties; and
- fuel/assembly manufacturing uncertainties.

The objective is to study the effect of the first three uncertainty sources. These are all characterized as input uncertainties.

There is a constant effort to update and to improve nuclear data but their precision is limited due to uncertainties of underlying measurements and theoretical parameters. Since neutronic calculations are based on the quantification of nuclear data, their uncertainties affect the precision of the neutronic outputs directly (Zhu et al, 2015).

Calculated uncertainty results can be assessed either through code to code comparison or via comparison with experimental data. The uncertainty in computer codes is affected by the unavoidable approximations, limitations and inadequacy that are related to modelling. Hence sensitivity and uncertainty analyses are carried out to supplement the results (Salah et al, 2006).

The multigroup cross section uncertainties are propagated into the few-group cross sections, which will be used in Phase II (full core).

1.3 The HTGR.

The High Temperature Gas-Cooled Reactor is gas cooled and is graphite moderated. It is a generation four (GEN IV) reactor and also a candidate for the Next Generation Nuclear Plant (NGNP). It was selected since it can provide electricity and high temperature heat that is required for commercial applications (Hicks, 2011). Apart from its industrial applications, the HTGR boasts inherent safety features, safeguards and sustainability features that make it a desirable option for power production. These features include high efficiency, very high burnup, proliferation resistance and economic competitiveness (Sihlangu, 2016).

The material design and composition of the HTGR is responsible for its inherent safety features. The Tristructural Isotropic (TRISO) coated particles can retain their integrity for temperatures up to 1600^0C. These particles retain all radionuclides under accident conditions. The graphite moderator has very high durability at very high temperatures. The helium is an inert and neutronically transparent gas, therefore, it will not react chemically and radiologically with any materials of the core and also not affect the neutron economy. Additionally, in a properly designed system, during a loss of coolant scenario, decay heat is removed by heat transfer through the graphite structures to the surroundings, thus preventing excessive temperature increases in the core.

South Africa has shown interest in the pebble bed reactor design. South Africa's only HTGR commercial programme was the conceptual Pebble-Bed Modular Reactor. The project began in 1998 and was terminated in 2010 (Thomas, 2011) due to a discontinuation of funding from the

government. Other countries that have developed HTGRs are the United States, France, Germany, China, Korea and Japan (Hicks, 2011). The 10 MW High Temperature Reactor (HTR-10) is also a pebble-bed and is of interest in this work since it is one of the representations of the pebble-bed core designs defined for the IAEA CRP on HTGR UAM (Hao et al, 2018). The validation results produced by Hao et al (2018) for the HTR-10 are instrumental in the validation chapter of this thesis (Chapter 8). The design of the HTR-10 is stipulated by Montierth et al (2009).

The Japanese High Temperature Test Reactor (HTTR) is modelled in this work for the purpose of validation of calculated results. The HTTR's main objective is to demonstrate the features of HTGRs and lay solid ground for new generations of HTGRs. The MHTGR-350 is also studied in this work. Typically, MHTGRs are small sized reactors which are factory built, have short construction periods and require small initial capital investment (Dong, 2016).

Both the MHTGR-350 and the HTTR are complex to model. Their complexity stems from the need for hexagonal geometries, hexagonal arrays as well as the double heterogeneity of the fuel. In the MHTGR-350, not only is the fuel double heterogeneous but so are the burnable poisons. The HTTR has increased geometrical complexity since its geometries include dodecagonal geometries, cone-shaped geometries, varying enrichments, varying fuel block types, and so on. Another prismatic HTGR is the Very High Temperature Reactor Core Assembly (VHTRC), which has the function of obtaining experimental data. The VHTRC is described in the International Handbook of Reactor Physics Experiments Benchmark (NEA, 2013). This reactor has been studied as part of the experimental validation of HTGR lattice physics for the IAEA CRP on HTGRs (Bostelmann and Strydom, 2017).

1.4 Overview of codes

SCALE is a suite of tools developed and maintained within the Reactor and Nuclear Systems division of the Oak Ridge National Laboratory (ORNL). It has a wide number of applications and capabilities in nuclear safety and design (Rearden, et al, 2015). SCALE has a suite of codes for criticality calculations and for sensitivity and uncertainty analysis in continuous energy (CE) and multigroup energy (MG).

The following criticality SCALE codes are used in this work:

- KENO-VI – Three Dimensional (3D) Monte Carlo eigenvalue criticality code (MG/CE).
- NEWT – Two Dimensional (2D) discrete ordinates deterministic code with flexible meshing capabilities (MG).

The sensitivity and uncertainty codes are:

- TSUNAMI – sensitivity and uncertainty analysis in MG and CE for one (1D), two (2D) and three (3D) dimensional geometries.
- Sampler – Super-sequence that operates by stochastic sampling in MG.

Each code quantifies the effects of uncertainties in nuclear data. Each of these tools are discussed in Section 3.1. In terms of TSUNAMI, only CE TSUNAMI is applicable to this work since the traditional MG TSUNAMI doesn't accommodate the double heterogeneity of the fuel.

1.5 NWURCS

North West University Reactor Code Suite (NWURCS) is a suite of codes built in Fortran, which was developed at the School of Mechanical and Nuclear Engineering, NWU. It has the capability of generating input files for a few reactor systems. It currently generates inputs for KENO-VI, NEWT, MCNP6, and RELAP5 and is currently on its second version. Version 1 was used successfully to model the VVER (Nyalunga et al, 2016) and the EPR (du Toit and Naicker, 2018). NWURCS has not been used to model the HTGR. The complexity of the HTGR comes from its double heterogeneity. This will test the modelling capability of NWURCS. Version 2.1 of NWURCS was used in this work.

1.6 Problem statement

Uncertainty methods are vastly replacing conservative methods for safety and licensing analysis. The key goal of uncertainty analysis is to provide the analyst with safety margins. High Temperature Gas Reactors (HTGR) have their own peculiarities that make them complex to model such as their double heterogeneity, large graphite content and high temperatures. An efficient uncertainty analysis methodology that accommodates the complexity of the HTGR must be established.

1.7 Aim and objectives

The aim of this research is to propagate uncertainties for prismatic type HTGRs. Uncertainty analysis methods and sensitivity analysis methods are established and applied to the conceptual design of the General Atomics MHTGR-350 fuel compact and single fuel block. These uncertainty techniques are verified by being applied to an experimental design of the block type HTGR, which is the HTTR.

The objectives are:

- To model the HTGR whilst sufficiently treating the double heterogeneity of the coated particles, i.e. fuel and burnable poisons.
- To establish uncertainty methods with geometry capabilities that can sufficiently model the HTGR.
- To carry out sensitivity studies coupled with convergence studies so that the models are sufficiently converged and optimized without impinging on computational time for use in the uncertainty analysis.
- To propagate uncertainties using SCALE codes in 2D and 3D.
- To verify NWURCS' HTGR modelling capability on the complex critical and subcritical benchmark HTTR models.
- To apply the established uncertainty methods and optimization methods to the HTTR reactor core.

1.8 The main contribution of this research/thesis

In recent years there has been a drive towards using BEPU codes to quantify uncertainties related to reactor analysis and to predict safety limits. The HTGRs have their own peculiarities that make it complex to model and quantify uncertainties. For this reason, the CRP is launched. It is an international collaboration with participation from the Institute of Nuclear and New Energy Technology (INET) at Tsinghua University (China), GRS (Germany), IAEA (Austria), Idaho National Laboratory (USA), KAERI (Korea), Kurchatov Institute (Russia), North Carolina State University (USA) and NWU (South Africa). Each contributor performs calculations using their own choice of uncertainty codes for the phases and exercises of the IAEA CRP on HTGR UAM. Finally, a collective technical document consisting of all the contributions is aimed to be published in 2019.

This thesis falls within the framework of the IAEA and reflects a part of the NWU contribution to the IAEA CRP on HTGR UAM. NWU's contribution is the propagation of the uncertainties in Phase I as well as uncertainty quantification of the HTTR.

This thesis addresses modelling of the HTGR systems and identification of SCALE codes that are best suited to sufficiently perform calculations on the HTGR systems.

In terms of modelling, methods to treat the double heterogeneity as well as the stochastic nature of the fuel and burnable poisons are further developed and the related uncertainty is quantified.

Regarding optimization, it is important to optimize the setup of input parameters and code usage in terms of minimizing certain parameters such as time usage by the code. It is also important to establish the uncertainty that would arise from such optimizing studies. Such optimizations are therefore in essence sensitivity studies and are therefore important in a study such as this.

Therefore, in this context, optimization of the code parameters is another contribution in the study of uncertainty and sensitivity analysis. Part of the optimization presented in this work is published by Sihlangu et al (2018).

The related task of convergence is also studied, since it is also important to obtain results which have a smaller uncertainty than those for which the calculations are not sufficiently converged. Methods to sufficiently converge the code without impinging on time expenditure are further developed for the uncertainty codes.

The modelling and optimization techniques are applied to the experimental HTTR to validate these techniques.

The IAEA CRP has identified three validation reactors. For the pebble-bed, the HTR-10 is the chosen reactor. For the prismatic design, the VHTRC and the HTTR are the chosen reactors. INET's uncertainty study on the HTR-10 using CE TSUNAMI-3D is presented in Hao et al (2018). GRS' uncertainty study on the VHTRC is presented in Bostelmann and Strydom (2017). NWU's uncertainty study on the HTTR is presented in this study.

This thesis also serves to validate the modelling capability of NWURCS, since it is being used to model the very complex HTTR benchmark design.

1.9 Outline of thesis

Chapter 2 contains the specific theory. The theory discussed in this chapter is fundamental to understanding how the SCALE 6.2.1 method and codes (Chapter 3) perform criticality and uncertainty calculations.

Chapter 3 discusses each of the SCALE sequences and their application to HTGRs.

Chapter 4 describes the systems studied in this work, the first system is the MHTGR-350 and the other is the critical HTTR benchmark design and the subcritical HTTR benchmark design.

Chapter 5 outlines the methodology. The modelling of the fuel compact and fuel block in CE and MG as well as the assumptions, approximations and limitations of the model are explained. The code parameters are discussed this chapter.

Chapter 6 presents the results for convergence and optimization of the criticality and uncertainty codes. Uncertainties due to nuclear data are presented here for the nominal cases.

Chapter 7 investigates the modelling of the coated particles of the HGTR in MG and CE using SCALE. The most efficient way to model LBP coated particles and fuel CPs is investigated and the related uncertainty is quantified.

Chapter 8 is the validation chapter. The modelling approach, criticality analysis and uncertainty methodology that was established in Chapters 5, 6 and 7 for the MHTR-350 is applied to the critical and subcritical benchmark HTTR. This chapter also presents modelling of the benchmark HTTR with NWURCS. A sensitivity study is conducted on the simplifications of the benchmark HTTR model.

Chapter 9 concludes the findings presented in Chapters 6, 7 and 8.

CHAPTER 2: THEORY

This chapter aims to provide the reader with the background theory that is fundamental to the codes discussed in Chapter 3. Fundamental to this chapter are explanations of nuclear data, cross section processing, resonance self-shielding, the few-group approximations, and uncertainty analysis techniques.

2.1 Cross sections

Essentially a cross section is the probability of a nuclear reaction taking place. A cross section is expressed by the quantity σ_x, such that (Duderstadt and Hamilton, 1976):

$$\sigma_x \equiv \frac{\text{reaction rate}/N_A}{I}, \tag{2.1}$$

where

$reaction\ rate$ has units of number of reactions / cm^2·s

I is the incident neutron beam intensity in units of number of neutrons / cm^2·s; and

N_A is the number of target atoms per cm^2.

σ_x is very small and its measurement is expressed as barn i.e. $1\ \text{barn} = 10^{-24}\text{cm}^2 = 10^{-28}\text{m}^2$. The unit for the cross section is that of area. The subscript x represents any reaction. The most important reactions are absorption, fission (which is a part of absorption) and scattering.

When a neutron strikes a nucleus it can either be scattered or absorbed and the total cross section σ_t, is the sum of the likelihood of scattering and absorption:

$$\sigma_t = \sigma_s + \sigma_a. \tag{2.2}$$

Thus $\frac{\sigma_a}{\sigma_t}$ is the probability that the neutron will be absorbed and $\frac{\sigma_s}{\sigma_t}$ is the probability that a neutron will be scattered (Lewis, 2008). The scattering cross section is the sum of the elastic and inelastic cross sections. In inelastic scattering some of the neutron's kinetic energy is transferred to the nucleus and the nucleus is left in an excited state. The excited nucleus can de-excite by releasing gamma ray(s). However, in elastic scattering, the struck nucleus is left in its ground state.

The absorption cross section, σ_a, includes the sum of the radiative capture cross section, σ_γ and the fission cross section, σ_f. Normally, only σ_γ and σ_f are considered, as shown in Equation 2.3:

$$\sigma_a = \sigma_\gamma + \sigma_f. \quad (2.3)$$

Microscopic cross sections are denoted by σ_x and macroscopic cross sections are denoted by Σ_x such that:

$$\Sigma_x = N\sigma_x, \quad (2.4)$$

where N is the number density of the isotope under consideration. Therefore, in terms of the macroscopic cross section, Equation 2.2 is written as $\Sigma_t = \Sigma_s + \Sigma_a$ and Equation 2.3 can be written as $\Sigma_a = \Sigma_\gamma + \Sigma_f$. The unit of the macroscopic cross section is cm^{-1}.

The macroscopic transport cross section Σ_{tr}, is not easily processed and requires μ_0, the mean scattering cosine of the scattering angle together with Σ_t and Σ_a:

$$\Sigma_{tr} = \Sigma_a + (1 - \mu_0)\Sigma_s = \Sigma_t - \mu_0\Sigma_s, \quad (2.5)$$

where Σ_t is the macroscopic total cross section, Σ_s is the macroscopic scattering cross section and $\mu_0 \approx \frac{2}{3A}$ (A is the atomic mass number of the scattering nuclei).

Cross section data are usually provided in specific format, such as the Evaluated Nuclear Data Files (ENDF). These ENDF files have been benchmarked extensively and checked for consistency in calculations, associated with experiments designed for data testing. The cross section data in ENDF files are represented as follows (Stacey, 2007):

- Pointwise tabulation in energy at low energies below the resonance region.
- Resolved resonance parameters and background cross sections in the resolved resonance region.
- Unresolved resonance statistical parameters and background cross sections in the unresolved resonance region.
- Pointwise tabulation in energy at energies above the resonance region.
- Pointwise tabulation of scattering transfer functions in energy and either pointwise in angle or as Legendre coefficients.

ENDF/B data files are organised according to materials, files and sections. Files describe subdivision of materials and files contain data for a certain class of information (e.g. MF = 3 contains cross sections) (Herman and Trkov, 2009). Sections are subdivisions of files and describe a particular reaction. Some of the common reactions and associated parameters are presented in Table 2-1:

Table 2-1 Common reactions and associated parameters in ENDF/B

MT	Reaction / Parameters
1	Total cross section
2	Elastic scattering (n, n)
4	Inelastic scattering (n, n')
16	Neutron-producing reaction $(n, 2n)$
18	Fission
102	Radiative capture (n, γ)
107	Charged particle reactions (n, α)
452	Nubar $(\bar{\nu})$
1018	Chi (χ)

Elastic scattering is abbreviated with the notation (n, n) and inelastic scattering is abbreviated as (n, n'). Radiative capture refers to when a neutron is captured by the nucleus and gamma ray(s) are emitted and is abbreviated with the symbol (n, γ). Neutron-producing reactions are abbreviated with $(n, 2n)$ and $(n, 3n)$. In the $(n, 2n)$ reaction, one neutron is extracted from a struck nucleus whilst in the $(n, 3n)$ reaction, two neutrons are extracted from a struck nucleus. Charged particle reactions are either (n, α) or (n, p), this means that neutrons disappear as a result of absorption reactions. The parameter $\bar{\nu}$ is the average number of fission neutrons and the parameter χ is the fission neutron energy spectrum such that $\chi(E)dE$ is defined as the number of fission neutrons emitted with energy E in $E + dE$ per fission neutron (Duderstadt and Hamilton, 1976).

2.2 Resonance cross sections

Scattering and absorption cross sections usually exhibit resonance peaks at neutron kinetic energies corresponding to excited states of a compound nuclei. These excited states correspond to the excitation energy brought by the incident neutron during compound nuclide formation. For odd mass isotopes, resonances occur from a fraction of 1 eV up to a few thousand eV, and for the even mass fuel isotopes, resonances occur from a few eV to about 10 000 eV. At lower energies, resonances are well separated but at higher energies the resonances are not well separated.

2.3 Doppler broadening

As the fuel temperature increases, the widths of the resonances of the isotopes in the fuel broaden, and in the context of neutrons slowing down, their probability for absorption increases. For low enriched fuel, the broadening of the absorption of ^{238}U dominates and this can reduce the

neutron flux in the vicinity of the resonance. This broadening of the resonances is known as Doppler Broadening.

2.4 Neutron transport

The basis of uncertainty analysis in this work is criticality calculations and the SCALE transport codes operate by solving the neutron transport equation to treat criticality problems. This equation is a form of the Boltzmann equation. The neutron transport equation can be tailored to many forms depending on the requirements of its application (Rearden et al, 2016).

Neutron balance for a given volume is essentially given as:

Rate of change of neutrons = net rate of generation of neutrons in collisions + rate of introduction of source neutrons – net rate of outflow of neutrons.

The time-independent neutron transport equation is as follows (Rearden et al, 2016):

$$\hat{\Omega} \cdot \vec{\nabla}\psi(\vec{r},\hat{\Omega},E) + \Sigma_t(\vec{r},E)\psi(\vec{r},\hat{\Omega},E) - \int_{4\pi} d\,\hat{\Omega}' \int_0^{\infty} dE' \Sigma_s\left(\vec{r},\hat{\Omega}' \rightarrow \hat{\Omega}, E' \rightarrow E\right)\psi(\vec{r},\hat{\Omega}',E') \quad (2.6)$$
$$= \chi(\vec{r},E) \int_0^{\infty} dE' \bar{\nu}(\vec{r},E')\Sigma_f(\vec{r},E')\psi(\vec{r},\hat{\Omega}',E') + S_E(\vec{r},E),$$

where

$\psi(\vec{r},\hat{\Omega},E)$ is the angular flux at position $\vec{r}$ per unit volume, in the direction $\hat{\Omega}$ per unit solid angle and at energy E per unit energy;

$\Sigma_t(\vec{r},E)$ is the total macroscopic cross section at position $\vec{r}$ and energy E;

$\Sigma_s(\vec{r},\hat{\Omega}' \rightarrow \hat{\Omega},\ E' \rightarrow E)$ is the macroscopic scattering cross section at position $\vec{r}$ with initial energy E' and the direction $\hat{\Omega}'$ to final energy E and direction $\hat{\Omega}$;

$\Sigma_f(\vec{r},E')$ is the macroscopic fission cross section at position $\vec{r}$ and energy E' (assumed to be isotropic);

$\bar{\nu}(\vec{r},E')$ is the number of neutrons released per fission event at position $\vec{r}$ and energy E';

$\chi(\vec{r},E)$ is the fraction of neutrons that are born at $\vec{r}$ and energy E; and

$S_E(\vec{r},E)$ is the external source.

The neutron transport equation can be reduced to a set of multigroup equations by integrating it over the energy width $\Delta E_g = E_{g+1} - E_g$ of group g.

In the eigenvalue problem the external source is typically zero, so the Equation 2.6 becomes:

$$\widehat{\Omega} \cdot \vec{\nabla}\psi(\vec{r}, \widehat{\Omega}, \mathrm{E}) + \Sigma_t(\vec{r}, E)\psi(\vec{\mathrm{r}}, \widehat{\Omega}, \mathrm{E}) - \int_{4\pi} d\,\widehat{\Omega}' \int_0^{\infty} dE' \Sigma_s\left(\vec{r}, \widehat{\Omega}' \rightarrow \widehat{\Omega}, E' \rightarrow E\right)\psi(\vec{r}, \widehat{\Omega}', E') = \frac{1}{k}\,\chi(\vec{r}, E) \int_0^{\infty} dE' \bar{\nu}(\vec{\mathrm{r}}, E')\Sigma_f\,(\vec{\mathrm{r}}, E')\psi(\vec{\mathrm{r}}, \widehat{\Omega}', E'). \tag{2.7}$$

In Equation 2.7, $\bar{\nu}$ is adjusted to $\frac{\bar{\nu}}{k}$ to obtain the form of the neutron transport equation for the k-eigenvalue problem (Lewis and Miller, 1993). In preparation for Section 2.11.1, this equation can be written in operator notation by defining operators B and F in terms of the Equation 2.8 and Equation 2.9. B is the neutron loss term and F is the fission neutron production term:

$$B\,\psi(\vec{r}, \widehat{\Omega}, \mathrm{E}) = \widehat{\Omega} \cdot \vec{\nabla}\psi(\vec{r}, \widehat{\Omega}, \mathrm{E}) + \Sigma_t(\vec{r}, E)\psi(\vec{r}, \widehat{\Omega}, \mathrm{E}) - \int_{4\pi} d\,\widehat{\Omega}' \int_0^{\infty} dE' \Sigma_s\left(\vec{r}, \widehat{\Omega}' \rightarrow \widehat{\Omega}, E' \rightarrow E\right)\psi(\vec{r}, \widehat{\Omega}', E'), \tag{2.8}$$

$$F\,\psi(\vec{r}, \widehat{\Omega}, \mathrm{E}) = \chi(\vec{r}, E) \int_0^{\infty} dE' \bar{\nu}(\vec{r}, E')\Sigma_f\,(\vec{r}, E')\psi(\vec{r}, \widehat{\Omega}', E'). \tag{2.9}$$

Hence Equation 2.6 can be written as:

$$B\psi(\vec{r}, \widehat{\Omega}, \mathrm{E}) = \lambda F\,\psi(\vec{r}, \widehat{\Omega}, \mathrm{E}), \tag{2.10}$$

where $\lambda = \frac{1}{k}$.

In applications, k is represented either as k_{eff} or k_{inf}, where k_{eff} is the multiplication factor of a finite system whilst k_{inf} is the multiplication factor of a infinite system.

The neutron transport equation holds under the following assumptions (Lewis and Miller, 1993):

- Neutrons may be considered as points.
- Neutrons travel in straight lines between points.
- Neutron-neutron interactions may be neglected.

- Collisions may be considered instantaneous.
- Material properties are considered isotropic.
- Nuclear properties of nuclei and the composition of materials under consideration are assumed to be known and time-independent unless explicitly stated.
- Only the expected or mean value of the neutron density distribution is considered.

2.5 Cross section processing

One form in which cross section data is available in raw ENDF data files is as pointwise data as a function of energy. For any given reaction, there would then be thousands of data points for the energy interval. Given this large number of data points, the library is then termed a continuous energy (CE) library. Cross sections processed in CE mode are read directly from this nuclear data library and need not be collapsed into groups. Although the CE data is stored on a very fine grid, interpolation can still be required (Herman and Trkov, 2009).

The multigroup cross sections are necessary since the so called deterministic solutions to the transport equation require that the cross section data be collapsed to a finite number of energy groups. Multigroup calculations are computationally inexpensive compared to the continuous energy calculations and have lower memory requirements. A number of codes process the ENDF files directly and these codes numerically calculate the integrals of type (Stacey, 2007)

$$\sigma_x^g = \frac{\int_{E_g}^{E_{g-1}} dE\,\sigma_x(E)W(E)}{\int_{E_g}^{E_{g-1}} dE W(E)}, \tag{2.11}$$

$$\sigma_s^{g\to g'} = \int_{E_g}^{E_{g-1}} dE\,\sigma_s(E)W(E)\int_{g'}^{E_{g'-1}} dE' p_n(E') \Big/ \int_{g}^{E_{g-1}} dE W(E)' \tag{2.12}$$

where

$\sigma_x(E)$ is the microscopic cross section of reaction x as a function of energy E;

$W(E)$ is a specified weighting function which maybe a constant, $1/E$, $\chi(E)$, etc;

g is the energy group;

σ_x^g is the weighted cross section of reaction x for energy group g;

$\sigma_s^{g\to g'}$ is the weighted cross section from energy group g to energy group g'; and

p_n is defined by Equation 2.13.

$$p_n = \int_{-1}^{1} d\mu \;\; P_n(\mu) p(E,\mu), \tag{2.13}$$

where

μ is the through angle at which the neutron is scattered;

P_n is the Legendre polynomial of order n; and

$p(E,\mu)$ is the angular distribution for scattering of a neutron for energy E.

These codes calculate the fine-group cross sections or the ultrafine group cross sections.

A large part of this work is based on the calculation of multi-group and few-group cross section data sets. This is performed on cell physics and lattice physics models, which are infinite systems such as the fuel compact (unit cell calculation) and the fuel block (lattice calculation).

Unit cell physics calculations solve the neutron transport equation for small infinite systems. Further cross section processing creates applicable MG constants for lattice physics calculations using the flux calculated in the unit cell calculations. This processing of the cross sections was discussed in the first part of this section. The fine-group cross sections obtained are then used in the lattice physics calculations to calculate the fine or ultrafine-group spectrum ϕ_g.

The fine or ultra-fine group cross sections together with the fine or ultrafine-group spectrum ϕ_g are then used via the flux-volume-weighted homogenization and condensation to obtain few-group (2 to 10) cross sections for thermal reactors or many-group (20 to 30) cross sections for fast reactors (Stacey, 2007). In this work cross sections are collapsed to 4 groups. These few-group cross sections are then used in the 3D full core models in subsequent steps.

Uncertainties are propagated from microscopic CE cross sections to MG microscopic cross sections. Uncertainties are also propagated from the MG microscopic cross sections into the few-group macroscopic cross sections.

2.6 The Extended Step-Characterization method

The deterministic method used in this thesis to solve the neutron transport equation is the discrete-ordinates method which is also known as the S_N method. The application of the discrete-

ordinates methods is difficult when it comes to complicated non-orthogonal geometries because of the nature of finite difference approximations for spatial derivatives, so an alternative is used which is the Extended Step-Characterization (ESC) method. In the ESC method, the neutron transport equation in Section 2.4 is solved along characteristic directions within a computational cell. Further details regarding this method is found in the publication by Rearden et al (2016). The deterministic methods are considerably more computationally efficient when compared to the Monte Carlo methods (introduced in the next section), and can be used in place of Monte Carlo methods to save computational time in most common applications.

2.7 Monte Carlo method

The Monte Carlo method is useful when it is difficult to describe physical phenomena (distribution functions, differential equations, balance equations and so on) using deterministic methods to solve the neutron transport equation. Monte Carlo methods are suited for systems with more complex geometry such as double heterogeneous systems. In CE mode, neutronic solutions for complex geometries are computed with high accuracy. Monte Carlo methods operate in a stochastic manner by random sampling of probability density functions. A specified large number of particle histories are performed, each particle history following the random process. The final answer is the average or rather the best estimate of many neutron histories. The standard error or the variance can also be calculated. A detailed description of the Monte Carlo method as applied in KENO-VI can be found in the publication by Rearden et al (2016).

2.8 Convergence of Monte Carlo neutron transport codes

Monte Carlo code convergence in terms of the fission source distribution, neutron flux and multiplication factor has been covered extensively in previous neutronics work published at the NWU (Montwedi, 2014; Sihlangu, 2016; Nyalunga, 2016; Maratele, 2016; du Toit, 2017) and is only discussed briefly in this work. The new SCALE 6.2 convergence tests to assess fission source convergence are used in this work to help determine the source convergence. These tests are designed to help simplify the determination of convergence for the user. The convergence of the fission source is characterized by the Shannon entropy (H_{src}). Prior to the SCALE 6.2 release KENO only provided plots of k_{eff} (or k_{inf}) by generation and average k_{eff} (or k_{inf}), which left the user to determine convergence by visual inspection (Maratele, 2016; Strydom et al, 2015). The H_{src} convergence diagnostics techniques have been included in KENO and these are imperative for monitoring source convergence. H_{src} is given by Equation 2.14 (Brown, 2006).

$$H_{src} = -\sum_{j=1}^{N} P_j \cdot \ln_2(P_j), \tag{2.14}$$

where P_j is the number of source sites in the j^{th} mesh element over the total number of fission sites N. A number of generations must be skipped so that the source can be considered converged. Given the number of active generations after this, the multiplication constant will be calculated for each active generation. Given this set of constants, the mean of the multiplication constant will be calculated together with the standard deviation.

2.9 The six-factor formula

The multiplication factor is used to assess the steady state criticality of the system of interest. In addition to being obtained by solution of the transport equation as shown in Section 2.4, it can also be expressed as (Stacey, 2007):

$$k_{\text{eff}} = \frac{\bar{\nu}\Sigma_f / \Sigma_a}{1+L^2 B_g^2} = k_{\text{inf}} P_{NL}, \tag{2.15}$$

where

L is the diffusion length;

B_g is the geometrical buckling;

$\bar{\nu}$ is the number of released fission neutrons;

P_{NL} is the non-leakage probability; and

k_{inf} is the multiplication constant for an infinite assembly with no leakage and is defined in the equation as:

$$k_{\text{inf}} = \bar{\nu}\Sigma_f / \Sigma_a. \tag{2.16}$$

k_{inf} can also be expressed as (Stacey, 2007):

$$k_{\text{inf}} = \eta f \varepsilon p, \tag{2.17}$$

where

ε is the fast fission factor which is the total fission neutron production rate/ fission neutron production rate in fissile nuclides;

f is the thermal utilisation factor which is the fraction of the absorbed neutrons which are absorbed in the fissile nuclides;

η is the number of fission neutrons produced for each neutron absorbed in the fissile material; and

p is the resonance escape probability and it is the probability that a neutron is not captured during the slowing down process.

2.10 General statistics

This section discusses the general statistical concepts that are involved in Monte Carlo calculations as well as in uncertainty analysis.

2.10.1 Mean and the standard deviation

The mean ($\bar{x}$) is the best estimate of x for a sample size of N with x_i an element of the sample (Taylor, 1997) such that:

$$\bar{x} = \frac{1}{N}\sum_{i=1}^{N} x_i. \tag{2.18}$$

The standard deviation shown in Equation 2.19, is the average uncertainty of the measurements $x_1, \ldots, x_N$. The use of $N-1$ in Equation 2.19 computes the sample standard deviation:

$$StdDeV(x) = \sqrt{\frac{1}{N-1}\sum_{i=1}^{N}(x_i - \bar{x})^2}. \tag{2.19}$$

Replacing $N-1$ with N, computes the population standard deviation. The variance measures the spread in values x_i and is computed from the square of the standard deviation.

The uncertainty of the best estimate $\bar{x}$ is the standard deviation of the mean, which is denoted as $SDOM$ and is given by Equation 2.20:

$$SDOM\ (x) = \frac{StdDev(x)}{\sqrt{N}}. \tag{2.20}$$

Details regarding the derivation of Equations 2.18, 2.19 and 2.20 can be found in the publication by Taylor (1997).

Using these definitions, the result of an MCNP, KENO, TSUNAMI or Sampler calculation is given by Equation 2.21:

$$\begin{aligned} \text{result} &= \text{best estimate } \pm \text{uncertainty}, \\ \text{result} &= \bar{x} \pm SDOM(x), \end{aligned} \tag{2.21}$$

$SDOM$ is also known as the standard error.

2.10.2 Covariance and correlation

Given N pairs of measurements (x_1,y_1), …, (x_N,y_N), of two quantities x and y, their covariance, $COV(x,y)$ is defined in Equation 2.22 (Taylor, 1997):

$$COV(x,y) = \frac{1}{N-1}\sum_{i=1}^{N}(x_i - \bar{x})(y_i - \bar{y}), \tag{2.22}$$

where $\bar{x}$ and $\bar{y}$ are sample means of the two stochastic variables.

The nuclear data uncertainties are characterized by the statistical measure of covariance, in the form of a covariance matrix. A practical definition of the covariance is “Covariance is a measure of how likely two parameters are to deviate from their reference condition in a consistent direction” (McEwan, 2013).

The linear correlation coefficient is defined by Equation 2.23 for a set of points (x_1,y_1), …, (x_N,y_N) (Taylor, 1997):

$$r = \frac{COV(x,y)}{StdDeV(x)StdDeV(y)}, \tag{2.23}$$

where $StdDeV(x)$ is defined in Equation 2.19 and $StdDeV(y)$ is the sample standard deviation for measurements $y_1, \ldots, y_N$. Substituting the expressions for $StdDeV(x)$, $StdDeV(y)$ and $COV(x,y)$ into Equation 2.23 gives Equation 2.24:

$$r = \frac{\sum(x_i - \bar{x})(y_i - \bar{y})}{\sqrt{\sum(x_i - \bar{x})^2 \sum(y_i - \bar{y})^2}}, \tag{2.24}$$

This measures the extent to which a set of points (x_1, y_1), …, (x_N, y_N), have a linear relationship between them (x and y). With $|r| \leq 1.0$, a value of 1.0 for r indicates a full correlation (y is linearly dependent on x) and 0.0 indicated no correlation (there is no linear relationship between x and y).

2.11 Uncertainty analysis techniques

There exists uncertainty information for the nuclear data of all nuclides as well uncertainty information for other parameters that are important to the particular system. It is possible to quantify the uncertainty in the multiplication factor due these data uncertainties. In terms of quantifying the uncertainty in the calculation due to nuclear data uncertainty, there are two methods in common use which are the sensitivity based methods and the Monte Carlo (stochastic) method.

2.11.1 The sensitivity based method

The first method is the conventional deterministic sensitivity/uncertainty (S/U) method. In the framework of this method the uncertainty in the multiplication factor is calculated deterministically by multiplying (using matrix multiplication) the sensitivity vector $\boldsymbol{S}$ and its transpose $\boldsymbol{S^T}$ by the covariance matrix $\boldsymbol{C}$ such that:

$$\sigma_k^2 = \boldsymbol{S_k C_{\alpha\alpha} S_k^T}. \tag{2.25}$$

Equation 2.25 is colloquially known as the “sandwich rule” and is used to calculate the uncertainty of the response given the estimated sensitivity (Zhu et al, 2015).

The components of this equation are discussed next.

σ_k^2 is the variance of the multiplication factor. $\vec{\alpha}$ is a vector which represents the nuclear data parameters and its elements are $\left(\alpha_{x,g}^i\right)$. The index i is varied over all isotopes, x is varied over all reactions and g is varied over all energy groups.

The covariance matrix ($\boldsymbol{C_{\alpha\alpha}}$) is the symmetric $M \times M$ matrix which contains the variances and covariances in the nuclear data. The variances are the diagonal elements and the covariances are the off-diagonal elements. The parameter M is the product of the number of nuclide-reaction pairs and the number of energy groups.

The elements of $\boldsymbol{C_{\alpha\alpha}}$ are given by:

$$\left(C_{\alpha^i_{x,g}\alpha^j_{y,g'}}\right) = \frac{COV(\alpha^i_{x,g}, \alpha^j_{y,g'})}{\alpha^i_{x,g}\alpha^j_{y,g'}}. \tag{2.26}$$

Similarly to i, the index j is varied over all isotopes, similar to x, the index y is varied over all reactions for each isotopes and similar to g, the index g' is varied over all energy groups.

The numerator of Equation 2.26 is given by:

$$COV\left(\alpha^i_{x,g}, \alpha^j_{y,g'}\right) = \langle \delta\alpha^i_{x,g}, \delta\alpha^j_{y,g'} \rangle. \tag{2.27}$$

where $\delta\alpha^i_{x,g}$ and $\delta\alpha^j_{y,g'}$ are the differences between the expected values and the values of the nuclear data parameters and $\langle \quad \rangle$ represents the integration over $\alpha^i_{x,g}$ and $\alpha^j_{y,g'}$, weighted with a probability density function.

$\boldsymbol{S_k}$ is the sensitivity row vector of length M, which is a one dimensional matrix (a matrix with only one row) of sensitivity coefficients. For the nuclear data parameters, $\vec{\alpha}$, the elements of $\boldsymbol{S_k}$ are given by:

$$S_{k,\alpha^i_{x,g}} = \frac{\partial k/k}{\partial \alpha^i_{x,g}/\alpha^i_{x,g}}, \tag{2.28}$$

where k is the output parameter and $\alpha^i_{x,g}$ is any input parameter. When the input parameter is Σ_x (where Σ_x is a group-wise cross section), Equation 2.28 becomes:

$$S_{k,\Sigma_x} = \frac{\partial k/k}{\partial \Sigma_x/\Sigma_x}. \tag{2.29}$$

Equation 2.25 (the sandwich rule) is derived from a Taylor series expansion of the integral parameters as functions of the input parameters and this equation is a first order approximation. The detailed derivation is given by Zerovnik (2012). It is shown by Zerovnik (2012) that the covariance between two functions f_k and $f_{k'}$ is given by:

$$COV(f_k, f_{k'}) = \sum_{i,j=1}^{P} \frac{\partial f_k(\vec{\alpha}^0)}{\partial \alpha^i} COV\left(\alpha^i, \alpha^j\right) \frac{\partial f_{k'}(\vec{\alpha}^0)}{\partial \alpha^j}, \tag{2.30}$$

where

P is the number of parameters;

α^i are arbitrary parameters of the vector $(\vec{\alpha})$ of the function f_k;

α^j are arbitrary parameters of the vector $(\vec{\alpha})$ of the function $f_{k'}$; and

$\vec{\alpha} = \vec{\alpha}^0 + \vec{s}$, where $\vec{s}$ is the vector of corresponding parameter uncertainties.

Furthermore, as shown by Zerovnik (2012), this formula requires that f_k be expanded as a Taylor series about $\vec{\alpha}^0$ as given in Equation 2.31, where only the terms which are of first order are retained in the definition of Equation 2.30.

$$f_k(\vec{\alpha}^0 + \vec{s}) = \sum_{l=0}^{\infty} \frac{1}{l!} \left(\sum_{i=1}^{P} s_i \frac{\partial}{\partial \alpha^i} \right)^l f_k(\vec{\alpha}^0). \tag{2.31}$$

When f_k is the same as $f_{k'}$, then defining σ^2 as $COV(f_k, f_{k'})$, Equation 2.30 can be expressed as $\sigma^2 = \boldsymbol{S_k C_{\alpha\alpha} S_k^T}$, which is the sandwich rule (Zerovnik, 2012).

The S/U methods can be divided into the "Adjoint method" and the "One at a Time" method. The Adjoint method calculates the sensitivities using adjoint functions. The One at a Time Method operates by varying the input one by one and then observing the response in the output.

The first order perturbations of F, B and ψ of Equation 2.10 can be written as:

$$F' = F + \delta F, \tag{2.32}$$

$$B' = B + \delta B,$$

$$\lambda' = \lambda + \delta\lambda.$$

Given the transport equation in Equation 2.7 and using the first order perturbations of F, B and ψ, Perfetti (Perfetti, 2012) has shown that the sensitivity coefficients can be written as:

$$S_{k,\Sigma_x} = \Sigma_x \frac{\langle \psi^* \left(\lambda \frac{\delta F}{\delta \Sigma_x} - \frac{\delta B}{\delta \Sigma_x} \right) \psi \rangle}{\lambda \langle \psi^* F \psi \rangle}, \tag{2.33}$$

where

$\lambda = \frac{1}{k}$;

$\langle \ \ \rangle$ is the inner product operator;

Σ_x is the macroscopic cross section for reaction x;

ψ is the forward flux; and

ψ^* is the adjoint flux, which is the importance of events that occur during the lifetime of particle histories.

k can be either k_{inf} or k_{eff} depending on the case being studied. For specific reactions the numerator of Equation 2.33 can be split into three terms with the denominator remaining. Hence this equation can be written as:

$$S_{k,\Sigma_x} = \frac{C_s + C_f + C_x}{D}, \tag{2.34}$$

The three numerator "contribution" terms that are products of the forward and adjoint fluxes in region z in a system, which are (Perfetti et al, 2016):

- The scattering contribution C_s, which describes the correlation of the forward and adjoint fluxes in energy and in direction, (Equation 2.35).
- The fission source contribution C_f, which describes how the forward and adjoint fluxes are uncorrelated in direction, (Equation 2.36).
- The collisional contribution C_x for the reaction x, which contains the forward and adjoint fluxes that are completely correlated (Equation 2.37).

$$C_s(z, E \to E') = \int_{V_z} \int_{4\pi} \int_{4\pi} \psi(\vec{r}, E, \hat{\Omega}) \Sigma_S \left(\vec{r}, E \to E', \hat{\Omega} \to \hat{\Omega}'\right) \psi^*\left(\vec{r}, E', \hat{\Omega}'\right) d\hat{\Omega}' d\hat{\Omega} dV\,; \tag{2.35}$$

$$C_f(z, E \to E') = \int_{V_z} \int_{4\pi} \bar{\nu}\Sigma_f(\vec{r}, E)(\vec{r}, E, \hat{\Omega}) d\hat{\Omega} \int_{4\pi} \frac{\chi(\vec{r}, E')}{4\pi} \psi^*\left(\vec{r}, E', \hat{\Omega}'\right) d\hat{\Omega}' dV; \tag{2.36}$$

$$C_x(z, E) = \int_{V_z} \int_{4\pi} \Sigma_x(z, E) \psi(\vec{r}, E, \hat{\Omega}) \psi^*\left(\vec{r}, E, \hat{\Omega}\right) d\hat{\Omega} dV. \tag{2.37}$$

In addition to the contribution terms is the expression D which can be expressed as:

$$D = \lambda \int_V \int_0^\infty \int_{4\pi} \bar{\nu}\Sigma_f(\vec{r}, E)\psi(\vec{r}, E, \hat{\Omega})\, d\hat{\Omega}\mathrm{dE} \int_0^\infty \int_{4\pi} \frac{\chi(\vec{r}, E')}{4\pi} \psi^*(\vec{r}, E', \hat{\Omega}') d\hat{\Omega}' dE' dV. \tag{2.38}$$

D is the denominator term and is defined as the adjoint weighted fission source term integrated over all regions and nuclides. The contributions C_s, C_f, C_x and D can be used to calculate the sensitivity coefficients for a neutron in energy group g in region z of a system (Perfetti et al, 2016).

The sensitivity coefficients for capture cross section, $S_{cap}(z, g)$, can be expressed as shown in Equation 2.39 and the sensitivity coefficient for the fission cross section, $S_f(z, g)$, can be expressed as Equation 2.40. The sensitivity coefficient for the scattering cross section, $S_s(z, g)$, is shown in Equation 2.41.

$$S_{cap}(z, g) = -\int_g \frac{C_{x=cap}(z, E)}{D} dE\,; \tag{2.39}$$

$$S_f(z, g) = \int_g \left[\int_0^\infty \frac{C_f(z, E \to E')}{D} dE' - \frac{C_{x=fis}(z, E)}{D}\right] dE\,; \tag{2.40}$$

$$S_s(z, g) = \int_g \left[\int_0^\infty \frac{C_s(z, E \to E')}{D} dE' - \frac{C_{x=sca}(z, E)}{D}\right] dE. \tag{2.41}$$

The sensitivity coefficient for $\bar{\nu}$ is expressed in Equation 2.42 and the sensitivity coefficient for χ(unconstrained) is expressed in Equation 2.43, since these terms only appear in Equation 2.36 in terms of the three terms in the numerator of Equation 2.34.

$$S_{\bar{\nu}}(z, g) = \int_g \left[\int_0^\infty \frac{C_f(z, E \to E')}{D} dE'\right] dE\,; \tag{2.42}$$

$$S_\chi(z, g) = \int_g \left[\int_0^\infty \frac{C_f(z, E \to E')}{D} dE'\right] dE. \tag{2.43}$$

In the above equations, the integral $\int_g \ldots dE$ means that the limits of the integral is set at the group g boundaries.

The deterministic method computes the first-order sensitivity coefficients of the output parameter of interest and then folds the sensitivities with the covariance matrix of the input nuclear data in Equation 2.25.

2.11.2 The stochastic method

The stochastic sampling method is a more recent approach. In the stochastic sampling method, a set number of input files (N) are generated. In these files specific input variables are identified which have uncertainties that would affect the result. These variables are then perturbed randomly using presumed probability distributions creating N distinct input files for N calculations and N output files are subsequently produced. The uncertainty is found by analysing the distribution of the outputs.

Dependencies between the input variables can exist and are taken into account using the covariance matrices. The resulting uncertainties depend both directly on the choice of input and the input covariance matrix. In this study Sampler is the uncertainty code that uses this method and the nuclear data and its covariance matrix form the basis for the input. It is noted that other parameters such as the CP diameter can also be varied with or without the use of covariance data.

2.12 Continuous energy UQ methods

The conventional approach for Uncertainty Quantification (UQ) using perturbation theory in SCALE is MG TSUNAMI. The need to compute higher fidelity sensitivity coefficients as well UQ for advanced reactor designs are some of the factors that have led to the idea of generating sensitivity coefficients using CE based methods (Perfetti, 2012). Sensitivity analysis with CE physics has shown improvements in accuracy (Perfetti, 2013).

The different methods for UQ in CE physics which are explored or mentioned in this study are the Iterated Fission Probability (IFP) Method and the Contribution Linked eigenvalue sensitivity/Uncertainty estimation via Tracklength importance Characterization method (CLUTCH). Other methods include a combination of both methods. The IFP method is used in SCALE but is also used in the Monte Carlo N-particle (MCNP) code and the Monte Carlo Code for Advanced Reactor Design and analysis (McCARD) as reported in Perfetti (2012).

The IFP method estimates the importance of events during a particle's lifetime (Rearden et al, 2016). The IFP method uses the notion that the importance of an event is proportional to the population of neutrons present in the system during some future generation that are descendants of the original event (Rearden et al, 2016). The IFP method requires storage of region, isotope, reaction and energy-dependent reaction rates for every particle for a chosen number of latent generations.

The CLUTCH method is a Contribution Linked method and is the preferred choice since the CLUTCH method calculates sensitivity coefficients with the highest degree of efficiency (Perfetti, 2016). The CLUTCH method was developed by Perfetti (2012) as academic research and is recorded in great detail in reference (Perfetti, 2012). The CLUTCH method is based on the Contribution Theory which was developed by Mark Williams (Rearden et al, 2016). In the work done by Perfetti, the CLUTCH method is compared to other methods for computing eigenvalue sensitivity coefficients. The CLUTCH method performed well in terms of accuracy, speed, efficiency and memory and was comparably better than the conventional MG TSUNAMI approach. The CLUTCH method has a lower memory footprint than the IFP method and the MG TSUNAMI method. The IFP method had the largest memory footprint and the amount of memory required for an IFP complex problem calculation could easily exceed 100 gigabytes (Perfetti, 2012). In the thesis written by Perfetti (2012) it is also shown that the CLUTCH method takes much less computational time when compared to the IFP method and the MG TSUNAMI method. The IFP method is easier to use since it doesn't require a spatial mesh whilst the accuracy of the results produced by the CLUTCH method relies on the proper definition of the spatial mesh.

The IFP and CLUTCH methods are discussed further in Section 3.8.

CHAPTER 3: THE REACTOR CODES

This chapter discusses the various codes in the SCALE package that are applicable to this work. The codes are defined and the important parameters that are applied to this work are also discussed. The input generator NWURCS is defined and discussed.

3.1 The physics treatment in SCALE

The CE treatment is more accurate and versatile and has the capability of modelling without major approximations (Leppanen and DeHart, 2009). However, it is computationally expensive and the double heterogeneity of the fuel drastically increases run time. In the CE treatment, the calculations are only performed at temperatures available in the data libraries. The MG treatment in SCALE has superior runtime performance and provides efficient and effective solutions (Rearden et al, 2015). A comparison of the computational expenditure is presented in Chapter 6.

3.2 Nuclear data

Nuclear Data is the basic input to neutronic calculations. It describes the different reactions of neutrons with the atomic nuclei defined in the core (Zwermann, et al, 2014). A number of collaborating nuclear data agencies collect published experimental and theoretical cross sections (Hart et al, 2013) which form part of the nuclear codes and are kept up to date. SCALE 6.2 includes the addition of the nuclear data library ENDF/B-VII.1 for CE calculations and the corresponding 252-group library for the multigroup calculations. The ENDF/B-VII.1 cross section library has updated carbon capture cross sections when compared to the previous version of the library which is the ENDF/B-VII.0 (Bostelmann and Strydom, 2017). These carbon cross sections have a large impact resulting in large differences in calculations using ENDF/B-VII.1 and ENDF/B-VII.0. Since the HTGR is comprised of large amounts of graphite, using the more updated library is crucial, when propagating the uncertainties due to nuclear data. Hence ENDF/B-VII.1 is used to perform all the calculations in this work.

Bostelmann and Strydom (2017) reports a difference of several hundred pcm in the criticality calculations of the VHTRC full core, fuel block and fuel pin calculations using CE KENO-VI of SCALE 6.2 between the ENDF/B-VII.0 and ENDF/B-VII.1 library. The ENDF/B-VII.0 library applied to the CE KENO VHTRC criticality also showed an overestimation of the experimental results by several hundred pcm whilst the ENDF/B-VII.1 calculations were more comparable to the experimental results by a few hundred pcm (Bostelmann and Strydom, 2017). For the MHTGR-350 fuel compact and fuel block the differences were reported to be 100-300 pcm between the ENF/B-VII.0 and ENDF/B-VII.1 library.

In literature, it has been noted that there is a bias of 200-500 pcm for the 238-group library in LWR systems when compared to the CE results. Specifically, in the study by Gehin et al (2010), the difference between CE and MG 238-group library is 336 pcm (Gehin, et al, 2010). The 252-group library provides a more detailed representation of the ^{238}U resonance structure. The MG results computed with 252-group library are more consistent with the CE results (Rearden et al, 2016).

SCALE also has neutron cross section covariance data for neutron interactions and fission yields for use in sensitivity analysis and uncertainty analysis in TSUNAMI and Sampler. The 252-group neutron cross section covariance data derived from ENDF/B.VII.1 (252groupcov7.1) is used for the MG calculations. The 238-group neutron cross section and its covariances are derived from ENDF/B-VII.0 library.

It should be noted that the ENDF/B-VII.0 and 238-group structure is only used for the criticality calculations presented in this work for comparison with other literature (Maratele, 2016; Naicker et al, 2016; Strydom et al, 2015). The HTTR has been studied by other authors (Bess and Fujimoto, 2014; Bess, 2010; Chiang et al, 2014; Ilas and Gehin, 2010; Ilas et al, 2012) using ENDF/B-VII.0, hence HTTR calculations are computed in this thesis with this library to allow for comparison with other publications.

The nuclear data libraries, ENDF/B-VII.0 and ENDF/B-VII.1 are generated with the AMPX (which is an acronym for Automation of MUG, POPOP4 and XLACS) codes. More details on AMPX can be found in (Wiarda, et al, 2016).

3.3 The SCALE method and basic definitions

Computations with SCALE are characterized by the type of analysis, i.e.

- criticality analysis;
- radiation shielding;
- reactor physics;
- activation, depletion and decay;
- sensitivity analysis and uncertainty analysis (i.e. TSUNAMI and Sampler).

The SCALE codes contain a number of modules, and these can be distinguished as:

Control modules: The control modules automate the use of functional modules and data to perform system analysis e.g. CSAS*,* TSUNAMI-3D-K6 *and* TRITON*.*

Functional modules: Well established computer codes that are executed by the Control module/sequence e.g.: KENO-VI*,* NEWT *and* SAMS 6*.*

The purpose of the transport codes is to:

- Calculate the multiplication factors and flux distributions of fissile systems.
- Calculate collapsed cross sections when using deterministic codes.

The purpose of the uncertainty codes in SCALE is to:

- “Identify important processes in safety analysis and design” (Rearden et al, 2016).
- “Provide a quantifiable basis for neutronics validation for criticality safety and reactor physics analysis” (Rearden et al, 2016).
- “Quantify the effects of uncertainties in nuclear data and physical parameters for safety analysis” (Rearden et al, 2016).

The SCALE codes applicable to this work as well as their functions are summarized in Table 3-1.

Table 3-1 A summary of the codes used in this work

Analysis Function	**Control Module**	**Functional Module**		
Reactor physics	TRITON	XSProc	NEWT	
Criticality safety	CSAS6	XSProc	KENO-VI	
Uncertainty analysis	CE TSUNAMI-3D-K6	XSProc	CE KENO-VI	SAMS 6
	Sampler	XSProc	MG KENO-VI, NEWT	

3.4 Material processing and XSProc

XSProc (Cross section Processing) processes material input and provides a temperature and resonance-corrected cross section library based on the physical characteristics of the problem being analysed. XSProc can operate as a stand-alone code or be used as part of an integrated sequence (TRITON, CSAS). For MG calculations, XSProc provides resonance self-shielding as well as energy group collapse and spatial homogenization for systems that can be represented in cell data input. Cross sections are generated on a microscopic basis as necessary.

Self-shielding of multigroup cross sections is required in SCALE sequences. The cell data block takes care of the resonance self-shielding. XSProc calls two codes for generating the fluxes, viz. BONdarenko AMPX Interpolator (BONAMI) and Continuous Energy Transport Module/ Produce

Multigroup Cross sections (CENTRM/PMC). Self-shielding calculations with BONAMI are fast and are always performed for all SCALE sequences. BONAMI uses the Bondarenko factors to treat self-shielding. Bondarenko factors are multiplicative correction factors that convert the generic unshielded data into problem-dependent self-shielded values (Rearden et al, 2016).

The CENTRM/PMC method is a more rigorous approach to self-shielding treatment of the MG cross sections and replaces the BONAMI results over the resolved resonance ranges of important absorber nuclides. Shielded cross sections processed with CENTRM/PMC are usually more accurate than the BONAMI cross sections (Rearden et al, 2016). CENTRM executes BONAMI first. CENTRM calculates the pointwise flux spectra by solving the deterministic neutron transport equation for all unit cells described in the input, using a combination of the shielded MG data from BONAMI and CE data. The energy group collapsing is carried out by PMC once the fluxes have been determined by CENTRM. Only the CENTRM/PMC method is applicable for double heterogeneous systems.

Realistically the HTGR has a stochastic particle distribution and each particle differs from the next. For non-uniform configurations, BONAMI and CENTRM assume that the fuel is arranged in an infinite lattice of identical cells (Rearden et al, 2016).

With the CE cross section library, resonance cross section processing is not necessary for calculations using the CE methodology.

3.4.1 The doublehet treatment

In order to treat the double heterogeneity of the HTGR fuel, CENTRM/PMC calculations are performed at the two levels of heterogeneity. In the first level of heterogeneity, CENTRM calculations are done for each type of coated particle using a spherical unit cell to represent the array of multi-layered fuel particles distributed in the graphite matrix. Space-dependent fluxes from these calculations are used to compute disadvantage factors (fuel-average flux divided by cell-average flux) for generating cell-averaged cross sections representative of the homogenized fuel region. The new cell weighted cross section mixture preserves most of the characteristics of the original heterogeneous cell (Wang et al, 2014). These are then used to calculate the flux distribution in the second level of heterogeneity (fuel element).

The CE cross sections are then used in the CENTRM transport calculation corresponding to a 1D unit cell model for the array of fuel elements, with homogenized number densities for the fuel compact (taken from the calculation described in the preceding paragraph). Self-shielding of double heterogeneous cells requires multiple CENTRM/PMC passes.

3.5 Transport codes

SCALE is equipped with 1D, 2D and 3D codes that solve the neutron transport equation either stochastically or by discrete-ordinates. Two of these functional modules as well their control modules are discussed in this section.

3.5.1 CSAS6/KENO-VI

There are two variants to the KENO code. One is the KENO-V.a and the other is KENO-VI. The latter is used in this work. KENO-VI is a transport code used for criticality safety analysis (Rearden et al, 2016). It is based on the Monte Carlo method for eigenvalue calculations. KENO-VI has identical solution capabilities as its sister code KENO-V.a but the geometry packages differ, with KENO-VI being based on the SCALE Generalized Geometry Package (SGGP) geometry, which boasts the ability to model very complex geometries such as the hexagonal arrays of the HTGR and VVER reactors and the dodecagon of the HTTR permanent reflector.

It is the Criticality Safety Analysis Sequence (CSAS) with KENO-VI that assesses the multiplication factor and flux distributions of fissile systems in continuous and multigroup modes.

3.5.2 TRITON/NEWT

Transport Rigor Implemented with Time-dependent Operation for Neutronic depletion (TRITON) is the reactor physics control module that provides NEWT with the capability of performing deterministic transport calculations for 2D geometries; the 2D transport calculations are executed with TRITON/NEWT.

NEWT also supports collapsing of cross sections. The flux weighted collapse is done by material number and cross sections for each nuclide in each material are collapsed to a specified or default group structure based on the average flux in that material. When a nodal homogenization block is specified then one set of cross sections for the node is also calculated (Rearden et al, 2016).

3.6 CE parameters

3.6.1 Problem dependent doppler broadening and Doppler Broadening Rejection Correction in CE.

The data in the CE libraries are provided per isotope at specific temperatures. These temperatures may not match the desired temperature of the calculation. CE KENO-VI operates by selecting the nearest temperature when the temperature specified in the input is not available, but this can cause a bias of several hundred pcm (Rearden et al, 2016). The manner in which

Doppler broadening is carried out is controlled by the parameter "DBX". SCALE gives the user the following options:

- $DBX = 0$ To select the nearest temperature.
- $DBX = 1$ To perform problem-dependent corrections for the resolved and unresolved resonance ranges.
- $DBX = 2$ To perform also corrections for the $S(\alpha, \beta)$ thermal scattering data.

$DBX = 2$ is the default and it is the selected parameter for this work. The choice of the DBX parameter has no effect on the time (Rearden et al, 2016).

The Doppler Broadening Rejection Correction (DBRC) only applies in the CE mode and is a method that takes into account the varying cross sections in terms of the target velocity distribution. When a neutron collides with a heavy nucleus, elastic scattering occurs, the velocity and direction of the scattered neutron depends on the thermal motion of the target nucleus (Hart, 2013; Rearden et al, 2016). These studies have shown that the resonance scattering caused by thermal motion of heavy nuclei can have a significant effect on the criticality calculations.

KENO-VI simulates elastic collisions between a thermal neutron and a target nuclide based on a neutron at thermal energies by using the scattering law data, provided that the data is available. If thermal scattering law data are not available in the nuclear data library, elastic scattering is treated with the free gas approximation in the KENO library. However, for heavy nuclides with 0 K scattering libraries available, the DBRC method can also be used.

The energy cut-off (in eV) up to which the DBRC method will be used on nuclides can be varied and is known as the DBH. The energy cut-off down to which the DBRC method will be used on nuclides for which the DBRC is enabled can also be varied. This parameter is known as the DBL. The DBH and the DBL are studied in Section 6.1.2. It is therefore of interest to note the effect of varying of these limits on the multiplication and uncertainty parameters. Previous studies have shown that the choice of this parameter is important, however the sensitivity to the lower energy limit and effect on the uncertainty propagation has not been shown in HTGRs. This has been done for LWRs in MCNP (Sunny et al, 2013).

The fuel packing, fuel enrichment and fuel temperature cause HTGR criticality calculations to be the most affected by this phenomenon (Sunny et al, 2013). One should note that the HTGR operates at very high temperatures and the effect of the DBRC is more pronounced with an increase in temperature.

3.7 MG parameters

3.7.1 Coarse-mesh finite-difference acceleration in NEWT

The NEWT iterative approach requires *inners* and *outer*s iterations. *Inner* iterations are used to solve spatial fluxes in each energy group to generate updated source terms. *Outer* iterations use these source terms to converge to all energy groups. The source iteration approach can converge slowly especially in systems with a large graphite content such as the HTGR, hence the coarse-mesh finite-difference acceleration (CMFD) formulation must be applied. The CMFD option is available in NEWT.

The CMFD formulation uses a simplified representation of a complex problem, in which selected rectangular regions are derived from the global NEWT Cartesian grid and homogenized. CMFD acceleration uses coupling correction factors for each homogenized cell to homogenize the constituent ESC-based polygonal cells dynamically during the iterative solution process such that the heterogeneous transport solution can be preserved.

The original implementation of CMFD is only applicable to the rectangular-domain configurations. Therefore, alternate CMFD acceleration methods have been developed to accommodate triangular and hexagonal geometries, which are the “unstructured” and “partial unstructured” methods. The unstructured CMFD is based on the conventional net current approach whilst the partial unstructured CMFD method is based on partial currents. Both methods assume the same structural computational grid (Kim and DeHart, 2011).

The SCALE manual recommends that the unstructured or partial unstructured CMFD acceleration is applied for hexagonal geometries (Rearden et al, 2016).

3.7.2 Dancoff factor

When neutronic calculations are conducted that involve the coated particle, it is imperative that the Dancoff factor calculation be taken into consideration. For uniform lattice calculations, XSProc calculates the Dancoff factor automatically and this factor need not be calculated explicitly (Rearden et al, 2016). The Dancoff factor is required for arbitrary arrangements of fuel elements. It is characterized by a random CP distribution and the Dancoff factor for TRISO fuel particles is defined as the average probability that a resonance neutron emitted by a cosine current distribution from the surface of a fuel kernel enters another fuel kernel without a experiencing collision (Ji et al, 2014).

In SCALE 6.2, Dancoff factors are used to correct self-shielded multigroup cross sections for a given problem when the automatic calculation is considered inadequate, either as input to

BONAMI or to determine an equivalent cell for CENTRM (Rearden et al, 2016). There exists the McDancoff programme in SCALE 6.2, which is designed to calculate the Dancoff factor in complicated geometries. The limitation of this code is that it only accounts for the fuel kernel interactions within a pebble (Qin et al, 2016).

3.8 Sensitivity and uncertainty codes

SCALE is equipped with a suite of computational tools for sensitivity analysis (SA) and uncertainty analysis (UA). The tools used in this thesis are CE TSUNAMI-3D and Sampler.

3.8.1 CE TSUNAMI

CE TSUNAMI-3D calculates the sensitivity coefficient in one forward calculation whilst the MG TSUNAMI requires an adjoint and a forward calculation, as illustrated in Figure 3-1. In this figure, the code BONAMIST is shown. BONAMIST is a sensitivity version of BONAMI mentioned in Section 3.4. This code computes the problem-dependent multigroup cross sections along with their sensitivities to the input data.

CE TSUNAMI-3D is used to compute the uncertainty in the multiplication factor together with its sensitivity to energy-dependent cross section data for each reaction of each nuclide in a system model. The use of CE physics in comparison to MG physics improves the accuracy of the sensitivity coefficient (Rearden et al, 2015).

MG TSUNAMI is the conventional/traditional calculation methodology, but it has limited use in HTGR systems due to the doubly-heterogeneous nature of the coated particle. In order to run a MG TSUNAMI calculation, one would have to homogenize the double heterogeneous fuel. This is inaccurate as homogenization of fuel does not treat self-shielding. Hence only the CE TSUNAMI-3D is used.

The CE TSUNAMI method differs from the MG TSUNAMI method for the following reasons:

1. It does not require a separate adjoint Monte Carlo calculation. CE TSUNAMI tallies the sensitivity coefficient contributions directly as depicted in Figure 3-2.
2. No spatial flux mesh is used for tallying neutron fluxes. But a spatial mesh is required for the CLUTCH method.
3. CE TSUNAMI does not use Legendre moments for capturing the angular dependence of the neutron fluxes.
4. CE TSUNAMI does not require the calculation or knowledge of material volumes within the elements of the spatial mesh flux.

5. CE TSUNAMI does not require implicit sensitivity calculations to account for the effects of cross section adjustments related to the incorporation of problem-dependent, self-shielded MG cross sections.

Two separate methods exist for the UA and SA in CE TSUNAMI. The first is the IFP method and the second is the CLUTCH method. The CLUTCH method is the selected method in this work due to its faster run time and computational efficiency. The CLUTCH method has an extremely low memory footprint but has more user complexity in comparison to the IFP method since its accuracy depends on the proper definition of the $F^*(\vec{r})$ mesh. The function of $F^*(\vec{r})$ is to provide an estimate of the average importance of a fission neutron at a location $\vec{r}$. The convergence of this function is assessed in Section 6.4 for the MHTGR-350 systems and Section 8.4 for the HTTR systems.

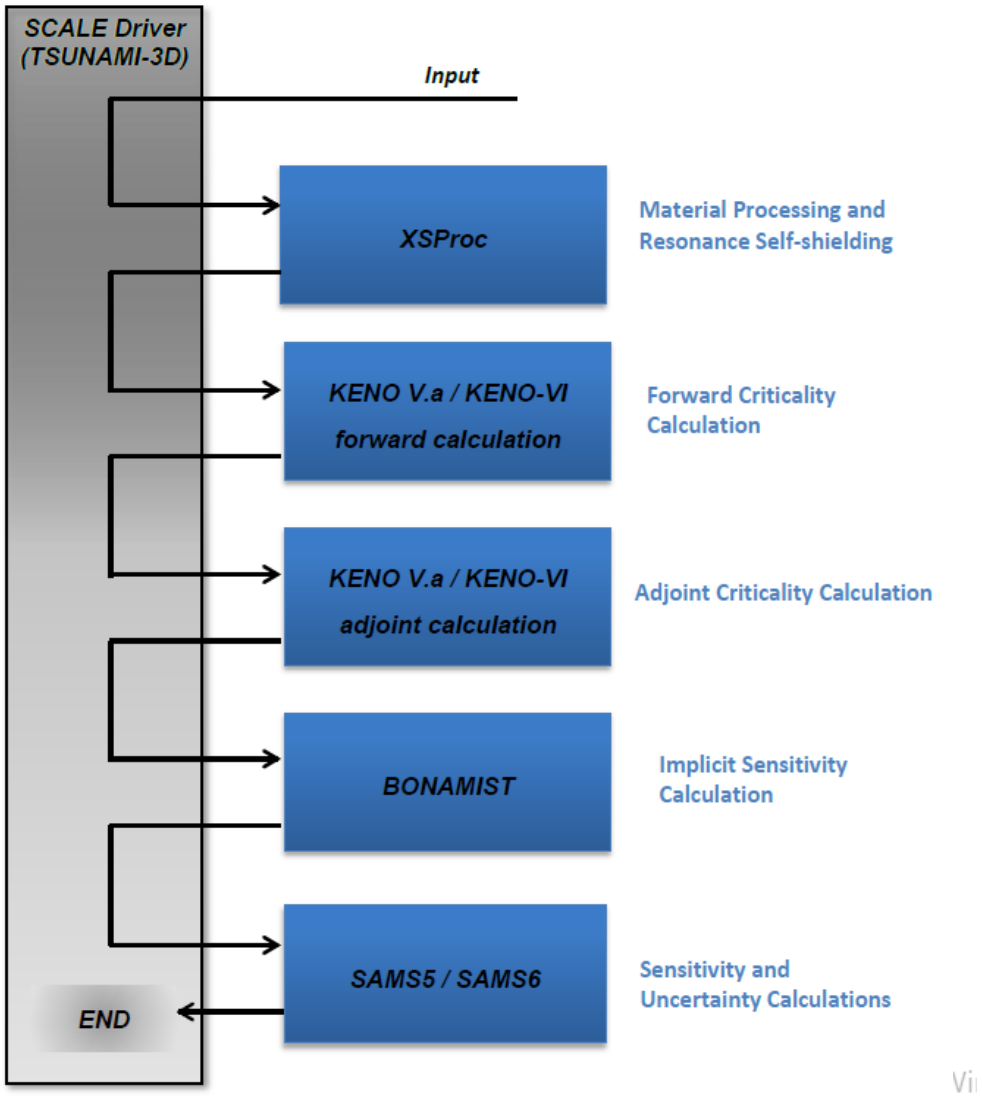

Figure 3-1 SCALE driver for MG TSUNAMI (Rearden et al, 2016).

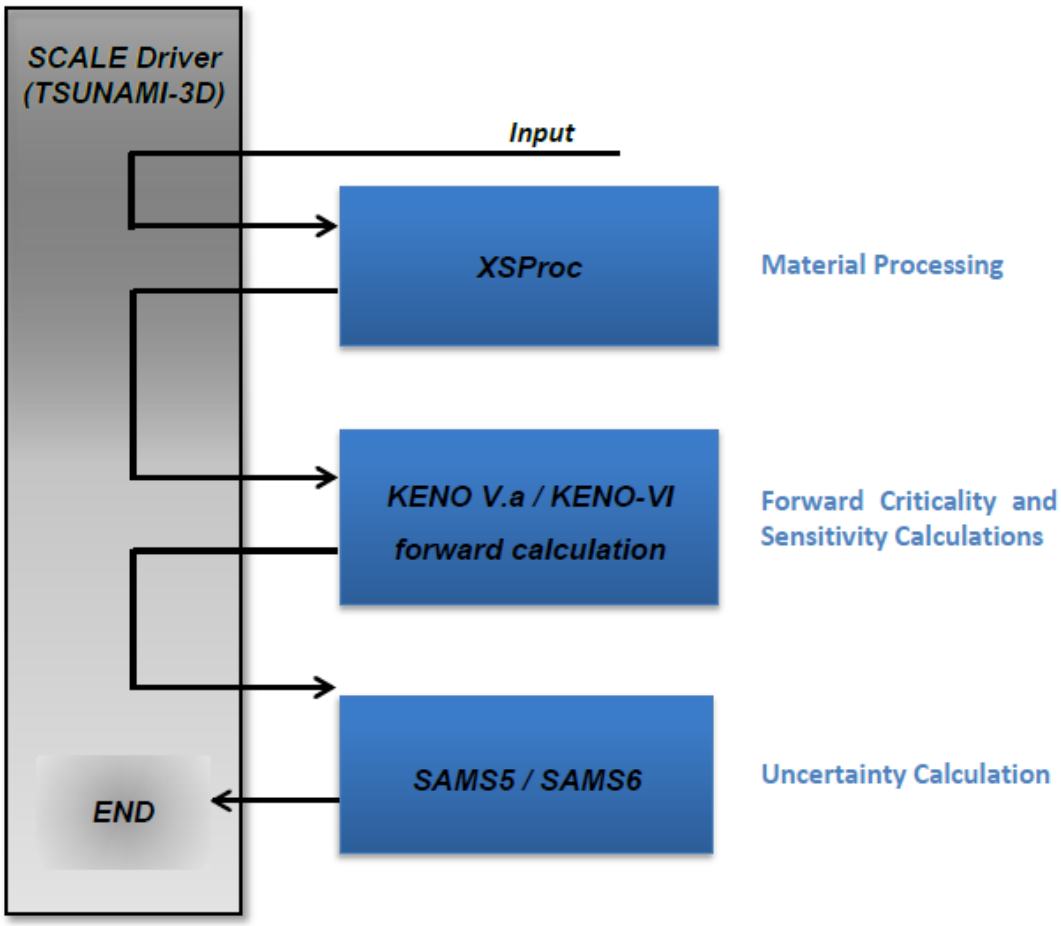

Figure 3-2 SCALE driver for CE TSUNAMI (Rearden et al, 2016).

(i) The IFP method

The IFP method requires storing reaction rate tallies for a particle that initiates an event, known as a progenitor, for some number of generations until the average population of the progenitor's descendants in the system, or asymptotic population, is obtained. The IFP process is shown in Figure 3-3. A number of generations, referred to as the latent generations, must be skipped before calculating the asymptotic population for an event to guarantee that the progenies of that event have had sufficient time to converge to a true estimate of the asymptotic population. Twenty is typically a conservative number of latent generations (Rearden et al, 2016) and ten is the default number of latent generations. The asymptotic population is tallied by scoring the fission neutron production of the progeny of an event in the asymptotic generation, and is used to weight reaction rate tallies for this progenitor to produce sensitivity coefficient estimates.

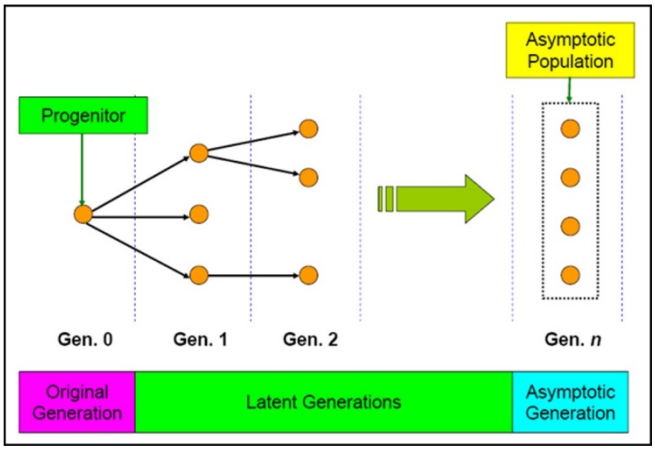

Figure 3-3 The IFP process (Rearden et al, 2016).

(ii) The CLUTCH method

The CLUTCH method calculates the average importance of events during a neutron's lifetime by examining how many fission neutrons are created by that particle after those events occur.

Consider a neutron source Q, which is equal to the fission source of a system:

$$Q = \lambda F \psi. \tag{3.1}$$

The source is multiplied by the adjoint flux and integrated over phase space, which gives

$$< \psi^* Q >= \lambda < \psi^* F \psi >. \tag{3.2}$$

The importance of a neutron in phase space τ_s is calculated from Equation 3.3, that is deduced from Equation 3.2:

$$\psi^*(\tau_s) = \frac{\lambda}{Q_s} \int_V G(\tau_s \to \vec{r}) F^*(\vec{r}) d\vec{r}, \tag{3.3}$$

where

Q_s is the neutron source in phase space, such that $Q_s = Q_s(\tau_s \to \vec{r})$; and

$G(\tau_s \to \vec{r})$ is the transfer function and is defined as the expected number of fission neutrons generated in all energies and directions due to a neutron emitted in phase space and can be expressed as:

$$G(\tau_s \to \vec{r}) = \frac{1}{Q_s}\int_V \int_{\hat{\Omega}} \nu\,\Sigma_f(\vec{r},\, E)\psi(\vec{r}, E, \hat{\Omega}|G(\tau_s \to \vec{r})Q(\tau_s))d\hat{\Omega}dE, \tag{3.4}$$

where

$\psi(\vec{r}, E, \hat{\Omega}|G(\tau_s \to \vec{r})$ is the flux created in phase space $(\vec{r}, E, \hat{\Omega})$ given the source $Q(\tau_s)$.

$$F^*(\vec{r}) \;= \int_E \int_{\hat{\Omega}} \frac{\chi(\vec{r},E)}{4\pi}\psi^*\big(\vec{r}, E, \hat{\Omega}\big)d\hat{\Omega}dE, \tag{3.5}$$

where $F^*(\vec{r})$ is the weighting function and is defined as the expected importance of a fission neutron emitted at $\vec{r}$.

The accuracy of the result computed by the CLUTCH method depends on the proper definition of $F^*(\vec{r})$ on the spatial mesh. Essentially the CLUTCH method calculates the integral of the transfer function, which is weighted by $F^*(\vec{r})$, to calculate the importance of every event in a particle's lifetime.

Example: The importance of a scattering collision is determined by tallying how many fission neutrons weighted by $F^*(\vec{r})$ at the sites where they are born are created by the neutron that emerges from the scattering collision.

The approach to calculating $F^*(\vec{r})$ takes advantage of the unconstrained fission spectrum sensitivity coefficient. From Equation 2.36 and Equation 2.41, the unconstrained fission spectrum sensitivity coefficient is given by:

$$S_{k,\chi}(\vec{r}) = \frac{1}{D}\frac{1}{k}\int_0^{\infty}\int_0^{4\pi} \bar{\nu}\Sigma_f(\vec{r}, E)\psi(\vec{r}, E, \hat{\Omega})d\hat{\Omega}\mathrm{d}E \int_0^{\infty}\int_{4\pi} \frac{\chi(\vec{r}, E')}{4\pi}\psi^*\big(\vec{r}, E', \hat{\Omega}'\big)d\,\hat{\Omega}'dE'. \tag{3.6}$$

The terms of Equation 3.6 can be arranged such that:

$$F^*(\vec{r}) \;= \frac{D \;\times S_{k,\chi}(\vec{r})}{\int_0^{\infty}\int_{4\pi}\frac{\bar{\nu}\Sigma_f(\vec{r}, E)\psi(\vec{r}, E, \hat{\Omega})}{k}d\hat{\Omega}dE}. \tag{3.7}$$

3.8.1.1 Rules for $F^*(\vec{r})$ convergence

- $F^*(\vec{r})$ is calculated and stored on the $F^*(\vec{r})$ mesh.
- $F^*(\vec{r})$ is only non-zero for regions containing fissionable material and $F^*(\vec{r})$ must cover all fissionable materials.
- $F^*(\vec{r})$ tallies are obtained during the "inactive" generations of a Monte Carlo calculation.
- The fission source must converge well enough during the inactive generations so that $F^*(\vec{r})$ is tallied in all fissile regions to a desired statistical uncertainty.
- The SCALE manual recommends that there are 50 to 100 inactive histories per voxel (a volume element in a regular 3D grid) to allow for $F^*(\vec{r})$ to converge. This recommendation is investigated in Section 6.4 and Section 8.4.
- The CLUTCH method performs the IFP method first.

3.8.2 SAMS

SAMS is the acronym for Sensitivity Analysis Module in SCALE, and its function is to calculate the sensitivity coefficients that predict expected changes of the calculated value of system responses such as k_{inf} and reaction rate ratios due to perturbations in constituent cross section data. In the MG treatment (MG TSUNAMI-3D), SAMS generates the sensitivity coefficients using a forward and adjoint calculation. In the CE treatment (CE TSUNAMI-3D) SAMS is only used to provide edits of sensitivity and uncertainty results. The sensitivity coefficients computed in CE mode are stored in a multigroup sensitivity data file.

3.8.3 Sampler

Sampler is a super-sequence that treats uncertainties from nuclear data and input parameters. It implements the stochastic sampling of uncertain parameters that can be applied to any type of SCALE calculation, propagating uncertainties throughout a computational sequence (Rearden et al, 2016). A number of passes are repeated through the computational sequence; each pass has a randomly perturbed sample of the requested quantities. The mean value and uncertainty of each parameter is reported in the output along with the correlation in uncertain parameters where multiple systems are sampled simultaneously with correlated uncertainties (Rearden et al, 2016).

The main components of a Sampler calculation are the procedures for perturbing input data, obtaining the desired responses, and performing statistical analysis of the output distributions.

For the nuclear data transport calculations, a master sample file containing perturbation factors for 1000 samples of the infinitely-dilute 1D data has been pre-computed and stored in the SCALE

data directory. For the depletion data perturbations, a set of 1000 decay data perturbations have also been generated with XSUSA and stored in decay-only ORIGEN library files. If N samples are to be run, Sampler then creates N input files, where each files uses a specific instance from the pre-computed perturbed data.

Sampler can perturb parameters other than the nuclear data in the N input files to create perturbed values of these parameters in these files as mentioned in Section 2.11.2.

3.9 Validation of the SCALE 6.2 code

Validation is an integral part of the code development process. SCALE 6.2 is validated for criticality calculations using a total of 401 unique critical experiments for KENO-VI and KENO-V.a (Marshall et al, 2013). This validation is reported by Marshall et al (2013). One of the findings in the work published by Marshall is that SCALE 6.2 generally provides lower biases than SCALE 6.1, i.e. the 252-group library shows a significant bias improvement compared to the 238-group library. The SCALE 6.2 and SCALE 6.1 versions of KENO-VI provide equivalent results. The validation for pebble-bed and prismatic HTGR criticality analyses using SCALE is reported in Ilas et al (2012).

Working parties such as the IAEA CRP on HTGR UAM use TSUNAMI and Sampler for benchmark calculations. Code to code comparisons are done and this helps to validate TSUNAMI and Sampler.

Some examples of other working parties that use TSUNAMI and Sampler are:

- OECD-NEA Working Party on Cooperation on Investigation of Covariance Data in General Purpose Nuclear Data Libraries (Salvatores and Palmiotti, 2018).
- OECD-NEA Light Water Reactor UAM Benchmark for UAM for Design, Operation and Safety Analysis (Ivanov, et al, 2013).

3.10 NWURCS

NWURCS is a suite of codes developed at the North-West University in South Africa. Its function is to produce inputs for KENO-VI, NEWT, MCNP6 and RELAP5. Version 2.1 of NWURCS was used in this work and this version was developed during the course of this work. Development of version 1.0 began in 2012 (Nyalunga et al, 2016). In this work NWURCS is used to generate the KENO-VI input models. NWURCS has not been verified for KENO-VI. It was verified for MCNP6 with an application to the model of the VVER-1000 (Nyalunga et al, 2016). One of the verification

methods was visual inspection of the MCNP6 plots. The multiplication factor of the full-core NWURCS VVER model was compared to the NWURCS 1/6 core model and the difference was within 1σ, essentially these models should be equivalent (Nyalunga et al, 2016). Additionally, NWURCS has been used for a coupled MCNP6-RELAP5 model with an application to the EPR (du Toit, 2017).

In this work, the unit cells and fuel block models of the MHTGR-350 were produced manually by the author. The HTTR is used for validating the models developed. Considering that the modelling for the unit cell and the fuel block of the MHTGR 350 system was well established in this work, the insight gained in this modelling was therefore carried over to the HTTR.

However, the HTTR had multiple definitions for the fuel block in the reactor core. Some of the changes amongst fuel blocks were enrichment, number of fuel pins, as well orientation. In terms of graphite blocks which contain control rod holes, some of the differences was the orientation of the control rods holes. Whilst the modelling of this core could be carried out manually, it could be prone to human error. Therefore, it was decided to use NWURCS to create the input model.

However, since NWURCS has not been used to model an HTGR other than in this work, it was therefore required to verify that NWURCS could be used to model this type of system. This verification is presented in Chapter 8. Once the verification was established as per the needs of this study, NWURCS was then used to model the HTTR reactor core.

3.10.1 NWURCS input generation.

The NWURCS input is contained in multiple folders which are used or generated by the user. Collectively the files in these folders band together to form the input file for NWURCS. The main folders operated by the user are the ixxxxx folder and the FAX folder.

The “ixxxxx” folder contains files that have information regarding the core layout, the core dimensions, the core arrays, temperatures and materials. Additionally, the coated particle files (“cparray_xxxx.i”) as well as the control rod definition files are found in this folder.

The “FAX” folder contains the geometry specifications for all the fuel assemblies. This includes the graphite blocks, fuel blocks, coolant channel blocks and control rod blocks.

The “ioxxxx” folder contains files that are generated and subsequently used by NWURCS. They can be viewed by the user but not edited. A few of the files in this folder are used to generate some of the files found in the “ixxxxx” folder for iterative use.

The “oxxxx” folder contains all the output. The generated input files for MCNP, NEWT, KENO-VI and RELAP5 are not kept in this folder.

CHAPTER 4: THE REACTOR SYSTEMS

This chapter presents the design of the systems studied in this work. The systems are described in terms of geometry, dimensions and materials. The MHTGR-350 is discussed as well as the HTTR. The design specifications of the MHTGR-350 are limited to the first two IAEA benchmark exercises of the CRP UAM on HTGR. The experimental design and the benchmark model of the HTTR are also covered in this chapter. The experimental design is presented in Sections 4.3 and 4.4. The benchmark model, which is based on the fully-loaded critical core is covered in section 4.5. The history and development of the reactors, as well as their function is also discussed briefly.

4.1 The MHTGR-350

The MHTGR-350 is a prismatic conceptual design from General Atomics that has existed since the 1980s (NEA/NSC/R(2017)4, 2018). The full core model is not studied in this work but for reference purposes the core design can be seen in Figure 4-1 and Figure 4-2. In addition, the design specifications can be found in (NEA/NSC/R(2017)4, 2018).

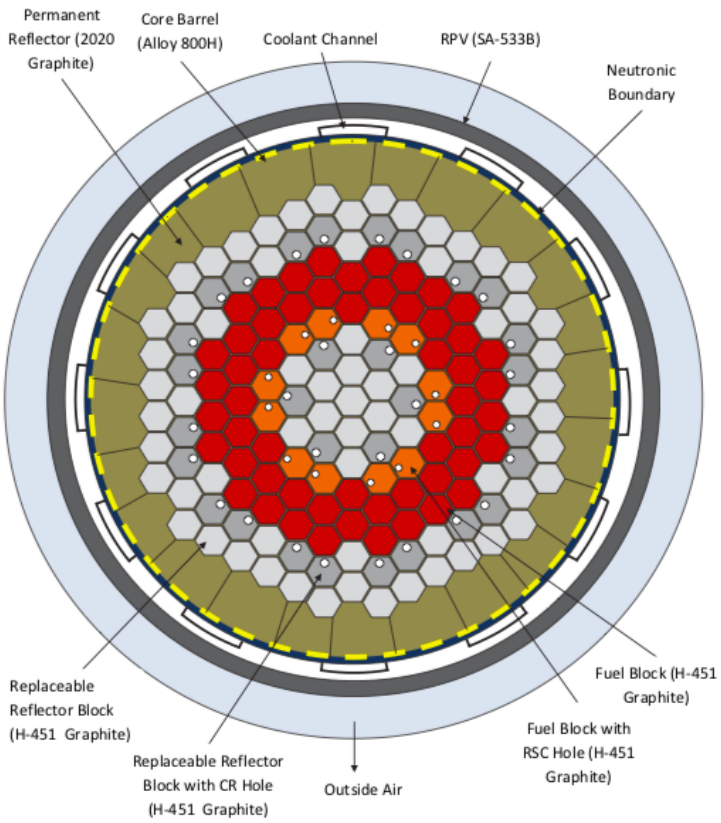

Figure 4-1 Horizontal view of the MHTGR-350 core (NEA/NSC/R(2017)4, 2018).

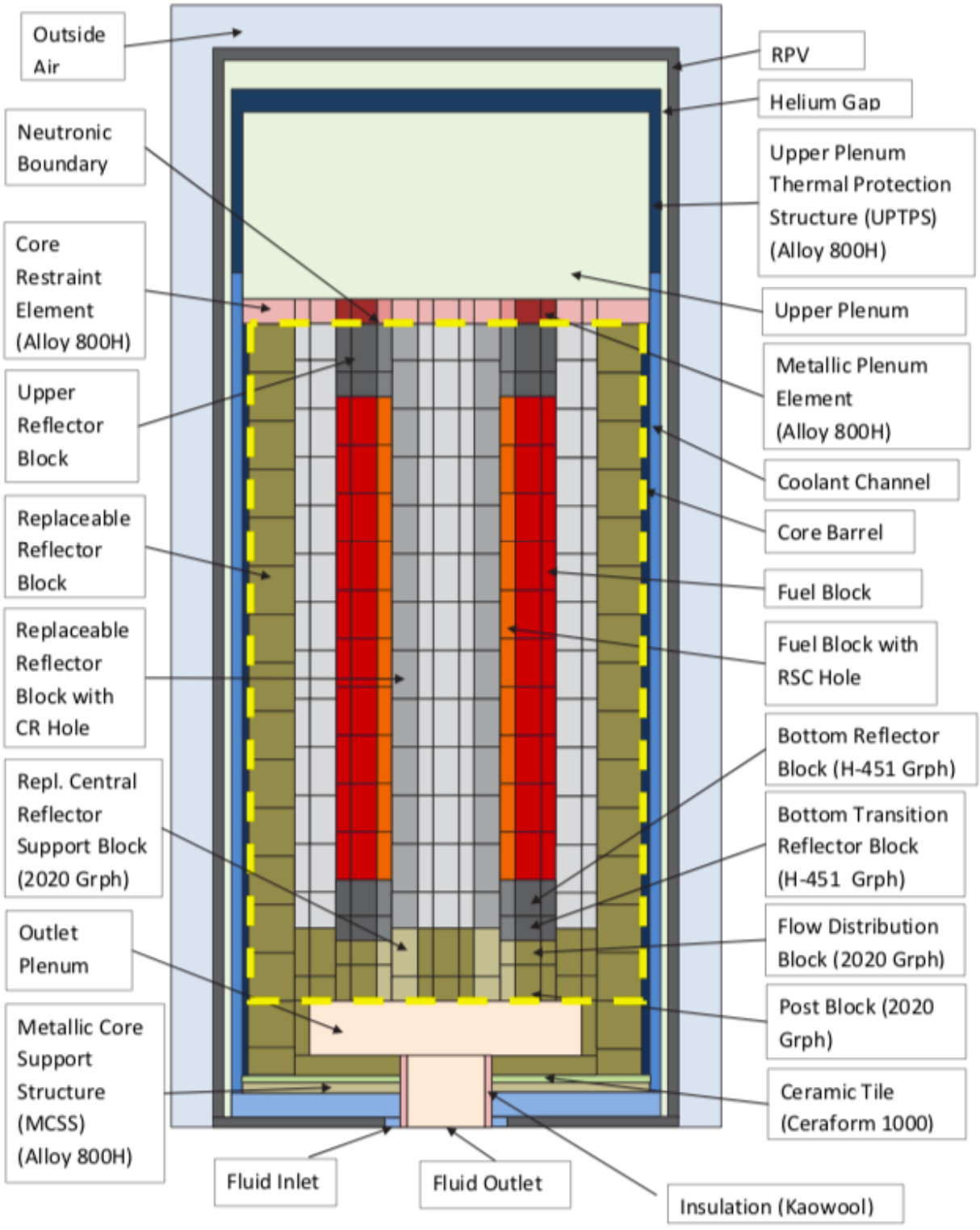

Figure 4-2 Vertical view of the MHTGR-350 core (NEA/NSC/R(2017)4, 2018).

4.1.1 MHTGR-350 timeline

A brief history of the MHTGR-350 development is presented in Table 4-1. Shown in Table 4-1 is the event that occurred as well as the year of occurrence.

Table 4-1 Timeline of the development of the MHTGR (Maratele, 2016)

Date/Period	*Event*
1980s	The design of the MHTGR was started by the design workers at INTERATOM (a German company).
1984	In the USA, a proposal was made that requires for further development of the MHTGR for a simpler and safer design. The proposal also required the MHTGR to facilitate economic growth and for its output power to be increased. The first was the MHTGR-200 MW reactor core design which was upgraded to the MHTGR-350 to increase economic competitiveness.

4.1.2 MHTGR-350 model specification

Only the heterogeneous single fuel block and the heterogeneous fuel compact of the MHTGR-350 are studied in this work. The dimensions of the fuel block and its constituents are shown in Figure 4-3, Figure 4-4, Table 4-2 and Table 4-3. The material specifications are shown in Table 4-2. The fuel kernel is composed of uranium oxycarbide ($UC_{0.5}O_{1.5}$) fuel with an enrichment of 15.5 wt%.

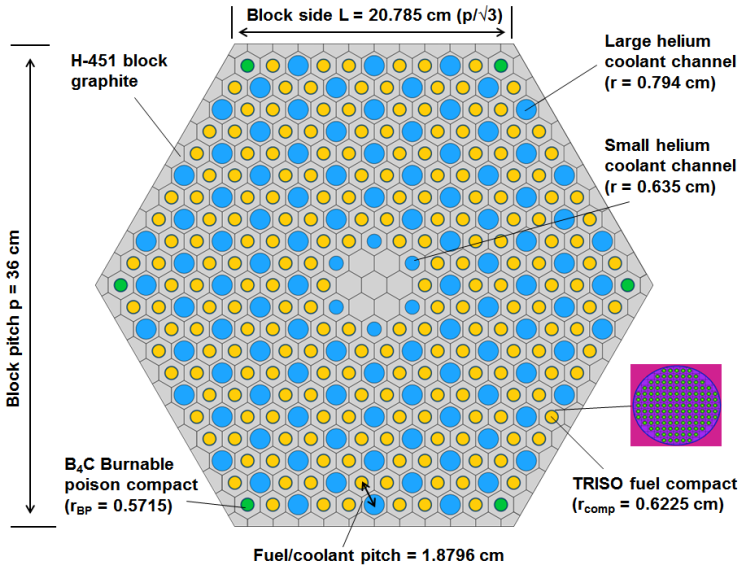

Figure 4-3 MHTGR-350 lattice cell for fresh single fuel block (Strydom et al, 2015).

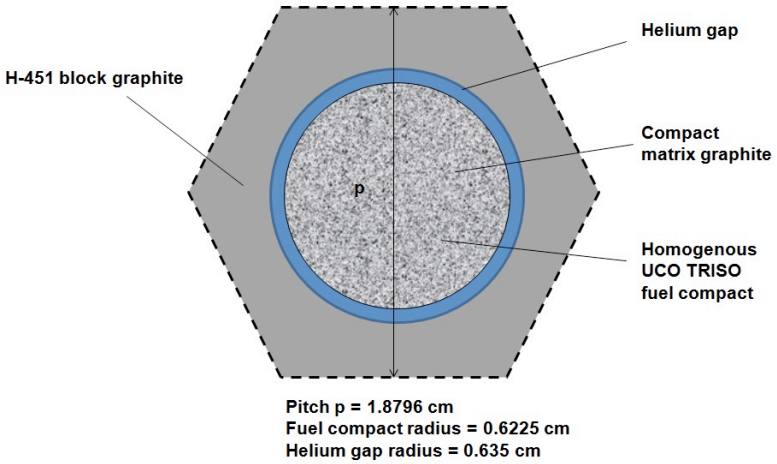

Figure 4-4 Lattice cell model for a fuel compact (Strydom et al, 2015).

Table 4-2 Specifications of the fuel compact and fuel block (Strydom et al, 2015)

Materials		**Outer Radius (cm)**	**Nuclide**	**Number Density (at/b-cm)**
TRISO fuel particle	Kernel	2.215E-02	^{235}U	3.6676E-03
			^{238}U	1.9742E-02
			^{16}O	3.5114E-02
			Graphite	1.1705E-02
	Porous Carbon	3.125E-02	Graphite	5.2646E-02
	IPyC	3.525E-02	Graphite	9.5263E-02
	SiC	3.875E-02	^{28}Si	4.4159E-02
			^{29}Si	2.2433E-03
			^{30}Si	1.4805E-03
			Graphite	4.7883E-02
	OPyC	4.275E-02	Graphite	9.5263E-02
LBP particle	Kernel	1.000E-02	^{10}B	2.1400E-02
			^{11}B	8.6300E-02
			Graphite	2.6900E-02
	Porous carbon buffer	1.180E-02	Graphite	5.0200E-02
	PyC	1.141E-02	Graphite	9.3800E-02
Burnable Poison compact matrix		-	Graphite	7.2701E-02
Fuel Compact Matrix		-	Graphite	7.2701E-02
Coolant Channels		-	^{4}He	2.4600E-05
H-451 Block Graphite		-	Graphite	9.2756E-02

Table 4-3 Parameters and dimensions of the fuel compact and block of the MHTGR-350 (Strydom et al, 2015)

Parameter	Dimension	Unit
Temperature (CZP)	293	K
Temperature (HFP)	1200	K
LBP Particle Packing Fraction	0.1090	-
Fuel Packing Fraction	0.35	-
Fuel compact radius*	0.6225	cm
Small coolant channel radius	0.6350	cm
Large coolant channel radius	0.7940	cm
Pin Pitch	1.8796	cm
Block Pitch	36.0	cm
Block Height	4.928	cm

*The fuel holes have the same radius as the small coolant channels hence there is a gap of 0.0125 cm

The burnable poisons of the MHTGR-350 are lumped in selected elements so that significant spatial self-shielding of the burnable poisons exists, therefore these burnable poisons are referred to as heterogenous or lumped burnable poisons (LBP) (Gupta,1989). In this work the term LBP is used to describe the burnable poisons of the MHTGR-350.

4.2 Introduction and history of the HTTR

The HTTR is a Japanese test reactor that was built in March 1991 and construction was completed in May 1996. It was constructed with the objective of establishing and upgrading the technological basis for advanced HTGRs. In addition, it has the objective of conducting various irradiation tests (IAEA-TECDOC-1382, 2003). It is half the core size of future HTGRs.

4.2.1 HTTR timeline

A summarized history and development of the HTTR is presented in Table 4-4. The event that occurred is shown in the second column and the date of occurrence is shown in the first column.

Table 4-4 Timeline of the HTTR reactor (Shiozawa et al, 2004)

Date/Period	*Event*
1987	Revision of the construction of the Japan Atomic Energy Research Institute (JAERI) HTGR based on the long-term Program for Development and Utilization of Nuclear Energy.
1989	Construction of the HTTR was approved by the Japanese government.
November 1990	JAERI obtained an installation permit from the government.
January 1991	First approval of the HTTR design and construction methods from the Scientia and Technology Agency.
March 1991	Construction work on the HTTR began.
August 1991	Excavation was completed.
May 1992	Construction of the concrete base-mat was completed.
November 1992	The reactor containment vessel was installed. Additionally, its pressure-proof and leakage tests were passed successfully.
1994	The reactor pressure vessel, intermediate heat exchanger, primary helium circulators and primary pressurized water cooler were installed.
1994	JAERI obtained uranium material for the first fuel loading.
October 1995	The first pressure test for the primary cooling system was successfully executed.
December 1995	Construction of the reactor building was completed by closing the temporary opening for carrying in large components.

Table 4-4 *(continued)*

October 1996	Comprehensive and functional tests for each system began and several malfunctions were found.
October 1997	Manufacture of fuel rods was completed.
December 1997	Assembly of fuel elements was carried out in the reactor building.
March 1998	Improvements of the malfunctions found from the tests done in 1996 were improved and completed.
April 1998	Preparation for the first fuel loading of the HTTR began.
1 July 1998	The first fuel loading commenced.
10 November 1998	1st criticality was achieved with a core of 19 columns.
16 December 1998	Loading of all 150 fuel assemblies was completed.
January 1999	The criticality tests were executed, which confirmed the core characteristics of the HTTR.
August 1999	All improvements were completed and the reactor was ready for the rise-to-power test.
September 1999	The rise to power test began.
7 December 2001	The HTTR achieved full power of 30 MW and at a reactor coolant temperature of 850 ^{0}C.
6 March 2002	The operation permit was issued by the Ministry of Education, Culture, Sports, Science and Technology.
19 April 2004	The test operation was carried out with reactor outlet coolant of 950 ^{0}C.

4.3 THE HTTR experimental reactor design

It is a 30 MWTh prismatic core with an outlet temperature of 950 ^{0}C. This reactor design has 12 different fuel enrichments ranging between 3.4 and 9.9 wt% ^{235}U with the average being 6% (Iyoku

et al, 2014). The variation of enrichments reduces the maximum fuel temperature and increases the outlet temperature of helium.

Initial criticality was achieved with a core of 19 columns but a fully loaded core consists of 30 fuel columns. The specifications of the HTTR are presented in Table 4-5.

Table 4-5 Major specifications of the HTTR

Input Parameter	**Nominal/Mean Value**
Thermal power	30 MW
Inlet temperature/Outlet temperature	395 ^{0}C / 850 ^{0}C
Primary Coolant Pressure	4 MPa
Fuel	Low Enrichment UO_2

The full core HTTR specifications can be found in the document HTTR-GCR-RESR-001(Bess et al, 2009). This name, HTTR-GCR-RESR-001, will be used in all further reference to this document. HTTR-GCR-RESR-001 is a benchmark evaluation report for the fully-loaded, cold-critical, configuration of the HTTR start-up core. It is available in the International Handbook of Evaluated Reactor Physics Benchmark Experiments (IRPhEP) handbook.

4.3.1 The reactor pressure vessel, core and reflectors

The reactor core components are arranged in the reactor pressure vessel (RPV), which is made of 2.25 Cr – 1 Mo steel (Shiozawa et al, 2004) and has a height of 13.2 m as well as a diameter of 5.5 m. The core components are piled up cylindrically to form the core. The horizontal and vertical view of the core can be seen in Figure 4-5 and Figure 4-6. The active core has an equivalent diameter of 2.3 m and an effective height of 2.9 m. The actual active core diameter is 3.258 m. The permanent reflector is in the shape of a dodecagon and combined with the active core has a diameter of 4.250 m. The sides of the permanent reflector have a total thickness of 0.99 m and the top and bottom permanent reflectors each have a height of 1.16 m. The replaceable reflector has 9 control rod columns, 12 replaceable reflector columns and 3 irradiation columns. The active core region consists of 7 control guide columns and the fully loaded core consists of 30 fuel columns. The thin and thick annular cores have 18 and 24 fuel columns respectively (IAEA-TECDOC-1382, 2003). Each hexagonal block has a width of 36.0 cm across the flats. The width across the flats is 36.2 cm at CZP. The height of the blocks is 58.0 cm with the exception of the hexagonal blocks in the 9th layer of the control rod guide columns and irradiation columns (IAEA-TECDOC-1382, 2003).

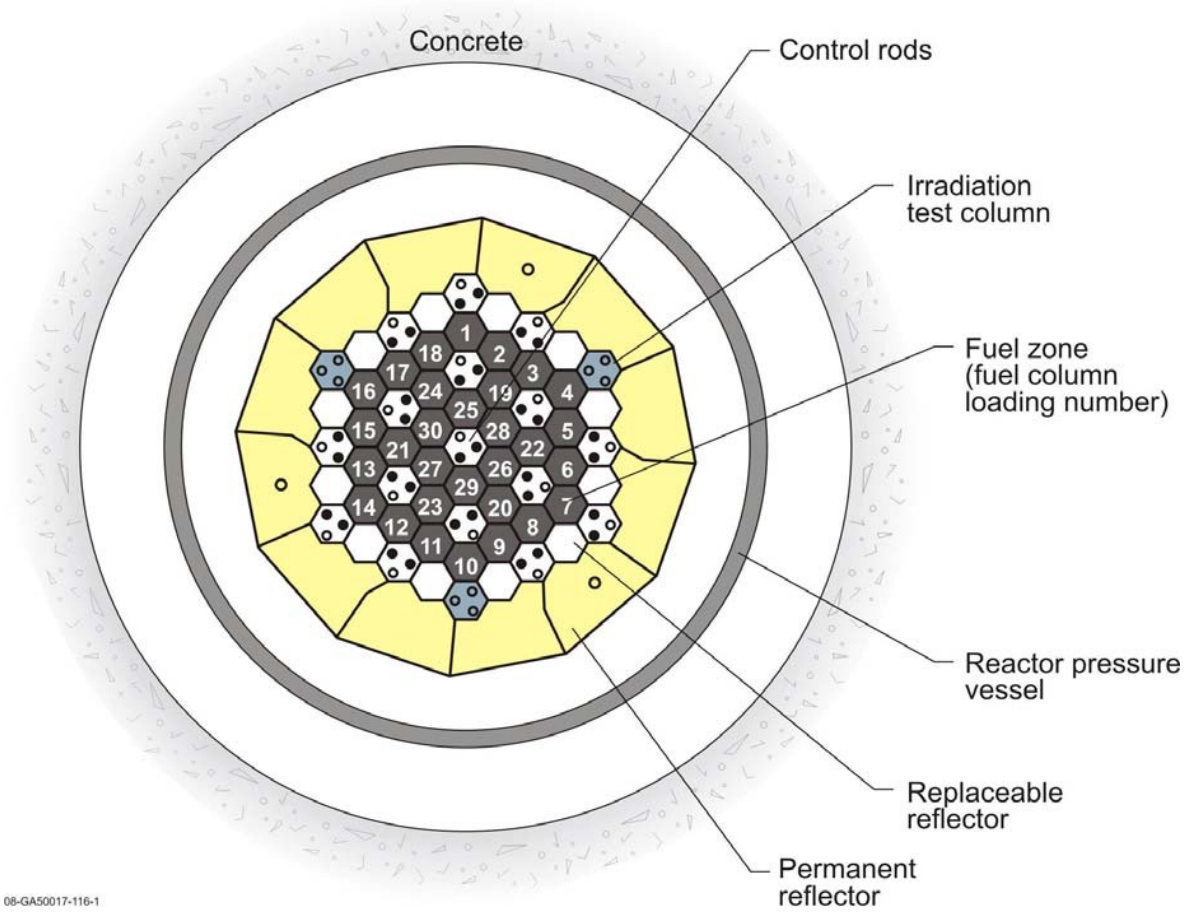

Figure 4-5 Horizontal view of the HTTR (HTTR-GCR-RESR-001).

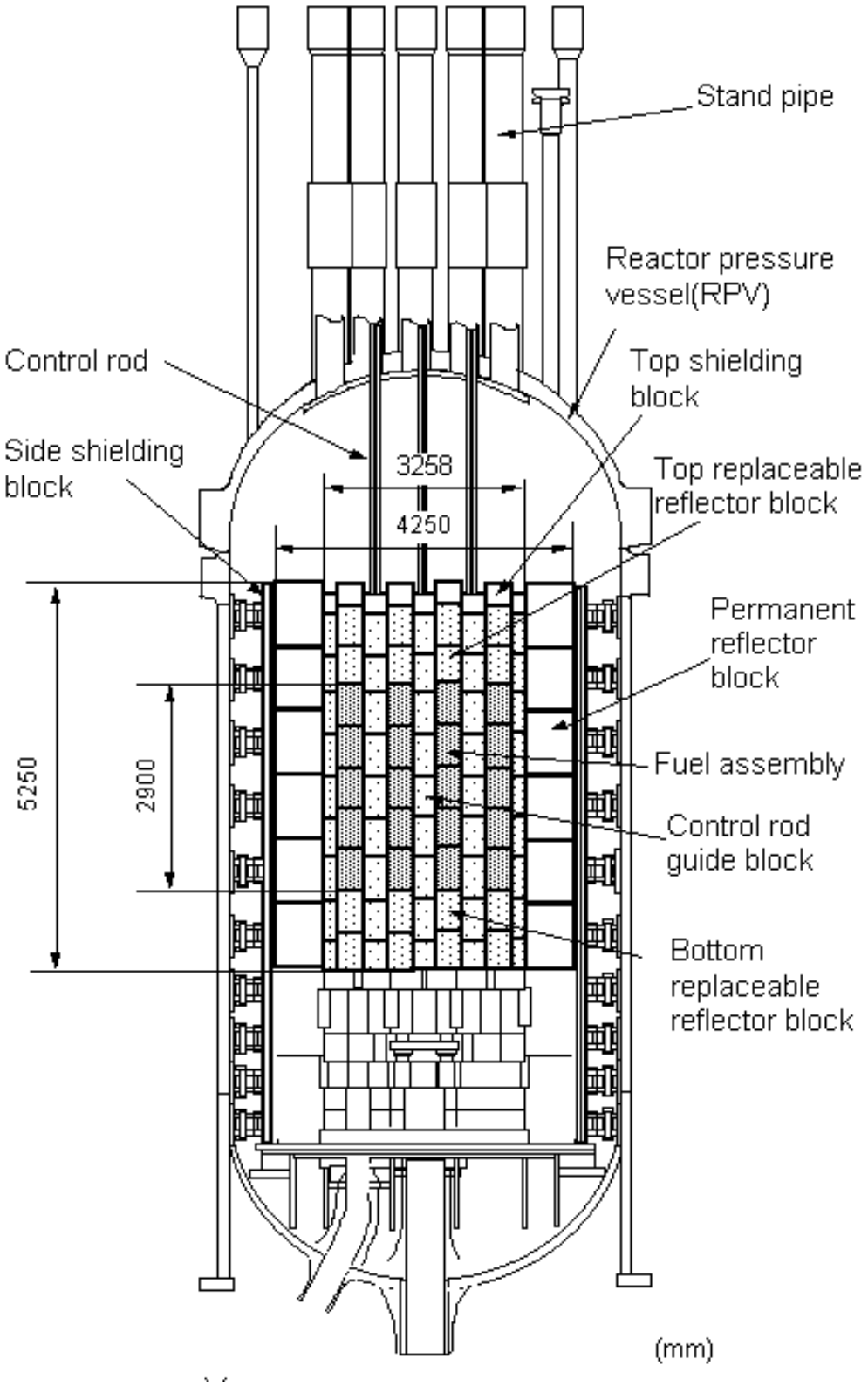

Figure 4-6 Vertical view of HTTR (IAEA-TECDOC-1382, 2003).

4.3.2 Fuel assembly/block

Each column has 5 fuel assemblies, 2 top reflector blocks and 2 bottom reflector blocks. There are two types of fuel assemblies, one has 31-pins and the other has 33-pins. The two different fuel assemblies are shown in Figure 4-7 and Figure 4-8. Each fuel assembly is composed of a fuel graphite block, 2 BPs and coolant holes. The fuel rods are placed in the coolant holes with an end cap at the bottom of each coolant channel. The fuel rods have a diameter of 41 mm and the BPs are inserted into 2 of the BP insertion holes. The burnable poisons have a different pitch from the fuel as shown in Figure 4-7 and Figure 4-8.

The fuel assembly is classified by the uranium enrichment, number of fuel rods, and the type of BPs. There are 12 enrichments to reduce the maximum fuel temperature and increase the outlet temperature of the gas. The fuels with higher enrichments are placed in the upper and outer core region to reduce the maximum fuel temperature.

The 31-pin fuel blocks are placed in the outer region and the 33-pin fuel blocks are placed in the inner region as shown in Figure 4-9 (a). Fuel zone 1 and 2 contain the 33-pin blocks and fuel zone 3 and 4 contain the 31-pin blocks. A zone can be considered as a column of blocks stacked in the axial direction. These zones can be identified by the matching the fuel zones in Figure 4-9 (b) with Figure 4-9 (c). The arrangement of the fuel blocks in Figure 4-9 (c) can be matched to Figure 4-9 (d).

4.3.3 Reflector blocks

The replaceable reflector blocks are placed above and below the fuel assemblies. These blocks have coolant channels that have an inner diameter of 23 mm and the arrangement of these coolant channels is consistent with the arrangement of the fuel rod holes (41 mm diameter) in the fuel assemblies within the same column. The ninth layer of the control rod guide columns is 48 cm in height. This gives the reactor a staggered vertical appearance.

4.3.4 Fuel

The HTTR consists of 3 types of fuel, only the A-Type is discussed since it is the primary fuel for irradiation tests. The A-type fuel has varying enrichments, the higher enrichments are placed in the higher and outer region of the core as shown in Figure 4-9 (c) and Figure 4-9 (d). The fuel rods consist of 14 fuel compacts in a graphite sleeve. The fuel compact is a hollow cylinder with an inner diameter of 10 mm, an outer diameter of 26 mm and a height of 39 mm as shown in Figure 4-10. The total number of fuel compacts used in the core is approximately 66780. The total number of fuel rods used in the core is approximately 4770. There are approximately 12987

coated particles in the fuel pin (Gehin, et al, 2010). The coated particles are shown in Figure 4-11 and the dimensions of all the HTTR core components are shown in Table 4-6.

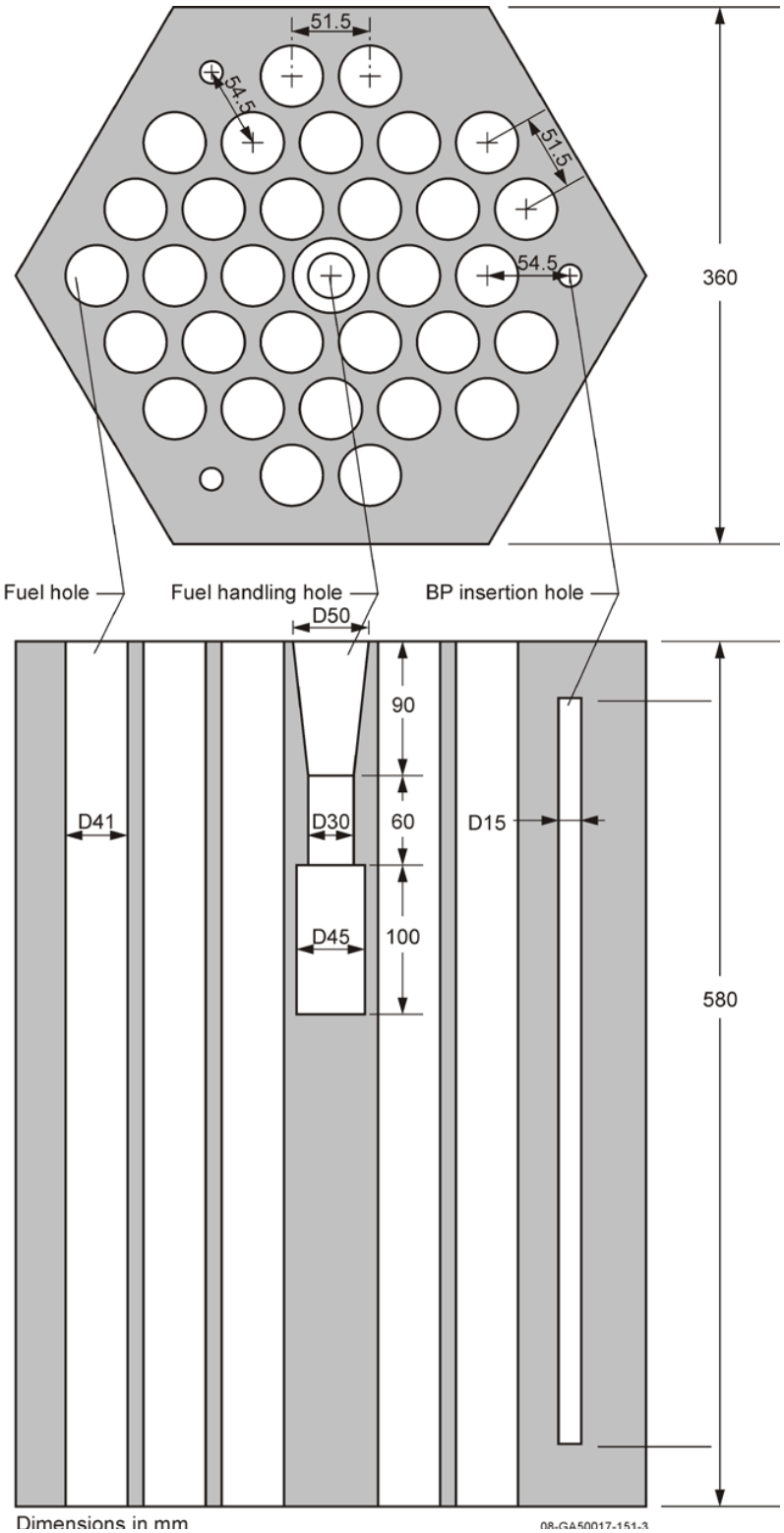

Figure 4-7 The fuel blocks of the 31-pin fuel block (Ortensi, et al, 2010).

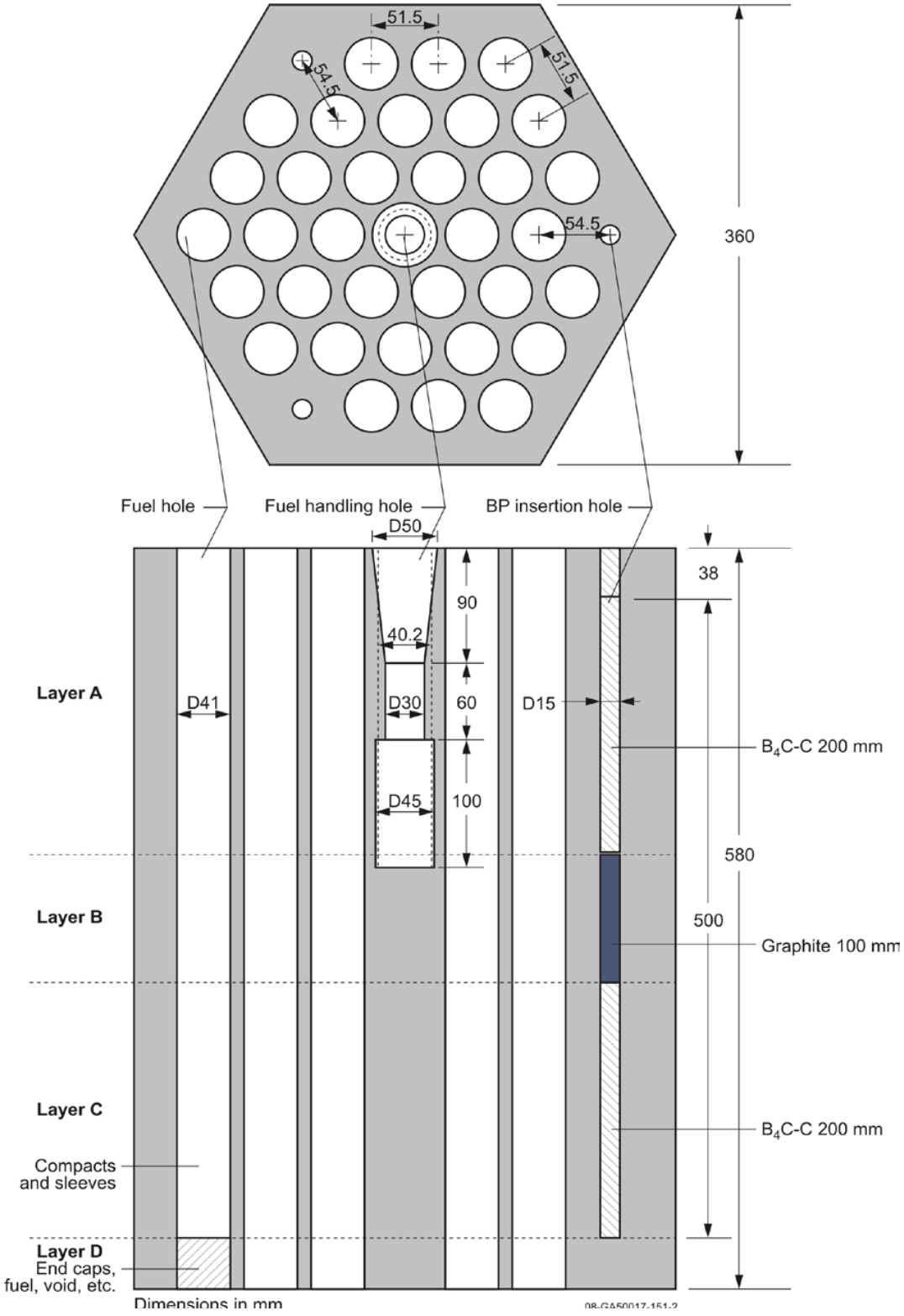

Figure 4-8 The fuel blocks of the 33-pin fuel block **(**Ortensi, et al, 2010).

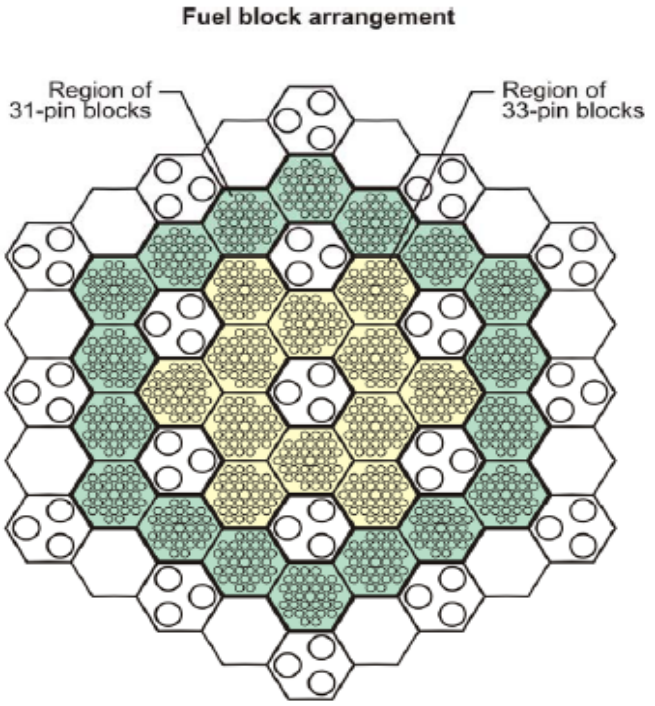

(a)

Uranium Enrichments of the HTTR Core (I

Layer[a]	Fuel Zone Number[b]				BP[c]
	1	2	3	4	
1	6.7	7.9	9.4	9.9	2.0
2	5.2	6.3	7.2	7.9	2.5
3	4.3	5.2	5.9	6.3	2.5
4	3.4	3.9	4.3	4.8	2.0
5	3.4	3.9	4.3	4.8	2.0

(a) Layer number from top fuel block.
(b) ^{235}U enrichment (wt.%).
(c) Nat-B concentration (wt.%).

(b)

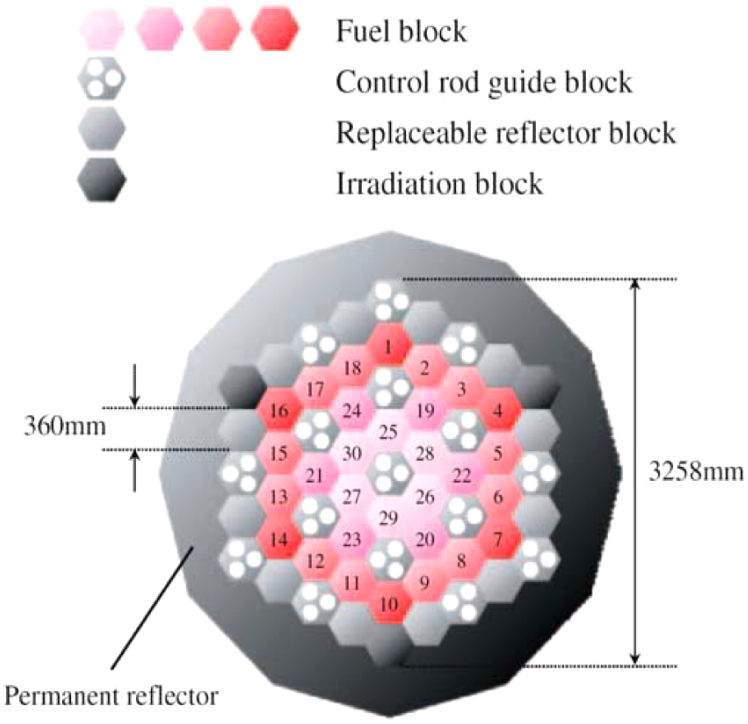

(c)

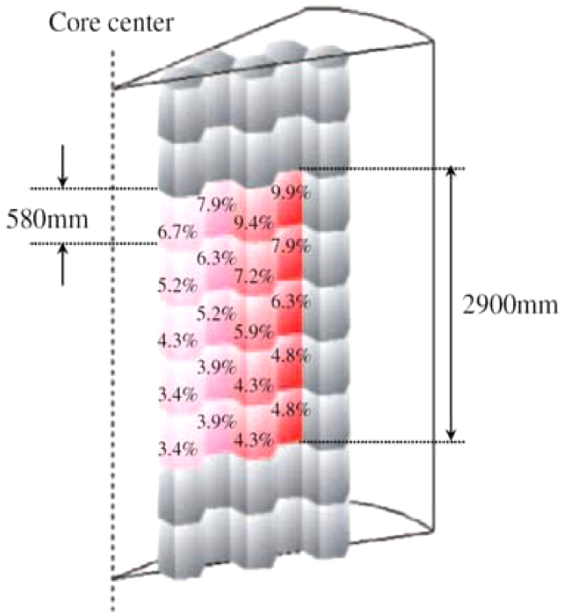

(d)

Figure 4-9 Arrangement of fuel blocks in core (HTTR-GCR-RESR-001).

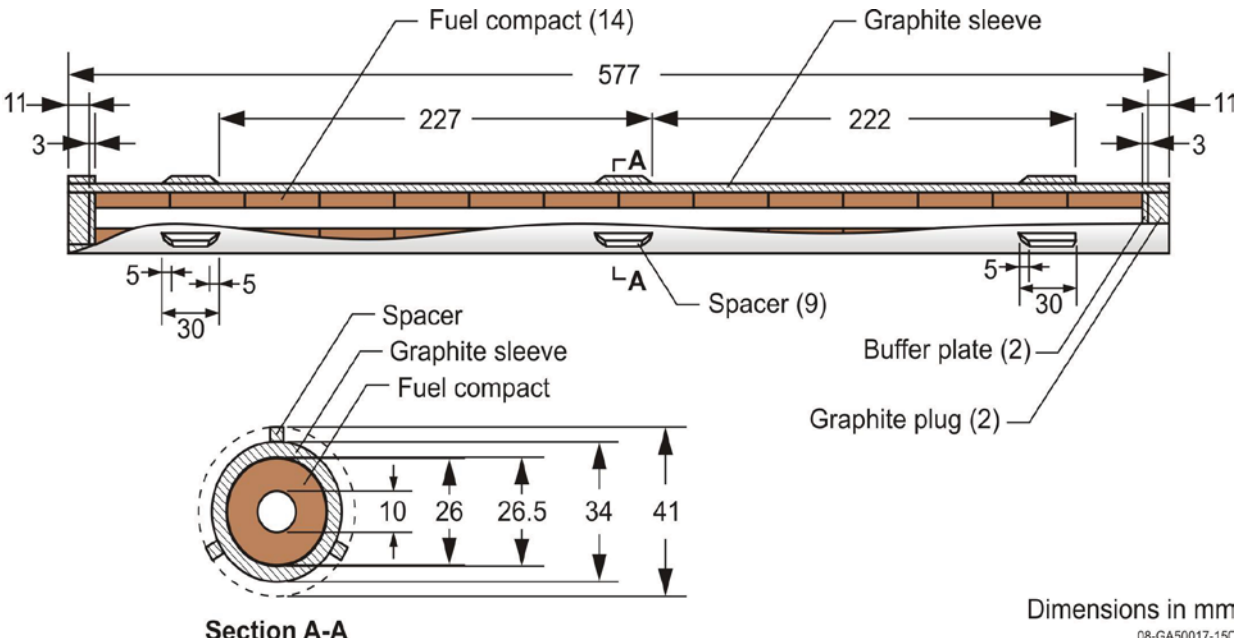

Figure 4-10 The fuel rod of the HTTR (HTTR-GCR-RESR-001).

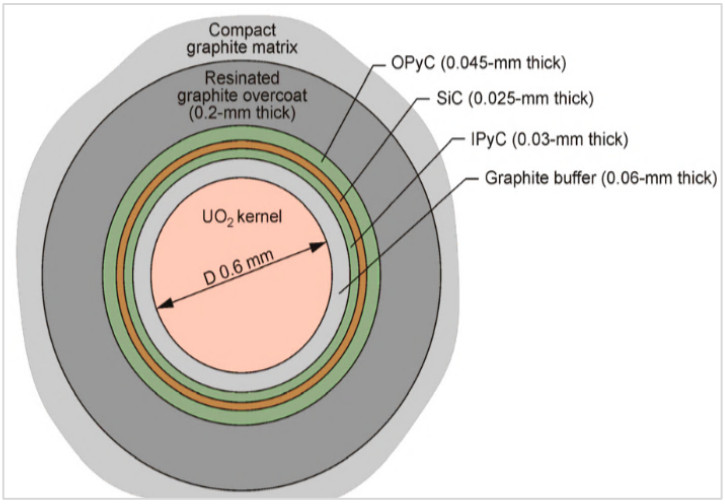

Figure 4-11 Coated fuel particle of the HTTR (HTTR-GCR-RESR-001).

Table 4-6 Dimensions of the HTTR core components

Input parameter	Nominal/Mean Value
Core height	2.9 m
Effective core diameter	2.3 m
Diameter of the core	3258 mm
Reflector top thickness	1.16 m
Reflector Side thickness	0.99 m
Reflector bottom thickness	1.16 m
Number of fuel blocks	30
Number of control rod guide blocks	16
Number of irradiation blocks	1
Number of replaceable blocks	1
Layers of fuel assemblies	9
Active fuel assembly height	29 cm
Fuel block height	58 cm
Fuel block width across flats	36 cm
Fuel Rod	
Type	Hollow cylinder
Fuel hole diameter	4.1 cm
Graphite sleeve thickness	3.75 mm
Effective length	54.6 cm
Number of fuel compacts	14
Fuel compact	
Fuel compact stack outer diameter	2.6 cm
Fuel compact stack inner diameter	1.0 cm
Packing Fraction (vol %)	30 – Type A and B-3 35 – Type B-1 and Type B-2
Height	39
Coated Particles *(A-type)*	
Low-density PyC	60 micrometer
High-density PyC	30 micrometer
SiC	25 micrometer
High-density PyC	45 micrometer

4.4 Reactivity control

Neutron absorption is controlled by two systems i.e. BPs and the control rods. The absorber materials in both systems are B_4C/C. There are two BP holes in each fuel block and one of the BP holes is left empty. Similarly, there are three control rod holes in the control rod blocks and one hole is left empty. The control rods have different orientations and the BPs in the fuel blocks also have different orientations as illustrated in Figure 4-12.

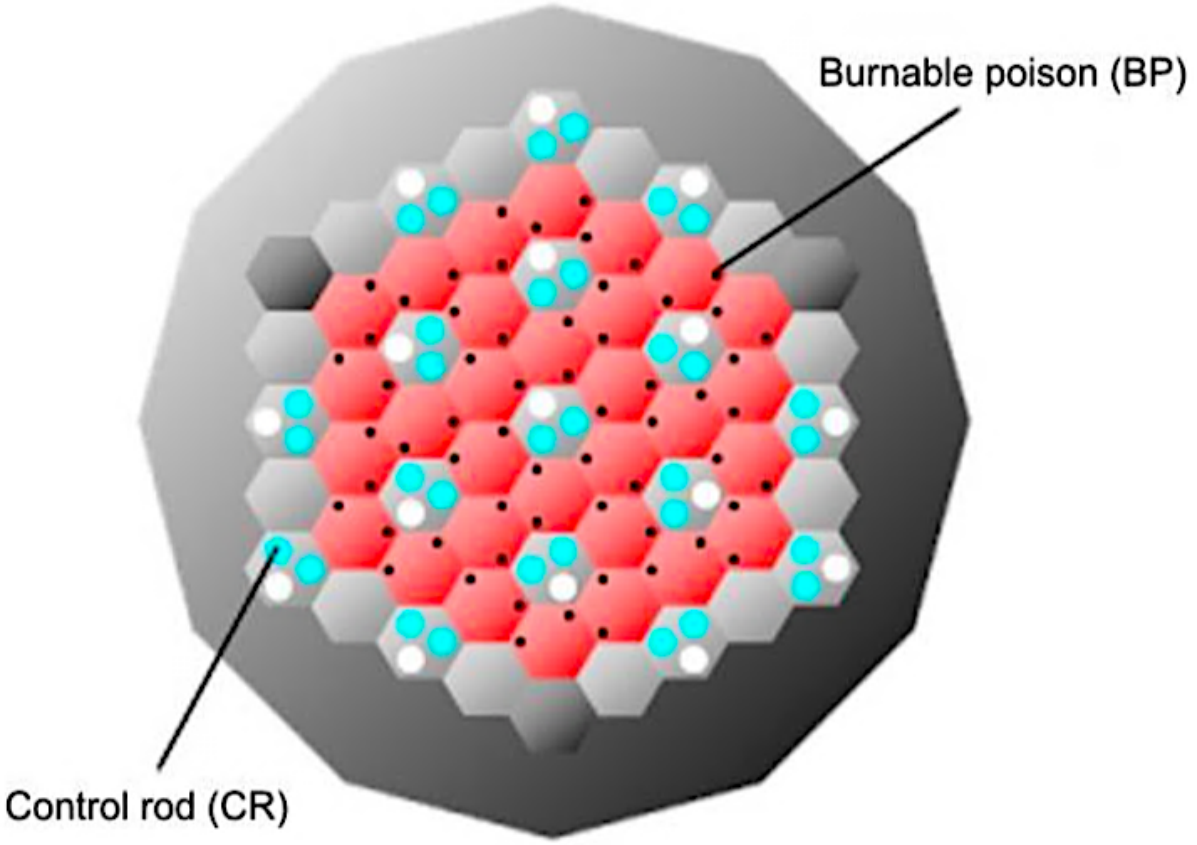

Figure 4-12 The orientation of the control rods and burnable poisons in the core (HTTR-GCR-RESR-001).

4.4.1 Burnable poisons

The BP rod has a diameter of 14 mm and a height of 500 mm (IAEA-TECDOC-1382, 2003); HTTR-GCR-RESR-001). The BP pellets are made of B_4C/C composite material. There are two types of burnable poisons as shown in Table 4-7 and Figure 4-13. One is called the H-I type and the other the H-II type. The two types are differentiated by their densities, natural boron concentration and number of BP pellets.

The large initial excess reactivity from fresh fuel is counteracted through the use of BPs. Optimization of the specifications for the BPs reduces deviation from the optimum power distribution due to burnup effects. It then becomes possible to operate the reactor during full power operation at 950 ºC without changing the insertion position of the control rods.

Table 4-7 Burnable poison pellet and graphite specification (IAEA-TECDOC-1382, 2003)

Burnable Poison Pellet		
	H-I type	H-II type
Density (g/cm^3)	1.79	1.82
Natural boron concentration (wt%)	2.22	2.74
Diameter (mm)	13.9	13.9
^{10}B abundance ratio (wt%)	18.7[(a)]	18.7[(a)]
Graphite Pellet		
Density (g/cm^3)	1.77	
Diameter (mm)	14.0	
Impurity (ppm)	0.37 (Natural boron equivalent)	

a) HTTR-GCR-RESR-001 suggests that these might be typographical errors or listed in atomic percent since natural boron has an abundance of 19.1 and 20.3 wt%

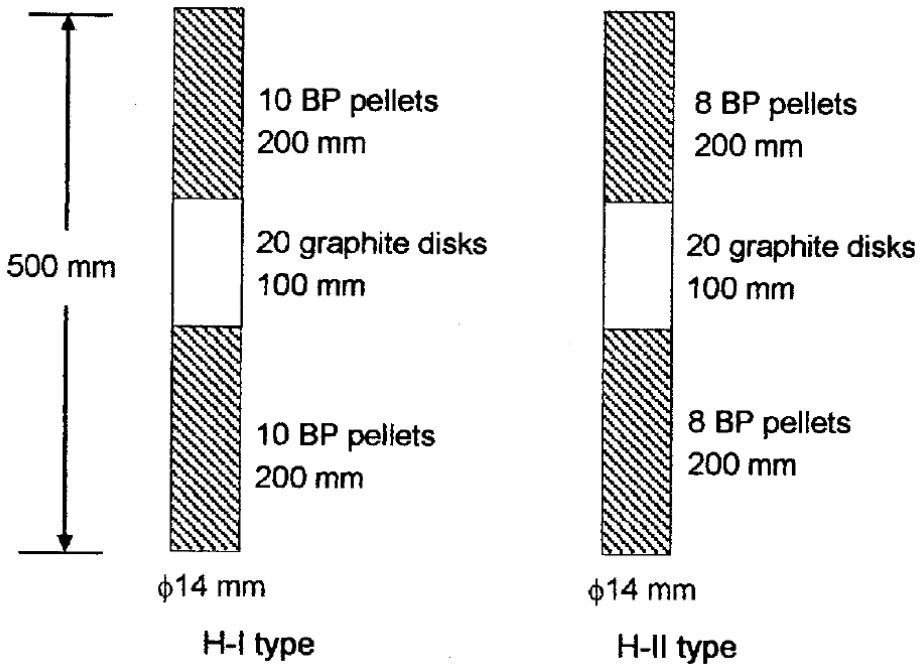

Figure 4-13 Configuration the two types of BP poisons (IAEA-TECDOC-1382, 2003).

4.4.2 Control rod guide block

Along with BPs, the control rods control the reactivity of the HTTR. There are 16 pairs of CRs in the core. Each control block contains 3 insertion holes. Only two of them are inserted and the last one is reserved as a reserve shutdown for emergency shutdown as shown in Figure 4-14. The control rods are designed to provide a shutdown margin of more than $0.01^{\Delta k}/_{k}$. The reserve shutdown system also provides more than $0.01^{\Delta k}/_{k}$.

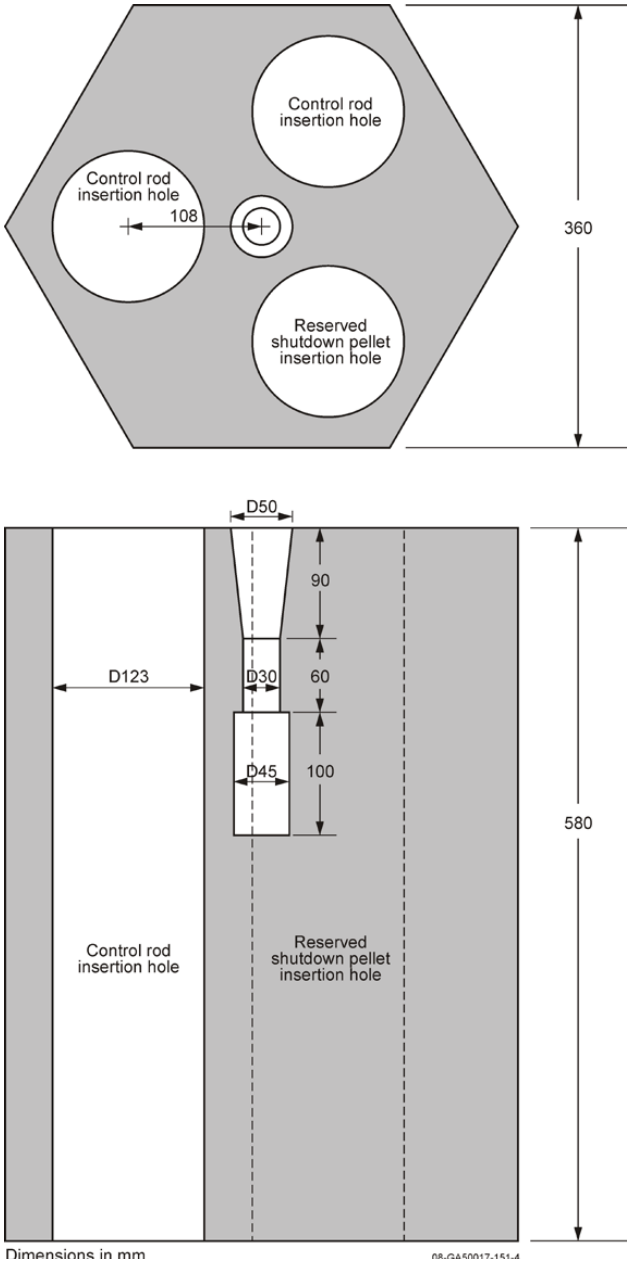

Figure 4-14 The control rod guide block (Ortensi, et al, 2010).

4.5 Simplifications of the HTTR model

In order to build the HTTR benchmark models, simplifications were made by the HTTR benchmark team (HTTR-GCR-RESR-001) when the data was not available or insufficient. The following simplifications were made:

- The permanent reflector was circularized with a radius of 212.2 cm instead of being modelled using a dodecagon. This is shown in Figure 4-15.
- The BP insertion holes were modelled with the same pitch as the fuel elements and this is shown in Figure 4-16 and Figure 4-17. This simplification is found to be insignificant using MCNP5 (Ortensi, et al, 2010).
- The density of both types of BP pellets is the same at 1.80 g/cm^3.
- The fuel handling positions, dowels and sockets were not included in the model as there are insufficient data specifications.
- The TRISO particles are modelled in an ordered matrix instead of random placement since Monte Carlo codes cannot easily model stochastic geometry.
- The depth to which the control rods, reserve shutdown system and instrumentation holes are drilled varies. In the benchmark design, the holes are drilled at a height of 106.0 cm above the bottom of the core as shown in Figure 4-18.
- In the experimental design the bottom reflector block has a height of 48 cm. Not enough data is available to model the bottom reflector therefore in the benchmark design this height is modelled exactly like the top reflector.
- Only the impurity of ^{10}B impurity component is considered in the materials. The effect of ^{11}B is negligible.

The benchmark model specified in HTTR-GCR-RESR-001 is similar to the experimental design and this is the benchmark that is modelled in this work.

The constituents of the HTTR benchmark model are shown in Figure 4-15 to Figure 4-21. Figure 4-15 shows the axial view of the full core model as well as the control rod blocks C, R1, R2 and R3. Figure 4-18 shows the positions of the control rods. The zeroth position of the control rods is 10 cm below the fuel region as shown in Figure 4-18. The critical positions for C, R1 and R2 are placed at 177.5 cm, whilst the critical rod position for R3 is 404.9 cm. The critical position of the core is illustrated in Figure 4-18. In the subcritical model, the C, R1, R2 and R3 control rod blocks are placed at a distance of 5.5 cm below the bottom of the fuel. The control rod geometry and materials are shown in Figure 4-19 (a) – (c).

Figure 4-20 shows the constituents of the fuel block which include the BP (Figure 4-20 (a)), the empty BP hole (Figure 4-20 (b)) and the fuel rod. Figure 4-20 (c) shows the model of the fuel rod. The top and bottom graphite blocks are shown in Figure 4-21. They are situated above and below the fuel assembly columns and have coolant channels in line with the fuel rods. The graphite blocks that form the reflector blocks are homogeneous blocks.

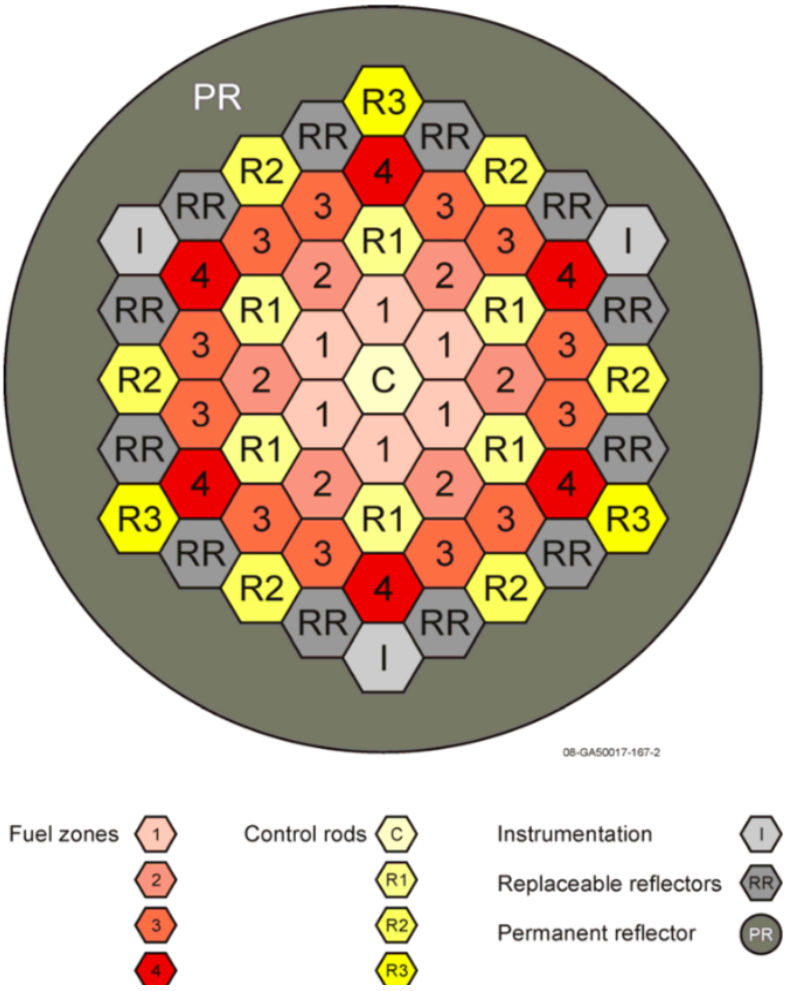

Figure 4-15 Full core and reflector of the benchmark model of the MHTGR-350 (HTTR-GCR-RESR-001).

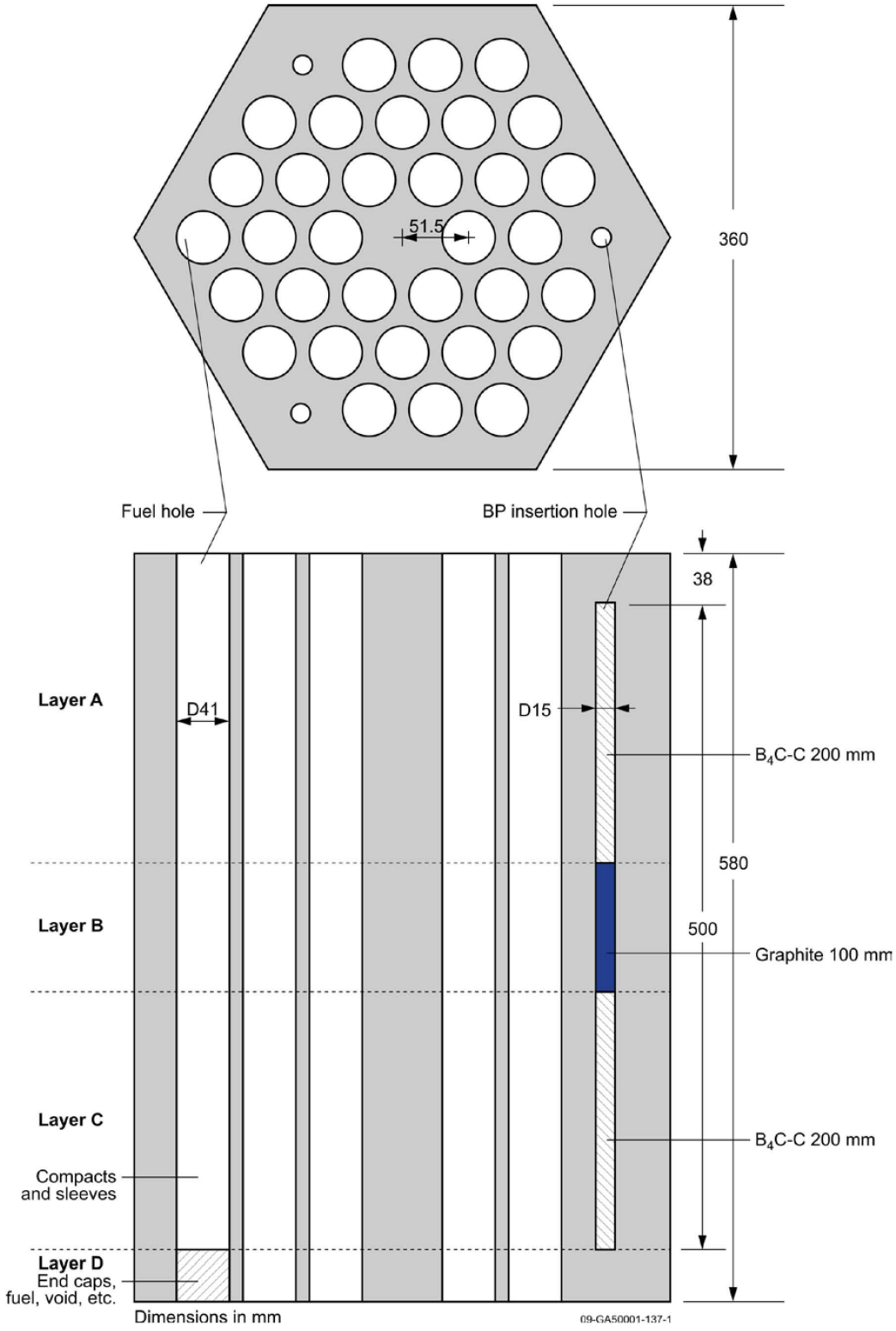

Figure 4-16 The 33-pin fuel block of the benchmark model (HTTR-GCR-RESR-001).

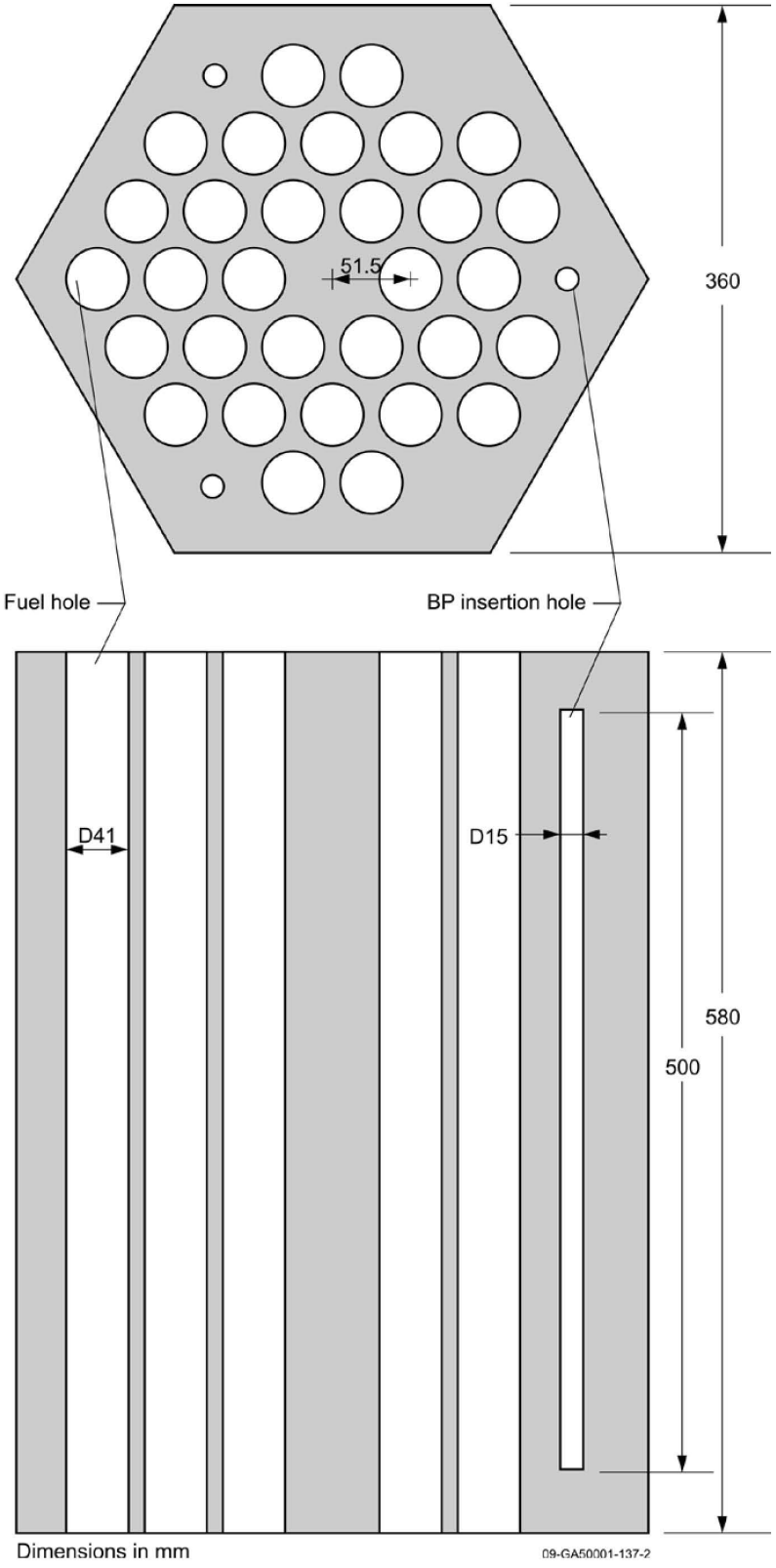

Figure 4-17 The 31-pin fuel block of the benchmark model (HTTR-GCR-RESR-001).

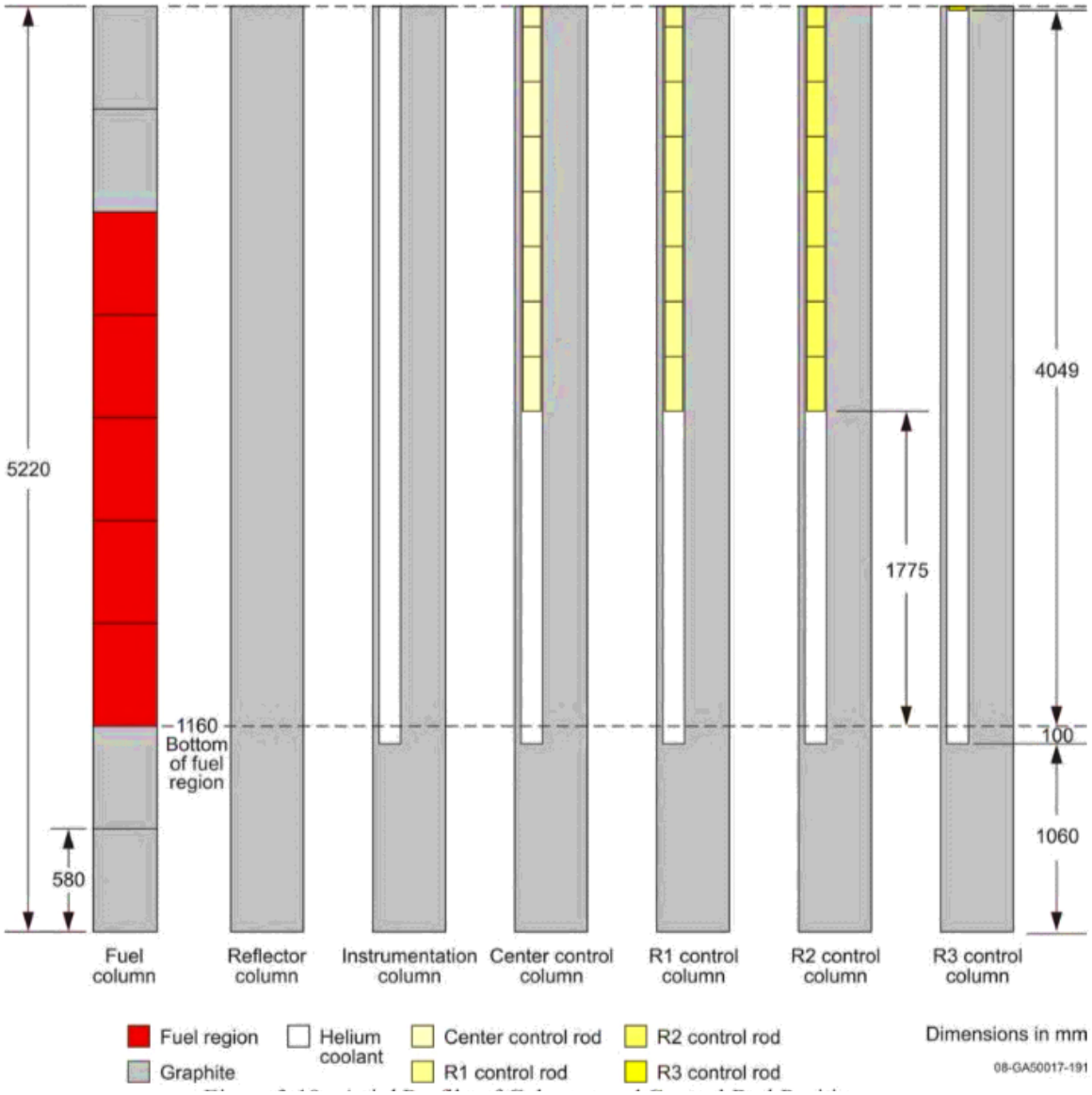

Figure 4-18 Benchmark definition of the positions of the control rods in the core (HTTR-GCR-RESR-001).

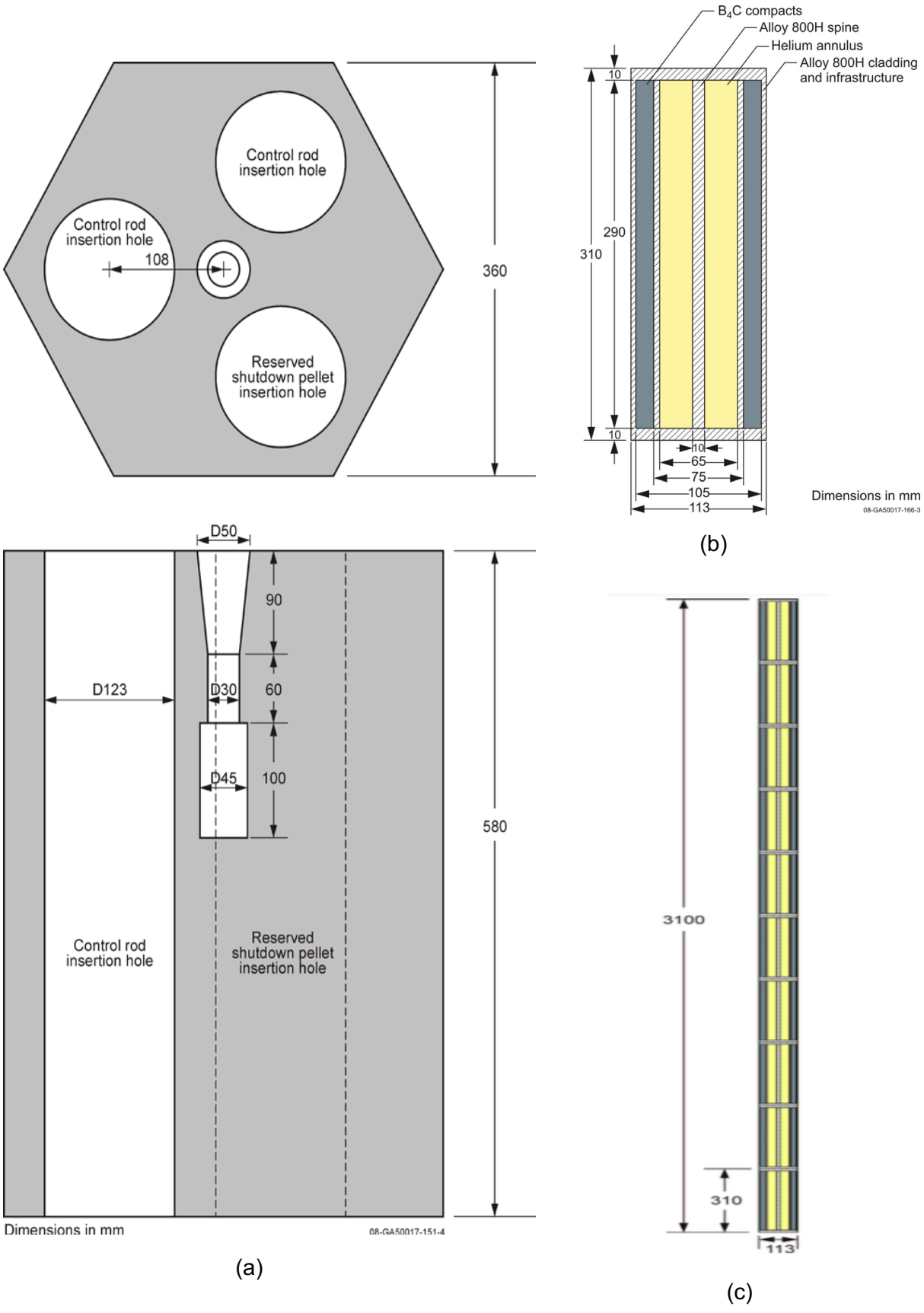

Figure 4-19 (a) The control rod block, (b) the control rod materials and (c) the full control rod (HTTR-GCR-RESR-001).

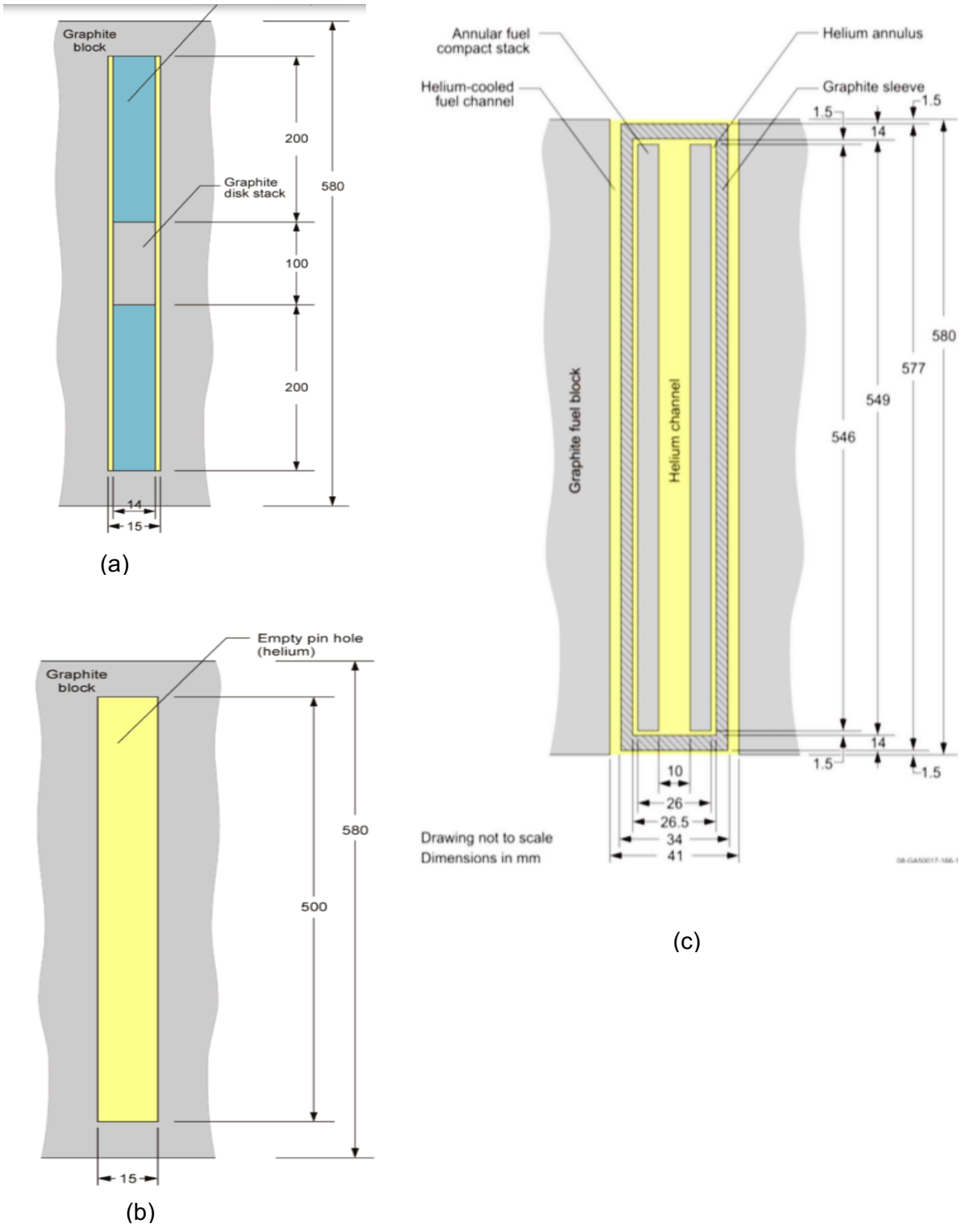

Figure 4-20 (a) The burnable poison, (b) empty BP hole and (c) the fuel rod (HTTR-GCR-RESR-001).

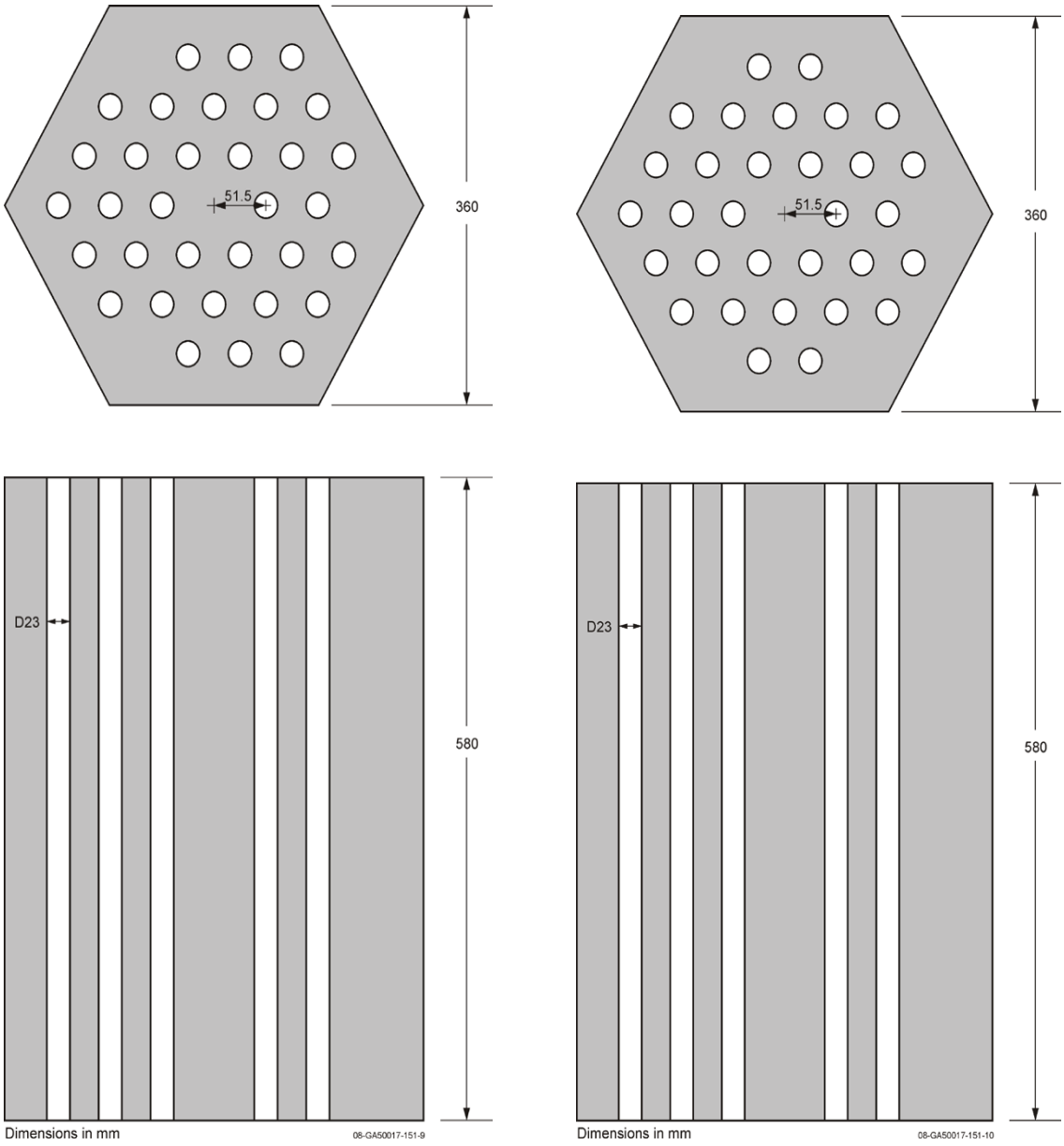

(a) (b)

Figure 4-21 (a) The 33-pin and (b) 31-pin of the top and bottom reflector blocks (HTTR-GCR-RESR-001).

4.6 Material and temperature specification of the benchmark model

The benchmark model temperature is at 293.65 K. The material specifications can be found in HTTR-GCR-RESR-001.

CHAPTER 5: METHODOLOGY

This chapter discusses the modelling of the MHTGR-350 fuel block and fuel compact in the CE and MG treatment using the SCALE 6.2 code. The first part of this chapter discusses the application of SCALE 6.2 transport codes in terms of the MHTGR-350. Various ways to model coated particles in SCALE are discussed. The second part of this chapter discusses the methodology for converging and optimizing calculations using the SCALE 6.2 uncertainty codes. The CE TSUNAMI convergence was developed in this work and is also published by Sihlangu et al (2018). The output information from the SCALE 6.2 uncertainty codes is explained in this chapter. Additionally, the model nomenclature is explained.

5.1 Double heterogeneity treatment in SCALE with CE physics

When modelling CPs explicitly, the most straight-forward approach is to represent CPs in an infinite regular lattice with a simple cubic arrangement. This method is a so called 'blind' procedure (Bomboni et al, 2012). It leads to the 'clipped' CPs at the peripheral of the compact and is an unrealistic representation of CPs in an HTGR reactor. In neutronic calculations it is imperative to model the coated fuel particles correctly hence CPs are best placed randomly in the fuel compact, if a truly random ordering is accepted.

Modelling the HGTR in CE physics requires explicit modelling of the reactor core. CE physics allows the user to model the reactor as close to reality as possible and hence the CE KENO model can be considered to be the reference model. CE physics allows proper representation of both the double heterogeneity and the stochastic random nature of the coated particles of the HTGR geometry.

5.1.1 Packing of MHTGR-350 coated particles in SCALE 6.2 CE

The fuel compact model in KENO-VI is defined explicitly and consists of a cubic lattice of coated particles. To ensure that there is no clipping at the boundary and that the fuel to moderator ratio is conserved as best as possible, the local packing fraction is increased so that the particles fit within the perimeter of the fuel compact. A fuel compact model is built and labelled KCE 000. Packing of the CPs depends on the global packing fraction (GV_f) and the local packing fractions (LV_f), which are given by Equations 5.1 and 5.2 respectively:

$$GV_f = \frac{(\#\ of\ CPs) \times V_{CP}}{V_{FC}}, \tag{5.1}$$

$$LV_f = \frac{V_{CP}}{V_{LAT}}, \tag{5.2}$$

where V_{CP} is the volume of the coated particle, V_{FC} is the volume of the fuel compact and V_{LAT} is the volume of the lattice element that defines the coated particle in the compact. The global packing fraction (GV_f) refers to the total number of TRISO particles compared to the entire fuel compact, whilst the local packing fraction (LV_f) refers to the TRISO pitch.

KCE 000

Model KCE 000 is the fuel compact of the MHTGR-350 and is modelled identically to the IAEA CRP on HTGR UAM (Strydom et al, 2015). There no clipping of the CP with the outer boundary. To achieve this, the global packing fraction (GV_f) is reduced from 0.35 to 0.3491 and the local packing fraction (LV_f) is increased from 0.35 to 0.4097. The dimensions of the cuboid enclosing the CP are 0.09100 cm in the x and y direction and 0.09856 cm in the z direction. There are 50 layers of coated particles arranged in in the cubic lattice with each layer consisting of 128 particles in the cross sectional view. The CP is centred at coordinates (0, 0, 0.04928) in cm. In total there are 6400 coated particles. For the base case model, the DBRC is applied to ^{238}U only. A reflective boundary condition is used since this is a fuel compact model. Model KCE 000 is shown in Figure 5-1 (a). This is chosen as the base case model for the fuel compact since it is modelled identically to the CRP definition and will be used for comparison with other models.

KCE 001

An alternative fuel compact is developed which is labelled model KCE 001. It is modelled with 53 layers stacked axially with each layer consisting of 121 particles. The global packing fraction is decreased from 35% to 34.98%. The local packing fraction is increased from 35% to 38.51%. Hence the coated particles are decreased from 6416 to 6413, therefore the number of particles in this model is closer to the benchmark value. Each CP is packed in a cuboidal element with dimensions of 0.09560 cm in the x and y direction and 0.0929 cm in the z direction. Model KCE 001 is shown in Figure 5-1 (b). Figure 5-1 (c) shows the TRISO coated fuel particle.

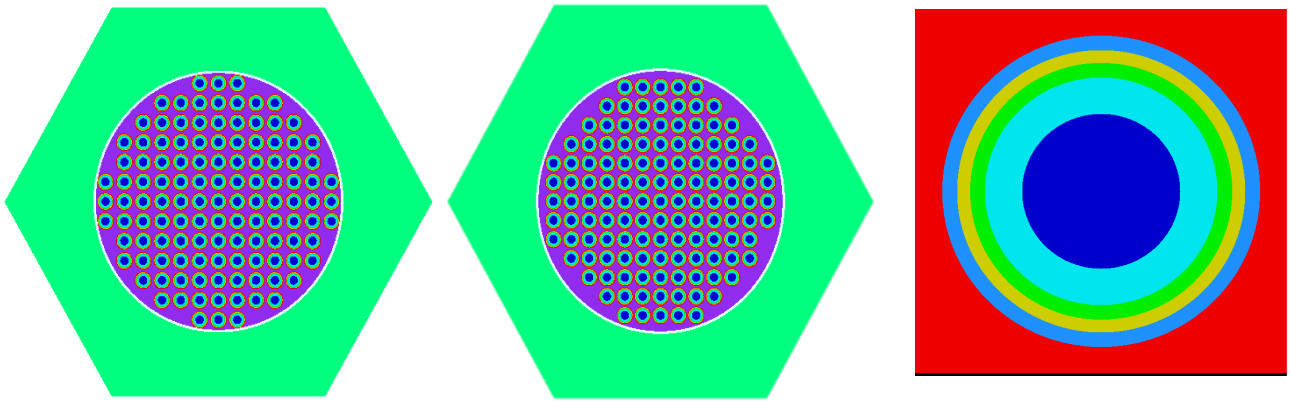

(a) (b) (c)

Figure 5-1 (a) KENO model KCE 000, (b) KENO-VI model of KCE001 and (c) fuel TRISO particle.

5.1.2 Algorithm to jiggle fuel coated particles in CE

Jiggling of coated particles refers to random placement of a fuel particle within its cuboidal element. In MCNP this method is known as 'On the Fly' random packing (Brown et al, 2005). Since KENO-VI like many other Monte Carlo codes does not have a stochastic geometry capability, a code that generates the input file is written in Fortran to jiggle the coated particles for a KENO-VI model. The algorithm to jiggle coated particles in CE KENO-VI is presented below:

- A random seed is used so that every time the input file is built a new set of random numbers are generated.
- The number of independent random positions is R_p and this value is user-defined.
- CP_i is the position of the coated particles, where $1 \leq i \leq R_p$.
- CP_i has the randomly generated coordinates (rx_i, ry_i, rz_i).
- As an example, if $R_p = 100$ then there are 100 independent random positions. If there are 6400 CPs in the compact, then these 100 positions will be repeated 64 times in the compact. However, the positions of these 64 CPs with the same R_p is also randomly distributed in the compact lattice.
- The coordinates (rx_i, ry_i, rz_i) of the random positions CP_i are calculated from Equations 5.3 to 5.5:

$$rx = \left(S_1 - \frac{1}{2}\right)\delta_x; \tag{5.3}$$

$$ry = \left(S_2 - \frac{1}{2}\right)\delta_y; \tag{5.4}$$

$$rz = \left(S_3 - \frac{1}{2}\right)\delta_z. \tag{5.5}$$

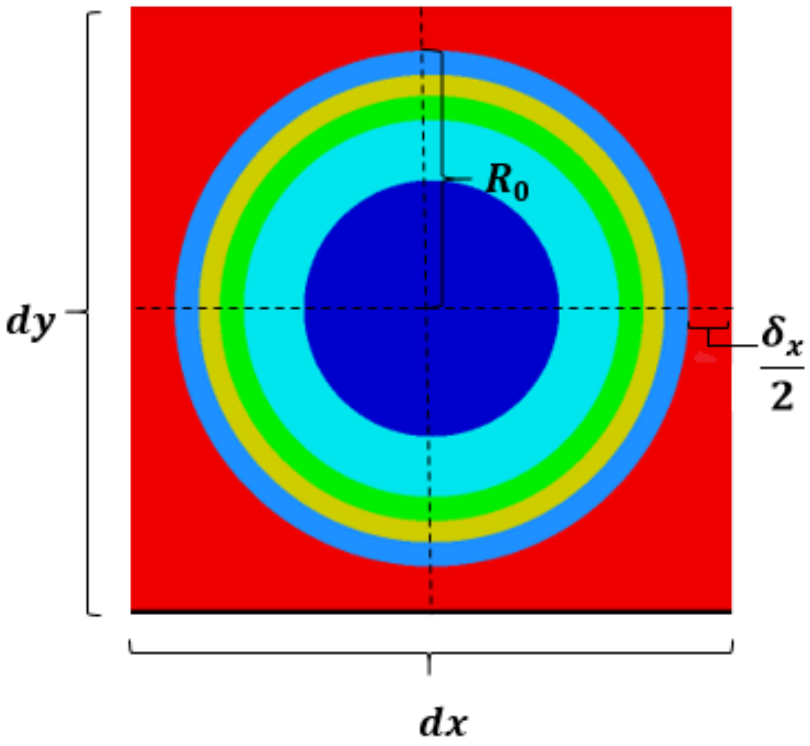

Figure 5-2 Fuel coated particle in a cuboidal element.

The parameters that are used in Equation 5.3 to Equation 5.5 are illustrated in Figure 5-2 and the parameters can be defined as:

- S_1, S_2, S_3 are random numbers between zero and one.
- δ_x, δ_y, δ_z are the maximum distances between the outer CP diameter ($2R_0$) and the lattice edges (dx,dy, or dz) and are shown in Figure 5-2.
- rx, ry and rz must be positive and negative hence the -1/2. The centre of the cuboid is chosen as the origin.
- rx, ry and rz must be chosen so that coated particle is not displaced past the edge of the cuboid – no clipping.
- It must also be ensured that the coated particle does not clip the compact outer surface.

Figure 5-3 shows the jiggled model with $R_p = 100$. In this study, jiggling is done for R_p of 100, 600,1600, 3200 and 6400 for the KCE 000. R_p is chosen to be 100, 1600, 3200 and 6416 for KCE 001.

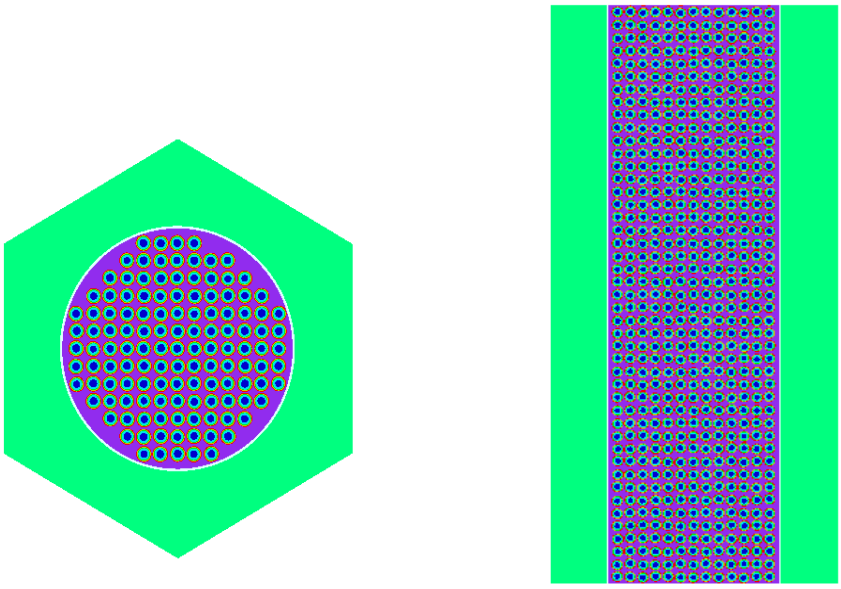

Figure 5-3 Jiggling of CPs with $N = 100$.

5.1.3 Full randomization of fuel coated particles in CE KENO-VI

Another Fortran code is written to completely randomize the placement of the coated fuel particles. This method is best since it is the closest to reality. The fuel mass can be conserved since the CPs are not arranged in a lattice and therefore the number of coated particles can be set to the required value but this method is costly in CPU-time for the KENO-VI calculation. Random particle distribution is achieved by using making use of holes in KENO-VI. A R_p number of holes are created having a cuboidal lattice geometry, these holes are then filled with the coated particles. The algorithm operates by displacing a CP from its original position in the cuboidal lattice to a new randomly selected position. It is ensured that each CP is moved from its original position to a random position through a number of iterations. The coated particles are tightly packed but there still exists space in the compact for the coated particle to be displaced. The fuel compacts with randomly located CPs are shown in Figure 5-4 (a) and Figure 5-4 (b).

It is computationally expensive given the resources available to simulate 6416 random positions using the non-MPI executable version of SCALE 6.2 that was available for this study. In a study done by Ho et al (2018) on an HTTR fuel rod with 18000 CPs and a height of 54.6 cm, it was shown that increasing the number of random positions, hence decreasing the height of the repeated axial layer, causes a change in k_{inf} that is within one sigma ($\sigma = \pm 0.00015$) but drastically increases time. In the publication by Ho et al (2018), 333 random positions (R_p) are chosen with a repeated axial height of 0.1 cm for an HTTR fuel compact, this produced a k_{inf} equivalent to the HTTR fuel compact model with 8658 CPs in a repeated axial length of 2.6 cm.

The model with $R_p = 8658$ took 4.7 times more of the calculation time than the $R_p = 333$ model but the $k_{\inf}$ only differed by 6 pcm. Therefore, it is not necessary to simulate a large number of different random positions if one accepts an error of around 6 pcm. Accordingly, in this study, the complete randomization is done for simplified simulations. For example, taking a sixteenth of the coated particles specified in the benchmark compact, one gets 401 random positions placed in a fuel compact height of 0.308 cm (6.25% of original height) as shown in Figure 5-4 (c).

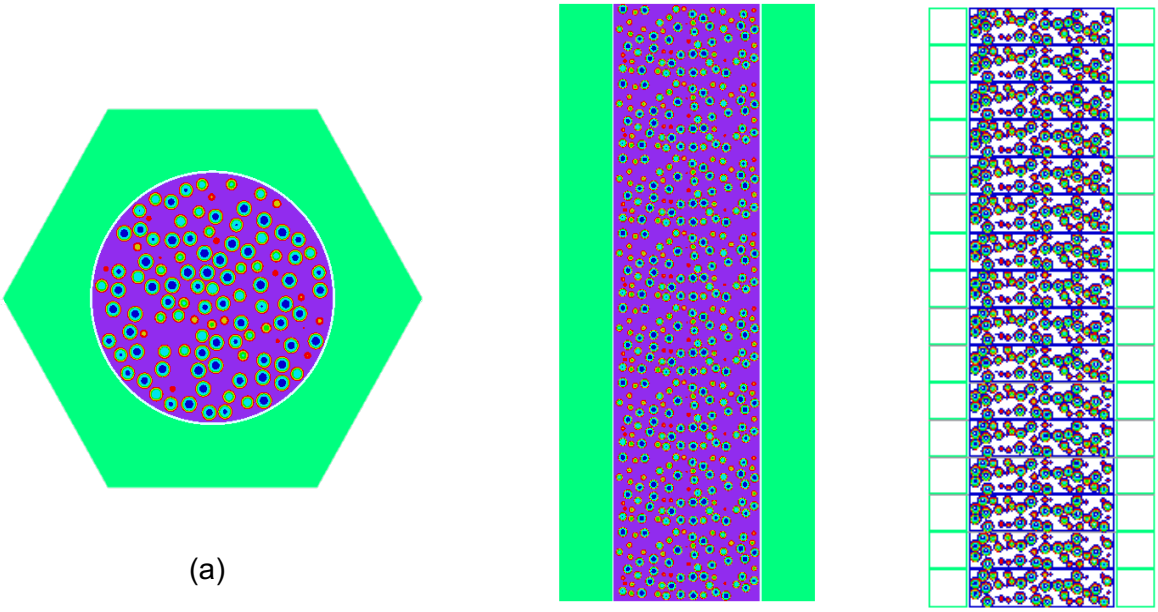

(a) (b) (c)

Figure 5-4 Randomized fuel compact model.

5.1.4 Modelling of the lumped burnable poisons in CE physics

The total number of LBP Bistructural Isotropic (BISO) particles is not specified in the IAEA CRP MHTGR-350 benchmark document (Strydom et al, 2015) but the packing fraction is 10.9%. Given this, the LBPs are also modelled using a cubic lattice without clipping, as shown in Figure 5-5 (a). A layer of 455 coated LBP particles is distributed in a square lattice with a pitch of 0.0229 cm. The compact has 103 axial layers of particles; each layer has a height of 0.047582 cm. The global packing fraction is altered from 0.109 to 0.1088 and the local packing fraction is altered from 0.1090 to 0.1176. The total number of particles in the LBP compact is 46865 BISO particles (Figure 5-5 (b)) and none of the particles are clipped. In this thesis, the packing and the randomization of the LBP are not treated but are important and yet unresolved topics in the uncertainty analysis of the MHTGR-350.

(a) (b)

Figure 5-5 KENO-VI model of (a) the LBP compact and (b) the LBP BISO particle.

5.1.5 The fuel block CE model

The fuel block CE model consists of fuel compact unit cells, LBP compacts, small and large coolant channels as well as graphite blocks. The KENO-VI model is shown in Figure 5-6. The fuel is modelled as discussed in Section 5.1.1. For the base model the fuel compacts labelled KCE 000 are used for the base case definition of the fuel block and the LBP is modelled as stipulated in Section 5.1.4. The base case CE single fuel block model at HFP corresponds to Exercise I-2a of the IAEA CRP on HTGR UAM and is labelled KCE 100.

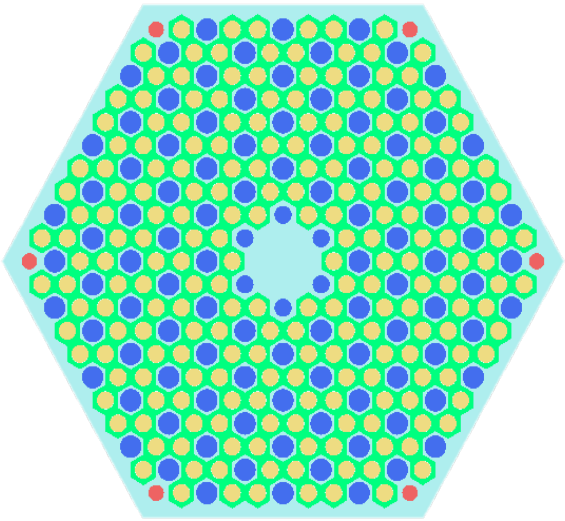

Figure 5-6 KENO-VI model of the single fuel block.

5.2 Modelling the MHTGR-350 fuel block in MG

The MHTGR-350 MG fuel block model is visually similar to the CE fuel block (Figure 5-6), however the required self-shielding treatment and the collapsing of group constants changes the methodology. The single fuel block model at HFP corresponds to Exercise I-2a of the IAEA CRP on HTGR UAM.

5.2.1 Double heterogeneous treatment of the fuel in MG physics using SCALE

The doublehet function which is discussed in Section 3.4.1 is used to model the MHTGR-350 fuel. The doublehet is the most efficient approach to modelling CPs of HTGR systems in MG using SCALE (Ilas et al, 2012; Goluoglu and Williams, 2005; Gehin et al, 2010). The doublehet function ensures that the fuel to moderator ratio in the fuel compact is conserved. The doublehet function MG KENO-VI has shown to under estimate the CE KENO-VI $k_{\inf}$ calculation by 569 pcm for the MHTGR-350 fuel compact by Strydom et al (2015) and by 637 pcm for the HTGR fuel block by Leppanen and DeHart (2009) for the HFP case.

5.2.2 Modelling of the lumped burnable poisons in MG physics

Strydom et al (2015) modelled the fuel block in 3D using MG KENO-VI and the LBP were modelled with the LBP BISO particles fixed in a lattice. The authors did not state whether they treated self-shielding of the LBP using XSProc of SCALE 6. KENO-VI is a 3D code so lattice representation in the axial direction is also possible.

In 2D, the lumped burnable poisons in MG are rather complex to model especially in NEWT, which is a 2D code. The conventional method to model LBP is by homogenization, but this has shown to underestimate $k_{\inf}$ by more than 1000 pcm due to self-shielding effects (Strydom et al, 2015). The doublehet function ensures self-shielding is treated in MG, therefore this work proposes using the doublehet function to model LBP. The doublehet function is designed to model coated particles that must contain fissile or fissionable isotopes, however the LBP does not contain such isotopes. In this work an attempt is made to find a way to model the burnable poisons in MG physics sufficiently using the LBP Trace method. This investigation is presented in Section 7.5.

5.3 CE KENO-VI parameters and convergence

An important parameter that would influence CE KENO-VI calculations is the DBRC. The significance of this parameter was explained in Section 3.6.1. The effect of the DBRC on the multiplication factor is assessed in Section 6.1.2.

There are other parameters that could also be tested such as:

- TTL: The temperature tolerance of the requested temperature, within which continuous energy cross sections fall. The default is -1.0, which means that the closest temperature to the requested temperature is used.
- $FRE:$ Enables or disables the use of the free gas treatment. The default is Yes.
- $UUM:$ Enables or disables the use of unionized parameters. The default is No.

The default is used for the parameters TTL, FRE and UUM. However, the experience that was already gained in the project in terms of computational time and resources indicated that the study of these parameters might not be completed within the project time. It has therefore been deferred for a later study.

Although the input manual for KENO-VI was studied comprehensively (Rearden et al, 2015), it is also possible that there are other parameters which were not identified in this study, but might be important. The assessment of further parameters has therefore also been deferred for a later study when these parameters become apparent.

When performing a KENO-VI criticality calculation, the source distribution must be converged before the counting statistics are commenced. Since this was therefore necessary in order to obtain high fidelity results, the CE KENO-VI convergence study is presented in Section 6.1.1.

5.4 MG KENO-VI parameters and convergence

At the end of each generation, KENO-VI produces the multiplication factor and its associated information for that generation. It is imperative that the source is converged before the multiplication factor is recorded. The source convergence parameters are NSK and NPG which are the number of skipped generations and the number of neutrons per generations respectively. The default parameters are $NSK = 3$ and $NPG = 1000$ for KENO-VI in CSAS, whilst the default values for KENO in CE TSUNAMI-3D are $NSK = 50$ and $NPG = 1000$. The KENO-VI source convergence study for MG is presented in Section 6.1. The convergence of the multiplication factor is governed by GEN. The default values for GEN are 203 and 550 for CSAS and CE TSUNAMI-3D, respectively.

The accuracy and efficiency of an MG KENO-VI calculation is controlled by the SZF, ISN, and SCT parameters. These parameters are important for generating problem specific self-shielded cross sections. SZF is the spatial mesh factor, ISN is the order of angular quadrature and SCT is the number of discrete scattering angles. The optimization of these parameters is not discussed

in this work since it has been done previously by Maratele (2016) and Naicker et al (2016). The recommendations from Naicker et al (2016) are $SZF = 0.4$, $SCT = -1$ and $ISN = 32$.

5.5 NEWT convergence and optimization parameters

The NEWT iterative approach discussed in Section 3.7.1 is dependent on the number of inner and outer iterations as well as the convergence criterion. The convergence of a NEWT calculations is controlled by the following parameters. $Epseigen$ is the convergence criterion for k_{eff} and the default value is 0.0001. $Epsinner$ is the spatial convergence criterion for inner iterations and the default is 0.0001. $Epsouter$ is the spatial convergence criterion for outer iterations and the default value is 0.0001. $Epsilon$ simultaneously sets all spatial and eigenvalue convergence criteria to the same value and individual defaults are used if epsilon is not specified. *Inners* is the maximum number of inner iterations in an energy group. The default is 2. $Outers$ is the maximum number of outer iterations; the default is 250.

P_n is the order for scattering in the mixture, the default is one. $Sides$ is the number of sides of the polygon used to model a cylinder (default is 12), and grids is the number of mesh points used to discretize the spatial domain. Sn is the order of the Sn level quadrature set and Sn is an even number between 2 and 16. The default is 6.

The CMFD option allows the user to either select “no” for rectangular or “yes” for partial. The default is no. $CMFD = yes$ (unstructured CMFD method) is recommended for triangular and hexagonal-domain configurations (Rearden et al, 2016). The parameter $xycmfd$ simultaneously specifies the same number of fine-mesh cells per coarse mesh cell in the x and y direction.

In this thesis P_n scattering is set to 2 for all materials and $Epseigen$ is set to 5×10^{-8}, as recommended by Naicker et al (2016). This value is small enough such that that the convergence of the solution would not influence the optimization studies within the required accuracy.

5.6 Convergence of CE TSUNAMI

The CLUTCH method has more user complexity in comparison to the IFP as it is dependent on the convergence of the $F^*(\vec{r})$ function. The use of the $F^*(\vec{r})$ function is to provide an estimate of the average importance of a fission neutron at location $\vec{r}$. The $F^*(\vec{r})$ function must be satisfactorily converged over the defined meshes before it can be applied to calculate the uncertainties. The parameter which can be used to study the convergence of this function is the total number of inactive histories, INH.

As INH is increased, there should be a value beyond which $F^*(\vec{r})$ remains statistically constant. However, $F^*(\vec{r})$ is not a direct output edit. Therefore, the following edits can be studied as a function of INH instead: $\%\Delta k/k$, the error in $\%\Delta k/k$ and the $F^*(\vec{r})$ convergence statistics. Now, INH is given as:

$$INH = NPG \times ING, \tag{5.6}$$

where NPG is the total number of source points and ING is the number of inactive generations in the problem. Due to the statistical nature of the calculation, one can keep NPG constant and study the change in ING instead of the change in INH when testing the convergence of $F^*(\vec{r})$. The total number of inactive histories, INH, is also specified by the equation:

$$INH = A \times m \times n \times p, \tag{5.7}$$

where $m \times n \times p$ is the mesh dimension and A is the number of inactive histories per mesh voxel with the total number of voxels being $m \times n \times p$.

Equating 5.6 and 5.7 we get:

$$ING = A \times m \times n \times p/NPG. \tag{5.8}$$

With NPG taken to be constant as discussed above, one can therefore test the convergence of $F^*(\vec{r})$ as a function of A and the mesh dimension $m \times n \times p$. As a recommendation (Rearden et al, 2016), there should be 10-100 inactive generations per voxel, i.e. A should have values between 10 and 100. When the CE TSUNAMI calculation is started, a given number of latent generations (CFP) must be carried out before the $F^*(\vec{r})$ function is calculated in the inactive generations ING. This means that the total number of generations that are skipped before the active KENO-VI calculations are commenced is:

$$NSK = CFP + ING. \tag{5.9}$$

Note that in the TSUNAMI-3D input, A is not a direct input parameter. The parameters NPG, NSK, CFP and (m, n, p) are input, and A is calculated using Equations 5.8 and 5.9, i.e.

$$A = \frac{(NSK - CFP) \times NPG}{m \times n \times p}. \tag{5.10}$$

The definition of CFP in the SCALE 6.2 manual is not clear so three examples were executed to confirm Equation 5.9 and Equation 5.10. All examples have identical models, i.e. a heterogeneous MHTGR-350 fuel compact model except that the CFP is varied in the models.

Example 1:

$$GEN = 5000$$
$$NSK = 10$$
$$CFP = 2$$
$$NPG = 1000$$
$$MESH = 10 \times 10 \times 10$$

Using Equation 5.10, $A = 8$. The warning message in the CE TSUNAMI output file is given in Figure 5-7.

```
***** warning ***** keno message number k6-325 follows:
Only 8.00E+00 particle histories are being used to populate F*(r) tallies
per F*(r) mesh interval. This may lead to poorly-converged F*(r) estimates
and inaccurate sensitivity coefficients! At least 10-100 inactive particle
histories should be simulated per mesh interval to obtain accurate F*(r) scores.
```

Figure 5-7 Warning message for Example 1.

Example 2:

$$GEN = 5000$$
$$NSK = 10$$
$$CFP = 5$$
$$NPG = 1000$$
$$MESH = 10 \times 10 \times 10$$

Using Equation 5.10, $A = 5$. The warning message in the CE TSUNAMI output file is given in Figure 5-8.

```
***** warning ***** keno message number k6-325 follows:
Only 5.00E+00 particle histories are being used to populate F*(r) tallies
per F*(r) mesh interval. This may lead to poorly-converged F*(r) estimates
and inaccurate sensitivity coefficients! At least 10-100 inactive particle
histories should be simulated per mesh interval to obtain accurate F*(r) scores.
```

Figure 5-8 Warning message for Example 2.

Example 3:

$$GEN = 5000$$
$$NSK = 15$$
$$CFP = 5$$
$$NPG = 1000$$
$$MESH = 10 \times 10 \times 10$$

Using Equation 5.10, $A = 10$. The CE TSUNAMI output file gives no warning message.

5.7 Convergence of Sampler

The convergence and optimization of Sampler depends on the number of samples (N) as well as the convergence of the corresponding transport calculation. Prior to running Sampler/KENO, MG KENO-VI must be sufficiently converged. Prior to running Sampler/NEWT, NEWT must be sufficiently converged.

5.8 Output information

The output information from the uncertainty and transport codes that are applicable to this thesis are discussed in this section.

5.8.1 KENO-VI

The main KENO-VI result that is recorded in this work is the multiplication factor (k_{eff} or k_{inf}) and its associated statistical deviation due to the Monte Carlo method.

5.8.2 CE TSUNAMI-3D

CE TSUNAMI produces the relative standard deviation (RSD) (which is equal to $\%\Delta k/k$) due to cross section data. Δk can be calculated using Equation 5.11:

$$\Delta k = RSD \times k_{\text{eff}}/100. \tag{5.11}$$

TSUNAMI also produces the contributions to the uncertainty in k_{eff} by individual contributors in descending order. The nuclide-reaction to nuclide-reaction covariance matrix responsible for the uncertainty contribution is given followed by the contribution to the uncertainty in terms of $\%\Delta k/k$. The value of the $\%\Delta k/k$ for the uncertainty contributors is given as an actual value and not a relative value, adding the square of these values with positive signs and subtracting the squares of negative values equals the total uncertainty (Rearden et al, 2016). It is noted that the uncertainty contributors are given in positive and negative values and negative values are the

result of anti-correlations in the cross section covariance data. The largest contributors to uncertainty are reported since they are the most probable source of computational bias. Each contributor is known as a nuclide-reaction pair and consists of the specific nuclide and reaction (or parameter) combination (Goluoglu et al, 2004). Some of the possible reactions and parameters were shown in Table 2-1.

The notation that is used in SCALE to represent the nuclide-reaction pairs for all the cases studied in this work is given in Table 5-1.

Table 5-1 Examples of nuclide-reaction pairs applicable to this work.

Nuclide-reaction pairs	**Description**
$^{235}U(\vec{\nu})$ / $^{235}U(\vec{\nu})$	The nuclide-reaction pair for nubar of ^{235}U
$^{238}U(n,\gamma)$ / $^{238}U(n,\gamma)$	The nuclide-reaction pair for radiative capture of ^{235}U
c-graphite elastic / c-graphite elastic	The nuclide-reaction pair for elastic scattering of neutrons in graphite
^{235}U fission / $^{235}U(n,\gamma)$	This is the nuclide-reaction pair for the fission for ^{235}U fission with the radiative capture of ^{235}U
^{235}U fission / ^{235}U fission	This is the nuclide-reaction pair for the fission of ^{235}U

TSUNAMI-3D also produces the sensitivity plots which are graphic representations of the changes in k_{eff} due to changes in a cross section versus the cross section energies. Along with the sensitivity plot the energy, region and mixture integrated sensitivity is also reported, which evaluates the similarity between two systems.

5.8.3 NEWT

In this work, NEWT is primarily used for its k_{inf} and macroscopic cross sections output.

Three sets of cross section data are studied from the NEWT output. These are the:

I. Macroscopic cross sections for the mixtures in the original group structure (Σ_{mixture}).
II. Few-group cross sections by nuclide (Σ_{nuclide}).
III. Homogenized macroscopic cross sections for nodal calculation (Σ_{nodal}).

The naming convention using Σ_{mixture}, Σ_{nuclide} and Σ_{nodal} is being used to facilitate the discussion.

Typically for HTGRs, cross sections are collapsed to four groups and six groups. In this thesis the cross sections are collapsed into four groups as shown in Table 5-2. The 4-group structure is the same as the one used in VSOP (Teuchert et al, 1994; Reitsma et al, 2005).

Table 5-2 Energy bins for 4-group collapsing

Group	Upper Energy
1	20 MeV
2	100000 eV
3	29 eV
4	1.86 eV

The format in which Σ_{nodal} is written differs from $\Sigma_{mixture}$ and $\Sigma_{nuclide}$ since the Σ_{nodal} is generally passed to nodal analysis codes such as NESTLE (NESTLE, V5.2.1, 2003). The Σ_{nodal} output includes a region-averaged $k_{\inf}$, transport corrected cross sections and two interpretations of absorption. The first interpretation of absorption is the directly collapsed cross section, the second interpretation of absorption is a more consistent definition of absorption as applied in nodal calculations (Rearden et al, 2016). This is defined as total cross section minus scatter cross section.

5.8.4 Sampler

Sampler prints the average value and the standard deviation calculated from all the samples generated. In this work the average $k_{\inf}$ and its standard deviation are of interest. Sampler/KENO-VI can print this response in the output whilst Sampler/NEWT cannot print the responses in the output file. Therefore, in Sampler/NEWT, a Fortran code is written to extract the $k_{\inf}$ value from each sample and the standard deviation is calculated. Each NEWT sample also produces macroscopic cross sections so therefore the cross sections are also extracted by the Fortran code script and their standard deviation is calculated.

5.9 Base case models

A summary of the base case models is presented Table 5-3. The criticality calculations are performed for the base case models using CE KENO-VI, MG KENO-VI and NEWT. These results are also compared to the results from other literature to verify the models developed in this work. The multigroup base case fuel block models are modelled with homogenized BP and doublehet fuel. The CE base case fuel block models are modelled with lattice fuel and lattice LBP.

Table 5-3 Summary of base case models of the MHTGR-350

Model	Code	IAEA Exercise	System	Fuel	BPs
KCE 000	CE KENO-VI	I-1b	Unit Cell	Lattice	-
KMG 000	MG KENO-VI	I-1b	Unit Cell	Doublehet	-
KCE 100	CE KENO-VI	I-2a	Fuel Block	Lattice	Lattice
KMG 100	MG KENO-VI	I-2a	Fuel block	Doublehet	Homogenized
NMG 100	NEWT	I-2a	Fuel block	Doublehet	Homogenized

The nomenclature for the models is as follows:

- The first letter describes the transport code used, therefore “K” is KENO and “N” is NEWT.
- The second two letters describe the mode. “CE” is continuous energy and “MG” is multigroup.
- The last three digits “000” indicate the model. A zero in the first digit describes a fuel compact and “1” in the first digit indicates a fuel block. The last digit denotes a variation of the model.

For example, KCE 000 is a CE KENO fuel compact calculation and KMG 101 is a MG KENO fuel block calculation with a variation (e.g. packing fraction might be different from KMG 100).

5.10 Comparison of results.

The following definitions are used in comparing results. When comparing two value X_1 and X_2 of a given parameter, both the difference and the percentage difference is used. The difference is given by:

$$Diff = X_1 - X_2. \tag{5.12}$$

When comparing two values for k, Equation 5.13 is used:

$$k_{diff} = k_1 - k_2. \tag{5.13}$$

where k_1 and k_2 are two different values of k.

k_{diff} is reported in units of pcm which is obtained by multiplying a given value of k by 1×10^5 pcm. This is an approximation since units of pcm are defined in terms of the reactivity (Sihlangu, 2016) and not the multiplication factor.

Differences between two values for cross sections or two values for $\%\Delta k/k$ are reported in $\%\ diff$ such that:

$$\%\ diff = 100 \times \left| \frac{(X_1 - X_2)}{(X_1 + X_2)/2} \right|, \tag{5.14}$$

where X_1 and X_2 are the two values for comparison.

5.11 Specific nomenclature

The reader should note that the words ‘mesh’ and ‘grid’ are used interchangeably in the NEWT part of this work.

CHAPTER 6: SENSITIVITIES STUDIES OF THE MHTGR-350 MODELS

This chapter addresses the sensitivities studies that are performed on the MHTGR-350 models. This is within the context of the convergence of calculations and the optimization of input parameters of the SCALE 6.2 transport codes and uncertainty codes. It is imperative to obtain converged results so that there is no bias and to ensure the reliability of uncertainty information.

It is also important to obtain reliable uncertainty information and accurate results without impinging on the time expenditure of a calculation, hence the optimization study becomes necessary. In this regard, one method in which optimization studies can be carried out is through repeating a number of calculations by choosing different values for a chosen parameter and finding the best option in terms of certain criteria. This is in essence sensitivity studies.

In a previous study at the North-West University (Naicker et al, 2016), the optimization study was performed only for the homogeneous fuel compact model. The optimization in the present study is performed on the heterogeneous fuel compact and fuel block. This chapter begins with converging and optimizing the transport code, followed by a presentation of the criticality calculations produced by the transport codes. The uncertainty codes are optimized and the uncertainty is quantified for the base case fuel compact and fuel block.

6.1 CE KENO-VI convergence and optimization

6.1.1 CE KENO-VI convergence of base case models

Convergence of CE models is controlled by the parameters NSK and NPG. These parameters are set such that the fission source is well distributed over all volumes that contain fissile material. Furthermore, to achieve the preferred standard error bound, GEN must also be set.

One of the features of the SCALE 6.2 release is the ability to perform source convergence tests. The SCALE 6.2 code performs 3 convergence tests i.e.

- **Test1**: Is the final fission source converged?
- **Test2**: Are all the active generations within epsilon of the average?
- **Test3:** Are there adequate active generations after the source is converged?

Table 6-1 shows source convergence tests results for 30000 source points and 50000 source points. A fuel block which consists of graphite in place of BPs at CZP was used for the convergence study. Additionally, 50 generations were skipped. This study was performed in MG

KENO-VI. Once the MG KENO-VI convergence parameters are obtained, these parameters are then applied to the CE KENO-VI calculation, to assess if these parameters still hold.

Table 6-1 KENO-VI convergence tests for the fuel block based on NPG

	$NPG = 30000$					$NPG = 50000$				
GEN	k_{inf}	σ pcm	Test1	Test2	Test3	k_{inf}	σ pcm	Test1	Test2	Test3
150	1.50722	41	P	P	P	1.50673	35	P	P	P
200	1.50718	33	P	P	P	1.50678	33	P	P	P
250	1.50723	29	P	P	F	1.50715	22	P	P	P
300	1.50723	25	P	P	F	1.50721	19	P	P	P
450	1.50706	20	P	P	F	1.50706	15	P	P	P
600	1.50714	17	P	P	F	1.50702	15	P	P	P
750	1.50726	15	P	P	F	1.50712	12	P	P	P
900	1.50733	13	P	P	F	1.50711	11	P	P	P
1200	1.50723	12	P	P	P	1.50700	9	P	P	P

Test 3 for 30000 source points per generation fails for 250-900 generations, but passes for 150, 200 and 1200 generations. This inconsistency is a topic for future work. A convergence study was performed and omitted (from this thesis) for 5000 and 10000 source points per generation because all of the test3 results failed for all generations between 150 and 1200 even though all of test1 and test2 passed. Failure of any of these test indicates that the fission source was still moving during the active generations. A total of 50000 source points per generation was selected since all three of the convergence tests were passed for any given number of generations.

A standard error (σ) of 15 pcm is chosen to be consistent with Strydom et al (2015) and Naicker et al (2016). It was found that 450-550 active generations would be adequate for KENO fuel assembly calculations to achieve this value. It was therefore decided to use 450 active generations. A plot of the generational Shannon entropy versus generation is shown in Figure 6-1. This figure along with Figure 6-2 and Figure 6-3 will help determine the number of inactive generations which should be skipped.

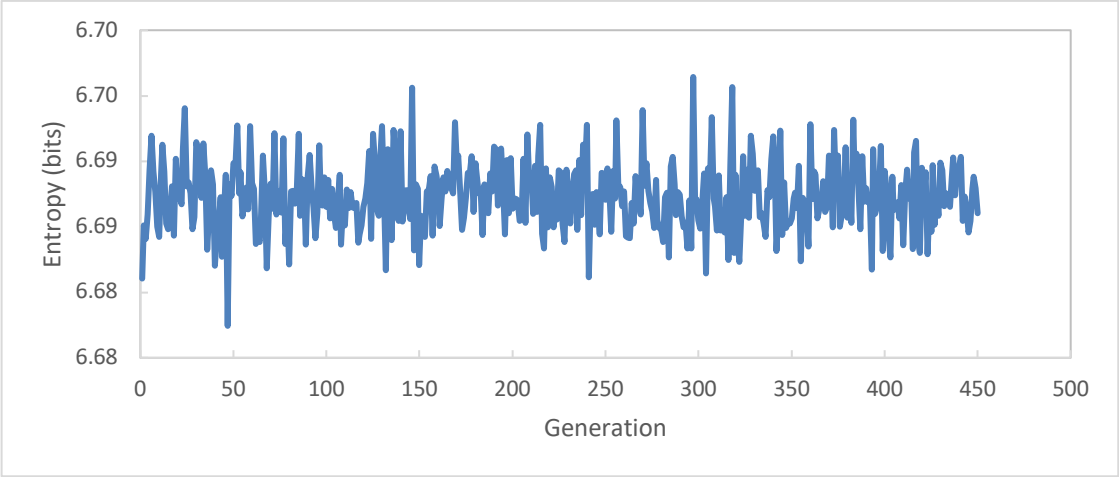

Figure 6-1 Generational entropy for 50000 source points per generation.

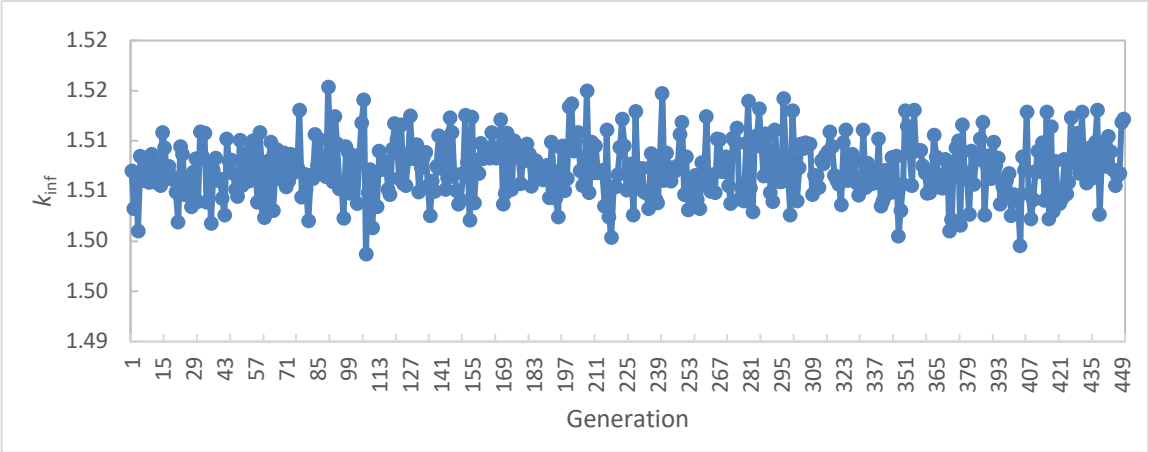

Figure 6-2 Generational k_{inf} for 50000 source points per generation.

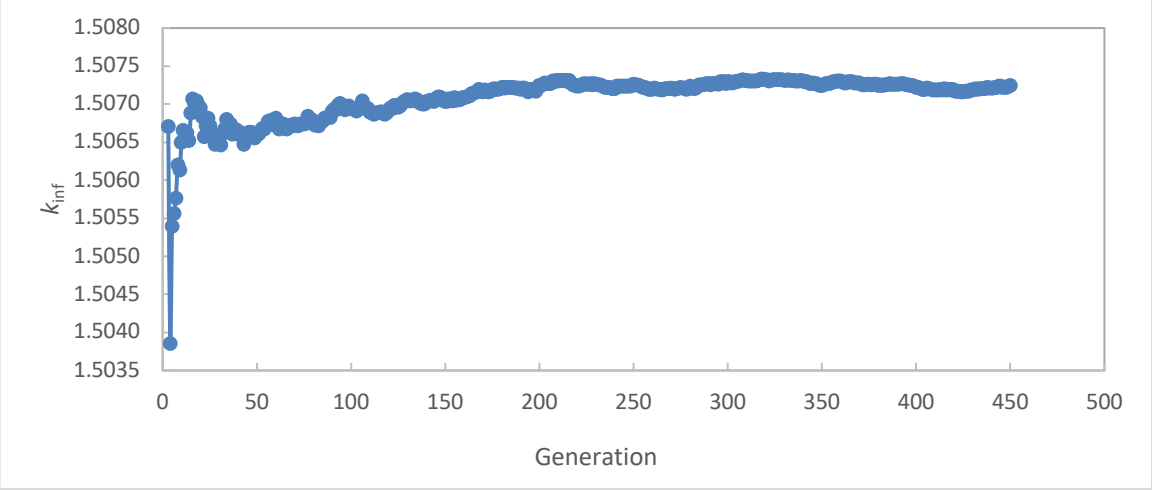

Figure 6-3 Average k_{inf} for 50000 neutrons per generation.

The average k_{inf}, shown in Figure 6-3, converges after 200 generations although all three of the convergence tests were passed for $NSK = 50$ (Table 6-1). The reliability of the convergence tests is confirmed by computing k_{inf} for both $NSK = 50$ and $NSK = 200$ as shown in Table 6-2. GEN and NPG is kept constant at 500 and 50000 respectively. Table 6-2 shows a difference of 13 pcm, which is within 1σ. Using 200 skipped generations has a 19.23% calculation time penalty. Therefore 50 generations were used instead of 200. Column 4 shows the absolute difference between column 2 and column 3.

Table 6-2 k_{inf} value for two different values of NSK

	$\boldsymbol{NSK = 50}$	$\boldsymbol{NSK = 200}$	$\boldsymbol{k_{diff}}$ **(pcm)**
$\boldsymbol{k_{\mathrm{inf}}}$ [σ(pcm)]	1.50756 (14)	1.50743 (13)	13
Time [hrs]	8.033	9.95	1.91

These first few generations are known as skipped or inactive generations. With 50 inactive generations chosen from a total of 500 generations, there are therefore 450 active generations and 50000 neutrons per generation were chosen. This calculation was performed on an Intel® Core ™i5-3210M CPU, with 2.50 GHz processor base frequency, an installed memory of 4.0 GB and a 64-bit operating system.

In summary the KENO-VI convergence parameters are listed in Table 6-3. The convergence parameters in Table 6-3 were tested for the CE mode and the convergence tests were passed. The standard error was found to be between 15 and 18 pcm. The standard deviation can also be specified in the KENO-VI input by using the "SIG" parameter in which the KENO-VI calculation will terminate at the specified standard error.

Table 6-3 The selected convergence parameters

NPG	***GEN***	***NSK***	**σ (pcm)**
50000	500	50	15 -18

6.1.2 Doppler Broadening Rejection Correction

If thermal scattering law data are not available in the nuclear data library, elastic scattering is treated with the free gas approximation in the KENO library. However, for heavy nuclides with 0 K scattering libraries available, the DBRC method can also be used. In addition, one needs to

also set the lower and upper energy limit for which the DBRC is applied, and it is therefore of interest to note the effect of varying of these limits on the multiplication and uncertainty parameters. Previous studies, (Strydom et al, 2015; Becker et al, 2009; Rearden et al, 2015) have shown that the choice of this parameter is important, however the sensitivity to the lower energy limit (DBL) and the effect on the error propagation was not shown.

The DBRC is applied to the CE model of the fuel compact (Table 6-4) and fuel block (Table 6-5) and the lower temperature limit is varied. The upper limit was not varied since the default was at 210 eV and this value was larger than the internal energy of the material. In this case, the internal energy of the material was approximated by using the average translational energy of an ideal gas using the formula $k_{av} = 3/2\, k_B T$, where k_{av} is the average translational energy, k_B is the Boltzamnn constant and T is the temperature of the gas.

The values $k_{\inf}$ and the computational time are recorded. Case 2 is the reference case and the computational time of all other cases is compared to the reference case.

Table 6-4 Effect of DBRC and its temperature cutoffs on KCE 000 (Exercise I-1b) at HFP

Case	Description	$k_{\inf}[\sigma(pcm)]$	Time
1	$DBR = 0, DBL = \text{default}$	1.25664 (18)	0.98983
2	$DBR = 1, DBL = \text{default}$	1.25015 (16)	1
3	$DBR = 2, DBL = \text{default}$	1.25008 (18)	1.04082
4	$DBR = 1, DBL = 0.01$	1.25049 (16)	0.99968
5	$DBR = 1, DBL = 0.1$	1.25028 (18)	1.36021
6	$DBR = 1, DBL = 0.15$	1.25005 (16)	1.00969

The SCALE 6.2 manual states that the options for DBRC are 0, 1 or 2 which select no DBRC, DBRC for ^{238}U only or DBRC for all major nuclides, respectively. The manual also states that DBRC is only available for ^{238}U which therefore implies that setting $DBR = 2$ is most probably equivalent to setting $DBR = 1$. Thus, there is a conflict in the manual, however in this study DBR is set for both option 1 and 2.

Setting DBRC to 1 for KCE 000, in Table 6-4, lowers $k_{\inf}$ by 649 pcm compared to setting it to 0. This compares well for the INL models in (Strydom et al 2015), where the ENDF/B-VII.0 library is used, and the difference is found to be 647 pcm for the MHTGR-350 fuel compact. However, changing from DBRC 1 to DBRC 2 which is the difference between the DBRC applied to ^{238}U

versus the DBRC applied to all actinides changes the multiplication factor by only 7 pcm. This is case 2 and 3 of Table 6-4. This difference is likely due to Monte Carlo statistics if setting DBRC to 2 sets it back to 1, since then no difference would be expected.

Setting $DBR = 2$ increases runtime by 0.04082, this also likely due to Monte Carlo statistics. The defaults for the energy range in which the DBRC is applied are $DBL = 0.4$ eV and $DBH = 210$ eV. The temperature of the materials at HFP is estimated to be 0.155 eV and at CZP the estimation is 0.03875 eV. The DBL is adjusted so it includes the HFP setting and CZP setting. The default value for DBH is quite far from these values and so it was not tested.

Lowering DBL to 0.1 eV for the fuel compact and the fuel block increases run time by 36.02% and 10.78% respectively, but only has a 20 pcm impact on $k_{\inf}$ for both models. It will be shown later that the error due to the nuclear parameters is far larger than this value. Therefore, within the current uncertainty data limits, using the default value of $DBL = 0.4$ eV will not compromise the accuracy by much.

Table 6-5 Effect of DBRC and temperature cut-offs on KCE 100 at HFP using CE KENO-VI

Case	Description	$\boldsymbol{k_{\inf}[\sigma(pcm)]}$	*Time*
1	$DBR = 0, DBL = default$	1.06453 (19)	0.99523
2	$DBR = 1, DBL = default$	1.06092 (19)	1
3	$DBR = 2, DBL = default$	1.06073 (19)	0.99870
4	$DBR = 1, DBL = 0.01$	1.06089 (20)	0.98894
5	$DBR = 1, DBL = 0.1$	1.06078 (21)	1.10731
6	$DBR = 1, DBL = 0.15$	1.06074 (19)	1.00023

For the fuel block, application of the DBRC to ^{238}U changes $k_{\inf}$ by 361 pcm as shown in Table 6-5. It has also been shown that the DBRC algorithm applied to the HTTR full core model decreases k_{inf} by 231 pcm using MCNP5 (Becker et al, 2009).

Similar to the fuel compact, activating the DBRC (in the fuel block case) for the additional uranium isotopes has an insignificant effect on $k_{\inf}$. Application of the DBRC at HFP shows to have significant changes in $k_{\inf}$. Therefore, the effect that the DBRC has on the nuclear data uncertainty must be quantified and this study is shown in Section 6.6.1.

6.2 NEWT convergence

NEWT convergence is governed by the size of the grids, Sn and CMFD acceleration, which are discussed in this section.

6.2.1 NEWT convergence and optimization for the fuel compact (NMG 000)

Grid dimension rules for CMFD acceleration

The NEWT optimization was performed on the heterogeneous fuel compact at CZP/HFP. NEWT calculations on fuel that is covered in graphite takes a longer time to converge, hence the CMFD acceleration is applied. $CMFD = 3$ was shown to accelerate computational time by a factor of 7.5 for a prototypic HTGR fuel assembly (Kim and DeHart, 2011) whilst $CMFD = 2$ was shown to accelerate time by a factor of 10.4. Differences in k_{inf} between $CMFD = 2$ and $CMFD = 3$ are reported to be 0.0018 pcm, which is a very negligible difference (Kim and DeHart, 2011).

For $CMFD = 3$ and $CMFD = 2$, the grid dimensions for the discreet ordinates solution must be a multiple of 4, hence grids 4 × 4, 8 × 8, 12 × 12 … 56 × 56 are assessed as well as the *Sn* values (2, 4, 6 … 16) are used to study the behaviour in terms of $CMFD = 2$ and $CMFD = 3$. The coarse-grid cells for the lower order diffusion, such as the finite difference scheme in the x and y directions must be equivalent to the higher order solution and also a multiple of 4. This constraint is set so there are no tiny coarse grids at the edges of the hexagon for the simplified lower order calculation used to accelerate the solution. In this case the coarse grid is set to 4. Hence for grids 4 × 4, 8 × 8, 12 × 12 … 56 × 56, $xycmfd$ is set to 1, 2, 3 … 14, respectively.

NEWT optimization in terms of CMFD

The selected grid sizes are 4 × 4, 8 × 8, 12 × 12, 16 × 16, 20 × 20, 24 × 24, 32 × 32, etc. It was not possible to carry out NEWT calculations with 1000 outer iterations for grid dimensions of 20 × 20, 24 × 24, 32 × 32 and so on, using $CMFD = 2$. Therefore, the outer iterations are increased to 5000. Furthermore, the calculation could not be completed for grid sizes of more than 32 × 32. The inner iterations were set to match the outer iterations, but this did not solve the problem. Therefore, $CMFD$ is set to 3 since this is a more robust solver and will be able to accommodate further grid discretization of the MHTGR-350 fuel compact.

It should be noted that in the above calculation, the various Sn values and the grid sizes were selected to test the $CMFD$ options, and complete sets for both these parameters were tried, although in some cases the calculations were not completed successfully.

The convergence of $k_{\inf}$ with respect to the Sn values and the grid sizes are discussed next, to obtain the optimal values, with $CMFD$ set to 3.

NEWT optimization in terms of Sn

Sn is assessed for all possible values. In general Sn is recommended to be greater than the default value, which is 6 (Sanchez et al, 2002). The maximum difference between successive values of Sn starting from $Sn = 8$ for all grids used is 6 pcm. $Sn = 6$ was not used since by visual inspection of Figure 6-4, $k_{\inf}$ does not seem to converge using this value. Since 6 pcm is a small value, and by further visual inspection of Figure 6-4, it is concluded that the value of $k_{\inf}$ converges at Sn equal to or greater than 8 for grid sizes, 8 × 8, 12 × 12, 16 × 16, 20 × 20, 24 × 24, 32 × 32 and 40 × 40, 48 × 48. Hence the recommendation is $Sn \geq 8$ for the NEWT MHTGR-350 fuel compact.

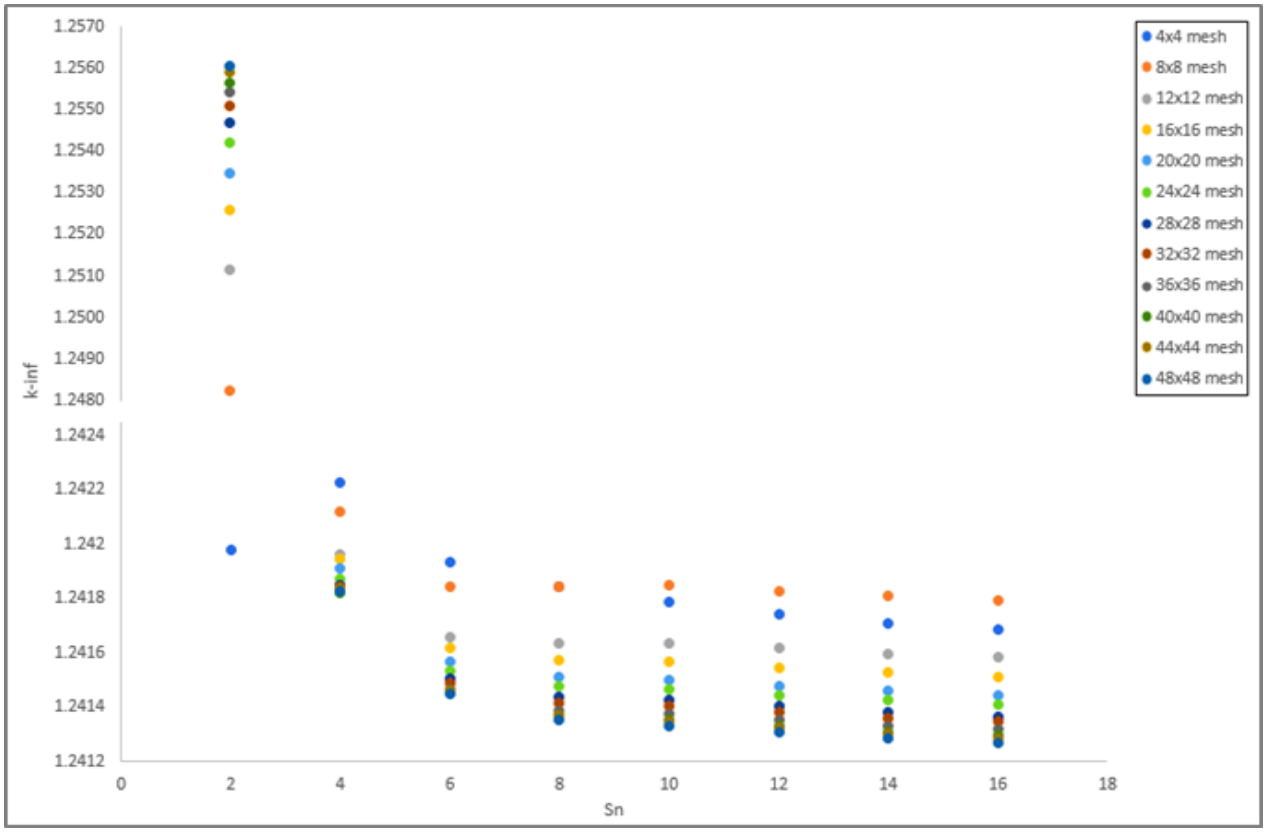

Figure 6-4 NEWT convergence of $k_{\inf}$ as a function of Sn for 12 different grids or meshes.

However, time increases in an exponential like behaviour as a function of increasing Sn. Therefore, it is not advisable to select values of Sn that are much higher than 8. In particular, for grids ≥ 12 × 12 and $Sn \geq 8$, time increases by 25 – 50% as a function of Sn and $k_{\inf}$ increases by 0.2 - 2.24 pcm as a function of Sn. Choosing values of Sn that are 12 - 16 is not advisable

since this only impacts k_{inf} insignificantly (less than 5 pcm) but increases the computational time by a factor of 2 - 4. The effect of Sn variation on time (in minutes) is shown in Figure 6-5.

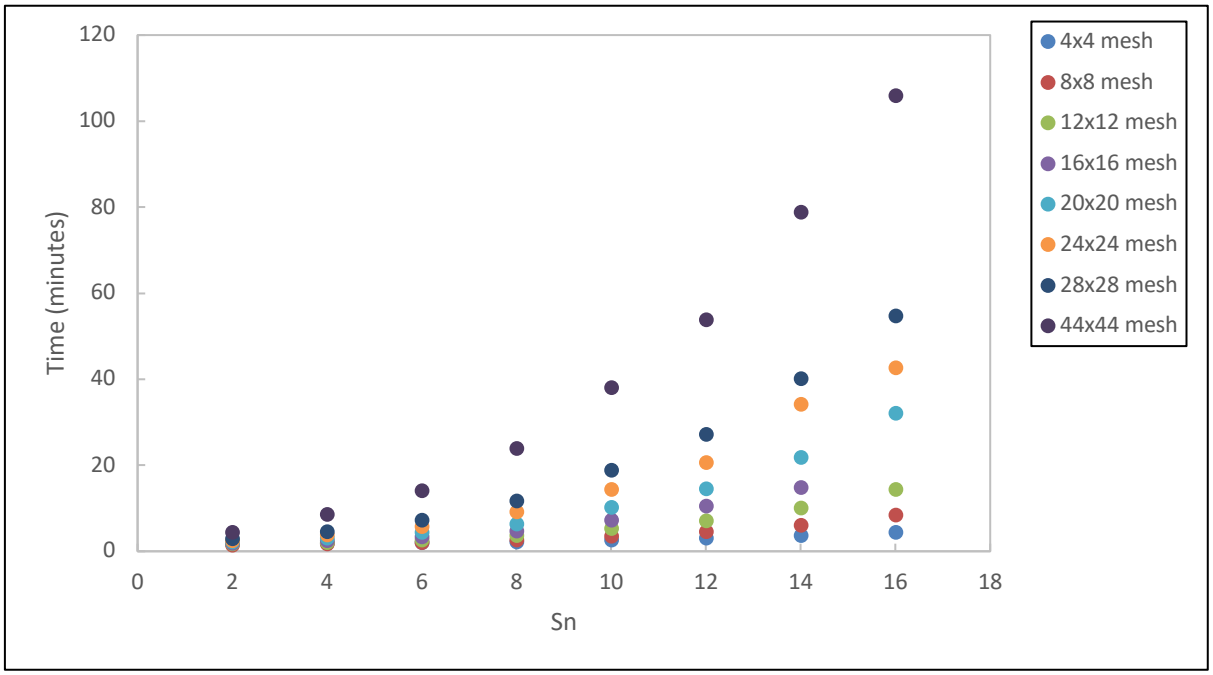

Figure 6-5 The effect of Sn on time expenditure.

Grid convergence

Since it was established that Sn should be equal to or greater than 8, values of $Sn = 8$ and $Sn = 10$ are assessed for grid convergence, with the results shown in Figure 6-6. Using a convergence criterion of 1 pcm, the grids converge at the 40 × 40 grid. However, time increases in an exponential like manner as a function of grid dimension as shown in Figure 6-7. One therefore needs to find the balance between grid convergence and executional time. Grid sizes of 8 x 8 and below are not recommended since their k_{inf} value differs by more than 20 pcm compared to grids 12 × 12. The convergence studies of the homogeneous compact cell showed that the calculations converged at grid sizes of 8 × 8 (Naicker et al, 2016). This therefore indicates that the heterogeneous case requires a finer grid definition.

The difference in k_{inf} between grid sizes 12 × 12 and 16 × 16 is 7 pcm and the difference in k_{inf} between grid sizes 12 × 12 and 40 × 40 is 21 pcm. However, time increases by a factor of 1.38 and 7.33 for the two comparisons respectively. Therefore, one can choose grid sizes between 12 × 12 and 40 × 40, depending on the executional time resources available and the standard error that can be accepted. It is not time-worthy to use the very fine grids, considering that the effect

on k_{inf} is very insignificant (less than 1 pcm). A grid structure of 40 × 40, which is shown in Figure 6-8 is recommended in this work and Sn is recommended to be 8.

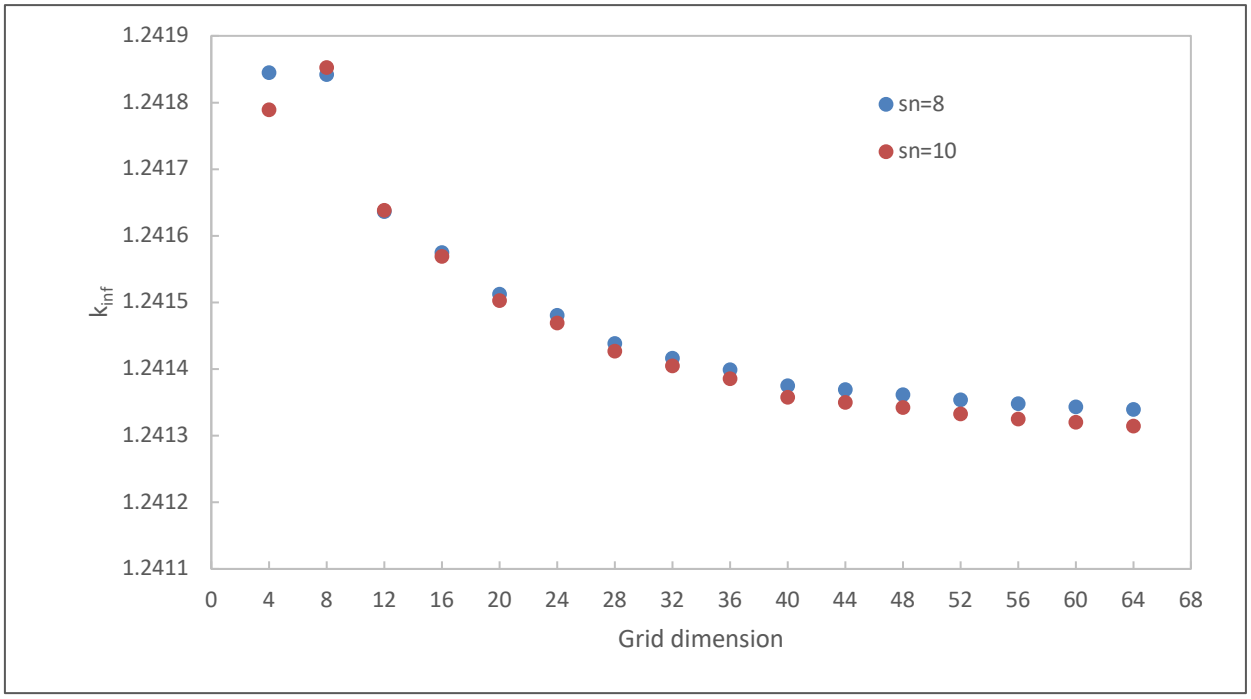

Figure 6-6 Convergence of k_{inf} in terms of grid dimensions for $Sn = 8$ and $Sn = 10$.

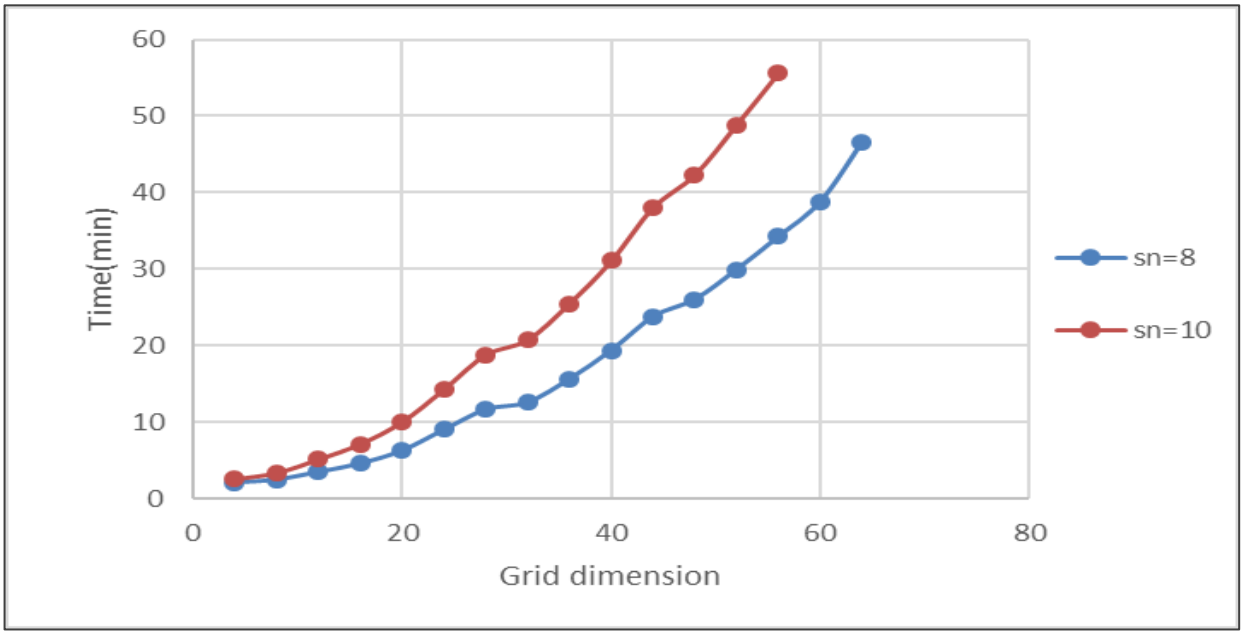

Figure 6-7 Computational time for grid dimensions with $Sn = 10$ and $Sn = 8$.

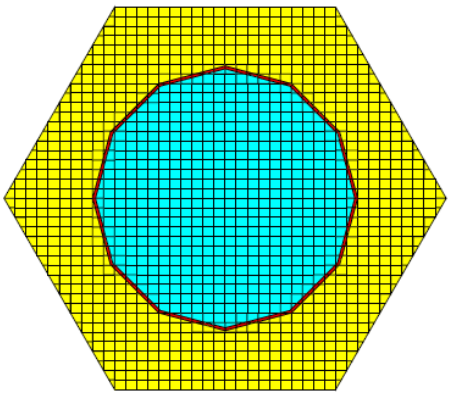

Figure 6-8 NEWT 40 × 40 grid configuration for the MHTGR fuel compact (NMG 000).

6.2.2 NEWT convergence and optimization for the fuel block (NMG 100)

$CMFD$ = 3 is used for the fuel block calculations, the number of inners and outers is set to 5000 and Sn is set at 10 as a recommendation from Section 6.2.1. For the fuel block calculation, a grid must be defined for the “fuel block" (global unit) and a grid must also be defined for the fuel compact, coolant channels and burnable poisons (unit cells). The grid in the global unit (n_x,n_y) must be a multiple of 4 and n_x must be equal to n_y. The grids in the unit cells (m_x,m_y) do not have to be a multiple of 4.

In the fuel block calculation, the unit cell grids are set to $(m_x = 4,\ m_y = 4)$ because the NEWT code stops working when ($m_x > 4$,$m_y > 4$) is set. The fuel compact grid size of ($m_x = 40$, $m_y = 40$), which was recommended in Section 6.2.1 could not be used for the compacts in the fuel block. Novotny et al (2016) states that the grid convergence results obtained from the heterogeneous fuel compact has a significantly higher influence than the single fuel block of the VVER 1000.

Varying the value of $xycmfd$ does not affect the value of the multiplication factor hence $xycmfd$ is set to 1. The global grid (n_x,n_y) is varied between (4,4) and (48,48). For (n_x,n_y) greater and equal to (52,52) the NEWT code stops working. The number of inner and outer iterations is increased to 10000 and the code still stops working.

In studying the behaviour of $k_{\inf}$ in Figure 6-9, one notices the $k_{\inf}$ increases steadily up to grid size 28, thereafter the behaviour becomes erratic. The difference between the highest and lowest $k_{\inf}$ values is 52 pcm, and from grid size 24 onwards, the difference between the highest and lowest $k_{\inf}$ is 35 pcm.

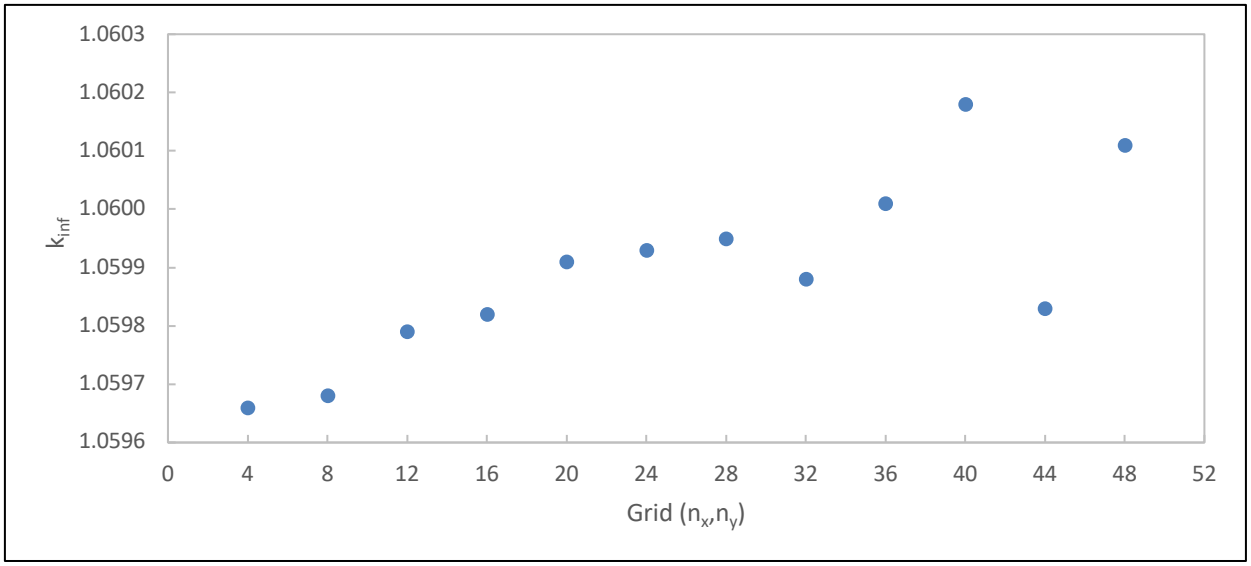

Figure 6-9 NEWT k_{inf} calculation for the fuel block with varying global unit grid.

It is difficult to judge whether convergence will be reached beyond the grid size of 28, and it is possible that numerical instabilities could be giving rise to this erratic behaviour. It was therefore decided to set the grid discretization for the global unit of the fuel block model at 24 × 24 and to bear in mind that this selection could introduce an error of around 35 pcm.

The time taken to complete a NEWT calculation is shown in Figure 6-10. Time increases with increasing grid refinement. The calculation at grid size 28 increases by a time factor of 1.35 in comparison with the calculation at grid size 24, with a change of 2 pcm. These NEWT convergence calculations were computed on an Intel® Xeon® W-1245 CPU, with 3.70 GHz processor base frequency, an installed memory of 64.0 GB and a 64-bit operating system. The recommended grid assignment for the NEWT MHTGR-350 models is shown in Table 6-6 and the NEWT graphical representation of the fuel block grids is shown in Figure 6-11.

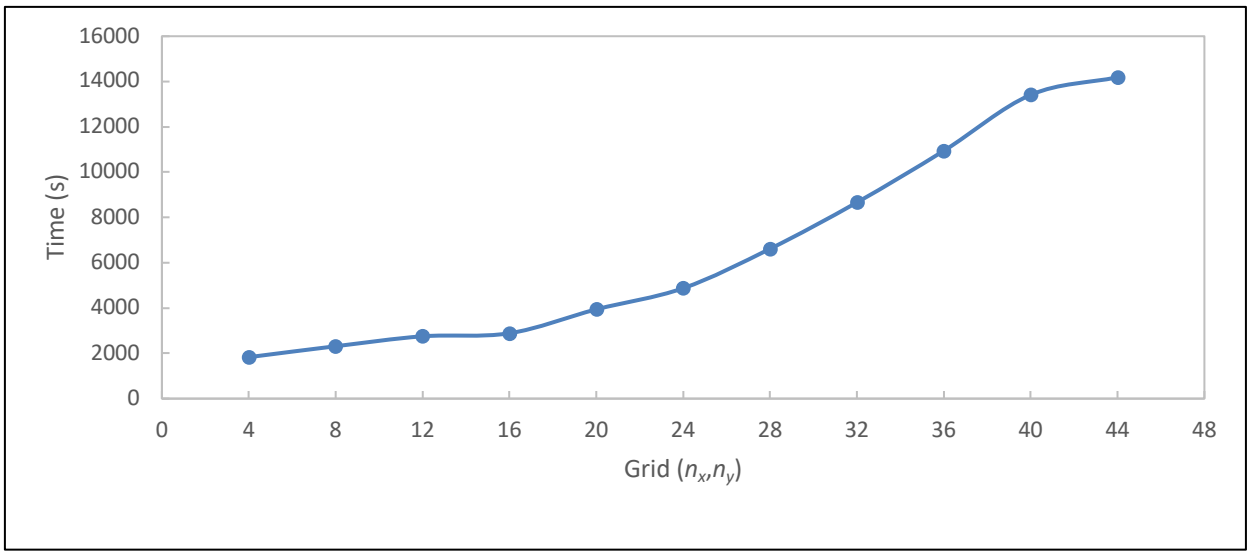

Figure 6-10 Time taken per NEWT calculation.

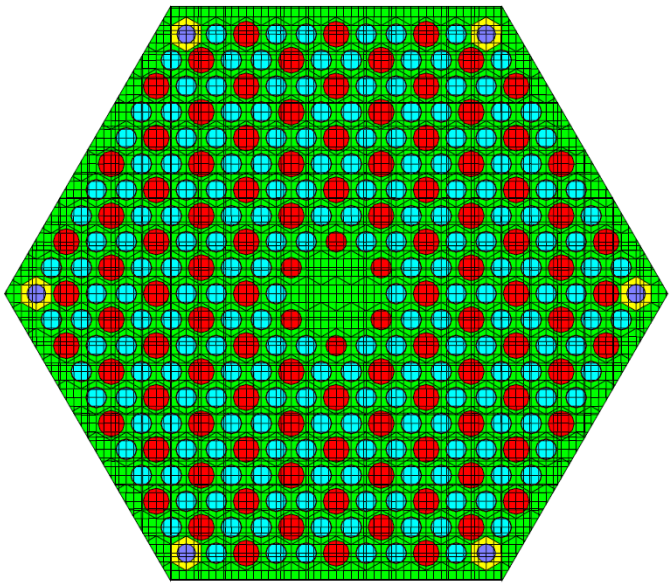

Figure 6-11 NEWT grid discretization for the MHTGR-350 fuel block.

Table 6-6 NEWT *Sn* values and grid discretization for convergence

	Sn	**Global Grid**	**Local Grid**
FUEL COMPACT (NMG 000)	8	40 × 40	-
FUEL COMPACT (NMG 100)	8	24 × 24	4 × 4

6.3 Base case criticality models

The nominal criticality results computed with KENO-VI and NEWT are shown in Table 6-7 for both SCALE 6.2.1 and SCALE 6.2.2 using the ENDF/B-VII.1 library for the CE calculations and the 252 energy group ENDF/B-VII.1 neutron cross section library for the MG calculations. Also shown in Table 6-7 are the results from Phase I of the IAEA CRP on HTGR UAM (Strydom et al, 2015) and (Naicker et al, 2016) which are shown in columns 4 and 5 respectively. The IAEA CRP results are computed with SCALE 6.2 beta3 with the 252 energy group ENDF/B-VII.1 library and the results reported by Naicker et al (2016) were computed using SCALE 6.1 with the 238 energy group ENDF/B-VII.0 neutron cross section library.

For the CE KENO-VI fuel compact calculations (KCE 000), the difference in $k_{\inf}$ between the two versions of SCALE 6.2 are 78 pcm and 619 pcm for CZP and HFP respectively. Comparing the results of SCALE 6.2.1, CE KENO-VI with that of the corresponding IAEA CRP result yields differences of 149 pcm and 9 pcm for CZP and HFP, respectively. The difference is much higher at CZP. These calculations were carried out using $DBR = 1$. Using $DBR = 0$, yields $k_{\inf}$ of 1.25664 and 1.25654 for SCALE 6.2.1 and SCALE 6.2.2, respectively, yielding a difference of 10 pcm. It is noted that only a single integer in the input file is changed to switch from $DBR = 0$ to $DBR = 1$. The large differences of 78 and 619 pcm therefore seem to arise when $DBR = 1$ is used and this requires further investigation. Therefore, only the SCALE 6.2.1 version is recommended for the CE calculations.

Table 6-7 Base case criticality for the MHTGR-350 fuel compact using transport codes

Model	$\boldsymbol{k_{inf}}$ $[\boldsymbol{\sigma(pcm)}]$ **SCALE 6.2.1**	$\boldsymbol{k_{inf}}$ $[\boldsymbol{\sigma(pcm)}]$ **SCALE 6.2.2**	$\boldsymbol{k_{inf}}$ $[\boldsymbol{\sigma(pcm)}]$ **IAEA CRP**	$\boldsymbol{k_{inf}}$ $[\boldsymbol{\sigma(pcm)}]$ **(Naicker et al, 2016)**
CZP				
KCE 000	1.37450 (16)	1.37528 (14)	1.37599 (15)	-
KMG 000	1.36349 (16)	1.36349 (17)	1.36361 (13)	1.36298
NMG 000	1.36128 (15)	1.36128 (15)	-	1.36327
HFP				
KCE 000	1.25035 (18)	1.25654 (15)	1.25044 (16)	-
KMG 000	1.24449 (17)	1.24449 (17)	1.24475 (15)	1.24315
NMG 000	1.24137 (15)	1.24137 (14)	-	1.24337

Identical results were obtained for the fuel compact MG KENO-VI calculations (KMG 000) using SCALE 6.2.2 and SCALE 6.2.1 at CZP and HFP. These results also compared well with the IAEA CRP results which used SCALE 6.2 beta3 with the 252 energy group library with the differences being 33 pcm and 26 pcm respectively. However, they differ from the results by Naicker et al (2016) which were carried out using SCALE 6.1 with the 238 energy group cross section library, with 96 and 134 pcm respectively. Identical k_{inf} values were also observed for the NEWT calculations using SCALE 6.2.1 and SCALE 6.2.2 at CZP and at HFP conditions (NMG 000). The version 6.2.1, NMG 000 results however differ by 200 pcm from the results by Naicker et al (2016).

It should also be noted that the MG calculations yielded lower k_{inf} values than the CE calculations as mentioned by Strydom et al (2015) and also shown in (Naicker et al, 2016; Leppanen and DeHart, 2009) for the fuel compact.

In this thesis, the MG KENO-VI results are lower than the CE KENO-VI results by 566 pcm at HFP and the difference between MG KENO-VI and CE KENO-VI is 569 pcm by Strydom et al (2015). MG KENO-VI result is lower than the CE KENO by 637 pcm by Leppanen and DeHart (2009). In the CZP case, the differences between the MG KENO-VI results and CE KENO eigenvalue results are larger than 1000 pcm.

The main difference between the MG and the CE calculations are in the MG self-shielding treatment in the unit cell to create the self-shielded cross sections. In both CZP and HFP cases, the double heterogeneous treatment could be a reason for the differences observed. In terms of the HZP case, the added complication of the resonance broadening of the cross sections must also be considered.

The base case criticality results for the single fuel block at HFP are compared in Table 6-8 for CE KENO-VI, MG KENO-VI and NEWT. The computed results are also compared to Phase I of the CRP results (Strydom et al, 2015). The CE fuel block results (KCE 100) compares well with the IAEA CRP result with the difference being 123 pcm for SCALE 6.2.1 and 215 pcm for the SCALE 6.2.2 comparison. The MG KENO result (KMG 100) differs from the CRP result by 212 pcm and the MG NEWT result differs from the CRP result by 384 pcm.

The fuel block MG results are lower than the CE result by more than 1500 pcm. This is as a result of the homogenization of the BP.

Table 6-8 Base case criticality for the single MHTGR-350 fuel block

Model	k_{inf} $[\sigma(pcm)]$ **SCALE 6.2.1**	k_{inf} $[\sigma(pcm)]$ **SCALE 6.2.2**	k_{inf} $[\sigma(pcm)]$ **IAEA CRP**
KCE 100	1.06091	1.06429	1.06214
KMG 100	1.04289	1.04289	1.04611
NMG 100	1.04517	1.04517	1.42990

The NEWT fuel block (in Table 6-8) calculations produce $k_{\inf}$ values that are higher than the MG KENO-VI by 221 pcm. This is consistent with the findings by Leppanen and DeHart (2009). In a publication by Leppanen and Dehart (2009), the NEWT $k_{\inf}$ computation for the fuel compact is lower than the MG KENO-VI calculation by 100 pcm. The prismatic block NEWT calculation for the HTTR fuel block were found to be higher than the MG KENO-VI calculation by 200-300 pcm.

The CRP NEWT results published by Strydom et al (2015) are higher than the MG KENO-VI calculation reported in this study. It is possible that the CRP used different MG convergence criteria from those used in this study.

6.4 CE TSUNAMI-3D convergence

The $F^*(\vec{r})$ function in the CE TSUNAMI code is converged for the MHTGR-350 fuel compact and single fuel block. The parameters required for convergence are defined for each system and the changes in parameters caused by the variation in the system are investigated.

6.4.1 $F^*(\vec{r})$ convergence for the MHTGR-350 fuel compact

The convergence of the $F^*(\vec{r})$ function used in the CE TSUNAMI-3D CLUTCH method is assessed using mesh sizes of 10 × 10 × 10, 20 × 20 × 20, 40 × 40 × 40, 60 × 60 × 60, 80 × 80 × 80 and 100 × 100 × 100. For each mesh size, the parameter A (as defined in Section 5.6 and Equation 5.10) is varied from 10 to 300. The aim is to determine the most efficient mesh size and the value of A for convergence. The latent generations are kept constant at 20 as suggested in the SCALE 6.2.1 manual (Rearden et al, 2016). Twenty latent generations are a very conservative number to obtain accurate sensitivities (Perfetti, 2012). The active generations are kept constant at 450 and skipped generations are set to 50. Figure 6-12 shows that the value of $\%\Delta k/k$ has a statistical spread with respect to both mesh size and A. Hence this parameter does not show any trend with respect to convergence and was not used to determine convergence of $F^*(\vec{r})$.

Figure 6-13 shows the percentage of the tallies that scored more than 50% uncertainty due to the statistical Monte Carlo method. As with all tallies based on the Monte Carlo method, it is desirable that these tallies show a small uncertainty to be more accurate. Therefore, as the number of skipped generations per voxel (A) increases, the uncertainty in the tallies decreases. Furthermore, different meshes were studied, and the data shows convergence as a function of increasing A, for each mesh studied. One can therefore choose a point along the x-axis beyond which the tallies that contain more than 50% uncertainty does not change much for all the meshes studied. This could for example be at 150, 200 and 250. On the other hand, points before 50 show that the number of tallies that contain more than 50% uncertainty is large.

Figure 6-14 shows the ratio of $F^*(\vec{r})$ mesh intervals that scored tallies as a function of A for each mesh size. The 10 × 10 × 10 mesh converges at $A = 150$. The 20 × 20 × 20 mesh converges at $A = 250$ and the 40 × 40 × 40 and 60 × 60 × 60 meshes converge at $A = 200$. The meshes of 80 × 80 × 80 and greater have almost equivalent ratios of scored tallies as shown in Figure 6-14. This means increasing meshes above 80 × 80 × 80 does not influence the convergence of $F^*(\vec{r})$.

It is seen that the finer the mesh size, the more inactive generations were required, hence more total generations required. This was due to Equation 5.6 and Equation 5.7. As $m \times n \times p$ increases, INH will increase (Equation 5.7) and consequently ING in Equation 5.6 will increase. The 10 × 10 × 10 and the 20 × 20 × 20 mesh size achieved convergence at a lower value of A. Hence the coarser mesh sizes are recommended.

The recommendations for the $F^*(\vec{r})$ convergence of the fuel compact model are:

- mesh size of 10 × 10 × 10; and
- $A = 200$.

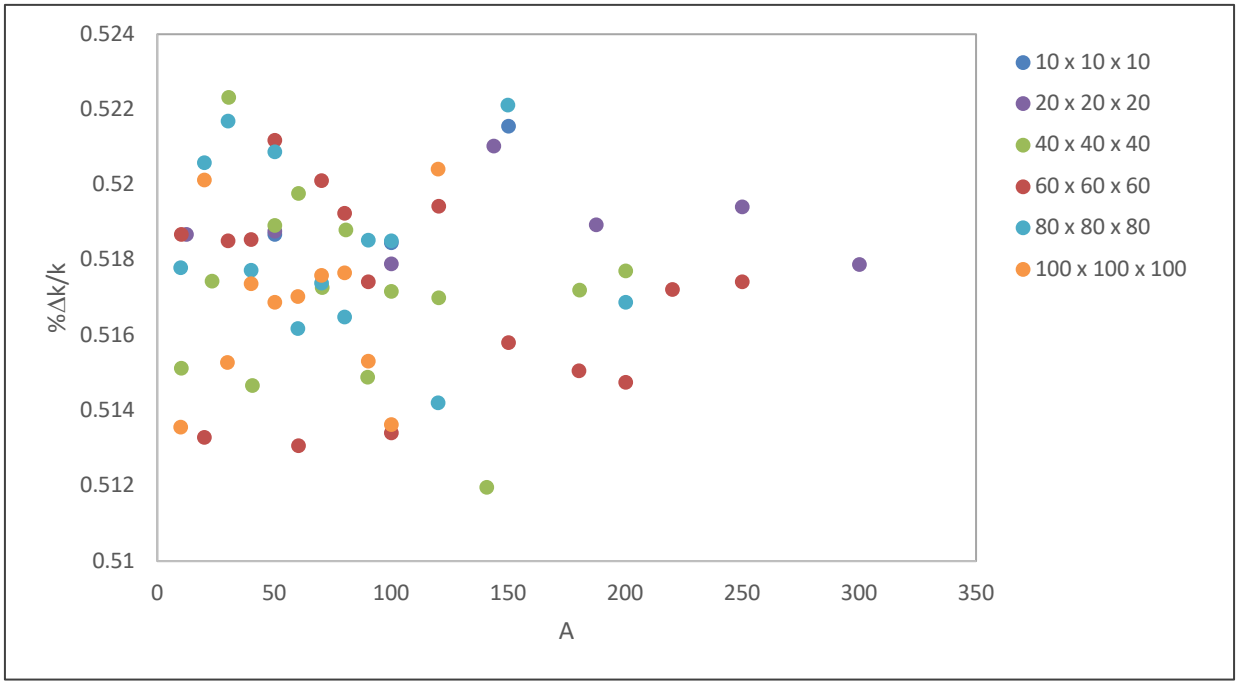

Figure 6-12 Relative standard deviation of k_{eff} due to cross section covariance data for the fuel compact.

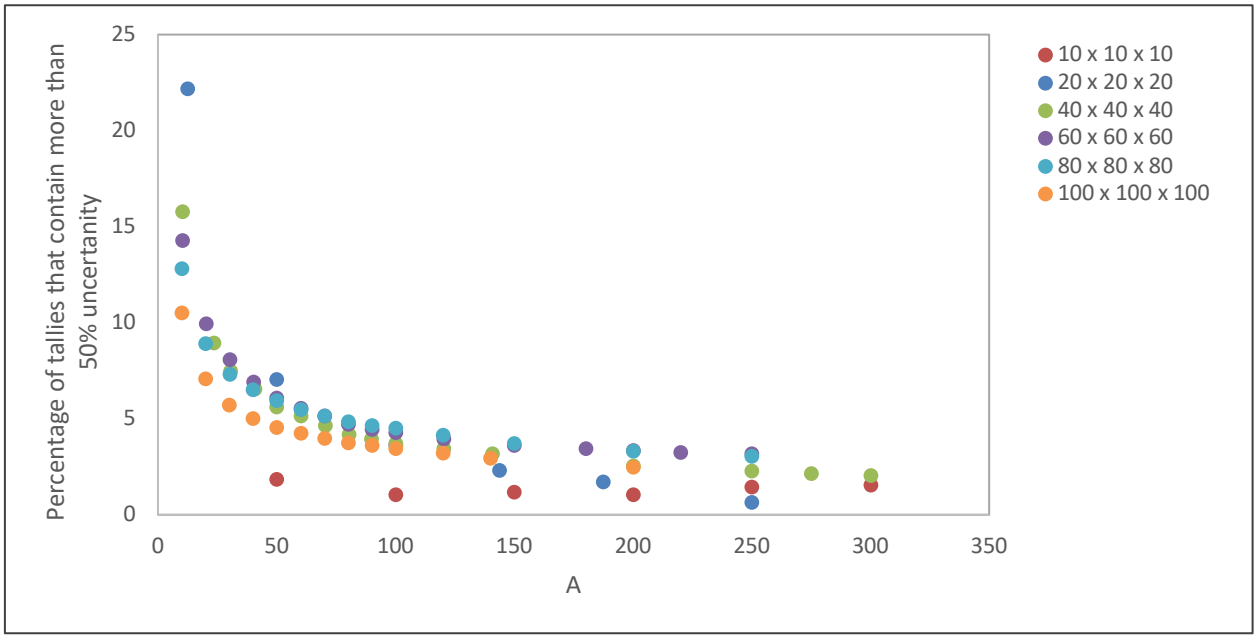

Figure 6-13 Percentage of $F^*(\vec{r})$ mesh tallies that contain more than 50% uncertainty for the fuel compact.

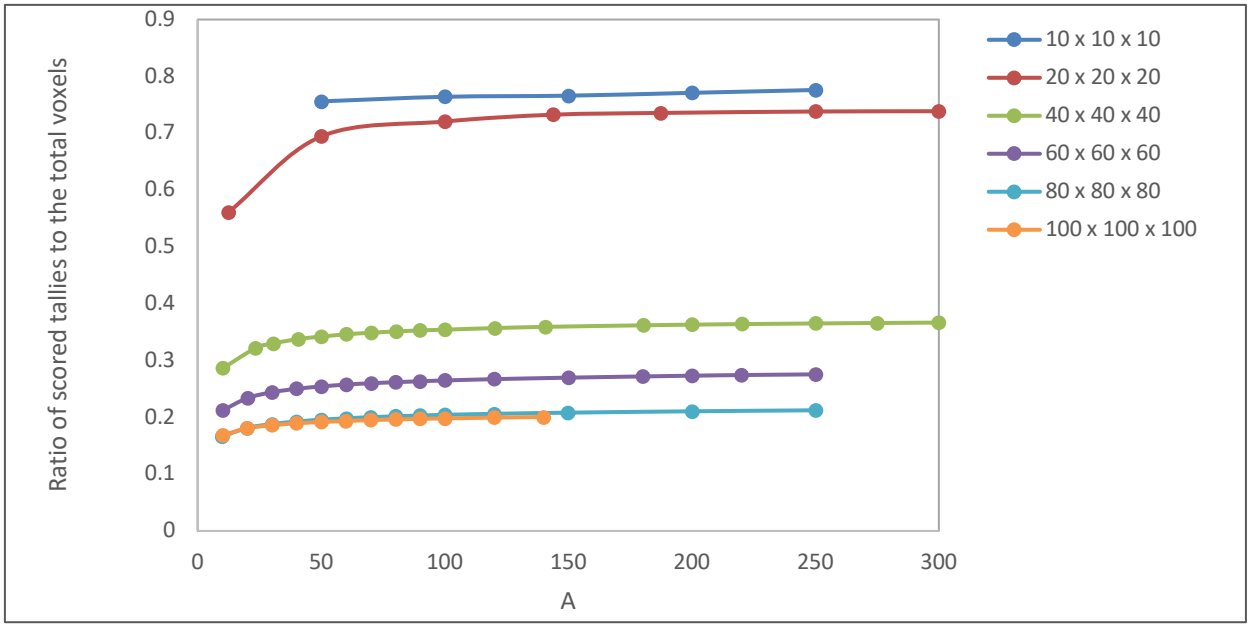

Figure 6-14 Ratio of $F^*(\vec{r})$ mesh intervals that scored tallies over the total $F^*(\vec{r})$ mesh intervals for the fuel compact.

6.4.2 $F^*(\vec{r})$ convergence for the MHTGR-350 fuel block

The $F^*(\vec{r})$ convergence is assessed for the fuel block. The three output edits are assessed in Figure 6-15, Figure 6-16 and Figure 6-17. In Figure 6-15, $\%\Delta k/k$ does not show any trend and cannot help determine convergence for $F^*(\vec{r})$. Figure 6-16 shows the percentage of voxels that scored more than 50% uncertainty and in this figure convergence is reached at $A = 200$ for all mesh sizes.

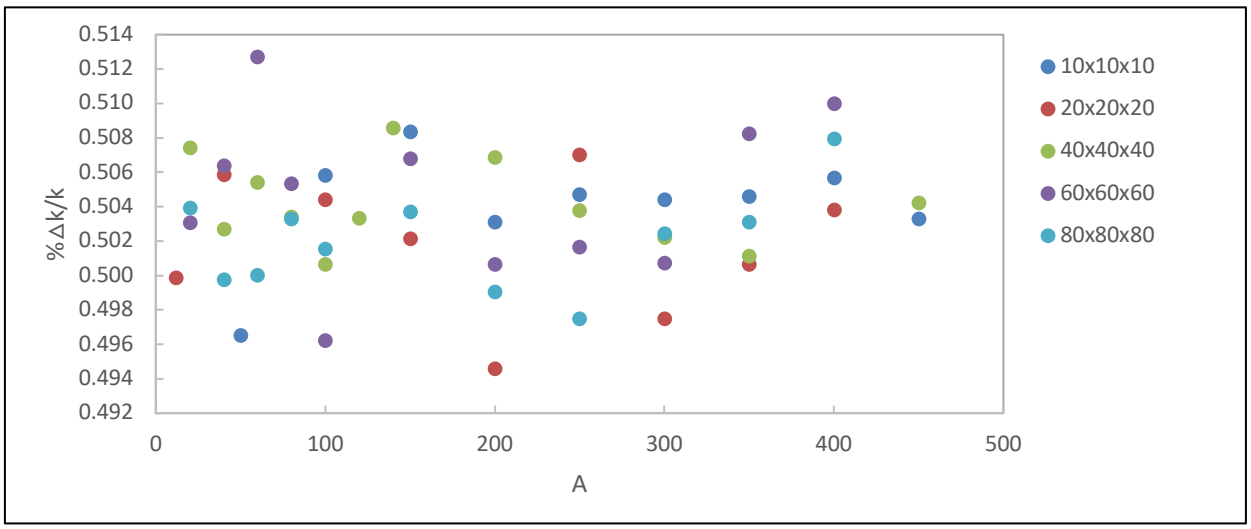

Figure 6-15 The relative standard deviation of k_{eff} due to cross section covariance data for the MHTGR-350 fuel block.

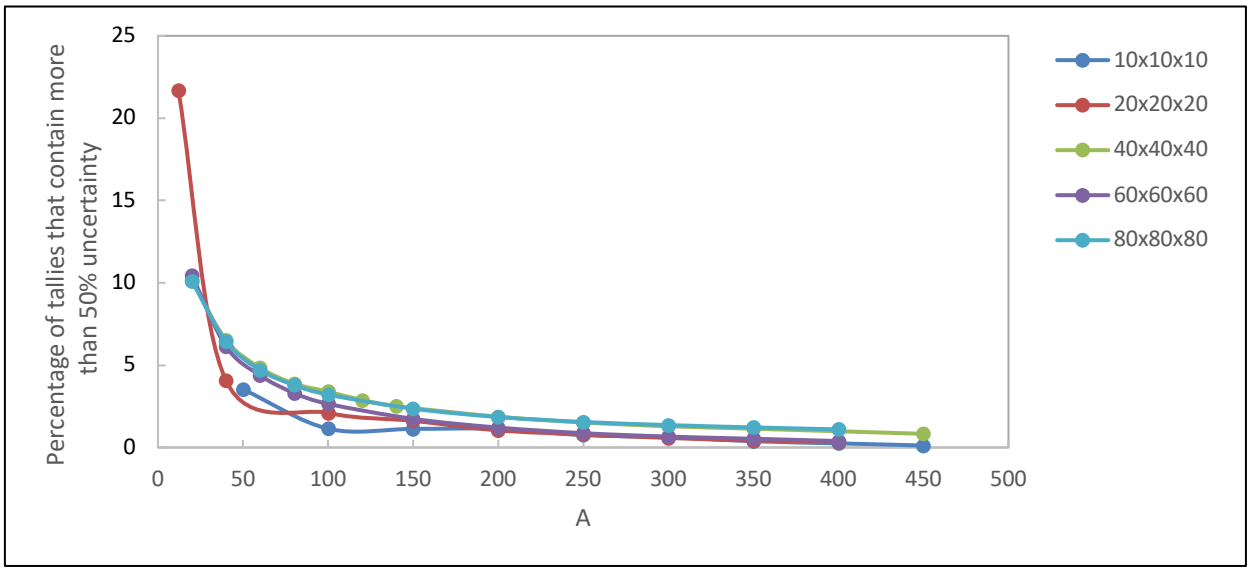

Figure 6-16 Percentage of $F^*(\vec{r})$ mesh tallies that contain more than 50% uncertainty for the MHTGR-350 fuel block.

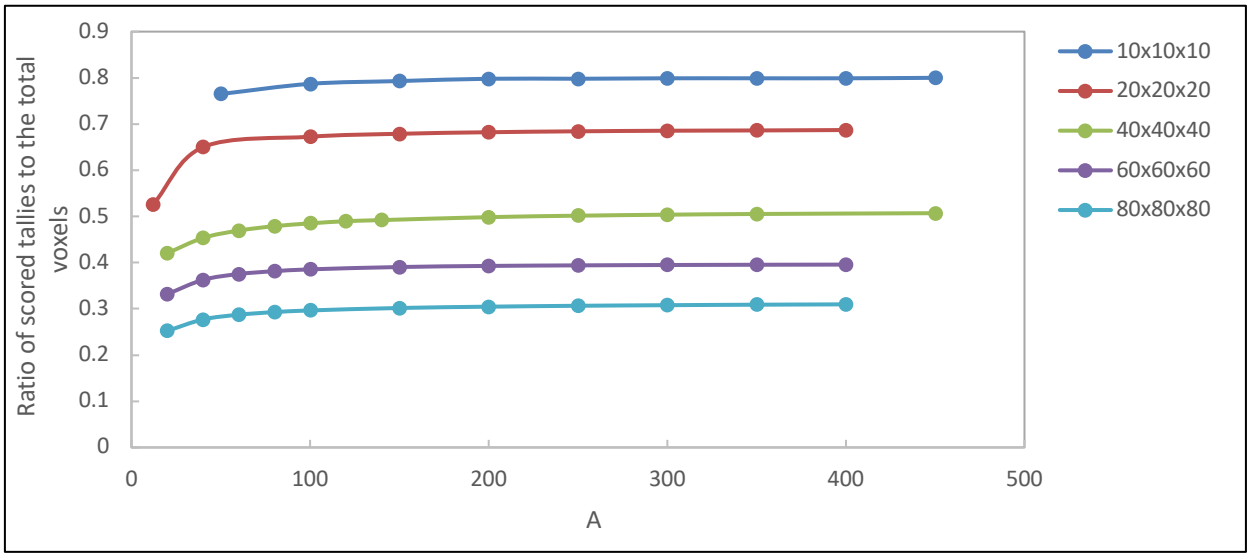

Figure 6-17 Ratio of voxels that scored tallies for the MHTGR-350 fuel block.

The fuel block and fuel compact produce convergence results that are not really distinct, and they also show very similar behaviour. The CE TSUNAMI-3D convergence parameters are listed in Table 6-9 and the spatial mesh is shown in Figure 6-18 for the fuel compact. The CE TSUNAMI-3D spatial mesh is shown in Figure 6-19. Only 2D projections of 3D meshes to the horizontal plane are shown in Figures 6-18 and 6-19

Table 6-9 Recommended CE TSUNAMI-3D convergence for the fuel compact and block

Model		***A***	**Mesh**
Fuel Compact	CE 000	200	10 × 10 × 10
Fuel Block	CE 100	200	10 × 10 × 10

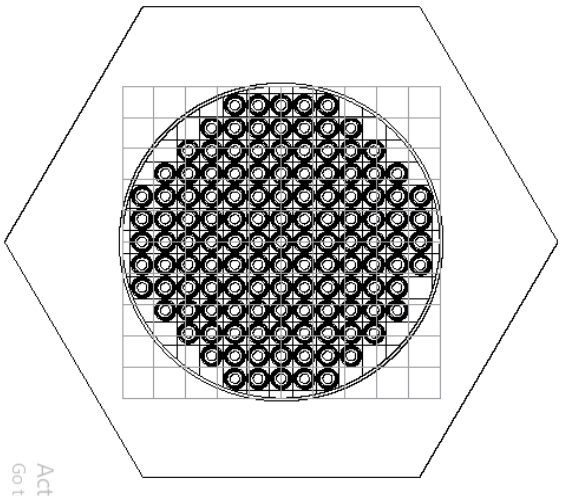

Figure 6-18 CE TSUNAMI-3D mesh for the fuel compact.

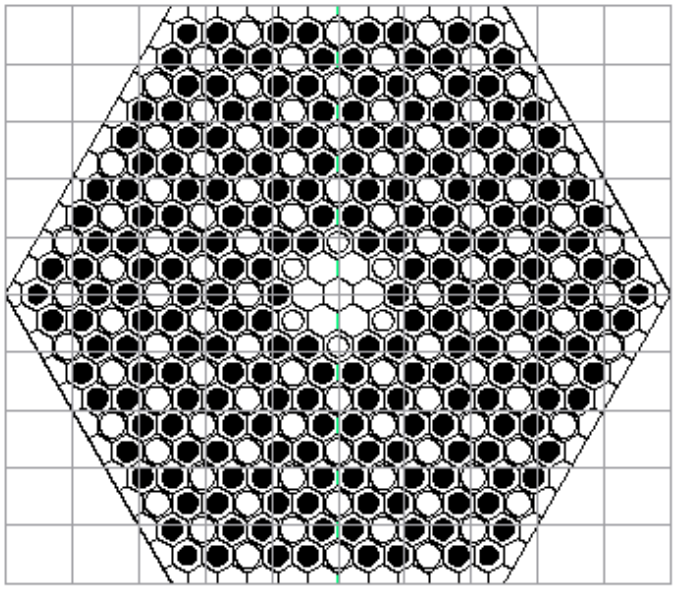

Figure 6-19 CE TSUNAMI-3D mesh for the fuel block.

6.4.3 Latent generation convergence

The effect of the latent generation on the $F^*(\vec{r})$ convergence is investigated on the MHTGR-350 fuel block. CFP is varied between 1 and 25, keeping in mind that the manual recommends $CFP = 10$ or 20 to be conservative. The following parameters are kept constant:

- mesh: $10 \times 10 \times 10$;
- $NSK = 26$ such that $A = 300$;
- $GEN = 476$ such that the active generations are equal to 450; and
- $NPG = 50000$.

In Section 6.4.2, A is recommended to be 200. In this section, a more conservative value of 300 is chosen for the parameter A. Figure 6-20 doesn't show any trend with respect to CFP except at $CFP = 25$. According to Equation 5.9, when $CFP = 25$ and $NSK = 26$, then the number of inactive generations (ING) available for $F^*(\vec{r})$ convergence is only 1. Recall that ING is an indirect parameter which is indirectly set by NSK and CFP. A CFP of 25 rendered the lowest value of $\%\Delta k/k$. The delta between the highest and lowest value of $\%\Delta k/k$ is 958 pcm. Therefore, it is not advisable to set a very high value for CFP such that the number of inactive generations (ING) available for $F^*(\vec{r})$ convergence is small (in this case the value is 1). The value of NSK should always be considered when setting CFP.

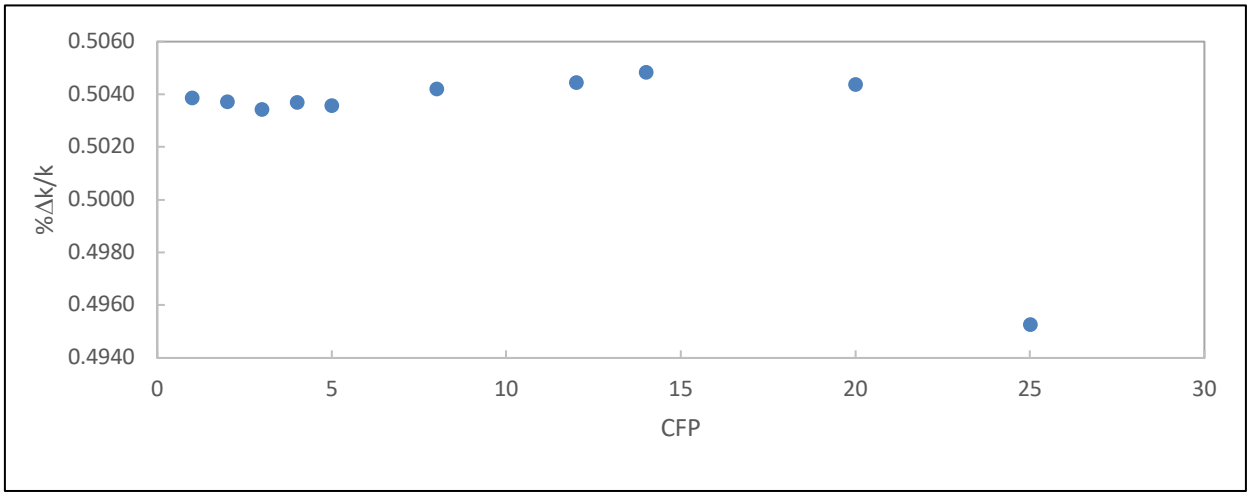

Figure 6-20 The effect of changing the latent generations on the uncertainty due to nuclear data.

The number of voxels that scored tallies in Figure 6-21 is constant for $CFP < 25$. In Figure 6-22 the percentage of voxels that scored more than 50% uncertainty remains zero up to $CFP = 14$, and then increases to 0.63% at $CFP = 20$. It is clear then that $CFP = 20$ is less desirable than $1 \leq$

$CFP \leq 15$. The Equation 5.9 in Section 5.6 shows that ING is equal to NSK minus CFP, therefore when CFP is 20, ING is 6 and when CFP is 25, then ING is 1. Hence in order to converge $F^*(\vec{r})$ adequately, CFP should be set such that inactive generations, $ING \geq 6$.

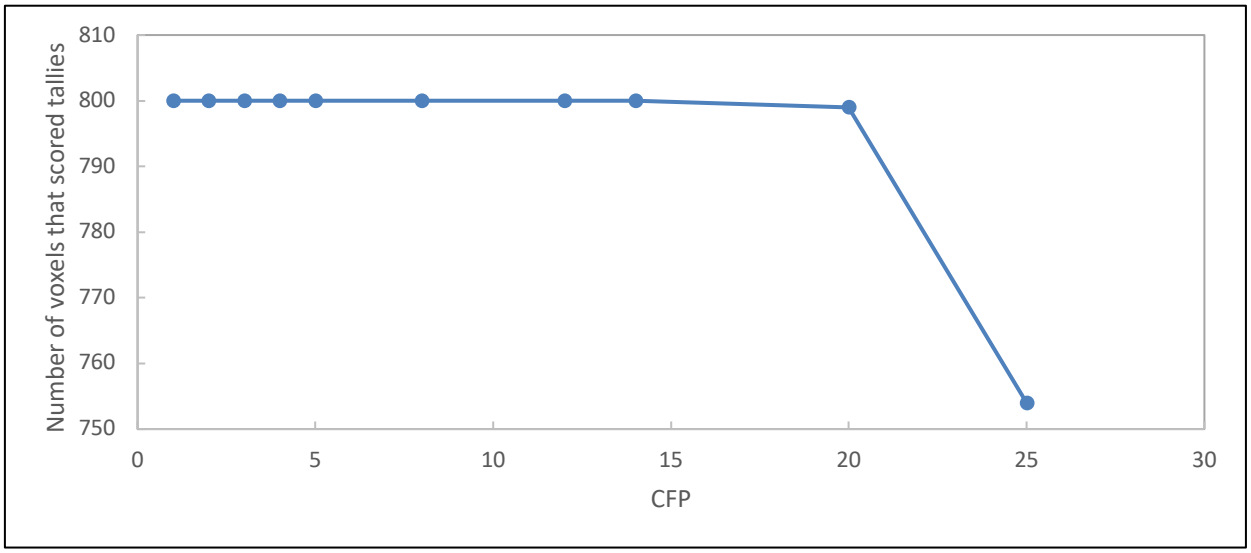

Figure 6-21 The effect of changing the latent generations on the number of voxels that scored tallies.

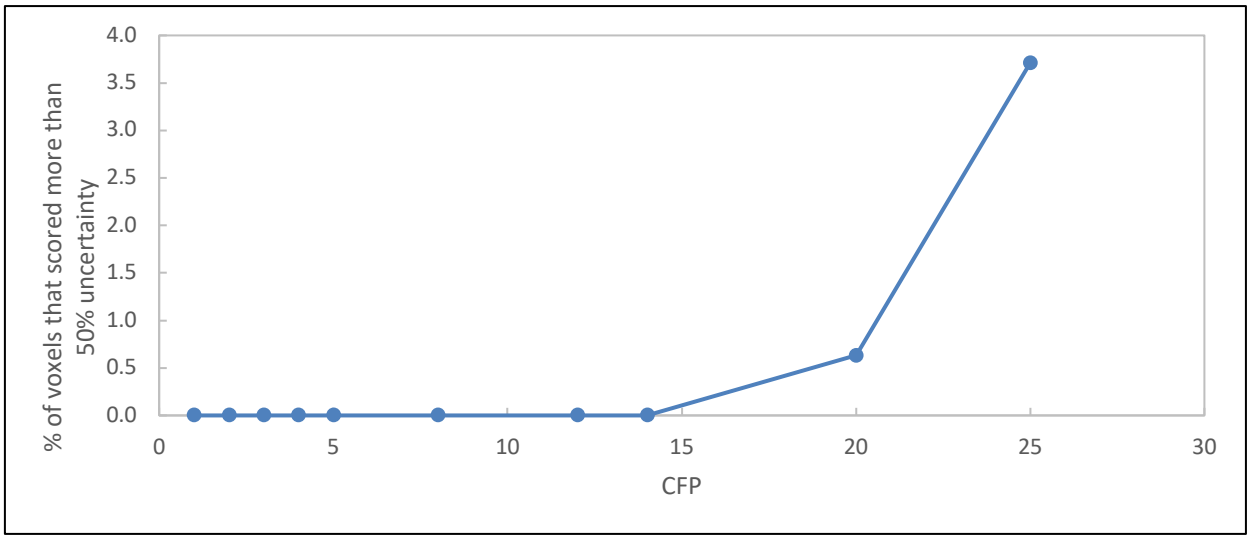

Figure 6-22 CFP vs % of voxels that scored more than 50% uncertainty.

Figure 6-23 shows the effect of varying CFP on the calculation time. The time is reported as a ratio in comparison to the calculation for $CFP = 1$. Using low values ($CFP \leq 5$) of latent generations requires double the calculation time than using more latent generations ($5 < CFP \leq 20$) but it does not have a significant effect on the value of $\%\Delta k/k$.

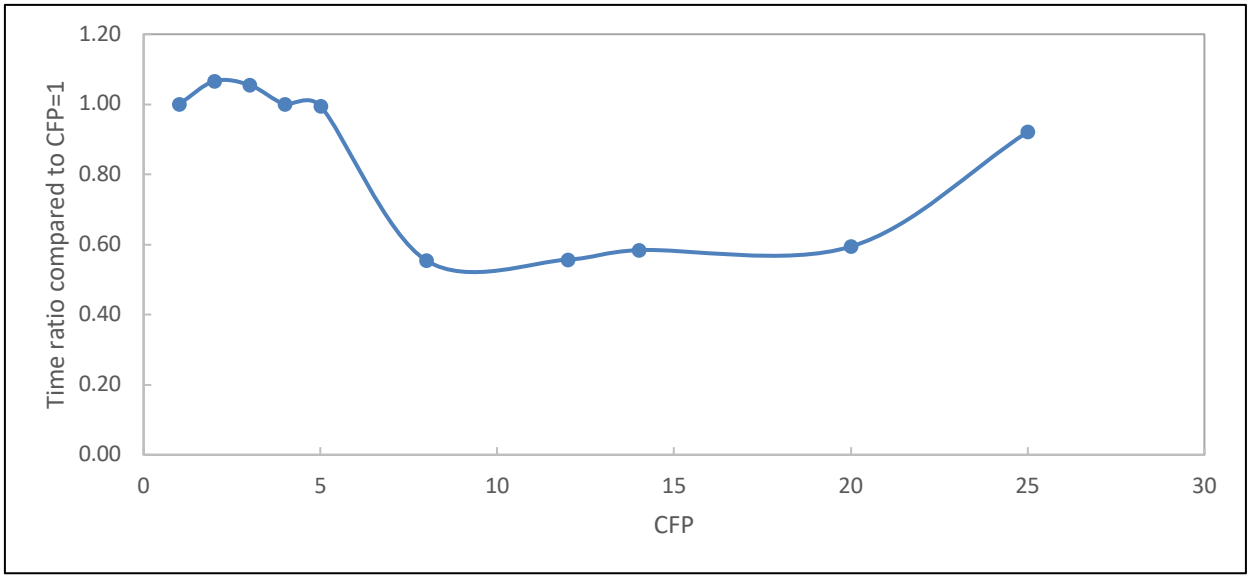

Figure 6-23 The effect of CFP on the calculation time.

6.5 Convergence of Sampler

Sampler/KENO and Sampler/NEWT are converged by varying the number of samples (N). The maximum number of samples is 1000 since the maximum number of data perturbations is 1000. The objective of this section is to find the number of samples at which Sampler/KENO and Sampler/ NEWT converge.

6.5.1 Sampler/KENO

SCALE 6.2.2 was used to run the Sampler/KENO calculations. However, when SCALE 6.2.1 was used, some samples gave a k_{inf} of zero or the samples did not run for the fuel block calculations. The reason for this is not known. It could be a possible issue with the SCALE 6.2.1 release. To remedy this, the output files can be deleted for the sample that did not run and Sampler can be executed again excluding the problematic samples so that all remaining samples do run. Sampler will only run the samples with no output files, i.e. it will not repeat the samples that have already been run and have outputs. This re-work will elongate the execution time of the Sampler calculation. An indication of the bias that would be introduced when using a smaller number of samples, after discarding the k_{inf} equal to zero samples is effectively running samples of smaller sizes. This study is shown in Section 6.5.2.

It was shown in Section 6.3 that the MG calculations producing the k_{inf} result using SCALE 6.2.1 and SCALE 6.2.2 are identical. Given the difficulty with the Sampler/KENO calculation using SCALE 6.2.1, it was therefore decided to only use SCALE 6.2.2 for Sampler/KENO calculations.

6.5.2 Comparison of Sampler/NEWT and Sampler/KENO

The Sampler NEWT calculations did not produce any samples with a k_{inf} of zero. The Sampler/ NEWT calculations took 3.16 times less time to complete one sample, when compared to Sampler/KENO-VI. Convergence is monitored in terms of k_{inf} and $\%\Delta k/k$ as a function of the number of samples and the comparison is shown in Figure 6-24 and Figure 6-25, respectively.

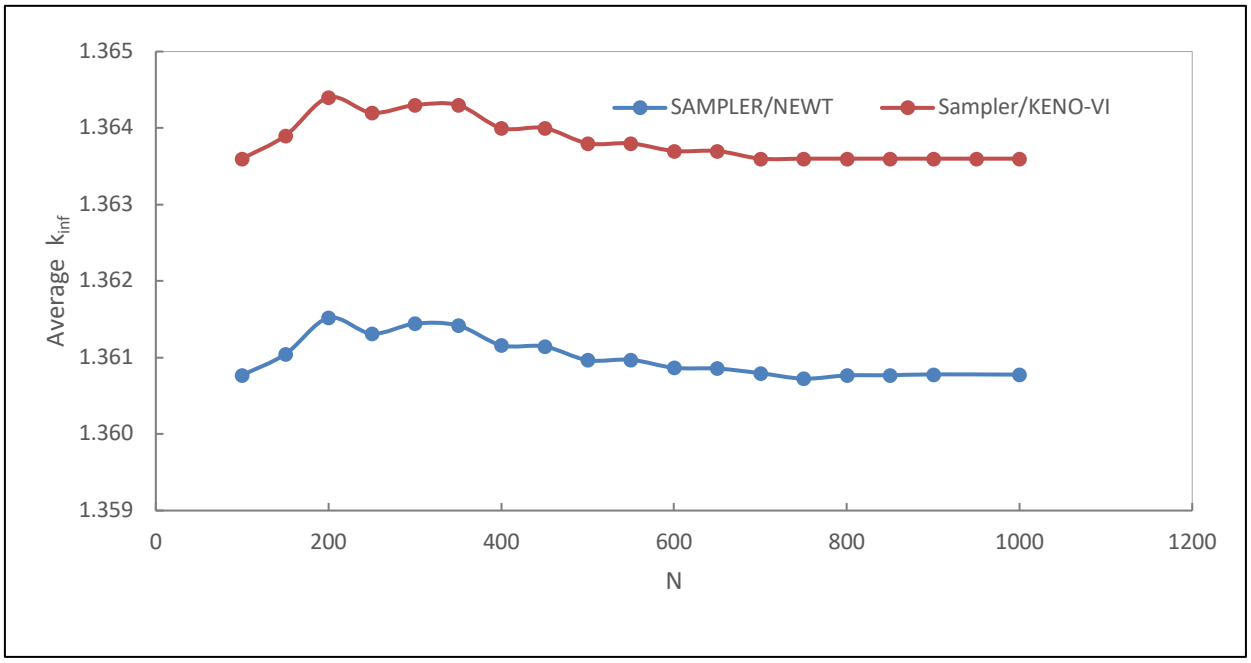

Figure 6-24 Convergence of Sampler with respect to the average k_{inf}.

Figure 6-24 shows that the samples converge at approximately $N = 800$ with a 10 pcm difference between $N = 600$ and $N = 800$. Figure 6-25 indicates convergence at $N = 600$. Therefore, we can say that $N = 600$ is sufficient for obtaining a converged value of $\%\Delta k/k$. For this particular case, sampling with less than 600 points will not yield converged values.

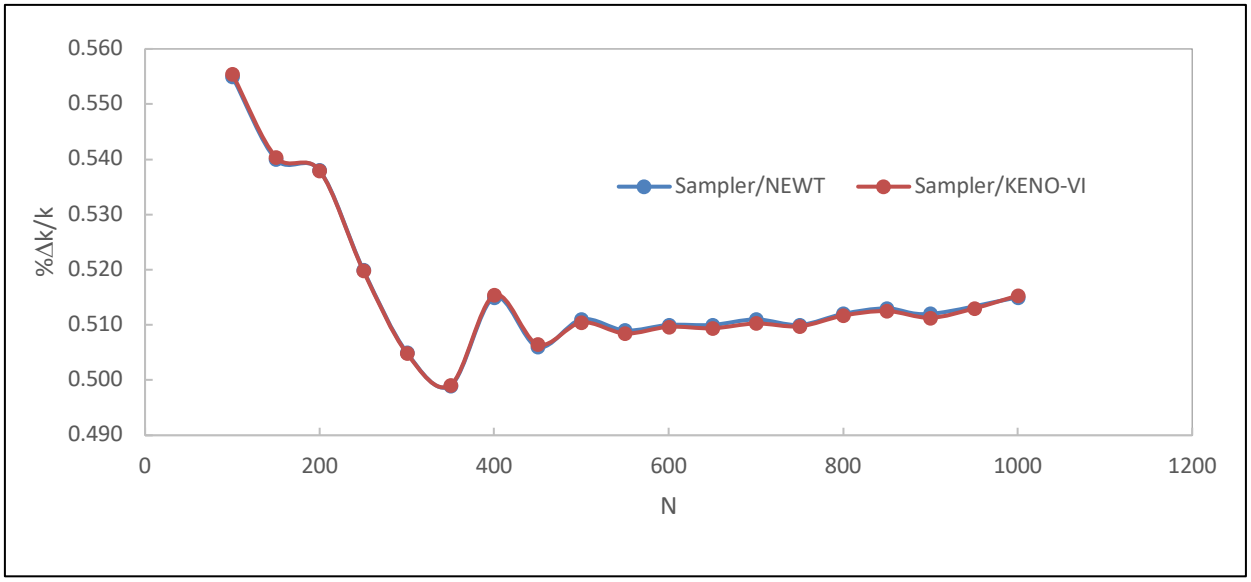

Figure 6-25 Convergence of Sampler/NEWT and Sampler/KENO-VI in terms of $\%\Delta k/k$.

6.6 Base case uncertainty results with CE TSUNAMI-3D and Sampler

6.6.1 Impact of DBRC on uncertainty quantification using CE TSUNAMI-3D

The effect of not applying the DBRC ($DBR = 0$) vs applying the DBRC to ^{238}U only ($DBR = 1$) is tested for the fuel compact and fuel block at HFP. Applying the DBRC to ^{238}U has shown a significant effect on k_{inf} in Section 6.1.2, therefore the resulting uncertainty should be quantified. The results are shown in Table 6-10.

Table 6-10 Effect DBRC at HFP on the uncertainty in using CE TSUNAMI-3D

Model	k_{inf}			$\%\Delta k/k$		
	$DBR = 0$	$DBR = 1$	k_{diff} (pcm)	$DBR = 0$	$DBR = 1$	$Diff$
KCE000	1.25669	1.25035	-634	0.54912	0.53570	-0.01342
KCE100	1.06416	1.06091	325	0.50216	0.50709	0.00493

Applying the DBRC to the ^{238}U cross sections in the fuel compact (KCE 000) at HFP decreases the uncertainty $\%\Delta k/k$ by 0.01342 whilst the same application to the single fuel block (KCE 100) increases the uncertainty $\%\Delta k/k$ by 0.00493. The effect of the DBRC is lower for the single fuel block in comparison to the fuel compact. To allow one to understand the effect of DBRC application on ^{238}U more clearly, Δk is calculated from Equation 5.11 and shown in Table 6-11. The difference in Δk is 20 pcm for KCE 000 (Exercise I-1b) and 3.6 pcm for KCE 100 (Exercise I-

2a). However, when one bears in the mind that the uncertainty due to the statistical nature of the Monte Carlo method is kept at around 15 pcm, then one should be careful when trying to interpret these differences in terms of physical reasons.

The conclusion is then that applying the DBRC at HFP has a large effect on the $k_{\inf}$ but not on the uncertainty due to nuclear data.

Table 6-11 Value of Δk for the option for $DBR = 0$ and $DBR = 1$

Model	$\Delta \boldsymbol{k}$ **(pcm)**		
	$DBR = 0$	$DBR = 1$	$Diff$ (pcm)
KCE 000	690	670	20.0
KCE 100	534	538	3.6

6.6.2 Uncertainty analysis for base case models

6.6.2.1 Relative standard deviation due to nuclear data

For the fuel compact at CZP, using CE TSUNAMI-3D, the Δk results (Table 6-11) and $\%\Delta k/k$ results (Table 6-10) are comparable for SCALE 6.2.1 and SCALE 6.2.2, with the differences being 8 pcm and 0.006 respectively. For the HFP case, the differences were 19 pcm and 0.013 respectively. For the fuel block in the HFP case, the differences were also small, being 4 pcm and 0.005 respectively. In these cases, DBRC was 1 for SCALE 6.2.1 and 0 for SCALE 6.2.2, for the reasons discussed in Section 6.1.2.

In addition to the CE TSUNAMI-3D calculations, Sampler calculations were also performed. It was established in Section 6.3 that the MG eigenvalue results for SCALE 6.2.1 and SCALE 6.2.2 are identical, hence calculations were carried out using SCALE 6.2.1 for Sampler/NEWT and SCALE 6.2.2 for Sampler/KENO-VI.

Only 600 samples were selected for the Sampler/MG KENO and the Sampler/NEWT calculation as established in Section 6.5. A second calculation with Sampler/NEWT using 1000 samples was also carried out since this is the maximum number of data perturbations. 1000 samples were not executed for Sampler/KENO-VI since it takes a very long time to execute. The results are shown in Table 6-12. Δk is again calculated from Equation 5.11. The restriction at this time is that the CE cross sections cannot be sampled and data perturbations are limited to MG calculations. Hence the Sampler/CE KENO calculation could not be done.

Δk computed from Sampler/NEWT and Sampler/MG KENO with 600 samples compared well with the differences being 1 pcm and 2 pcm for CZP and HFP respectively. The corresponding difference in $\%\Delta k/k$ was 0.001 for both cases.

When changing the sample size (N) from 600 to 1000 for the Sampler/NEWT calculation, $\%\Delta k/k$ increases by 0.005 for CZP and 0.004 for HFP. Comparing CE TSUNAMI-3D (SCALE 6.2.1) to Sampler/NEWT for 600 samples, these Δk differences were equivalent to 10 pcm and 3 pcm for CZP and HZP respectively. When comparing CE TSUNAMI-3D (SCALE 6.2.1) and Sampler/NEWT for 1000 samples, the Δk difference was 3 pcm for both HFP and CZP. Therefore, it can be said that there is a good agreement between the nuclear data uncertainty computed by Sampler/NEWT (or Sampler/KENO-VI) and the nuclear data uncertainty computed by CE TSUNAMI-3D. It could also be deduced that the neutron transport code parameters and the uncertainty code parameters used in these calculations are sufficiently set to produce well converged results.

Table 6-12 Uncertainty results due to nuclear data for the fuel compact

	$\boldsymbol{\Delta k}$	$\boldsymbol{\%\Delta k/k}$	$\boldsymbol{\Delta k}$	$\boldsymbol{\%\Delta k/k}$
	Fuel compact - CZP		Fuel compact - HFP	
CE TSUNAMI-3D - SCALE 6.2.1	0.00704	0.512	0.00671	0.536
CE TSUNAMI-3D - SCALE 6.2.2	0.00712	0.518	0.00690	0.549
Sampler/KENO-VI, $N = 600$	0.00695	0.509	0.00670	0.538
Sampler/NEWT, $N = 600$	0.00694	0.510	0.00668	0.539
Sampler/NEWT, $N = 1000$	0.00701	0.515	0.00674	0.543

The uncertainties are also compared for the fuel block in Table 6-13. The differences between CE TSUNAMI - SCALE 6.2.1 and CE TSUNAMI - SCALE 6.2.2 in the values of Δk and $\%\Delta k/k$ are 4 pcm and 0.005, respectively. For Sampler/NEWT ($N = 600$) and Sampler/NEWT ($N = 1000$), the difference in the values of Δk and $\%\Delta k/k$ are 3.6 pcm and 0.004.

The differences between CE TSUNAMI - SCALE 6.2.1 and Sampler/NEWT ($N = 600$) for Δk and $\%\Delta k/k$ are 19 pcm and 0.010, respectively. These differences are larger, possibly because the Sampler/NEWT and Sampler/KENO-VI fuel block model consists of homogenized LBP whilst the CE TSUNAMI models consist of lattice LBP. In Section 6.3, the LBP homogenization caused k_{inf} to decrease by more than 1500 pcm. Not only does homogenization of the LBP have an effect on the multiplication factor, it also has somewhat of an effect on the nuclear data uncertainty. Modelling of the LBP is further addressed in Section 7.5.

Table 6-13 Uncertainty results due to nuclear data for the fuel block

	Δk	$\%\Delta k/k$
	Fuel block - HFP	
CE TSUNAMI-3D - SCALE 6.2.1	0.00538	0.507
CE TSUNAMI-3D - SCALE 6.2.2	0.00534	0.502
Sampler/KENO-VI, $N = 600$	0.00519	0.496
Sampler/NEWT, $N = 600$	0.00519	0.497
Sampler/NEWT, $N = 1000$	0.00522	0.501

6.6.2.2 Top contributors to nuclear data uncertainty

Table 6-14 lists the order of the uncertainty contributors for the fuel compact and block. The order of the contributors is the same for the fuel compact and block. This order is not consistent with the homogeneous fuel compact case presented in other studies (Naicker et al, 2016; Bostelmann, Strydom et al, 2016). In these studies, ^{238}U(n, γ) / ^{238}U(n, γ) is the highest uncertainty contributor, followed by ^{235}U$(\bar{\nu})$ / ^{235}U$(\bar{\nu})$ where, $\bar{\nu}$ is the average number of neutrons per fission reaction. The fifth top contributor is ^{238}U elastic / ^{238}U elastic whilst the third and fourth ranked are consistent with Table 6-14. The percentage difference between the fuel compact and the fuel block is recorded in column 5. This percentage difference is calculated using Equation 5.14.

Table 6-14 Contributions to uncertainty in k_{eff} $(\%\Delta k/k)$ by individual energy covariance matrices for the HFP case

Rank	**nuclide-reaction pair**	$\%\Delta k/k$		$\%\ diff$
		Model KCE 000	**Model KCE 100**	
1	^{235}U$(\bar{\nu})$ / ^{235}U$(\bar{\nu})$	0.3511	0.3570	1.67
2	^{238}U (n,γ) / ^{238}U(n, γ)	0.2694	0.1983	30.39
3	^{235}U (n, γ) / ^{235}U (n, γ)	0.2278	0.1783	24.47
4	c-graphite elastic / c-graphite elastic	0.1458	0.1568	7.27
5	^{235}U fission / ^{235}U (n, γ)	0.1011	0.1191	16.35
6	^{235}U fission/ ^{235}U fission	0.06830	0.1111	47.71

The ^{238}U(n, γ) / ^{238}U(n, γ) and the ^{235}U(n, γ) / ^{235}U(n, γ) contributors for the fuel block (KCE 100) are lower than the fuel compact by a percentage difference of 30.39% and 24.47%, respectively. A possible explanation could be that the compact model has a neighbourhood of fuel compacts

only (by virtue of the reflective boundaries), whilst the fuel block consists of fuel compacts, c-graphite blocks, coolant channels and burnable poisons. The ratio between the uranium and the graphite becomes lower in the fuel block, hence the uncertainty contributions from the uranium nuclide-reaction pairs are lower for the fuel block case. The corresponding increase in c-graphite elastic / c-graphite elastic is a percentage difference of 7.27% for KCE 100 (single fuel block) compared to the KCE 000 (fuel compact) due to the increased c-graphite in the fuel block results.

The $^{235}U(\bar{\nu})$ / $^{235}U(\bar{\nu})$ contribution seems to be fairly unaffected by the change in system (from fuel compact to fuel block) with the percentage difference being 1.67%. The possible reason for the small change in ^{235}U $(\bar{\nu})$ / $^{235}U(\bar{\nu})$ is the role that $\bar{\nu}$ plays in the neutron transport equation. As can be seen from Equation 2.6, $\bar{\nu}$ is not dependant on the nuclide number densities as the macroscopic cross sections are. It also only appears with the term that contains the fissile cross section. This lack of dependence of $\bar{\nu}$ with the number densities could possibly be the reason why $^{235}U(\bar{\nu})$ / $^{235}U(\bar{\nu})$ does not show a large change.

The contribution for ^{235}U fission / ^{235}U (n, γ) is higher for the fuel block than the fuel compact. However, with the contribution for ^{235}U (n, γ) / ^{235}U (n, γ) showing a decrease with decreasing ^{235}U nuclei density in comparison to the c-graphite density, it is possible that the ^{235}U fission part of the contribution is what causes this increase. One also notes that the contribution for ^{235}U fission / ^{235}U fission also show this increase (appearing as rank 6 in the table). This could therefore show that the contributors associated with ^{235}U fission have a stronger influence on the propagated uncertainty than the interplay between the nuclei density of ^{235}U with that of c-graphite. However, one needs to also observe that the contribution for ^{235}U fission / ^{235}U (n, γ) is approximately 30% smaller than the top contributor, and the difference would be 5.08% and not 16.35%, if one uses the top contributor as the basis for comparison. In other words, in applying Equation 5.14, the average of the top contributor (rank 1) is used in the denominator of Equation 5.14 rather the average of the rank 5 contribution. This is further emphasized in terms of the ^{235}U fission / ^{235}U fission contributor. The percent difference would be 12.09% and not 47.71%, if the top contributor is used as a basis for comparison. Therefore, since these two contributors are the last two in terms of rank, the dominance of ^{235}U fission over that of the nuclei densities of ^{235}U and c-graphite in terms of uncertainty propagation cannot be established.

Sensitivity profiles represent the impact of perturbed cross sections and other nuclear parameters to the eigenvalue and eigenvalues are very sensitive to $\bar{\nu}$ hence it is always the first or second ranked contributor (Bostelmann and Strydom, 2017). The sensitivity profile of $^{235}U(\bar{\nu})$ is shown in Figure 6-26, the fuel compact and fuel block have an almost equal sensitivity per unit lethargy. The integral values shown in Figure 6-26 are approximately equal and the percentage difference

(calculated from Equation 5.14) between the integrals is 0.11%, hence the very small percentage difference shown in rank 1 of Table 6-14 (Bostelmann and Strydom, 2017).

The fuel block has more graphite (averaged per unit volume) over than the fuel compact as discussed earlier in this section, and therefore would cause more thermalization. This could cause the neutron spectrum to become softer. It was suggested above that the $^{235}U(\bar{\nu})$ / $^{235}U(\bar{\nu})$ contribution does not seem to be dependent on the nuclide number densities. One would therefore expect that the sensitivity due to $\bar{\nu}$ would then depend on the way the neutron flux behaves. This is because in a thermal reactor, increasing the thermal flux would increase the number of fission reactions and therefore increase the number of fission neutrons produced. Since $\bar{\nu}$ is the number of fission neutrons per fission reaction, increasing the overall number of fission neutrons produced in the system will therefore increase the $^{235}U(\bar{\nu})$ / $^{235}U(\bar{\nu})$ contribution to the uncertainty. A softer flux would therefore show a stronger sensitivity. One observes that this is the case as is shown in Figure 6-26. The sensitivity for the fuel block is larger than that for the fuel compact at the thermal energies (for energies less than around 1 eV) than that for the epi-thermal region. This could then also be used to explain the earlier result (in Table 6-14) where there is a slight increase in the $^{235}U(\bar{\nu})$ / $^{235}U(\bar{\nu})$ contribution to the uncertainty for the fuel block as compared with the fuel compact.

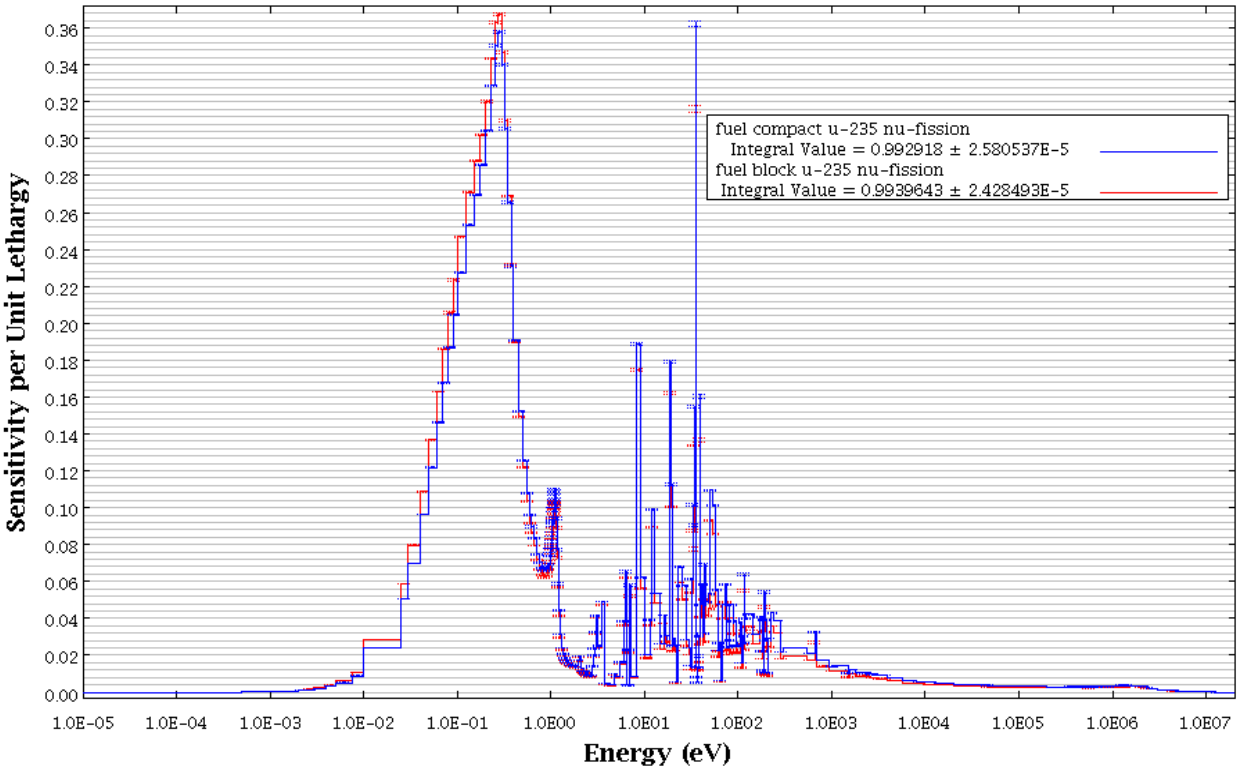

Figure 6-26 Sensitivity profiles comparison for $^{235}U(\bar{\nu})$.

The sensitivity profile for $^{238}U(n,\gamma)$ is shown in Figure 6-27. The fuel compact has a sensitivity integral of -0.228304 whilst the fuel block has a sensitivity of -0.171211. The fuel compact exhibits greater $^{238}U(n,\gamma)$ sensitivity (taking the absolute value) than the fuel block. The percentage difference (Equation 5.14) between these two integrals is 28.58%. Hence the percentage difference of 30.39% in rank 2 as shown in Table 6-14. It is also clear to see in Figure 6-27 that the sensitivities (taking the absolute values) in the resonance region (in this case it is visible between 1.5 eV and 1000 eV) for the fuel block is lower than that for the fuel compact. As was mentioned earlier, the ratio of the ^{238}U to that of c-graphite decreases from the fuel compact to that of the fuel block. There will therefore be relatively fewer $^{238}U(n,\gamma)$ reactions occurring in the resonance region. Therefore, the sensitivity profile for $^{238}U(n,\gamma)$ in the resonance region is lower for the fuel block in comparison with the fuel compact.

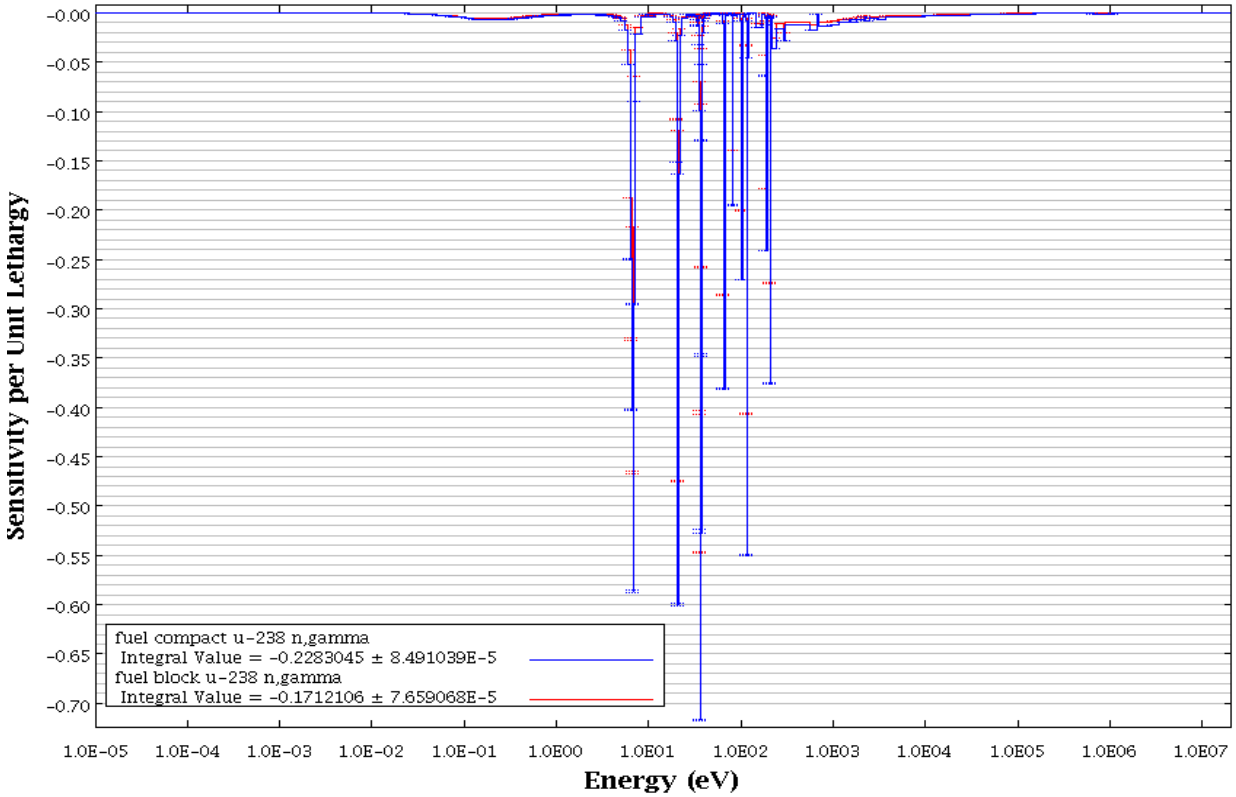

Figure 6-27 Sensitivity profiles comparison for $^{238}U(n,\gamma)$.

The sensitivity profile for $^{235}U(n,\gamma)$ is shown in Figure 6-28. The fuel compact $^{235}U(n,\gamma)$ sensitivity has an integral of 0.204128 and the fuel block has an integral 0.160434. The percentage difference between the integrals is 23.97%. Hence the percentage difference of 24.47% in rank 3 which was shown in Table 6-14. If one compares the sensitivity (taking its absolute value) as a function of energy, one notices that the sensitivities in terms of the fuel block is consistently lower than that for the fuel compact. The reason for this can be similar to that as that discussed above

for the sensitivity profile of ^{238}U(n, γ) in terms of the number density ratios of uranium with c-graphite.

The sensitivity profile of c-graphite elastic is shown in Figure 6-29, the integral value for the fuel compact is 0.223091 and the integral value for the fuel block is 0.302921. The percentage difference is 30.35%. The c-graphite elastic sensitivity of the fuel block is higher than that of the fuel compact hence the percentage difference in Table 6-14 for rank 4.

When one examines the sensitivity of c-graphite elastic as a function of energy, it is observed that the sensitivity for the fuel block is larger in the thermal region, and the sensitivity for the fuel compact is larger for the epithermal region. There are a few exceptions in the epithermal region of this. Since the c-graphite elastic / c-graphite elastic contribution increased when going from the fuel compact to the fuel block, this therefore suggests that the contribution to the uncertainty from c-graphite elastic is dominated by the contribution from the thermal region, at least for the fuel block.

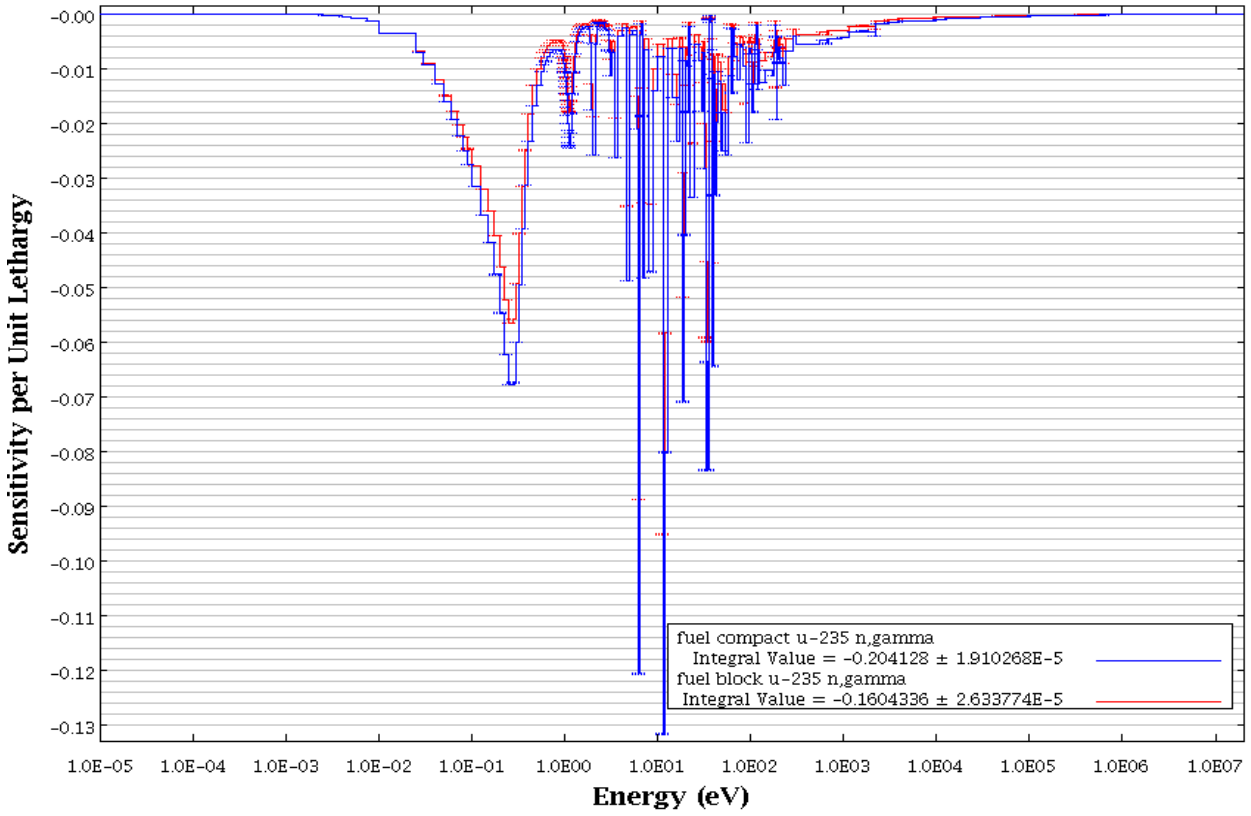

Figure 6-28 Sensitivity profile for ^{235}U(n, γ).

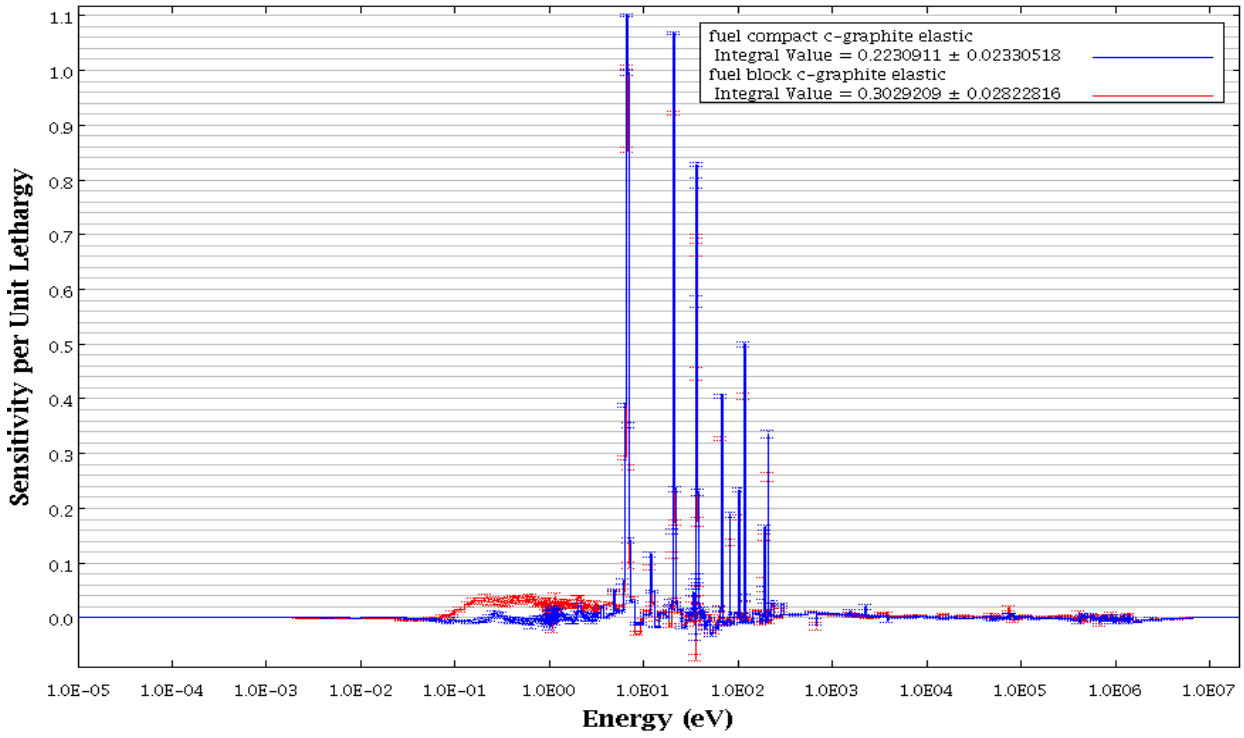

Figure 6-29 Sensitivity profile for c-graphite elastic.

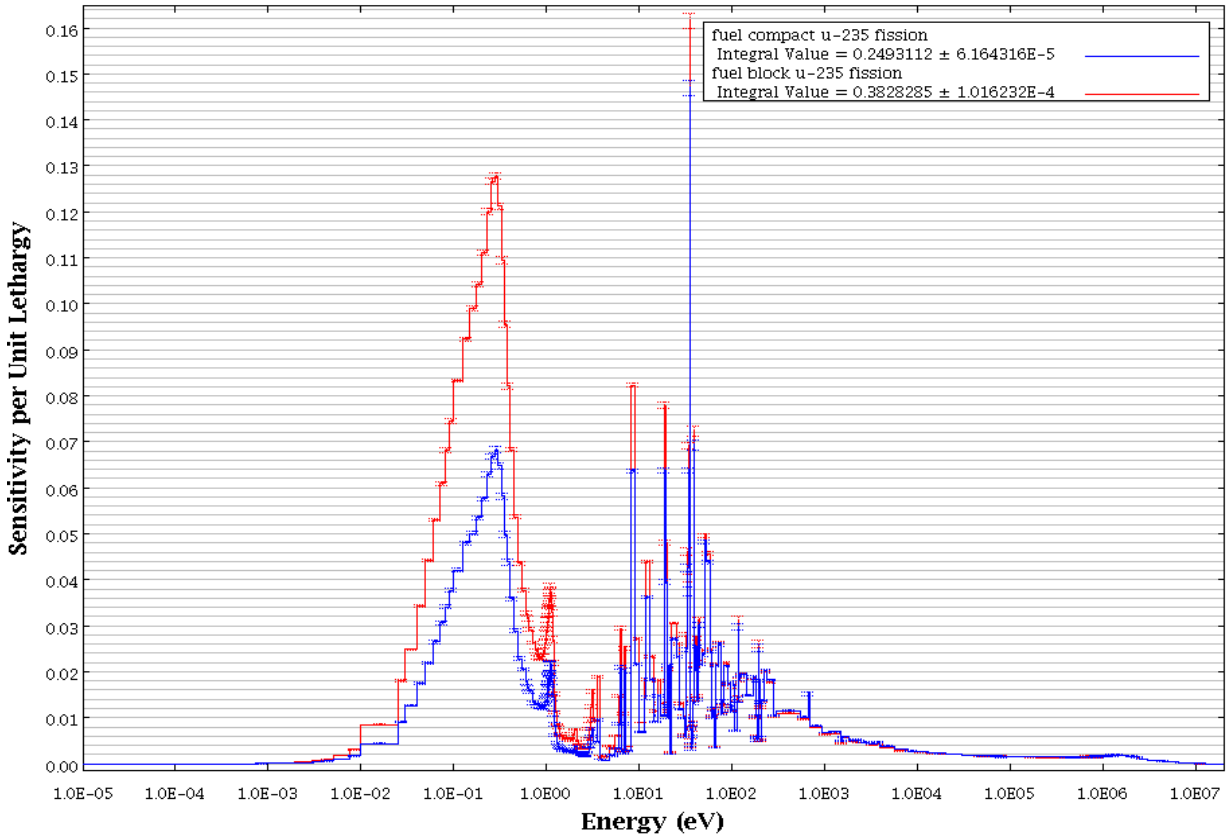

Figure 6-30 Sensitivity profile for ^{235}U fission.

Figure 6-30 shows the ^{235}U fission sensitivity profile for the fuel compact and fuel block. The integral value for the fuel compact is 0.249311 and the fuel block has an integral value of 0.382828. The percentage difference is 42.25%. The ^{235}U fission sensitivity of the fuel block is higher, hence the percentage difference in rank 5 and rank 6 in Table 6-14.

It is also noticed in Figure 6-30 that the sensitivity as a function of energy for the fuel block is larger than that for the fuel cell for the entire energy range. A possible reason for this was discussed earlier in this section in terms of the contributions from ^{235}U fission / ^{235}U (n, γ) and ^{235}U fission / ^{235}U fission. It is clear that when analysing all the sensitivity profiles as given above as a function of energy, the behaviour displayed in each profile must be evaluated in terms of the individual components. One should be careful in attempting to formulate a generalized trend.

6.6.2.3 Macroscopic cross sections for the fuel compact and block

The macroscopic cross sections of fuel compact (NMG 000) at CZP and HFP is shown in columns 3 and 4 of Table 6-15. The macroscopic cross sections of fuel block at HFP is shown in the fifth column.

Table 6-15 Homogenized nodal cross sections for the base case with Sampler/NEWT

Cross section*	Energy Group	NMG 000 - CZP	NMG 000 - HFP	NMG 100 - HFP
Σ_t	1	0.26586	0.26586	0.22078
	2	0.40019	0.40078	0.33419
	3	0.40936	0.41085	0.34168
	4	0.41466	0.41567	0.34682
Σ_{tr}	1	0.21116	0.21117	0.17515
	2	0.37712	0.37742	0.31485
	3	0.38348	0.38459	0.32092
	4	0.39973	039843	0.33273
Σ_a	1	0.00020	0.00020	0.00013
	2	0.00212	0.00235	0.00151
	3	0.00921	0.01091	0.00730
	4	0.01400	0.01174	0.00937
Σ_s	1	0.26566	0.26566	0.22065
	2	0.39807	0.39843	0.33268
	3	0.40015	0.39994	0.33438
	4	0.40066	0.40393	0.33745
Σ_f	1	0.00012	0.00012	0.00007
	2	0.00072	0.00072	0.00042
	3	0.00223	0.00226	0.00127
	4	0.01141	0.00954	0.00566

- The units for the homogenized cross-sections are cm^{-1}

In Table 6-15, the values of the macroscopic cross sections increase as the energy goes down to thermal energies. This is the expected behaviour of cross sections. The largest value excluding the total cross section is the transport cross sections. Since absorption is subsequently small, fission will also be small. The cross section of the fuel compact models (NMG 000) at CZP and HFP are approximately equivalent. All the macroscopic cross sections change significantly from fuel compact to the single fuel block. The cross sections of the fuel compact are larger than the fuel block (NMG 100) cross sections. The reason for this is explained in Section 7.5.3.

The uncertainties are propagated (for NMG 000 and NMG 100) and shown in Table 6-16. They are more significant (larger) in terms of the energy groups with higher energy. For example, the uncertainty propagated for the fission cross section of the energy group 1 for NMG 000 is 1.25193 and is larger than that of group 4, 0.35177. Although these uncertainties (in Table 6-16) are large, the actual cross section value in Table 6-15 is small. For example the absorption cross section for the fuel pin at CZP, in energy group one is 0.00020 but the $\%\Delta\Sigma/\Sigma$ is 3.345%.

Regarding the scattering cross sections, it should be noted that the analysis of the scattering cross sections is not complete, since the individual elements of the scattering matrix would also be required for nodal calculations. The scattering matrix gives the contribution of scatter from one group to another.

Excluding the scattering cross sections, the uncertainties due to the set of cross sections analysed above can be used to study the uncertainties in further analysis. One such analysis would be the impact of these uncertainties in core nodal studies, in which the multiplication factor and the core fluxes are calculated.

In terms of the calculation chain, these fluxes can be used to characterize the reactor power profile, which can then be used to calculate the temperature profile in the core using a suitable thermal hydraulic code. The contribution of the uncertainties due to the macroscopic cross sections discussed in this section can then be assessed by calculating the uncertainty in the core temperature profiles due to these uncertainties.

It is noted, however, that this would be the first in a series of analyses. More complicated analyses would require other considerations as well. For example, the uncertainties due to other group constants such as the diffusion constants, the calculation of the macroscopic cross sections for the graphite reflector blocks, and the isotopic change in the fuel assemblies due to depletion should be considered. Another important consideration would be the iterative coupling of the neutronic codes with the thermal hydraulic codes to obtain converged power and temperature profiles.

Table 6-16 Relative standard deviation ($\%\Delta\Sigma/\Sigma$) for the homogenized nodal cross sections for the base case models using Sampler/NEWT

$\%\Delta\Sigma/\Sigma$	Energy Group	NMG 000 - CZP	NMG 000 - HFP	NMG 100 - HFP
Σ_t	1	0.80862	0.80870	0.81541
	2	0.48995	0.48904	0.49402
	3	0.48850	0.48680	0.49185
	4	0.49023	0.49077	0.49311
Σ_{tr}	1	1.18060	1.17914	1.19028
	2	0.48992	0.49017	0.49402
	3	0.48999	0.48883	0.49352
	4	0.49689	0.49444	0.49602
Σ_a	1	3.34523	3.3437	3.93664
	2	0.81810	0.85106	0.79292
	3	0.33282	0.36697	0.30341
	4	0.26202	0.25555	0.19077
Σ_f	1	1.25193	1.25110	1.23148
	2	0.35032	0.35337	0.34765
	3	0.27886	0.28022	0.28200
	4	0.35177	0.33117	0.34077

6.7 Chapter summary

The findings in Chapter 6 for the MHTGR-350 base case models are:

- The CE KENO-VI and MG KENO-VI convergence parameters for the fuel block and fuel compact are $NSK = 50$, $NPG = 50000$ and $GEN = 500$.
- The NEWT convergence parameters are tabulated in Table 6-6 with $Sn = 8$ for the fuel compact and fuel bock model. The grid for the fuel compact is 40 × 40. The grid for the fuel block is 24 × 24 in the global unit and 4 × 4 for the local units.
- The $F^*(\vec{r})$ convergence parameters are $A = 200$ and the appropriate mesh is found to be 10 × 10 × 10.
- 600 samples are found to be sufficient for Sampler/NEWT and Sampler/KENO-VI convergence. Both Sampler/NEWT and Sampler/KENO produced similar results for the uncertainty due to nuclear data.
- The base case criticality models successfully compared to the results from IAEA CRP on HTGR UAM Phase I results.

- The uncertainty results are reported for the MG and CE cases using Sampler and NEWT, respectively. There is a good agreement between the MG and CE nuclear data uncertainty results.
- The top contributors to uncertainty are compared for the fuel compact and fuel block. These contributions will be compared to the HTTR fuel pin and fuel block in Chapter 8.
- The macroscopic cross sections along with their uncertainty due to nuclear data uncertainties are computed with Sampler/NEWT for the MG base case. These cross sections are investigated further in Chapter 7.

CHAPTER 7: FURTHER SENSITIVITY AND MODELLING METHODOLOGY STUDIES OF THE MHTGR-350

In this chapter the base case models are modified in terms of the modelling of coated particles. Existing coated particle modelling methodologies are further developed. The most efficient way of modelling BISO and TRISO particles is established and its impact on the nuclear data uncertainties and $k_{\inf}$ is investigated. The first part of this chapter addresses modelling in continuous energy (CE) and the sensitivity of $k_{\inf}$ to packing and randomization of the coated particles in the compact. The second part of this chapter addresses the moderator to fuel ratio. In order to compare MG and CE calculations, the moderator to fuel ratio must be conserved. HTGR CE calculations tend to not conserve the fuel to moderator ratio, since fuel may be lost due to the removal of clipped fuel particles. The last part of the chapter addresses the modelling of the LBP BISO particles. A method is developed to model the LBP coated particles using the doublehet function. The effect of these methods on the collapsed cross sections are investigated.

7.1 Effect of packing fraction

7.1.1 Packing of the MHTGR-350 fuel compact in CE

Model KCE 000 and KCE 001 that were in introduced in Chapter 5 (Section 5.1.1) are computed and their resulting multiplication factors are compared. Model KCE 000 is the base case model and model KCE 001 is the alternate packing which is more comparable to the IAEA benchmark definition of the MHTGR-350 compact. The two models have different local packing fractions (LV_f). The two models also have different global packing fractions (GV_f). The GV_f, essentially is determined by the number of particles. The definitions of LV_f and GV_f are shown in Equations 5.1 and 5.2. The LV_f, GV_f and the number of particles are shown in Table 7-1 for model KCE 000 and model KCE 001.

Table 7-1 Comparison of $k_{\inf}$ for the two different packing models

	LV_f	GV_f	number of particles
KCE 000	40.97%	34.91%	6400
KCE 001	38.51%	34.98%	6413

Table 7-2 $k_{\inf}$ for the fuel compacts at CZP and HFP

	KCE 000	KCE 001	k_{diff} (pcm)
HFP	1.25035	1.24765	270
CZP	1.37450	1.37152	298

The difference (k_{diff}) in the multiplication factors for model KCE 000 and model KCE 001 is shown in Table 7-2. The $k_{\inf}$ difference (k_{diff}) between KCE 000 and KCE 001 is 298 pcm at CZP. At HFP, the value of k_{diff} is 270 pcm. Therefore, there is a difference of 200-300 pcm caused by the variation in packing of CPs. Four cases are developed to determine whether the local packing fraction or the global packing fraction (number of CPs) has a larger effect on the $k_{\inf}$. These cases can be separated according to two parameters, viz. the number of coated particles per compact and the local packing fraction LV_f. Case A is model KCE 001 and case B is model KCE 100. The four cases are tabulated in Table 7-3. Cases A and D have 6400 CPs and cases B and C have 6413 CPs. Cases A and C have $LV_f = 40.97\%$ and cases B and D have $LV_f = 38.51\%$. In other words, in terms of LV_f, the lattice constants for A and C are equal and also for B and D. Case D is built by removing 13 CPs from the lattice structure of case B (indicated by the orange arrow in Figure 7-1) . Case C is built by adding 13 CPs to the lattice structure of case A (indicated by the blue arrow in Figure 7-1).

Table 7-3 Summary of cases for the packing fraction investigation

Case	Configuration of fuel compact case	LV_f	No of CPs
A	Model KCE 000	40.97%	6400
B	Model KCE 001	38.51%	6413
C	13 particles are uniformly added to case A	40.97%	6413
D	13 particles are uniformly removed from case B	38.51%	6400

In terms of the number of coated particles, Figure 7-1 shows that going from case A to case C (the blue arrow indicates an increase in CPs) results in a $k_{\inf}$ difference (k_{diff}) of 68 pcm and for case B and case D (the orange arrow indicates a decrease in CPs) the difference is 79 pcm (also shown by an arrow). However, when changing the local packing fraction (lattice constants), cases D and A show a difference of 281 pcm and cases B and C show a difference of 292 pcm. These differences are illustrated in Figure 7-1 at HFP. These results suggest that the lattice structure (as given by the local packing fraction) shows a greater sensitivity for $k_{\inf}$ than does the change

in the number of CPs (as given by the global packing fraction), albeit the change in the CPs was small (13 CPs).

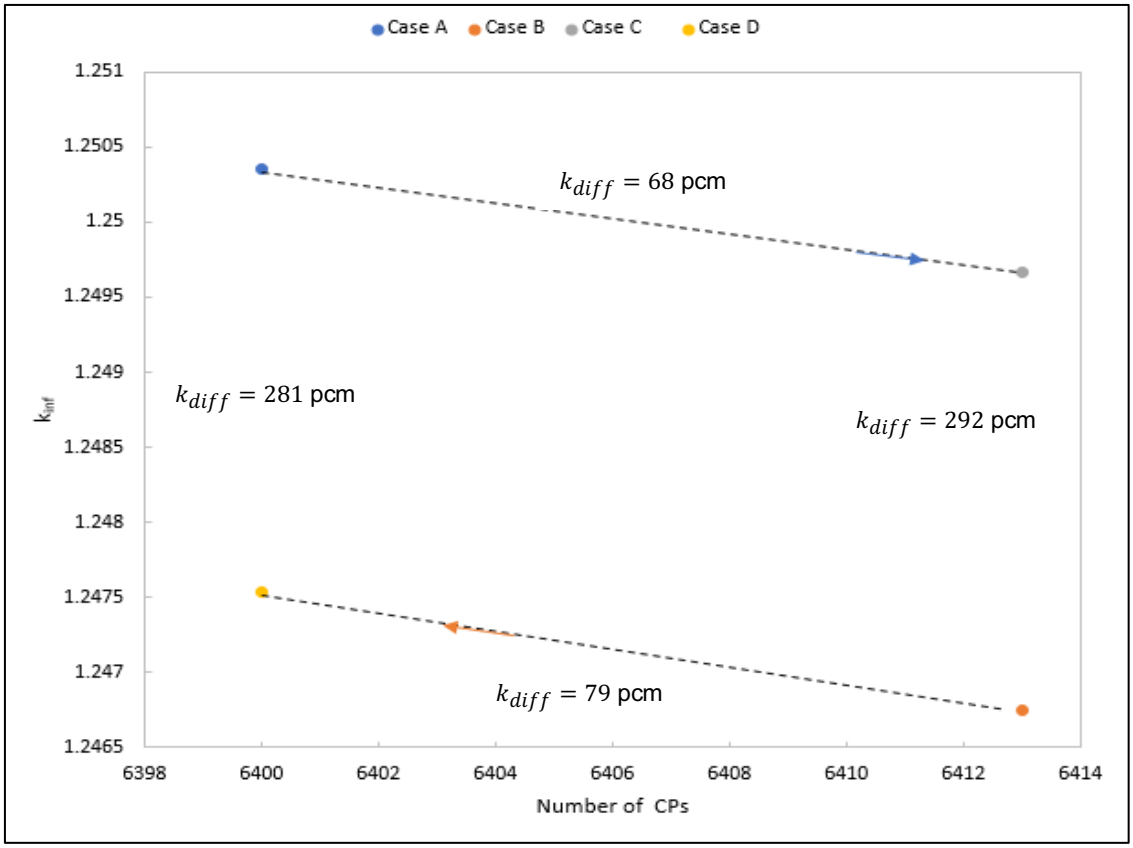

Figure 7-1 The effect of varying the number of CPs on the k_{inf} at HFP.

Figure 7-2 shows that the $\%\Delta k/k$ due to nuclear data ranges from 0.535% to 0.544% for the MHTGR-350 fuel compact using ENDF/B-VII.1. The $\%\Delta k/k$ difference between any two cases is represented by the parameter $Diff$, where $Diff$ is the difference between any given value of X_1 and any given value of X_2. The absolute value of $Diff$ is shown in Figure 7-2. When converted to Δk using Equation 5.11 these differences are small compared to the differences shown in Figure 7-1. It can therefore be concluded that although the effect of the lattice structure influences the value of k_{inf}, it does not influence the uncertainty in k_{inf}.

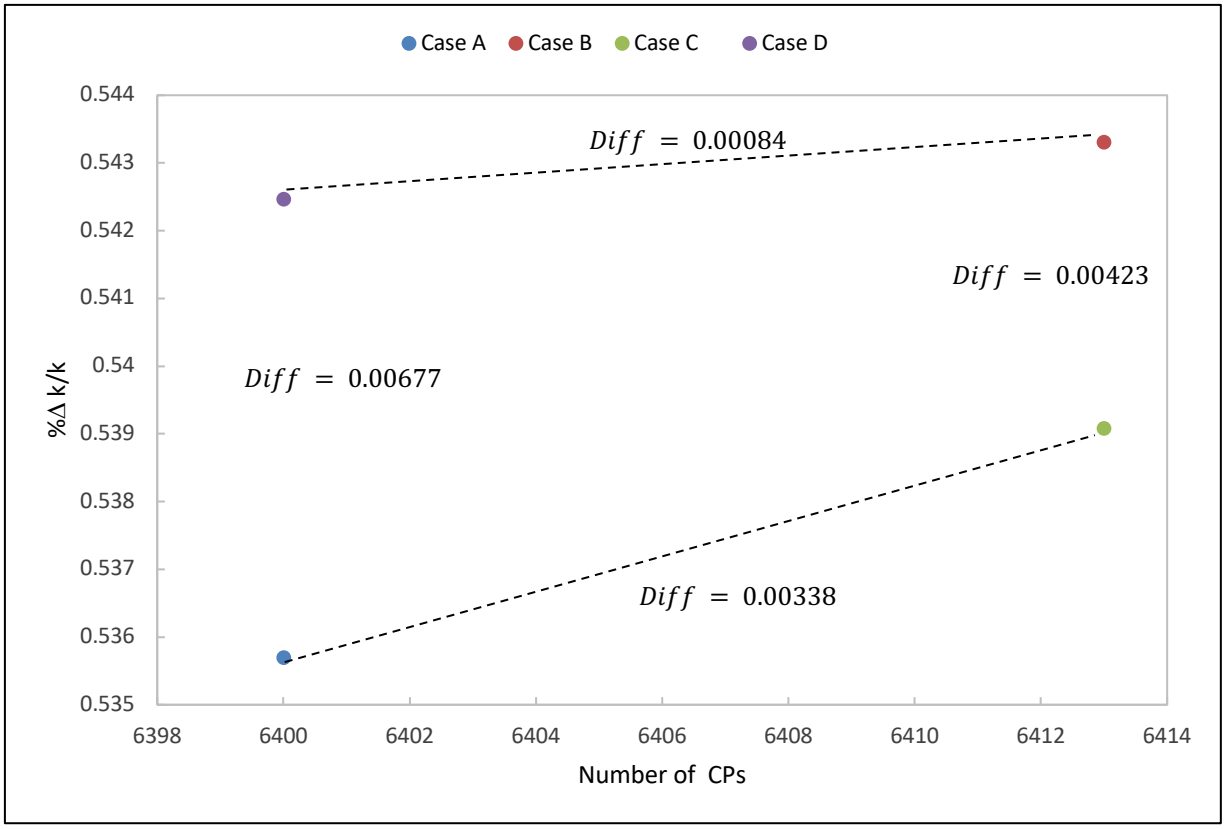

Figure 7-2 The effect of varying the number of CPs on $\%\Delta k/k$ at HFP.

For the CZP case, in Figure 7-3, the $k_{\inf}$ difference between case A and case C is 63 pcm (as shown by the blue arrow) and for case B and case D, the difference is 93 pcm (as shown by the orange arrow). This reflects the difference caused by the number of particles. For case A and case D in the CZP case, the difference is 205 pcm. The difference between case B and case C is 235 pcm. This reflects the difference caused by the local packing fraction. Similarly, for the HFP case, the $\%\Delta k/k$ differences, shown in Figure 7-4, are small with the largest difference being 0.00718.

It is noted that in decreasing the number of CPs (from Figure 7-1 and Figure 7-3), and keeping the packing fraction constant, the moderating ratio increases, where the moderating ratio is defined as the ratio of moderator number density to heavy metal number density. Since $k_{\inf}$ increases, this is an indication that the system is under-moderated. This is investigated further in Section 7.1.2.

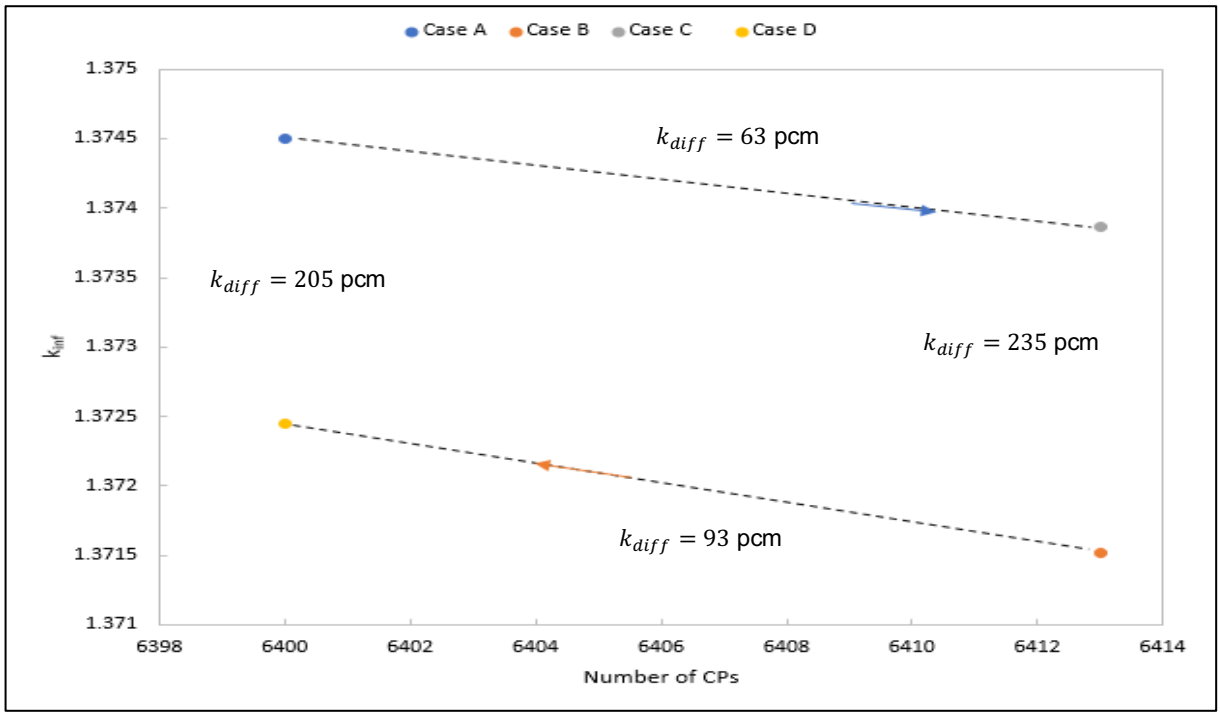

Figure 7-3 The effect of varying the number of CPs on the k_{inf} at CZP.

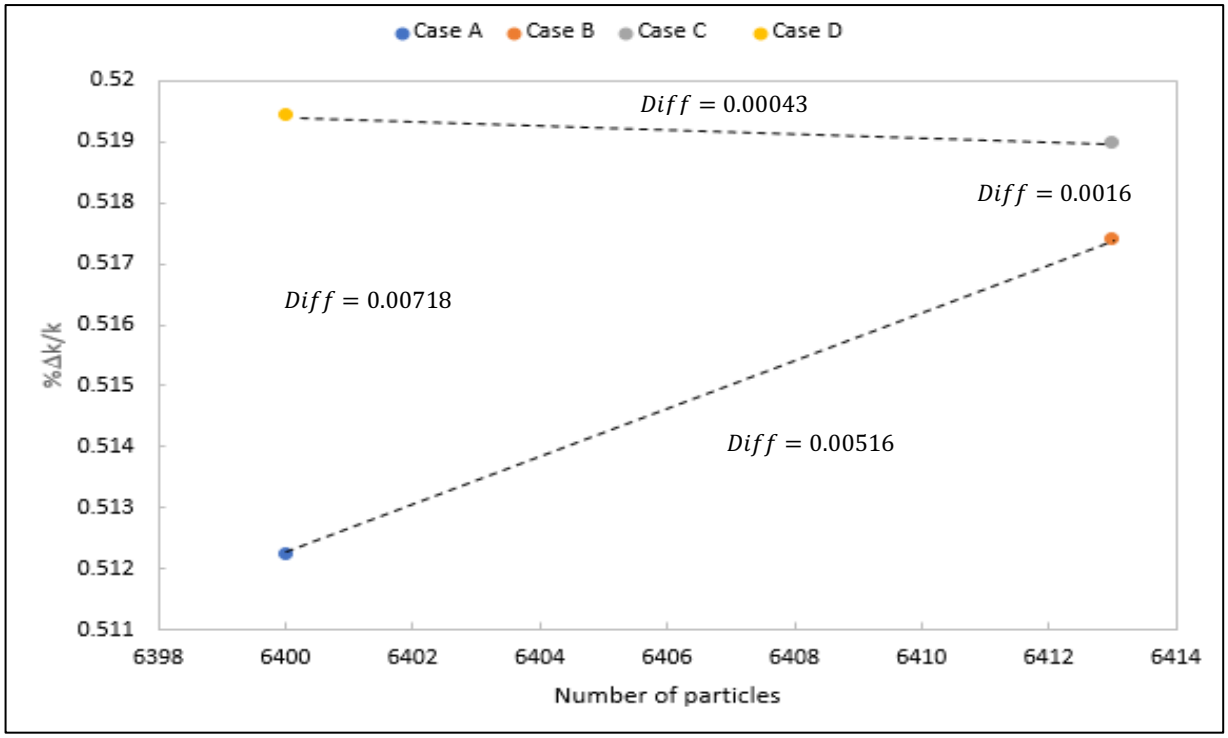

Figure 7-4 The effect of varying the number of CPs on $\%\Delta k/k$ at CZP.

7.1.2 Moderator to fuel ratio.

Varying the packing fraction can have an effect on the total number of particles and hence the moderator-to-fuel ratio ($V_m N_m / V_f N_f$) (Lewis, 2008), as seen in the previous section.

Figure 7-5 shows the moderator to fuel ratio ($V_m N_m / V_f N_f$) for the fuel compact of the MHTGR-350 fuel compact. The number of CPs is altered (increased and decreased) from the fuel compact fixed lattice model, $V_m N_m / V_f N_f$ is calculated and k_{inf} is recorded. Comparing Figure 7-5 and Figure 7-6, it can be seen that the MHTGR-350 fuel compact is in the under-moderated region. This is in confirmation with (Doc. No. 12-9051191-001, 2007) which states that HTGR fuel blocks are usually under moderated. The implication of this is that when additional moderation is introduced, for example by moisture ingress, the reactivity can be increased and thus can cause rapid power increases (Ball et al, 2012). This warrants further study on the full core model to test the effect.

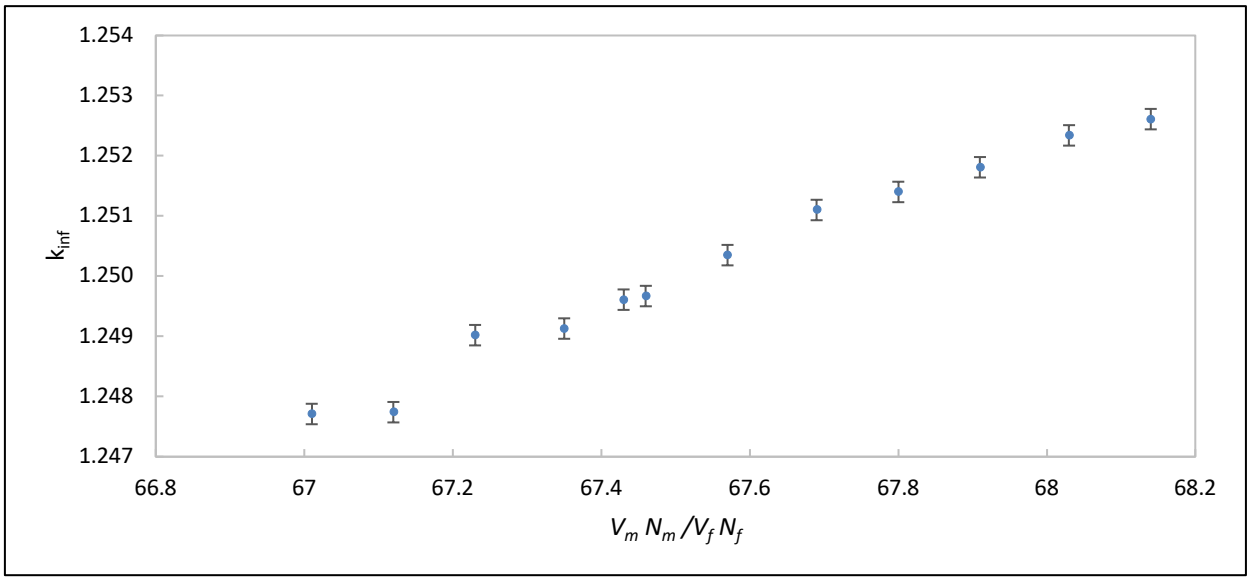

Figure 7-5 Moderator to fuel ratio vs $k_{\inf}$ for the MHTGR-350 fixed lattice fuel compact.

At 6416 particles the moderator to fuel ratio is 67.30. At 6400 particles the moderator to fuel ratio is 67.57 and at 6413 particles the moderator to fuel ratio is 67.43.

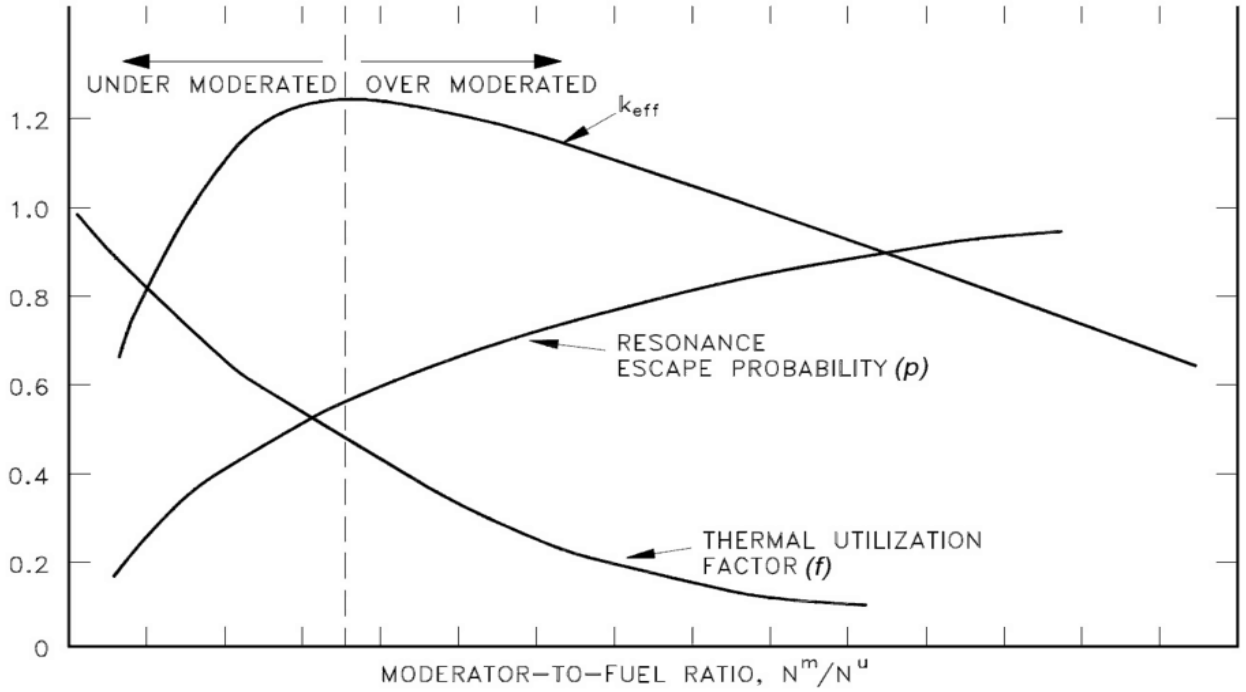

Figure 7-6 Moderator to fuel ratio vs k_{eff} (DOE-HDBK-1019/2-93, 1993).

7.2 Jiggling of coated particles

As discussed in Section 5.1.2, R_p is chosen to be 100, 600, 1600, 3200 and 6400 for KCE 000 and R_p is chosen to be 100, 600, 1600, 3200 and 6413 for KCE 001. As shown in Table 7-4, a total of 10 inputs are constructed for each position R_p and each input has different random locations. The average $k_{\inf}$ is calculated along with the standard deviation.

As can be seen from this table, varying R_p does not affect the value of k_{inf} significantly. This is because the packing fraction is high (35%), which implies that the cuboidal elements enclosing the coated particle are quite small. The coated particle does not have enough room to be jiggled due to the very small distances between different CPs. The nuclear data uncertainty is quantified in Table 7-5. There was a time penalty incurred by increasing R_p. However, this penalty could not be quantified since computers with different specifications were used. This penalty was assessed by user experience.

It can be seen from Table 7-4 that the difference in the multiplication factor between the ordered model and the jiggled model is within 1-2 standard deviations so therefore this difference is not significant statistically and jiggling has no effect on the multiplication factor. In Brown et al (2005) the effect of jiggling on full-core HTGR calculations was about 0.06% (or 60 pcm) compared to fixed lattice models using MCNP, for a standard deviation of 40 pcm. Therefore, jiggling has a very insignificant effect on the multiplication factor, especially if the packing fraction is high. The

larger the packing fraction the less space there is for the CP to be jiggled within the cuboidal element.

Table 7-4 The effect of jiggling for 6400 particles at HFP

KCE 000					
R_p	100	600	1600	3200	6400
Average k_{inf}	1.25004	1.25003	1.25004	1.25000	1.25005
Std dev	0.00014	0.00021	0.00016	0.00015	0.00016
KCE 001					
R_p	100	600	1600	3200	6413
Average k_{inf}	1.24664	1.24671	1.24748	1.24680	1.24672
Std dev	0.00018	0.00012	0.00021	0.00019	0.00013

Table 7-5 shows the uncertainty due to nuclear data for the jiggled models of KCE 000 and KCE 001. In Table 7-5, SAMS failed to execute for CE 000 with $R_p = 1600$ and SAMS also failed to execute for model KCE 001 with R_p set to 100, 600 and 6413. To remedy this, the number of skipped generations was increased from 200 to 210. The $\%\Delta k/k$ due to nuclear data for the fuel compact is 0.530 - 0.545 for the fuel compact regardless of whether the CPs are in a fixed lattice or jiggled.

Table 7-5 The effect on $\%\frac{\Delta \mathbf{k}}{\mathbf{k}}$ in terms of nuclear data uncertainies due to the jiggling of CPs using CE TSUNAMI-3D

KCE 000					
R_p	100	600	1600	3200	6400
$\%\Delta\mathbf{k}/\mathbf{k}$	0.53864	0.53844	0.53941	0.54592	0.53653
KCE 001					
R_p	100	600	1600	3200	6413
$\%\Delta\mathbf{k}/\mathbf{k}$	0.54036	0.54592	0.53391	0.53196	0.54274

7.3 Randomization

There is a several hundred pcm difference between the fixed lattice model and the random model. These differences are shown in Table 7-6. The literature discussed below suggests that random particle modelling is significant at a fuel compact level but becomes fairly insignificant as the system gets bigger. Furthermore, with 201 particles the random fuel compact calculation requires nine times more computational time.

Table 7-6 $k_{\inf}$ for the fuel compacts for the random CP configuration.

Model	$\boldsymbol{k_{\inf}}$	$\boldsymbol{k_{diff}}$ **(pcm)**
Ordered model (6400 CPs)	1.25035	reference
Random model ($R_p = 200$)	1.24597	438
Random model ($R_p = 401$)	1.24419	616

The large differences between the random and ordered model are as a result of the resonance escape probability, which was found to be 0.7% less for the random model when compared to the fixed lattice model (Ho, et al, 2017). It is easier for a neutron to escape the fuel region (and progress to the outer reflector) in an ordered model, whilst it is more difficult for a neutron to exit from random fuel particles (Ho, et al, 2017). Therefore, the random model captures more neutrons hence the resonance escape probability is lower.

Strydom et al (2015) computed the MHTGR-350 fuel compact and fuel block models with an ordered lattice of CPs and randomized CPs. The computations were executed using Serpent since this code has a built-in random particle capability. The discrepancies in $k_{\inf}$ for the fuel compact, single fuel block and mini-core were found to be 610 pcm, 441 pcm and 206 pcm respectively. From the MHTGR-350 results computed by Strydom et al (2015), it seems as if the discrepancies between the random and fixed/ordered model decrease as the system becomes larger. The small system (fuel compact) consists only of the CPs in graphite whilst the larger models have other effects coming from LBPs, reflectors and the helium gap and possibly the stochastic distribution of the coated particles becomes less important for the full core system. In Ardakani et al (2014), the k_{diff} between the random and fixed lattice model is 132 pcm for the fully loaded HTTR full core model.

In the publication by Ho et al (2017), the k_{diff} for the HTTR fuel compact between the fixed models and the jiggled models is 46 pcm whilst a difference of 857 pcm was reported for the fixed/ordered models versus the random model. Ardakani et al (2014) reports that the HTTR full core MCNPX results showed a difference of 100 - 200 pcm between the regular and stochastic arrangements. In the publication by Ardakani et al (2014) and a publication by Ho et al (2017), 333 random positions (R_p) are modelled in a fuel compact arbitrarily chosen whilst the HTTR has 13000 coated particles in a fuel compact. The publication by Ho et al (2018) shows that the random models render critical control rod positions results that are closer to the experimental results for the HTTR whole core model when compared to the jiggled models and the ordered models.

7.4 Comparison of uncertainties due to random, fixed and jiggled packing

It can be seen in Table 7-7 that the difference in the uncertainty propagated is small (0.00294 $\%\Delta k/k$) for the jiggled model in comparison with the ordered model. Converting this to Δk, the value is 7 pcm, which is close to that of the statistical uncertainty due to a single KENO calculation (15 pcm). CE TSUNAMI failed to compute when the completely random models were run and therefore this comparison is not available.

Table 7-7 Fuel compact $k_{\inf}$ and $\%\Delta k/k$ due to nuclear data for different CP configurations

Model	$\boldsymbol{\Delta k}$	$\boldsymbol{\%\Delta k/k}$
Ordered model	1.25035	0.53570
Jiggled model ($N = 100$)	1.25018	0.53864
Random model	1.24597	SAMS failed to execute

7.5 Modelling of the lumped burnable poisons.

Using the doublehet function to model LBP coated particles becomes particularly important for the NEWT models. The CE KENO-VI module of the SCALE code can be used to perform the CE $k_{\inf}$ calculation of the MHTGR-350. However, the deterministic codes such as NESTLE (NESTLE, V5.2.1, 2003) could be an alternative to KENO-VI for the eigenvalue calculations due to shorter runtimes. For example, a core calculation which takes NESTLE ~5 minutes to finish will cost KENO-VI 12 hours. This reduced time expenditure is imperative for uncertainty studies using the stochastic sampling method since hundreds of calculations are required. It should be noted that the NEWT lattice model is still necessary because the NESTLE core simulation requires the group constants generated by the transport calculation. These can be supplied by NEWT, which is a 2D discreet ordinates method. For a 2D system the general choice is the radial XY plane, therefore each single fuel block could have its own NEWT model. NEWT requires 252 energy groups collapsed cross section data sets for SCALE 6.2, ENDF/B-VII.1 library. This cross section set is obtained using the self-shielding codes BONAMI and CENTRM/PMC in the XSProc module. Therefore, the modelling of the BISO particle in this part of the calculation chain is important.

7.5.1 The LBP Trace method development

One method to model coated particles in NEWT (MG) is by homogenization but this has shown to decrease the value of $k_{\inf}$ significantly. Self-shielding of the LBP was not reported to have been carried out (Strydom et al, 2015). To consider self-shielding, coated particles can be modelled with the doublehet function in SCALE but this function requires that the coated particle consist of

fuel. Since LBPs do not contain fuel, a trace of fuel is added to the kernel of the BISO LBP particle. ^{238}U is chosen as the trace fuel material since fission in the LBP is unwanted. To determine this "trace" amount, ^{238}U is added to the kernel of the LBP BISO particles and $k_{\inf}$ is calculated for the MHTGR-350 fuel block. This amount of ^{238}U is decreased in increments until the added ^{238}U no longer effects the $k_{\inf}$, as shown in Figure 7-7. A constant value is reached at 10^{-4} atoms/b-cm and ends at 10^{-12} at/b-cm, which is considered the trace amount. Beyond 10^{-12} atoms/b-cm, the NEWT code stops working. The addition of a trace of fuel to the LBP kernel of the MG MHTGR-350 model is the definition of the LBP Trace model and the method is referred to as the LBP Trace method. The results obtained from the LBP Trace model must be compared to the CE KENO-VI results since the latter is the closest to reality (and is considered the reference model). Therefore, the LBP Trace method must also be used in MG KENO-VI, and the behaviour of the trace is shown in Figure 7-7. It can be seen that the MG KENO-VI fuel block model responds to the addition of the trace ^{238}U identically to the NEWT fuel block model.

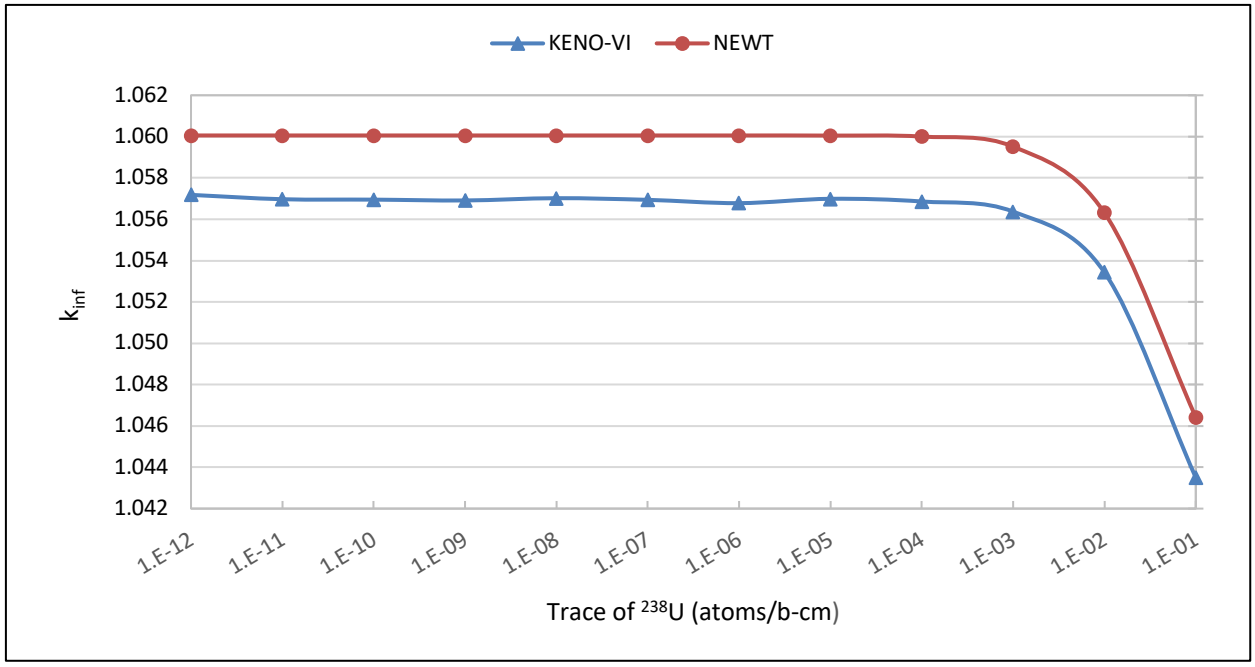

Figure 7-7 Response of $k_{\inf}$ to the variation of the LBP Trace amount of ^{238}U in the LBP at CZP.

Three MG models are defined. The first is the LBP Trace model which was developed. The second model has homogenized LBP and in the last model the LBP is also homogenized and boron in the LBP is reduced by a factor of 0.88 (12%). These models are labelled as cases A, B and C respectively. In case C the concentration of the boron in the LBP kernel is decreased so that $k_{\inf}$ is roughly equal to the CE fuel block calculation. Case A, case B and case C are summarized in Table 7-8. The number densities for the homogenized burnable poisons for Case

B and case C are shown in Table 7-9. The CE model with a fixed fuel compact lattice serves as the reference.

Table 7-8 Summary of models with different LBP definition

Case	Description
0	CE model with lattice LBP definition
A	MG fuel block with doublehet LBP
B	MG fuel block with homogenized LBP
C	MG fuel block with homogenized LBP and boron decreased by 12%

Table 7-9 Number density for the burnable poison of cases B and C

Case	^{10}B density (atoms/b-cm)	^{11}B density (atoms/b-cm)
B	8.32114E-4	3.35568E-3
C	7.32260E-4	2.95230E-3

Table 7-10 shows the multiplication factor results for the MG models versus the CE models. The differences shown in the fourth column are with respect to the reference CE case. It can be seen that homogenizing the LBP reduced the k_{inf} by more than 1500 pcm due to self-shielding effects. However, the LBP Trace method is more comparable to the reference model with an improvement of more than 1400 pcm.

Table 7-10 k_{inf} for the MHTGR-350 fuel block with MG treatment.

	Code	k_{inf}	k_{diff} (pcm)
Case 0	CE KENO-VI	1.06091	reference
Case A	NEWT	1.06000	-91
	MG KENO-VI	1.05718	-373
Case B	NEWT	1.04517	-1574
	MG KENO-VI	1.04289	-1802
Case C	NEWT	1.06187	76
	MG KENO-VI	1.05951	-140

7.5.2 Comparisons of cross sections of the MG model

The absorption cross sections were considered because of the interest in boron and these cross sections are collapsed to four groups. The cross sections that are compared are $\Sigma_{mixture}$, $\Sigma_{nuclide}$ and Σ_{nodal}.

7.5.2.1 Absorption macroscopic cross sections for the mixtures in the original group structure ($\Sigma_{mixture}$)

The mixture macroscopic cross section is assessed for the three cases A, B and C that were defined in Section 7.5.1. These are the cross sections which are produced by XSProc after the self-shielding calculations, and are the input cross sections for NEWT, which then performs the lattice physics calculations.

For cases B and C, the boron concentration in the LBP mixture is changed for the NEWT calculations, and therefore identical material definitions were supplied to XSProc, resulting in identical evaluations for cross sections $\Sigma_{mixture}$. Therefore, only cases A and B need to be compared, and the mixture absorption cross section is shown in Figure 7-8. The percentage difference between the macroscopic cross section for these two cases is plotted in Figure 7-9 using a logarithmic scale for the y axis.

It is observed that there are larger differences between the macroscopic cross sections in the thermal energy region (approximately group 245-250) with the largest difference occurring at group $\approx$ 248. The upper energy limit for group 248 is 0.0012 eV and lower energy limit is 0.001eV.

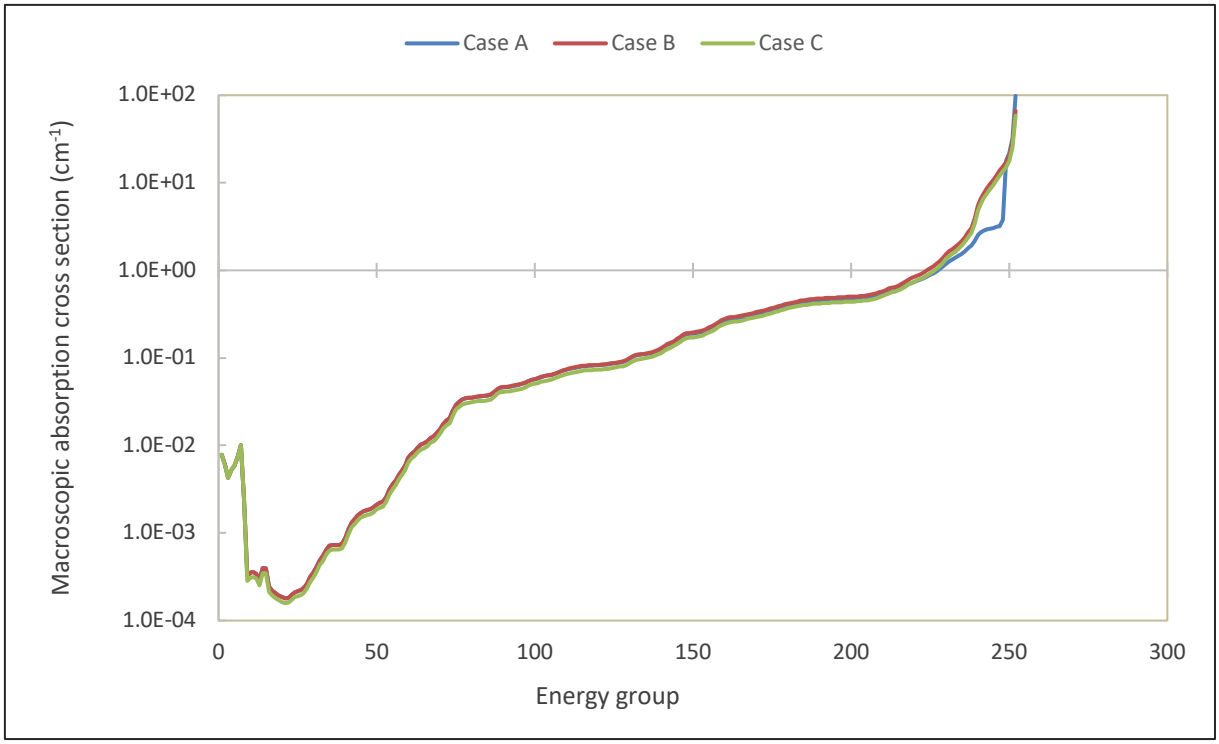

Figure 7-8 1D macroscopic absorption cross section for case A and case B.

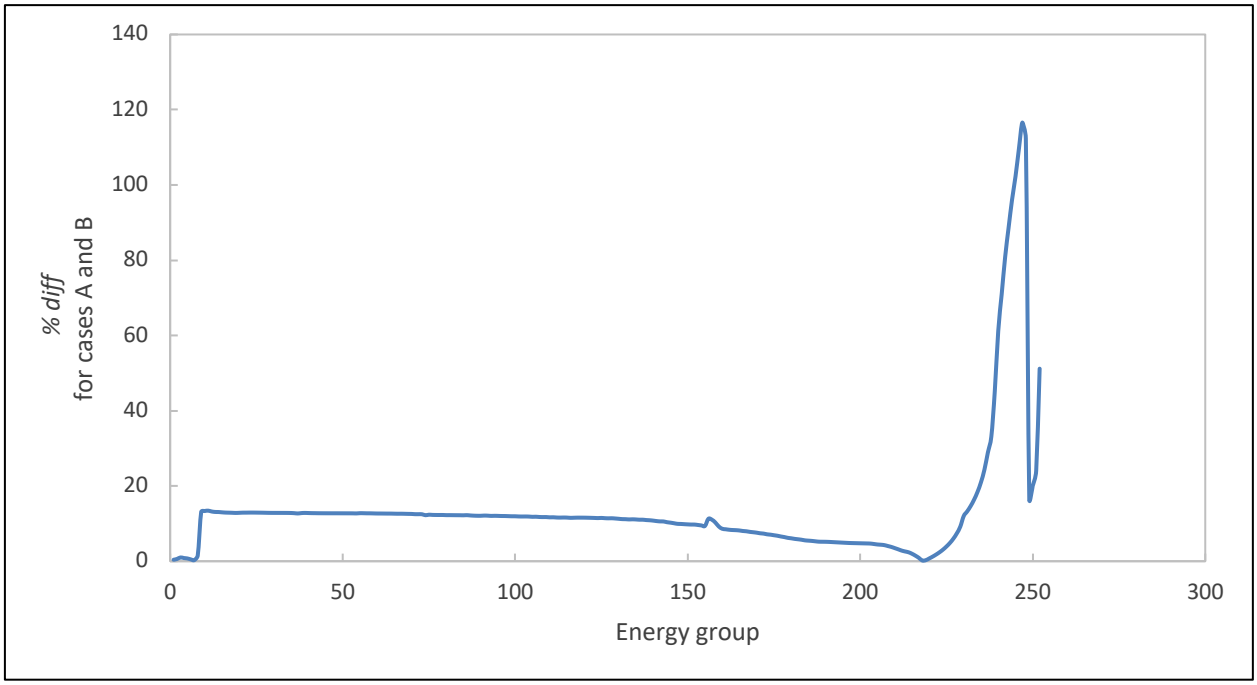

Figure 7-9 Difference between the mixture macroscopic cross section of case A and case B.

7.5.2.2 Few-group cross sections by nuclide for a mixture ($\Sigma_{nuclide}$)

The few-group cross sections are calculated in NEWT after the fluxes in the fuel assembly have been calculated for a single isotope using Equation 7.1.

$$\Sigma_x^{i,g} = \frac{\int_{E_g}^{E_{g-1}} \int_V \int_{4\pi} dE dV d\hat{\Omega} N_i(\vec{r}) \sigma_x^i(E) \psi(\vec{r}, \hat{\Omega}, E)}{\int_{E_g}^{E_{g-1}} \int_V \int_{4\pi} dE dV d\hat{\Omega} \psi(\vec{r}, \hat{\Omega}, E)}, \tag{7.1}$$

where the integral over dV is over the volume for which the few-group cross section is calculated, $\psi(\vec{r}, \hat{\Omega}, E)$ is the neutron angular flux at position $\vec{r}$, $\hat{\Omega}$ is the direction at which the neutron travels, and E is the energy of the neutron. In NEWT, the energy will be discretized into the fine group structure, and the integral involving $d\hat{\Omega}$ will be performed using an angular quadrature scheme. The cross section σ_x^i is defined for the isotope under consideration at $\vec{r}$ for reaction x and the index i is the nuclide. When all the isotopes in the volume V are considered, a summation over all these isotopes is required, and the equation becomes:

$$\Sigma_x^g = \frac{\int_{E_g}^{E_{g-1}} \int_V \int_{4\pi} dE dV d\hat{\Omega} \sum_i \left(N_i(\vec{r}) \sigma_x^i(E) \right) \psi(\vec{r}, \hat{\Omega}, E)}{\int_{E_g}^{E_{g-1}} \int_V \int_{4\pi} dE dV d\hat{\Omega} \, \psi(\vec{r}, \hat{\Omega}, E)}. \tag{7.2}$$

The NEWT output lists these cross sections; the data set is as per nuclide per mixture. Boron is only specified in the LBP compacts. In Figure 4-3, these would be the six unit cells with the green centres. Therefore, in terms of applying the Equation 7.2 above for the nuclides ^{10}B or ^{11}B, all volumes of Figure 4-3 will have zero number densities except for these six cells with green centres. The flux in the denominator of Equation 7.2, however, will not necessarily be zero for all volumes. Since only the boron isotopes need to be considered when comparing case A and C, the cross section *($\Sigma_{nuclide}$)* for ^{10}B or ^{11}B as calculated using Equation 7.2 is then is effectively the macroscopic cross section in the LBP compacts. Due to the symmetry of the six LBP compacts as shown in Figure 4-3, this effectively becomes studying a single LBP compact.

Only the absorption cross section of nuclide ^{10}B is studied since it is a stronger absorber than ^{11}B. The absorption macroscopic cross sections for the four groups are shown in Figure 7-10 with the percentage difference between the three cases shown in Table 7-11, calculated according to Equation 5.14.

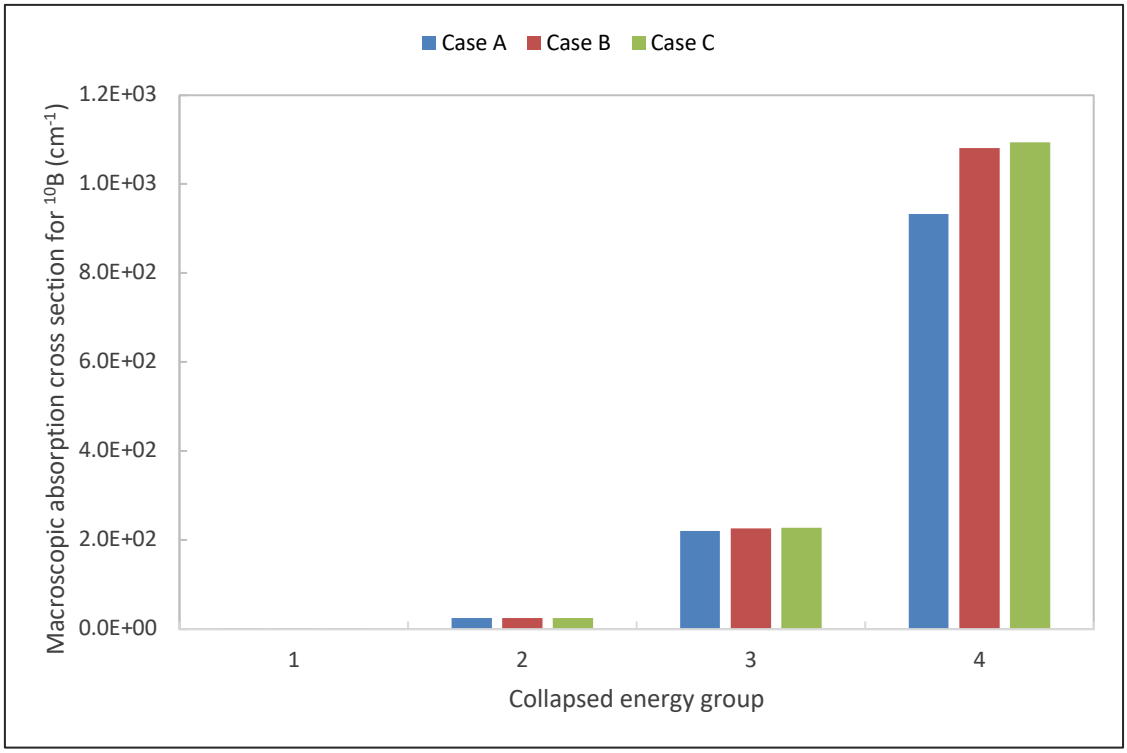

Figure 7-10 Absorption macroscopic cross section per nuclide (^{10}B).

Table 7-11 Percentage differences between the macroscopic ^{10}B absorption cross sections

	Group 1	**Group 2**	**Group 3**	**Group 4**
Case A/Case C	0.086%	0.998%	3.352%	15.789%
Case B/Case C	0.001%	0.356%	0.376%	1.115%

Case B is compared to case C since both methods have homogenized LBPs. Case A is compared to case C since these two produce comparable k_{inf} values. A percentage difference greater than 1% is considered to be significant. As can be seen, the models with homogenized LBPs have equivalent absorption cross sections whilst the fuel block with a trace LBP (case A) has a significantly lower absorption cross section in the thermal energy region, than the cases with homogenized LBP. The boron decrease by 12% in the homogenized LBP model (case C) causes a 1.115% difference in the thermal region with case B. The doublehet LBP Trace model (case A) is compared to case C since these models have comparable results for k_{inf}. A significant difference for case A and C is seen for groups 3 and 4. The biggest difference is for the fourth energy group which is in line with the findings in Section 7.5.2.1.

A similar trend is seen in the total cross section as shown in Figure 7-11. This figure shows that the ^{10}B cross section in the LBP Trace method is lower than the homogenized models in the thermal region. The percentage difference for Σ_t for ^{10}B for the 3 cases is shown in Table 7-12 and is approximately equal to the values shown in Table 7-11.

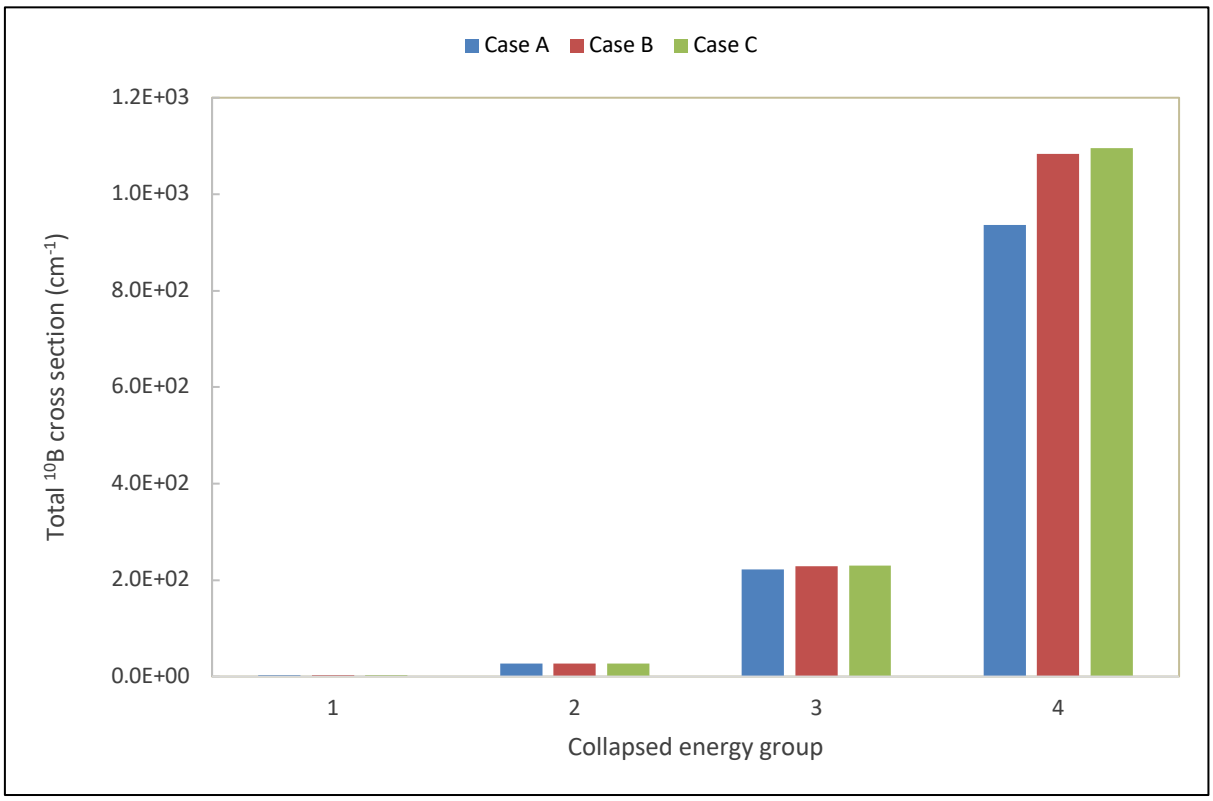

Figure 7-11 Total macroscopic cross section per nuclide (^{10}B).

Table 7-12 Percentage differences between the macroscopic ^{10}B total cross sections

	Group 1	**Group 2**	**Group 3**	**Group 4**
Case A/Case C	0.139%	0.941%	3.346%	15.785%
Case B/Case C	0.001%	0.326%	0.372%	1.112%

The ^{10}B macroscopic absorption cross sections in Figure 7-11 show that the doublehet is a weaker absorber in the thermal region than the homogenized model (with 12% less boron) even though the k_{inf} are equivalent. This also directly affects the total ^{10}B cross section. Since the macroscopic cross sections are calculated using Equation 7.1, it is also instructive to study the fluxes that are used in the equation. These are the fluxes calculated by NEWT.

Figure 7-12 shows the flux differences between the 3 cases, these differences are shown in arbitary units (a.u). The larger differences are seen at the thermal energy region, specifically at group 203-238 and the peaks are at group 230. The biggest flux differences are between case A and case B. This is consistent with the findings in the cross sections. Cases B and C also show significant differences, particularly in the thermal region, and this shows up in the larger difference of 1.112% of Table 7-12. One should not therefore state with certainty that the cross sections used in Equation 7.2 are more significant than the fluxes used.

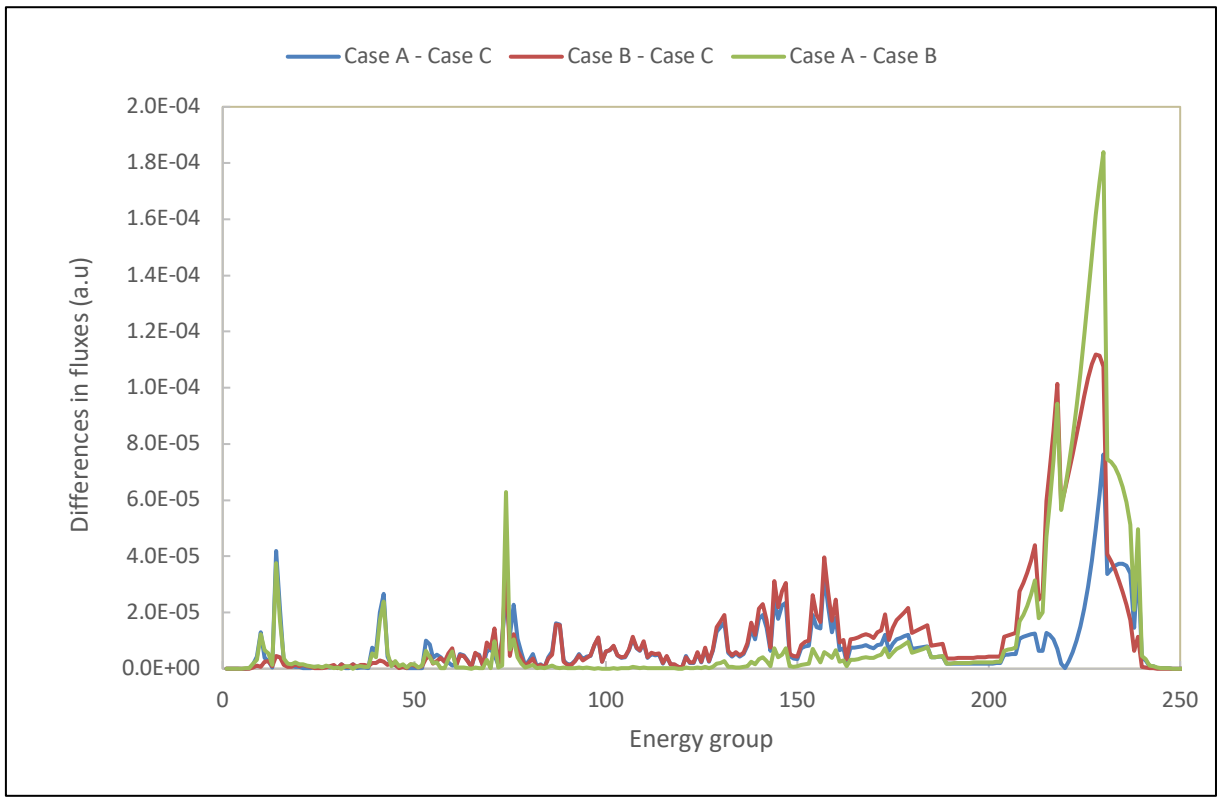

Figure 7-12 The absolute differences between the cases A, B and C.

7.5.2.3 Homogenized few-group macroscopic cross section for the nodal calculation (Σ_{nodal})

To obtain these cross sections, Equation 7.2 is applied. In this equation all the mixtures (with all the isotopes) are considered in solving the equation. These then are the cross sections that would be passed to the next calculation stage, which would be the nodal core solution.

Figure 7-13 shows the output results for the 3 cases of LBP modelling for the nodal calculation. The percentage differences of the nodal absorption cross sections are compared for the three cases. In energy groups 3 and 4, the absorption cross section for case B is higher than case C by $\geq$ 1% (possibly due to the larger boron concentration) as shown in Table 7-13. Although the

differences in $k_{\inf}$ for case B and case C is over 1500 pcm, the difference in the nodal absorption cross sections is not very large. However, one can use Equation 2.16 to obtain an estimate for the change in $k_{\inf}$. Differentiating Equation 2.16 with respect to Σ_a, one gets:

$$\frac{\partial k_{\inf}}{\partial \Sigma_a} = -\bar{\nu}\Sigma_f / {\Sigma_a}^2,$$

$$= -k_{\inf} / \Sigma_a. \tag{7.3}$$

Using incremental values instead of differential values one gets:

$$\frac{\delta k_{\inf}}{\delta \Sigma_a} = -k_{\inf} / \Sigma_a, \tag{7.4}$$

therefore,

$$\frac{\delta k_{\inf}}{k_{\inf}} = -\left(\delta\Sigma_a / \Sigma_a\right). \tag{7.5}$$

Taking the absolute value:

$$|\delta k_{\inf}| = k_{\inf}\left|\delta\Sigma_a / \Sigma_a\right|. \tag{7.6}$$

Equation 7.6 shows that, given the difference in the absorption cross section obtained from two different calculations, the difference in $k_{\inf}$ can be calculated.

Substituting the value of $k_{\inf}$ to be the average of case B and C (1.05332) and the largest absorption cross section shown in Table 7-13 (1.335%) into Equation 7.6 , one gets a value of 1427 pcm, which is in good comparison with that obtained. This therefore indicates that even though the difference in the nodal absorption cross section is not very large, their effect in calculating k_{eff} in the nodal calculation will most probably be important and lead to significant differences.

When case A is compared to case C the percentage difference is small compared to the values observed in the ^{10}B macroscopic cross section (Table 7-12). The total nodal cross sections show similar trends in the differences in the cross sections.

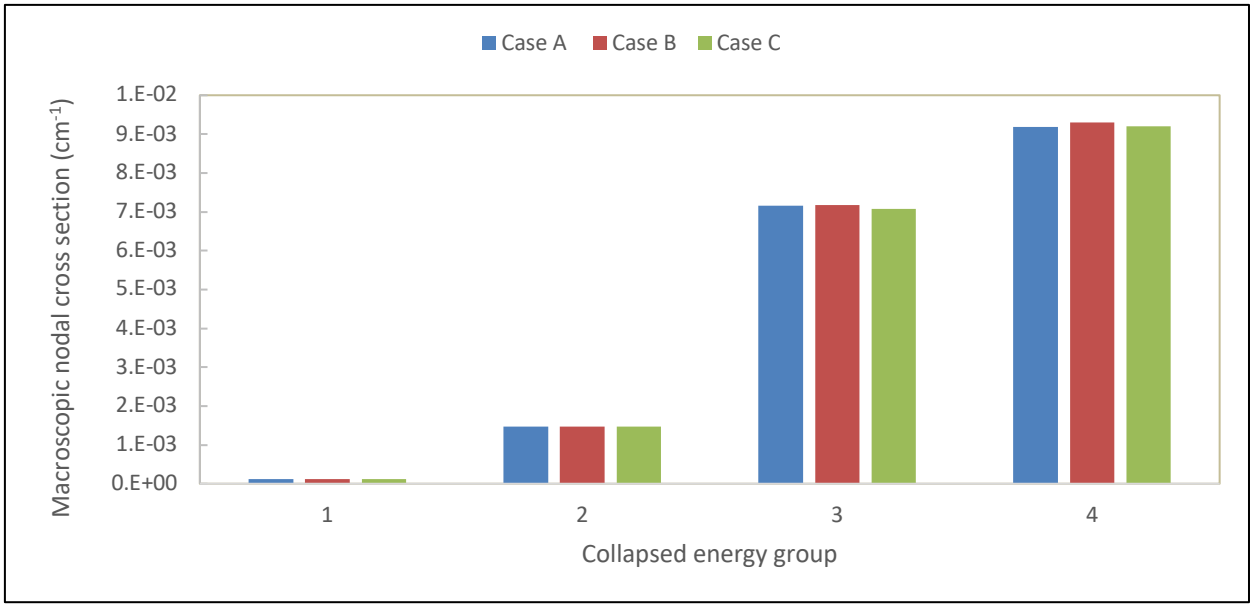

Figure 7-13 Macroscopic absorption cross section for the nodal calculation of the fuel block.

Table 7-13 Percentage differences between the macroscopic ^{10}B total cross sections

	Group 1	**Group 2**	**Group 3**	**Group 4**
Case A/Case C	0.357%	0.714%	0.978%	0.251%
Case B/Case C	0.346%	0.833%	1.335%	1.105%

Further investigation was required to understand this small difference that was obtained for the nodal absorption cross sections. There are only 6 LBP compacts compared to the large neighbourhood of graphite and fuel compacts. Therefore, case A is altered by increasing the number of burnable poisons in the fuel block so its effects are more apparent. This was carried out by filling the large coolant channels with LBPs. This was done progressively for three models, where each model had 12, 24 and 48 LBPs and these models shown in Figure 7-14.

Figure 7-15 shows the differences in the nodal cross sections between homogenized LBPs and the trace LBPs. It is clear that as the number of LBPs increases for groups 1, 2 and 3, the differences between the homogeneous treatment and the trace treatment become larger. This therefore shows that since six LBP compacts in the fuel block changes the multiplication factor by about 1500 pcm, using 12 or more LBP compacts will most probably have a much larger impact on the multiplication factor. Therefore, both the use of the LBP Trace method in modelling and the choice of the number of LBP compacts in the fuel block are important.

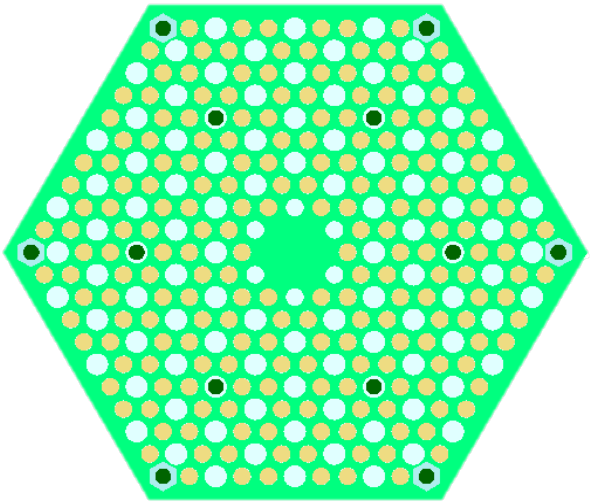

12 LBPs

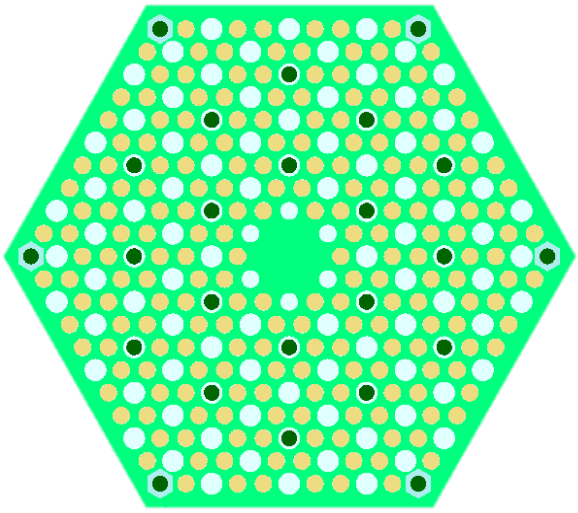

24 LBPs

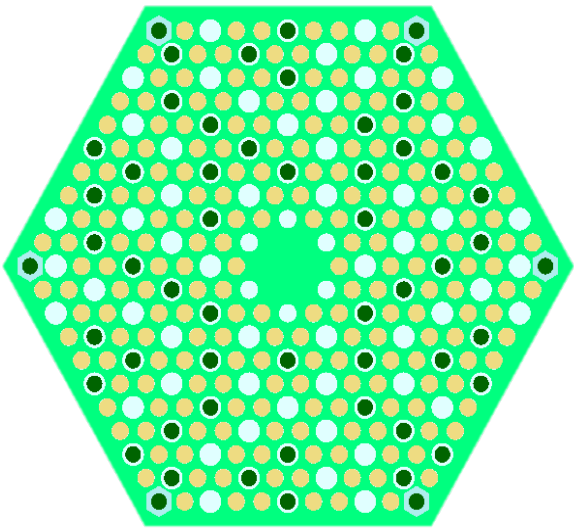

48 LBPs

Figure 7-14 MG fuel block models with additional LBPs.

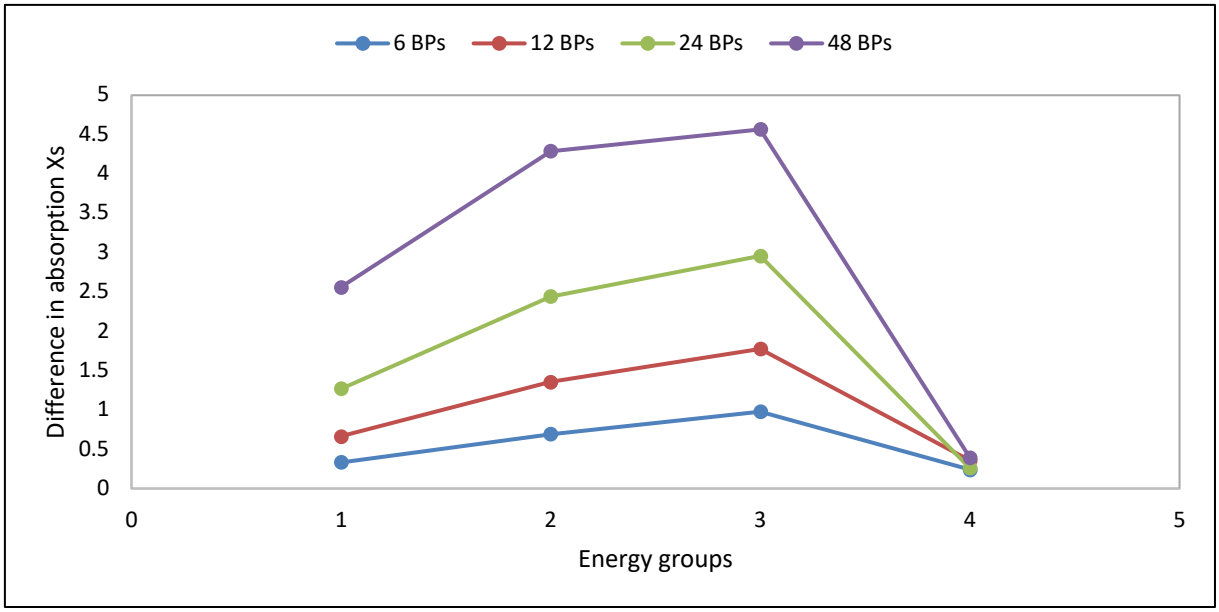

Figure 7-15 Difference between the nodal absorption macroscopic cross sections of case A and case C.

7.5.2.4 Uncertainty quantification

Table 7-14 shows the nuclear data uncertainties for case A, case B and case C as well as the reference case. Case A and case C produces a value of $\%\Delta k/k$ that is lower than the reference case by about 0.006. This is a 1.2% difference between case A and the reference case and a 1.4% difference between case C and the reference case. These differences can be considered negligible. Comparing case B with the reference case, the difference increases to 2%, but it is still small.

In terms of Δk, the difference of 0.010 $\%\Delta k/k$ corresponds to 19 pcm, which is approximately the same magnitude as statistical uncertainty of the KENO calculation. This therefore means that in terms of uncertainty contributions, the uncertainty due to modelling of the LBPs as per the different cases in the fuel block is far smaller than the largest contributor considered in this study. This is due to nuclear data uncertainties, which for the reference case is 0.507 $\%\Delta k/k$ or about 538 pcm. The Sampler/NEWT Δk and $\%\Delta k/k$ results for case A and case C are equal and almost equal, respectively. Case B produced slightly lower results for Δk and $\%\Delta k/k$.

Table 7-14 Δk and $\%\Delta k/k$ results for the cases of LBP models and the reference case.

Code	**Case**	$\boldsymbol{\Delta k}$	$\boldsymbol{\%\Delta k/k}$
CE TSUNAMI-3D/KENO-VI	Reference	0.00538	0.507
Sampler/NEWT	A	0.00530	0.501
	B	0.00519	0.497
	C	0.00530	0.500
Sampler/KENO-VI	A	0.00527	0.501
	B	0.00518	0.497
	C	0.00527	0.500

7.5.3 Uncertainty in cross sections due to nuclear data uncertainties using Sampler

In Section 7.4.2.3 only the nodal absorption cross sections are assessed and these calculations were performed with NEWT. In this section all other cross sections are considered for case A, case B and case C. The nodal cross sections obtained from the Sampler/NEWT calculations are equivalent for case A, case B and case C. Subsequently the $\%\Delta\Sigma/\Sigma$ are also equivalent for case A, case B and case C. Case B has homogenized LBP therefore case B is identical to the base case fuel block model, NMG 100. The nodal homogenized cross sections results for NMG 100 were shown in Table 6-15 and the $\%\Delta\Sigma/\Sigma$ was shown in Table 6-16.

In Table 6-15, it was seen that the fuel block cross sections are lower than the fuel compact models. This is as expected for the following reason: the fuel compact model is essentially an infinite system so it can be thought of a hexagonal fuel block with white/reflector boundary conditions consisting completely of fuel compacts in a graphite block, i.e. there are 324 fuel compacts. In the fuel block model coolant channels exist and these are filled with helium. In this model there are 210 fuel compacts. Since the total cross section of the fuel compacts is much larger than the total cross section of helium, the contribution of helium to the nodal macroscopic cross section as calculated using Equation 7.2 will be smaller.

7.6 Chapter summary

The findings in Chapter 7 are:

- The choice of the local packing is significant on a fuel compact level.
- The MHTGR-350 fuel compact is under moderated.

- Jiggling the coated particles had no effect on the k_{inf} and also had no effect on the uncertainty propagated using nuclear data uncertainty.
- All three LBP models produced nodal cross sections with small differences between them. However, the effect on the multiplication factor in the nodal calculation is expected to be significant.
- The uncertainty due to nuclear data was equivalent for all 3 LBP cases.

CHAPTER 8: VALIDATION WITH THE HTTR

This section aims to validate the criticality and uncertainty methods applied to the MHTGR-350 in Chapters 6 and 7. This is done by applying these methods to the experimental HTTR. The HTTR benchmark core model is built using NWURCS and the criticality results are compared to the experimental results as a base case problem. Version one of NWURCS has been used successfully at the NWU to build the VVER reactor core (Nyalunga et al, 2016), but not for the HTGR. The HTGR is a more complex design due to its double heterogeneity and large graphite quantities. Version 2.1 of NWURCS is used in this work.

This chapter begins with a verification of NWURCS' capability to model the HTTR, followed by CE TSUNAMI convergence for the HTTR. Finally, the full core model is built with NWURCS and the uncertainties and sensitivities are quantified. The reader should note that, regarding NWURCS, the verification is completed by comparing the fuel block model to the fuel block model reported by Ilas et al (2012). Therefore, the fuel blocks in the verification models are modelled identically to that by Ilas et al (2012). The full core HTTR models are built according to the benchmark specifications stipulated in HTTR-GCR-RESR-001(Bess et al, 2009). As mentioned in Section 4.3, HTTR-GCR-RESR-001 is a benchmark evaluation report for the fully-loaded, cold-critical, configuration of the HTTR start-up core. It is available in the International Handbook of Evaluated Reactor Physics Benchmark Experiments (IRPhEP) handbook.

For validation studies, it is important to choose a benchmark that is the most similar to the desired application. Systems which have similar sensitivities to nuclear data uncertainties are expected to be computed to comparable accuracy (Williams and Rearden, 2008). The HTTR is chosen for the validation study since it has strong similarities to the MHTGR-350 system. There are a number of similarities between the MHTGR-350 and HTTR, such as both systems are HTGRs with low enriched uranium, and TRISO fuel and the fuel blocks of both systems have a pitch of 36.0 cm. TSUNAMI quantifies the neutronic similarity between two systems and they are deemed neutronically similar if they have similar sensitivity profiles (Dahmani and Kastanya, 2013).

The ENDF/B-VII.0 library and ENDF/B-VII.1 library were used for these CE calculations. The ENDF/B-VII.0 library was used for the verification models, the critical full-core model and subcritical full core models. This was done to allow for comparison with other literature. All other models are computed with the ENDF/B-VII.1 library since it falls within the scope of this work.

CE TSUNAMI computes the sensitivity of k_{eff} due to cross section data. A sensitivity data file is produced in MG format. This data file consists of the sensitivity of k_{eff} due to each reaction of

each nuclide. The MG HTTR models could not be computed since NWURCS currently does not have the capability to build MG SCALE models.

8.1 Development of the HTTR full core using NWURCS

8.1.1 Packing and randomization

In Chapter 7, it was found that jiggling of CPs has a very insignificant effect on k_{inf} and the nuclear data uncertainty. Therefore, it can be assumed that the error caused by jiggling of CPs would also be insignificant for larger systems. It was also seen from literature that random placement of coated particles has an effect on k_{inf} at the fuel pin level but as the system gets bigger the effect on k_{inf} is small. Ardakani et al (2014) reports a difference of 100 - 200 pcm between the regular and stochastic full core HTTR models, but the random full core model requires more than 8 times computational time. In Chapter 7, it was reported that it took 9 times more computational time to complete a KENO-VI random fuel compact compared to a fixed lattice model. Due to limited memory and computational resources it was not possible to execute a SCALE calculation for the random HTTR full core model for this thesis.

Therefore, the coated particles are placed in an ordered model with no clipping. 12987 CPs are modelled, which is approximately equal to the 13000 particles, stated in HTTR design specification (Iyoku et al, 2004).

8.1.2 LBP Trace method

The BPs of the HTTR are B_4C disks rather than coated particles so the LBP Trace method was not needed in the validation. Furthermore, only the CE model was built.

8.1.3 Application of optimization parameters

An optimization study was conducted for the MHTGR-350 fuel block and fuel compact using CE TSUNAMI in Section 6.4. The HTTR fuel block differs geometrically from the MHTGR-350. Therefore, a convergence study for the MHTGR-350 is also conducted to assess if the same parameters for the MHTGR-350 also apply for the HTTR. The HTTR optimization study is discussed in Section 8.4. The optimization study is done for the fuel block and a single core layer, layer 3 is arbitrarily chosen.

8.2 Verification of the CE HTTR model

The 33-pin fuel model of a fuel block of the HTTR with a 6.3% fuel enrichment and 2.5 wt% BP absorber pin is used to verify the input file generation capability of NWURCS. The chosen fuel

block was also modelled by Ilas et al, (2012) to validate SCALE's capability of modelling HTGRs. In addition, a model is built manually in KENO-VI, this model is labelled 'Sihlangu' and is compared to the KENO-VI model generated by NWURCS. A further comparison is made to the results presented by Ilas et al (2012). In the publication by Ilas et al (2012), the burnable poisons are modelled with two 20 cm long sections of absorber material and the top and bottom separated by 10 cm of graphite disks (Ilas and Gehin, 2010).

The fuel block verification is followed by the core model verification. Since the HTTR benchmark core model is a very detailed model, further simplifications are made to make the verification task more manageable. The verification calculations are executed at CZP, i.e. 293.65 K and the library is the ENDF/B-VII.0 library. This library is chosen to allow for comparison with other literature.

8.2.1 Stepwise verification of NWURCS HTTR CE fuel block model

The fuel block model is built in increments starting with a homogeneous hexagonal model containing fuel only and the last model is the actual fuel block model. The number densities and materials used to model the fuel block are referenced from a publication by Ilas et al (2012). The fuel block models are defined as follows:

Model 801: A homogeneous fuel block model. Essentially this model is just a hexagon filled with uranium oxide fuel with 6.3% fuel enrichment. No fuel block gap is modelled. No other material is present.

Model 802: The fuel block is no longer homogeneous, but now consists of an infinite array of homogeneous fuel holes. The fuel holes extend from top to bottom (i.e. from 0.0 cm to 58.0 cm) and are filled with 6.3% enriched fuel. This model is shown in Figure 8-1.

Model 803: For this model, fuel rods are now annular and the annular fuel rods are modelled in an infinite array as shown in Figure 8-1. The fuel region is filled with 6.3% enriched fuel and extends from 1.7 cm to 56.3 cm The fuel block gap is modelled.

Model 804: The coated particle is introduced in this model as shown in Figure 8-1. Essentially this model is a hexagonal block filled with an infinite array of fuel rods. Each fuel rod is filled with coated particles.

Model 805: The full fuel block model, which has cylindrical-shaped fuel handling holes. The BPs are modelled with two 20 cm long sections of absorber materials at the top and bottom, separated by a 10 cm section made of graphite disks, as shown in Figure 8-2.

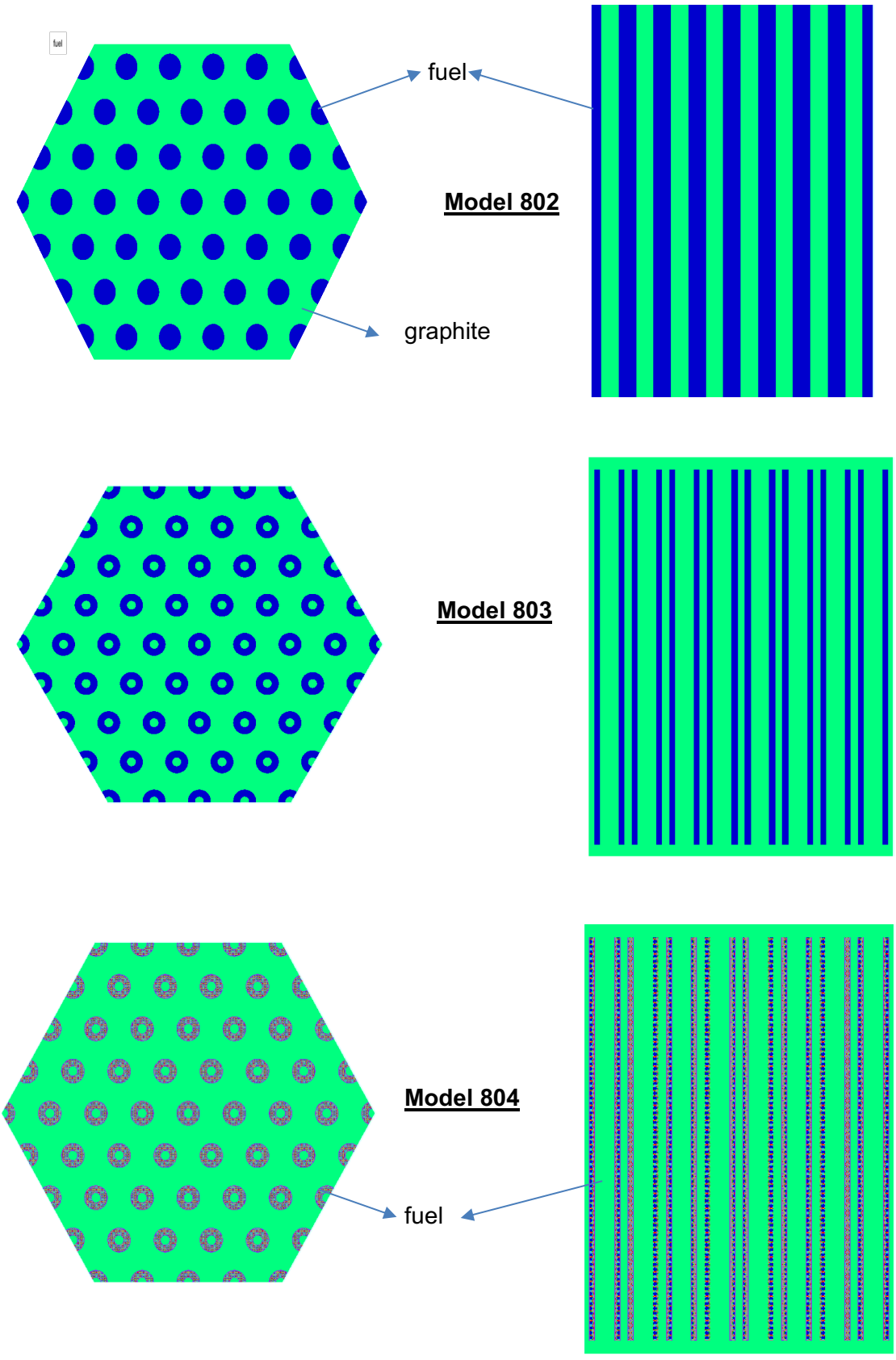

Figure 8-1 Model development of the HTTR.

Table 8-1 lists $k_{\inf}$ for both the NWURCS and manually written models (Sihlangu) for all the models 801 – 805. The differences between NWURCS and Sihlangu HTTR fuel block models are within 1-2σ. NWURCS underestimates the value of $k_{\inf}$ when compared to Sihlangu models except for model 801. Model 805 is the complete HTTR fuel block model as described by Ilas et al (2012) and shown in Figure 8.2. There is a 22 pcm difference between NWURCS and the Sihlangu HTTR fuel block model. NWURCS took 22.7 hrs to compute model 805 and the Sihlangu model took 10.3 hours to complete on an Intel® Core ™ i5-6500 CPU with 3.20 GHz processor base frequency. NWURCS takes 2.2 times more time to calculate.

Table 8-1 Verification of NWURCS in terms of $k_{\inf}$

	NWURCS	**Sihlangu**	k_{diff} **(pcm)**
Model 801	0.92526 (10)	0.92518 (9)	8
Model 802	0.95559 (11)	0.95586 (11)	-27
Model 803	0.97009 (12)	0.97042 (12)	-33
Model 804	1.44867 (14)	1.44888 (16)	-21
Model 805	1.33627 (17)	1.33649 (18)	-22

The fuel rods in the NWURCS models are modelled as 14 individual identical compacts as is in the experimental design. In the Sihlangu model the fuel rod is modelled as one unit since the compacts are identical. This is one of the differences between the two modelling techniques. However, the geometry modelled in terms of the full rod height is equivalent for both models.

8.2.2 Comparison of HTTR NWURCS fuel block model with literature

The NWURCS and Sihlangu fuel block $k_{\inf}$ results are compared to the $k_{\inf}$ results computed by Ilas et al (2012) as shown in Table 8-2 and the standard error is shown in column 3. The differences between the Ilas models and the NWURCS and Sihlangu model is 441 pcm and 463 pcm respectively. One of the reasons for the different values could be that different versions of the code were used. Ilas et al (2012) used version 6.1 of SCALE whilst SCALE 6.2.1 was used for the Sihlangu and NWURCS models. Another reason could be that there are normally many ways in which the geometry of a system can be modelled although this effect might not be as large as that due to using different versions of the code. The standard error in the fuel block results by Ilas et al (2012) is 27 pcm whilst the standard error in the NWURCS and Sihlangu models is 18 pcm.

In the model presented by Ilas et al (2012), the fuel handling hole (FHH) is modelled as stated in the experimental design (cone-shaped in the top third). The effect of modelling the FHH with a cone (as shown in Figure 8-3) instead of a cylinder is 12 pcm. Hence this effect is negligible.

Table 8-2 Comparison of NWURCS models with literature

Model	$k_{\mathbf{inf}}$	σ **(pcm)**
CE KENO-VI Ilas*	1.33186	27
MCNP5 Ilas*	1.33101	24
CE KENO-VI NWURCS	1.33627	17
CE KENO-VI Sihlangu *Cylindrical FHH*	1.33649	18
CE KENO-VI Sihlangu *Cone-shaped FHH*	1.33661	19

* Ilas calculations were performed with SCALE Version 6.1, the library was based on ENDF/B-VII. The MCNP version is 5

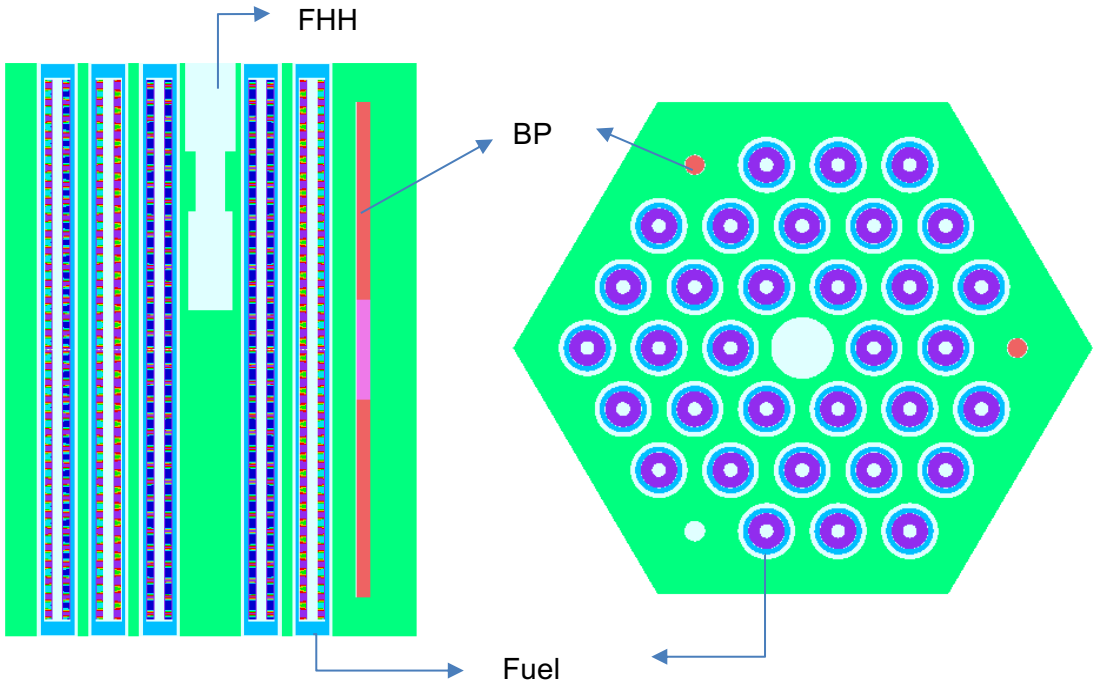

Figure 8-2 33 pin, 6.3 wt% ^{235}U enriched, 2.5 wt% BP fuel block with cylindrical FHH.

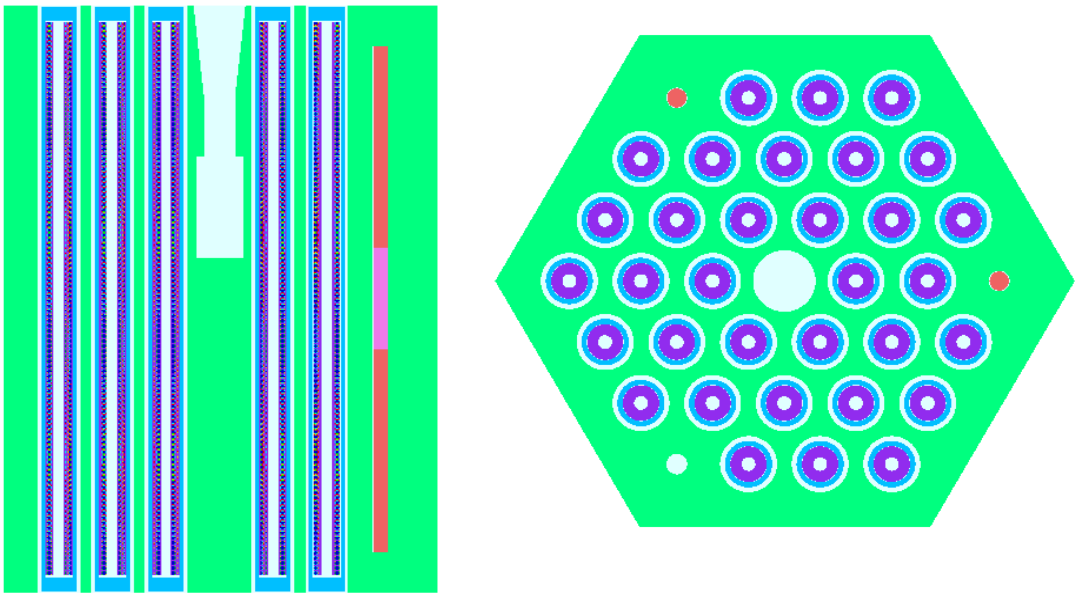

Figure 8-3 33 pin, 6.3 wt% ^{235}U enriched, 2.5 wt% BP fuel block with cylindrical FHH.

8.2.3 Verification of NWURCS HTTR CE full core model

In terms of the full core model, the NWURCS verification is carried out for a single core layer. The third core layer is arbitrarily chosen. This model is called model 806 and is shown in Figure 8-4. The third fuel row is modelled according to HTTR-GCR-RESR-001 as shown in Figure 8-4 but a few simplifications are made to the core layer model, which are:

- The BP has the same orientation throughout the entire core layer.
- The control rods are removed.
- FHH are removed since they are not a part of the benchmark model. The FHH were kept in Section 8.2.2 for the sole purpose of comparison with literature, since the models presented in the publication by Ilas et al (2012) have FHH in their models.

The reader should note that the BPs in the fuel blocks are modelled as stated in Chapter 4 and in the HTTR-GCR-RESR-001 document (Bess et al, 2009), i.e. the BP is modelled with 23.8 cm of absorber material at the top, a 10 cm section of graphite disks and a 20 cm bottom section of absorber material. The geometry of the fuel blocks that are used to build model 806 and model 807 are shown in Figure 8-5.

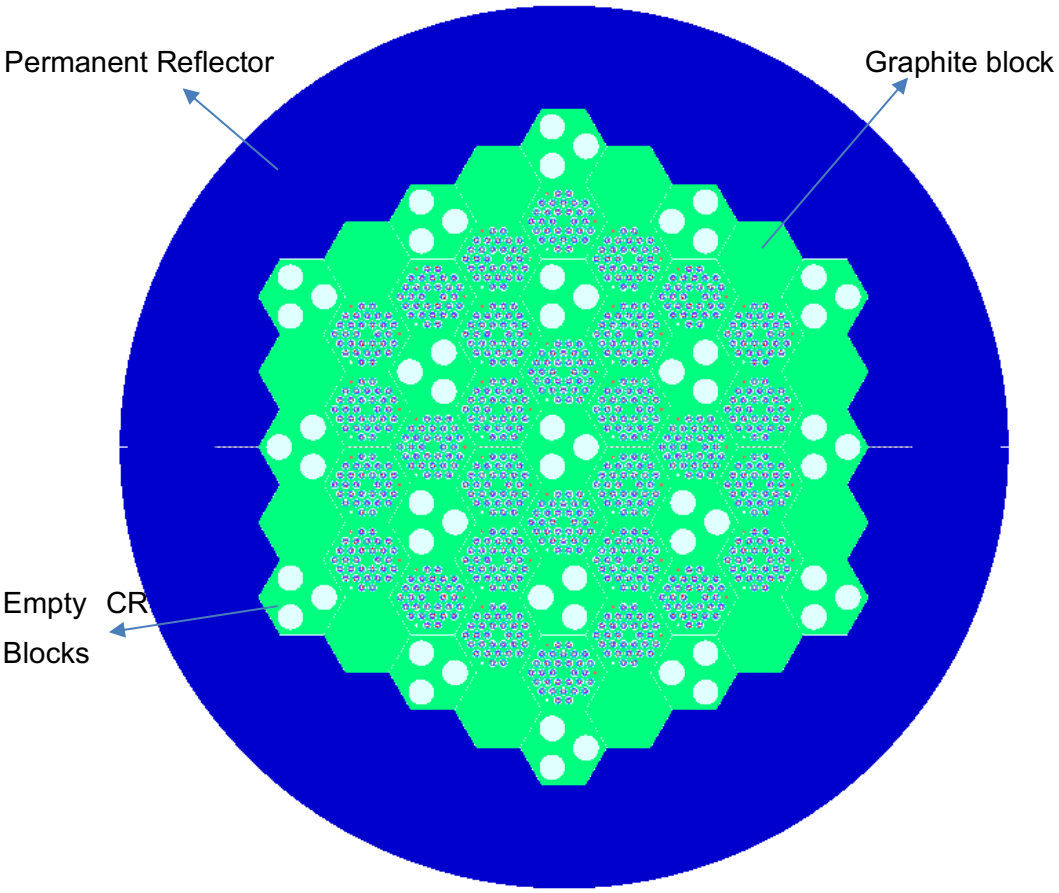

Figure 8-4 Cross sectional view of the HTTR simplified core layer (model 806).

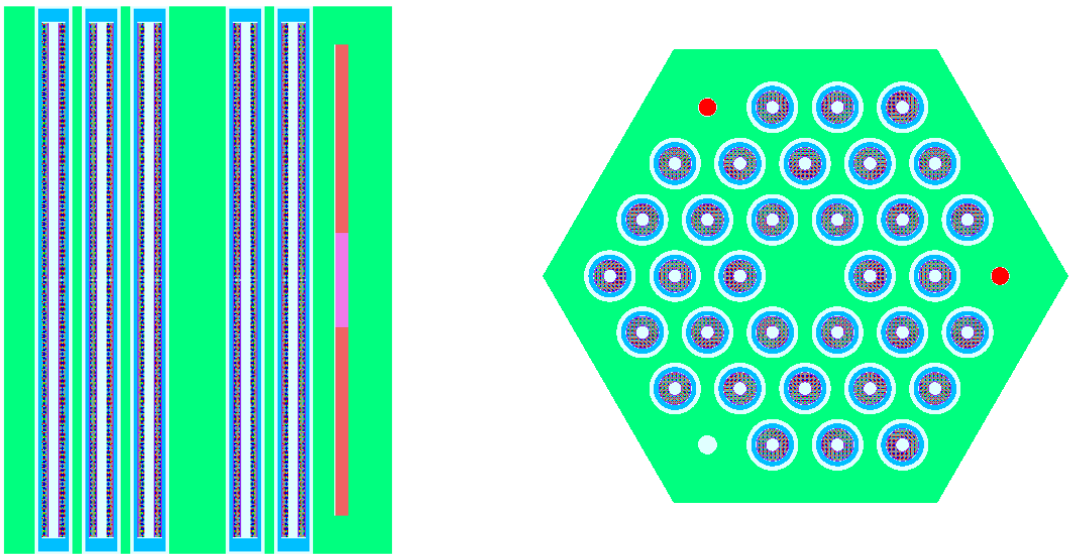

Figure 8-5 Benchmark model of the fuel block.

NWURCS' capability to model 9 core layers is also tested using the simplifications listed at the beginning of this section. The top two and the single bottom layers are graphite as described in Chapter 4. In this verification model, the 5 fuel layers are identical. This model is called model 807.

Table 8-3 shows that there is approximately a 20 pcm difference between the core models generated with NWURCS and the manually generated core models.

Model 806 and Model 807 each took approximately 23 hours to complete using NWURCS whilst it took 15 hours using the manually generated input file. The size of the fuel layer output file produced by NWURCS is 12 times larger than the output file produced by the manually generated model. These calculations were executed on an Intel® Xenon® W-2145 CPU, with 3.70 GHz processor base frequency and an installed memory of 64.0 GB.

Table 8-3 CE KENO-VI $k_{\inf}$ values for the simplified core models

	NWURCS	**Sihlangu**	$\boldsymbol{k_{diff}}$ **(pcm)**
Model 806	1.19950 (19)	1.19970 (21)	20
Model 807	1.14536 (18)	1.14558 (17)	22

8.3 NWURCS HTTR critical benchmark full core model.

The NWURCS full core model was generated using 120 fuel assembly files (FA files). All the files required for the NWURCS input were summarized in Section 3.9. The fuel assemblies are distinguished by the number of fuel pins, the fuel enrichment, the position of the BP rods and the BP enrichment. There are seven control rod files. These files are separated by the orientation of the 3 CR holes, the positioning of the CRs in 2 of these holes and the depth of the CRs. Figure 8-6 shows a portion of the third layer of the full core model.

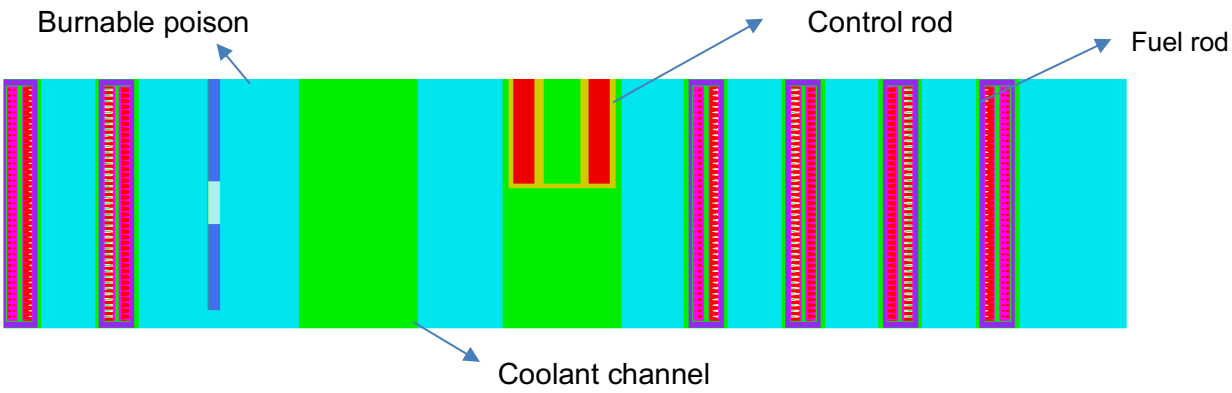

Figure 8-6 A portion of the axial view of the full core model.

8.3.1 Comparison of HTTR critical full core model with literature and the experimental results

The full core critical benchmark was modelled according to HTTR-GCR-RESR-001 (Bess et al, 2009) using NWURCS and the multiplication factor is shown in Table 8-4. The value of k_{eff} for the full core model built with NWURCS is compared to the k_{eff} values from publications by Bess (2012), Bess and Fujimoto (2014), Chiang et al (2014) and HTTR-GCR-RESR-001. The k_{eff} values reported by these publications is either computed using the ENDF/B-VII.0 or ENDF/B-VII.1 library.

The experimental value for k_{eff} was 1.0000 and this was obtained with the instrumentation. The benchmark value of 1.0025 represents the experimental value that has been adjusted for the removal of instrumentation during the actual experiment (Bess, 2010). This value of 1.0025 and not 1.0000 will be taken as the experimental or benchmark value. The ENDF/B-VII.0 and ENDF/B-VII.1 k_{eff} values computed by NWURCS are presented and their difference is calculated.

The k_{eff} produced from the ENDF/B-VII.1 data differs from the experimental results by 1011 pcm (approximately 1%), whilst the ENDF/B-VII.0 k_{eff} calculation differs from the experimental result by 2156 pcm. There is a 1145 pcm difference between the k_{eff} generated by the two libraries. This is consistent with the findings in Bostelmann, Hammer et al (2016) who modelled the VHTRC. The difference of approximately 1000 pcm was also found between ENDF/B-VII.0 and ENDF/B-VII.1 in this case. This improvement is most probably due to the update in carbon capture cross sections.

Table 8-4 Multiplication factor results for the HTTR full-core model

Model	k_{eff}	k_{diff} **(pcm)**	k_{diff} **(pcm)**
NWURCS KENO-VI ENDF/B-VII.0	1.02375 (20)	*reference*	1145
NWURCS KENO-VI ENDF/B-VII.1	1.01261 (20)	-1145	*reference*
Benchmark[a]	1.00250	-2156	-1011
HTTR-GCR-RESR-001- MCNP5 ENDF/B-VII.0[b]	1.02600 (14)	194	-
Bess and Fujimoto - MCNP5 ENDF/B-VII.0[c]	1.02290 (10)	-116	-
Chiang - KENO-VI - SCALE 6 - ENDF/B-VII.0[d]	1.02167 (79)	-239	-
Chiang MCNP5 ENDF/B-VII.0[d]	1.02113 (68)	-293	-
Chiang MCNP6.1 – ENDF/B-VII.1 [c]	1.01410 (10)	-	-149

a(Bess, 2012) b(HTTR-GCR-RESR-001) c(Bess and Fujimoto, 2014) d(Chiang et al, 2014)

Chiang et al (2014) reports that the difference between experimental results and the ENDF/B-VII.0 Monte Carlo code calculations is 2000 pcm to 3000 pcm, whilst HTTR-GCR-RESR-001 reports that the difference between k_{eff} computed by the Monte Carlo codes is approximately 2% (approximately 2000 pcm) greater than the experimental results. The MCNP5 ENDF/B-VII.0 k_{eff} results reported in HTTR-GCR-RESR-001 and by Bess and Fujimoto (2014) differ from k_{eff} calculated in this work by 194 pcm. Chiang et al (2014) calculated the MCNP 5, ENDF/B-VII.0 k_{eff} result to be 293 pcm less than the KENO-VI calculation reported in this work. The KENO-VI k_{eff} result reported by Chiang et al (2004) is 239 pcm less than the value reported in this work. Hence NWURCS was able to model the HTTR and rendered k_{eff} results that are in agreement with the other k_{eff} results (Bess and Fujimoto, 2014; Chiang et al, 2014; HTTR-GCR-RESR-001).

The difference of 1011 pcm obtained in this work is nevertheless still considerably large. This could be due to improper modelling of the impurities in the benchmark model. No impurity information was provided in the HTTR benchmark for some of the materials (HTTR-GCR-RESR-001). In this benchmark only the ^{10}B impurity is assessed. Ho et al (2018) suggests that the improper modelling of the graphite impurities is the most probable cause for this 1% bias.

Furthermore, no impurities have been modelled for the alloy or the coolant. Ardakani et al (2015) showed that modelling the amount of nitrogen in the core (as a result of power rising) improves the criticality results. Bess reports a k_{eff} result for the ENDF/B-VII.1 library that is 149 pcm less than the result reported in this work (Bess and Fujimoto, 2014).

8.3.2 Subcritical HTTR full core model

This section presents a criticality study for the full core subcritical model, with all CRs inserted. The HTTR-GCR-RESR-001 benchmark specifies that all the CRs are placed at a position of 5.5 cm below the bottom of the fuel. Due to a coding bug in NWURCS, this was not possible so the CRs are placed at a position 10 cm below the bottom of the fuel, as shown in Figure 8-7. The burnable poisons are the red cylindrical volumes shown in Figure 8-7.

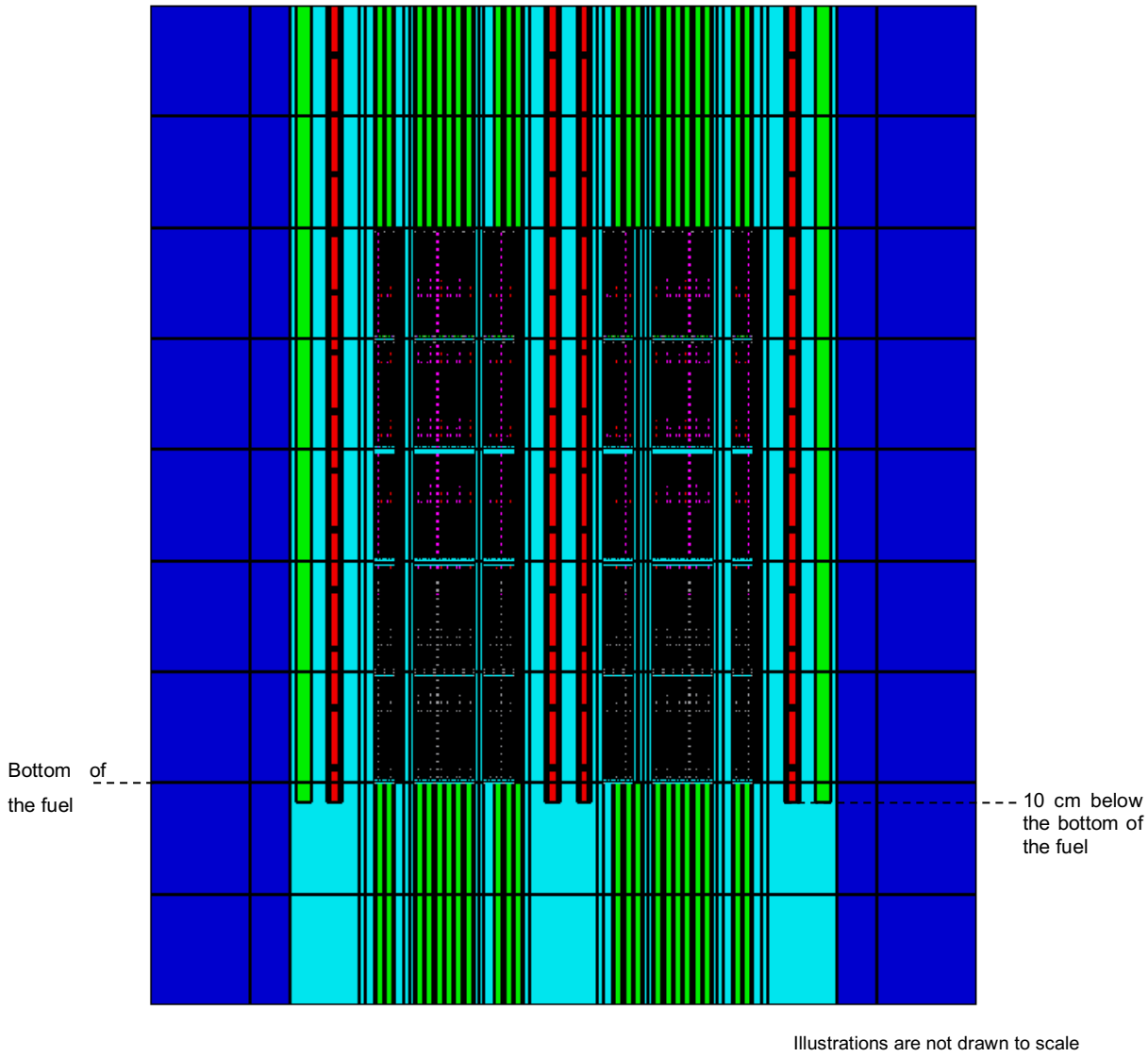

Figure 8-7 NWURCS/KENO-VI model of the subcritical HTTR core.

In Table 8-5, the NWURCS subcritical HTTR model results are compared to the benchmark results as well as other Monte Carlo calculations from the literature. The measured value for the

subcritical model is 0.6850 but a value of 0.6876 is taken as the benchmark value since it accounts for the bias in control instrumentation (Bess, 2010).

The k_{eff} result computed with KENO-VI ENDF/B-VII.0 compares well with the experimental result, differing from the experimental (or benchmark) value by 320 pcm. From the k_{eff} analysis done in Section 8.3.1, it is expected that the KENO-VI calculation using the ENF/B-VII.0 library would be higher than the experimental result by 2000 pcm. Bess (2010) reports a difference of 1230 pcm between an MCNP5 calculation of the subcritical model and the benchmark (experimental) value. However, it is found that there is no large bias.

A 1000 pcm difference is expected between the benchmark value and the computed (with Monte Carlo codes) values using ENDF/B-VII.1. The k_{eff} difference between the subcritical HTTR ENDF/B-VII.1 and the benchmark value is 30 pcm. Therefore, there is a better comparison between the benchmark value and the Monte Carlo calculations for the subcritical model then there is for the critical model.

The difference between NWURCS ENDF/B-VII.0 and NWURCS ENDF/B-VII.1 is 350 pcm. In Section 8.3.1 the difference between NWURCS ENDF/B-VII.0 and NWURCS ENDF/B-VII.1 is 1145 pcm. Therefore, there is also a better comparison between ENDF/B-VII.0 and ENDF/B-VII.1, when the system is subcritical.

It is quite clear that the insertion of the control rods has created this effect. To obtain further insight into this, one needs to start by investigating how the materials have changed and also how the neutron spectra have changed. The scope of the project in terms of time did not allow further investigation. Also, the computer bug in NWURCS in terms of the control rod position in the bottom layer of the core needs to be fixed and this also could not be carried out due to time constraints.

Table 8-5 The values of k_{eff} with all control rods inserted

Model	$\boldsymbol{k_{\text{eff}}}$	$\boldsymbol{k_{diff}}$ **(pcm)**	$\boldsymbol{k_{diff}}$ **(pcm)**
NWURCS KENO-VI ENDF/B-VII.0	0.69080 (20)	reference	350
NWURCS KENO-VI ENDF/B-VII.1	0.68731 (19)	350	reference
Benchmark[a]	0.68760	-320	30
CE KENO-VI - SCALE 6 - ENDF/B-VII.0[b]	0.69760 (9)	680	-
MCNP-5 ENDF/B-VII.0[a]	0.69990 (1)	910	-

a (Bess, 2012) , b (Ilas et al, 2012)

8.4 Optimization/convergence of $F^*(\vec{r})$ for the HTTR.

An $F^*(\vec{r})$ convergence study is conducted for the HTTR fuel rod, fuel block and one layer of the core. Similar to Section 6.4.1, the number of latent generations are kept constant at 20. The results obtained from this section are compared to the MHTGR-350 $F^*(\vec{r})$ convergence in Section 6.4.1. In this section, it is assessed how the convergence parameters change since the MHTGR and HTTR are geometrically different.

8.4.1 $F^*(\vec{r})$ convergence for the HTTR fuel block

The three output edits are shown in Figure 8-8, Figure 8-9 and Figure 8-10. Figure 8-8 shows a statistical spread with respect to both A and $\%\Delta k/k$. Figure 8-9 shows tallies that scored more than 50% uncertainty and a better or more clear convergence trend was seen in this figure. This was similar to what was seen in Figure 6-13 for the MHTGR-350 fuel block.

From Figure 8-9, it can be seen that the percentage of tallies that contain more than 50% uncertainty converges at $A = 300$ for all mesh sizes. The 20 × 20 × 20 mesh has more tallies that scored more than 50% uncertainty compared to all other mesh sizes. The reason for this is a topic for further investigation. The 10 × 10 × 10 mesh shows clear convergence at A = 200 in Figure 8-10. Judging from this figure the recommended mesh size is 10 × 10 × 10 since it converges quicker than the other meshes. This recommendation is consistent with the findings in Chapter 6. As previously mentioned the coarser meshes take less computational time. For the 10 × 10 × 10 mesh, A = 200 is also recommended for the fuel block, i.e. $NPG = 50000$, $NSK = 21$, $GEN = 471$.

When comparing Figure 8-8, Figure 8-9 and Figure 8-10, one is able to gauge convergence trends more reliably from Figure 8-10. From Section 6.4.1, the MHTGR-350 fuel block CE-TSUNAMI calculations also converged at $A = 200$ and the grid recommendation was 10 × 10 × 10.

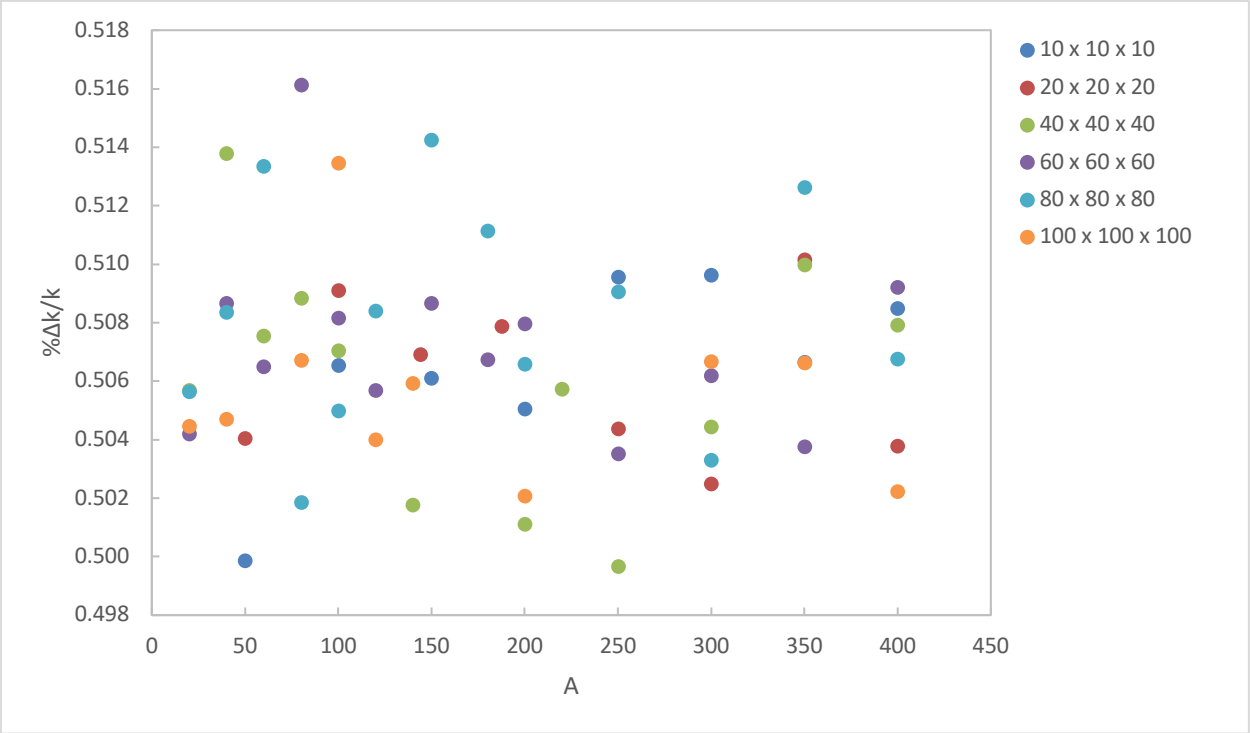

Figure 8-8 $\%\Delta k/k$ for the fuel block calculation of the HTTR.

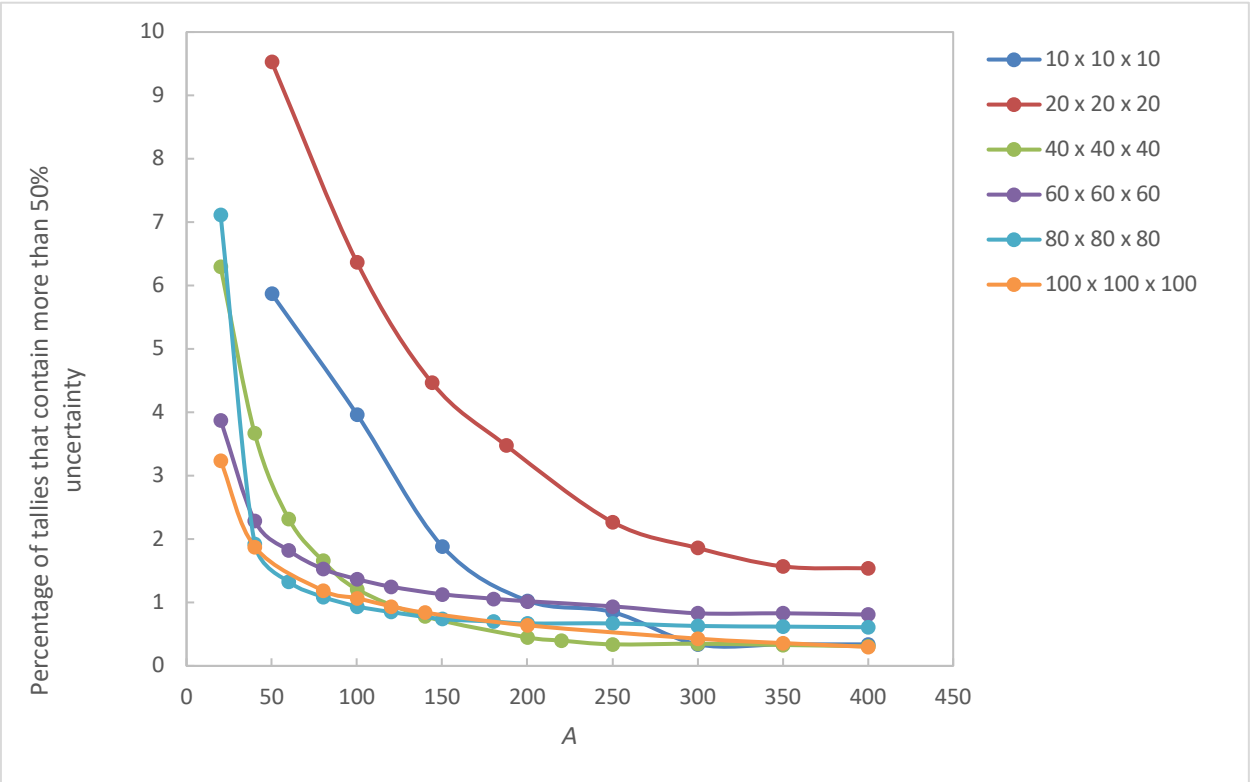

Figure 8-9 Tallies that scored more than 50% for the HTTR fuel block.

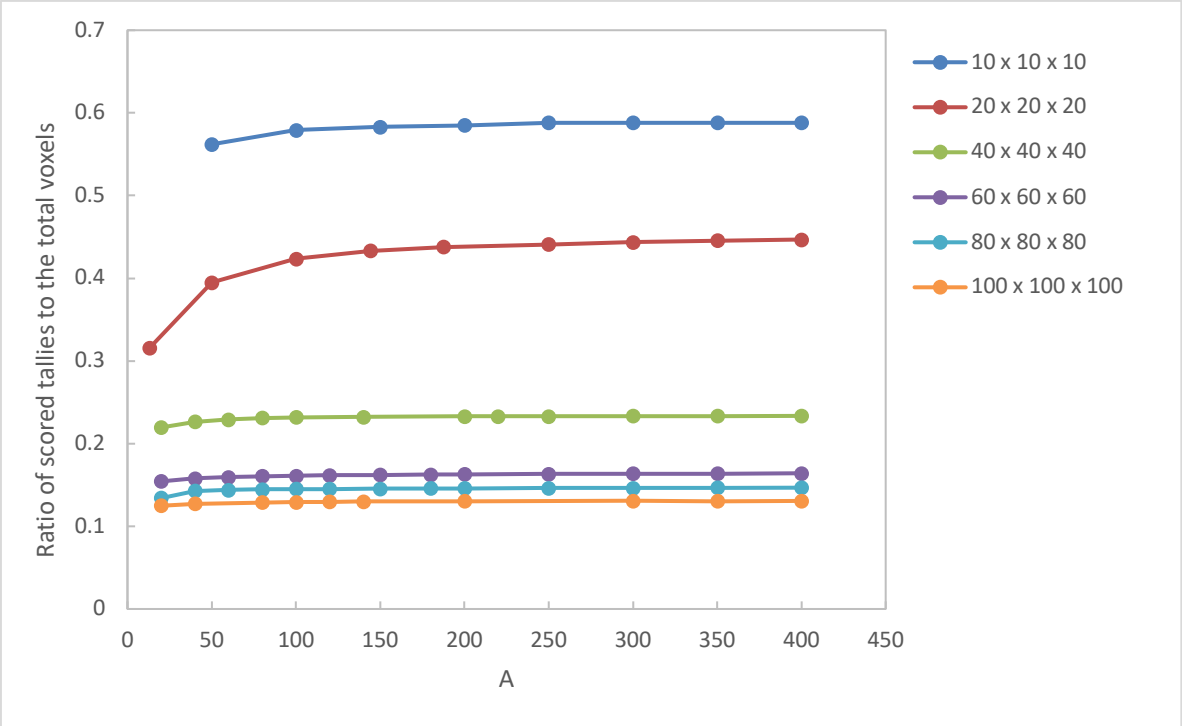

Figure 8-10 Ratio of voxels that scored tallies for the HTTR fuel block.

8.4.2 CE TSUNAMI convergence for a single active core layer.

The CE TSUNAMI convergence study presented in Chapter 6 and Section 8.4.1 is repeated for one of the HTTR core layers. The third active core layer (or fifth core layer) is chosen for this analysis. The illustration of this core layer can be seen in Figure 8-4.

Mesh sizes of $5 \times 5 \times 5$, $10 \times 10 \times 10$ and $20 \times 20 \times 20$ are chosen, which are coarse meshes. These coarse meshes are chosen because finer meshes are time consuming and do not produce better convergence statistics than the coarse mesh as stated in Chapter 6, Section 8.4.1 and in (Sihlangu et al, 2017). The $\%\Delta k/k$ is shown for mesh sizes $5 \times 5 \times 5$, $10 \times 10 \times 10$ and $20 \times 20 \times 20$ and shows no trend in relation to A or the mesh size. The mesh size of $5 \times 5 \times 5$ is assessed because the coarse grids show better convergence statistics. Since the core layer is a larger system, A is assessed up to the value of 1200. SAMS failed to calculate for $A = 1200$ for the $5 \times 5 \times 5$ mesh. For $A > 1200$, the convergence statistics for this mesh were the same, and an instance is shown in Figure 8-11.

The $\%\Delta k/k$ is shown in Figure 8-12 for mesh sizes $5 \times 5 \times 5$, $10 \times 10 \times 10$ and $20 \times 20 \times 20$ and shows no trend in relation to A or the mesh size.

```
F*(r) Convergence Statistics:
WARNING: Of the       45 F*(r) mesh intervals that scored tallies...
     0.00% of the F*(r) tallies contain more than 5% uncertainty;
     0.00% of the F*(r) tallies contain more than 10% uncertainty;
     0.00% of the F*(r) tallies contain more than 20% uncertainty; and
     0.00% of the F*(r) tallies contain more than 50% uncertainty.
```

Figure 8-11 Convergence statistics for the third active core layer, with a 5 × 5 × 5 mesh and $A > 1200$.

Figure 8-13 shows the percentage of tallies that scored more than fifty percent uncertainty. The 5 × 5 × 5 mesh converges at $A = 500$, the 10 × 10 × 10 mesh converges at $A = 100$ and the 20 × 20 × 20 mesh converges at $A = 400$. From these convergence points, zero percent of tallies scored more than 50% uncertainty.

Figure 8-14 shows the ratio of scored tallies to the total voxels. The 5 × 5 × 5 mesh converges at $A = 500$, the 10 × 10 × 10 mesh converges at $A = 200$ and the 20 × 20 × 20 mesh converges at $A = 200$. The ratio of voxels that scored tallies to the total voxels for the 5 × 5 × 5 mesh is constant at 0.36.

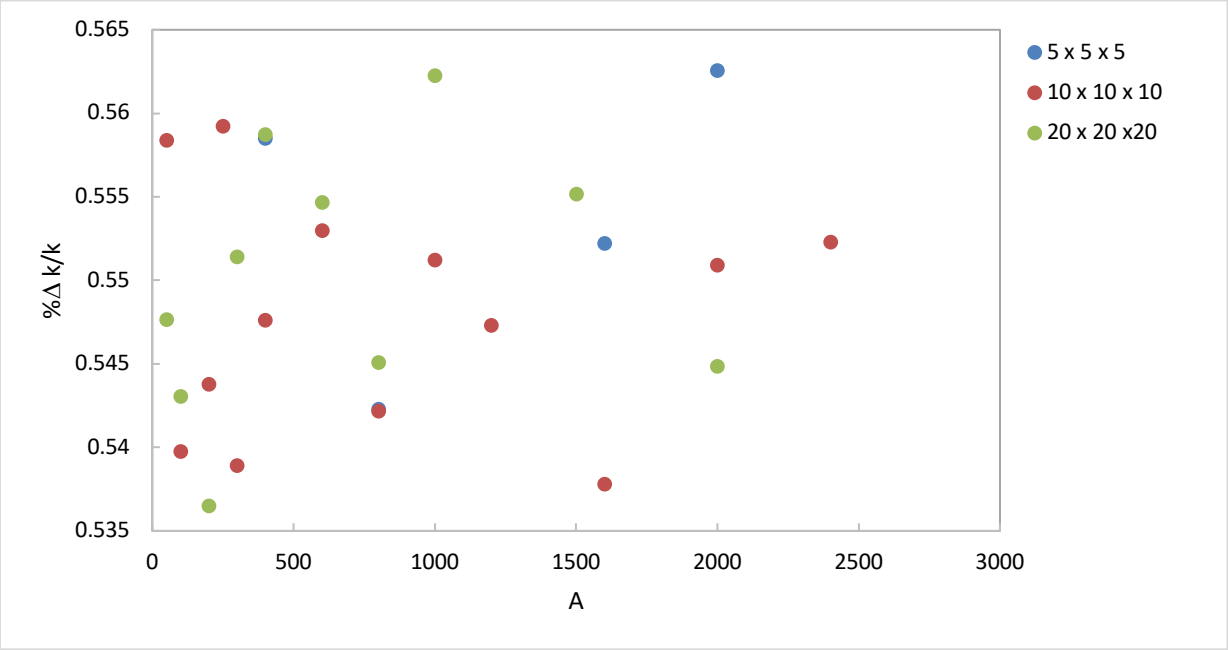

Figure 8-12 $\%\Delta k/k$ for the fuel block calculation of the HTTR.

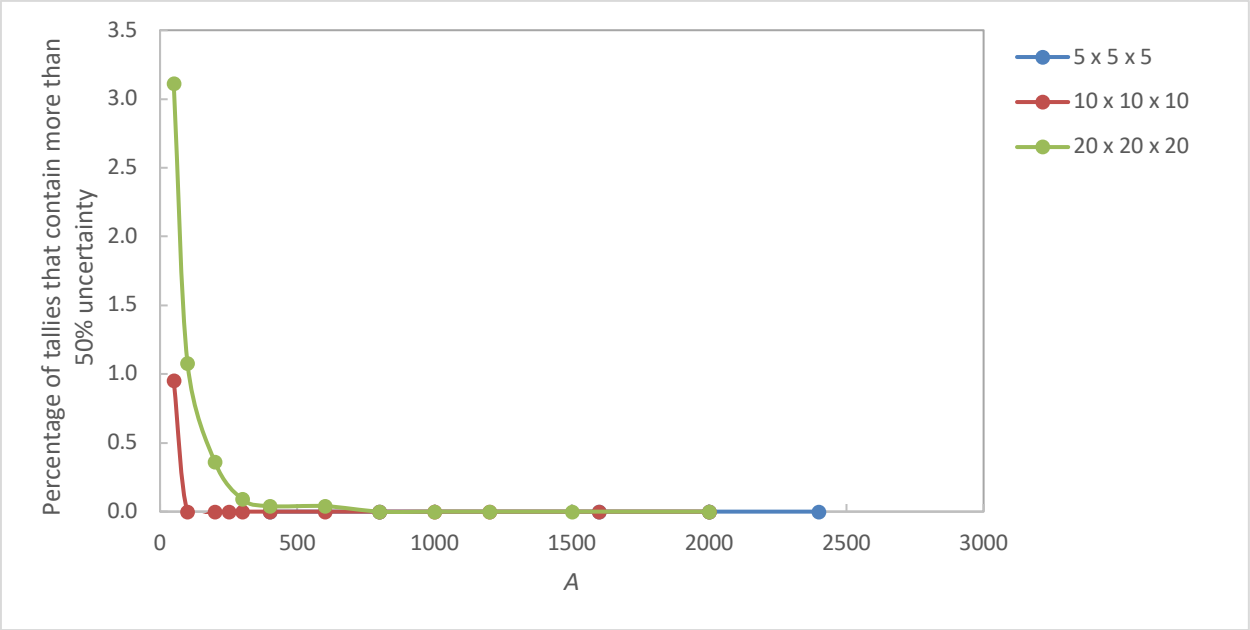

Figure 8-13 Percentage of tallies that scored more than 50% uncertainty.

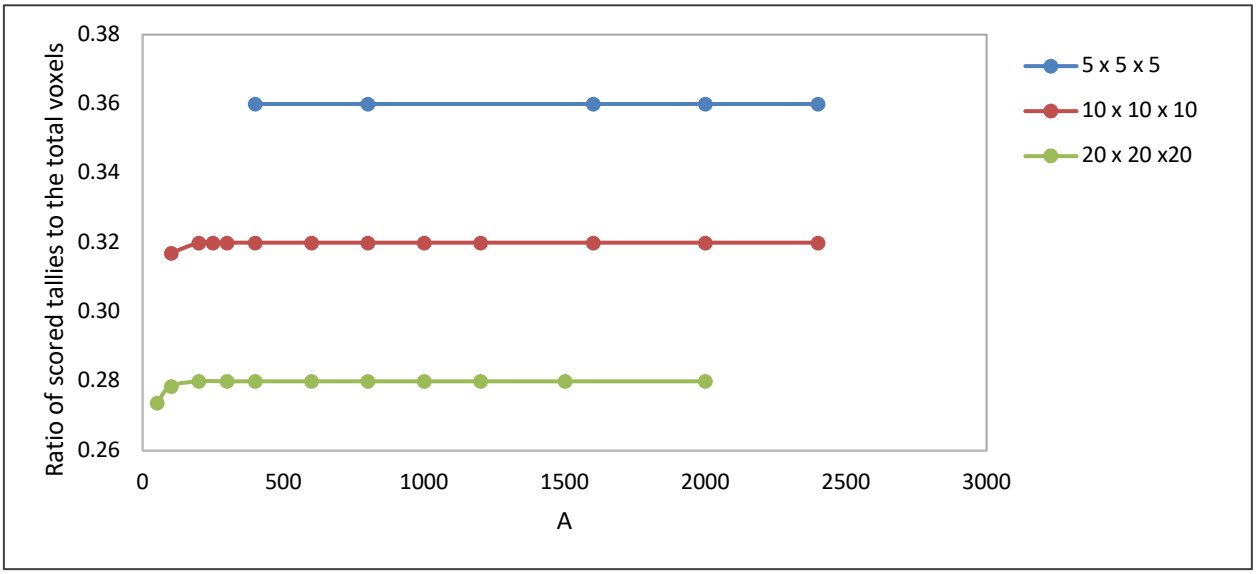

Figure 8-14 Ratio of voxels that scored tallies.

The $5 \times 5 \times 5$ mesh is the recommended mesh, although it requires a higher value of A. This grid requires less generations to converge. However, to be consistent with the other systems (Section 6.4.1, Section 6.4.2, and Section 8.4.1), the $10 \times 10 \times 10$ mesh is selected for calculations presented in this work.

8.5 Comparison of $F^*(\vec{r})$ convergence between the HTTR and the MHTGR-350

The value of the parameters that converged for the MHTGR-350 fuel block are the same as the value of the parameters for the HTTR fuel block. The HTTR core slice also produced convergence parameters in agreement with the fuel block model. Thus, with the HTTR system showing similar convergence behaviour to the MHTGR-350 system presented in Section 6.4, the CE TSUNAMI-3D parameters necessary for convergence are the same regardless of the HTGR system. An $F^*(\vec{r})$ convergence study could not be completed for the full core HTTR model, due to limited computer resources in terms of the number of machines available. The full core CE TSUNAMI model takes a long time to execute. Therefore, it was assumed the full core model required the same convergence parameters:

- Coarse meshes rather than fine meshes are preferred for the spatial definition of the $F^*(\vec{r})$.
- Meshes less than $20 \times 20 \times 20$ are recommended due to time constraints.
- The parameter A should be set to be equal to or greater than 200 depending on the mesh size.

The convergence parameters that are recommended and are used in this work are summarized in Table 8-6.

At this point, a note should also be made on the methodology that was developed to study the $F^*(\vec{r})$ convergence. Since both the HTTR and MHTGR-350 gives similar trends in the figures and also the same parameters for convergence, it indicates that this methodology can be considered to be adequate in terms of application to HTR systems. It was mentioned in the previous sections that SAMS failed to execute for certain cases. This could then be due to numerical instabilities or other aspects of numerical analysis rather than the methodology used.

Table 8-6 TSUNAMI convergence parameters

	A	Mesh
HTTR		
Fuel Block	200	$10 \times 10 \times 10$
Single Active Core Layer	200	$10 \times 10 \times 10$
MHTGR-350		
Fuel Compact	200	$10 \times 10 \times 10$
Single Fuel block	200	$10 \times 10 \times 10$

8.6 Sensitivity and uncertainty analysis of the HTTR fuel pin, block and core layer

8.6.1 Fuel pin UQ and fuel block UQ.

The fuel pin model of the HTTR was constructed manually since NWURCS does not have the capability of generating fuel pin models. The fuel pin is modelled with 6.3% fuel enrichment, which is the average fuel enrichment. The findings for the fuel pin are $k_{\text{inf}} = 1.37235$ and the uncertainty due to nuclear data is 0.54775 $\%\frac{\Delta k}{k}$ with Δk being 750 pcm. Ho et al (2017) reports that the k_{inf} value for the HTTR fuel pin is 1.37478 using MCNP6 with the ENDF/B-VII.1 neutron data library, this value is approximately 200 pcm greater than the value found in this study.

The HTTR fuel pin value for k_{inf} computed in this thesis is very close to the MHTGR-350 value reported in Table 6-7 which was $k_{\text{inf}} = 1.372450$ and the uncertainty due to nuclear data for the MHTGR-350 fuel compact is 0.51200 (Table 6-12). The top six uncertainty contributors for the HTTR fuel rod are recorded in Table 8-7. The top contributor is the ^{235}U $(\bar{\nu})$ / ^{235}U $(\bar{\nu})$ nuclide-reaction pair, followed by the ^{238}U (n,γ) / ^{238}U (n,γ) contribution.

The 33-pin fuel block with fuel enrichment of 6.3% is modelled and the top 6 contributors to uncertainty are recorded in Table 8-7. The findings are $k_{\text{inf}} = 1.33263 \pm 0.00016$ and $\%\frac{\Delta k}{k} = 0.51359 \pm 0.0023$ with $\Delta k = 684$ pcm.

The top six uncertainty contributors are compared for the fuel pin and fuel block of the HTTR using the percentage difference (Equation 5.14) and is shown in Table 8-7. An analysis was presented in Section 6.6.2 (for the MHTGR-350) where it was shown that when going from the compact to the fuel block, the ratio of the number densities between the uranium and graphite isotopes changes. The subsequent uncertainty contributions then also changed. A similar analysis can be applied to the HTTR cases. Therefore, the discussion is presented with comparison of the HTTR results with that of the MHTGR-350 results. The HTTR fuel pin and MHTGR-350 fuel compact are shown in Figure 8-15 (a) and Figure 8-15 (b) respectively. The HTTR fuel block and MHTGR-350 single fuel block are shown in Figure 8-16 (a) and Figure 8-16 (b) respectively. The order of the top six uncertainty contributors for the HTTR is shown in Table 8-7 and the top six contributors for the MHTGR-350 which were shown in Table 6-14 are also shown in Table 8-7. The order of the top six contributors for HTTR fuel pin is consistent with the order of the contributors of the MHTGR-350 fuel compact and single fuel block. The order changes slightly for the HTTR fuel block and this slight change is seen between the c-graphite elastic/ c-graphite elastic contribution and the ^{235}U fission/ ^{235}U (n,γ) contribution.

The $\%\Delta k/k$ contribution of ^{235}U ($\bar{\nu}$) / ^{235}U ($\bar{\nu}$) remains the top contributor and does not change very much between the HTTR fuel pin and HTTR fuel block. The ^{235}U ($\bar{\nu}$) / ^{235}U ($\bar{\nu}$) contribution increases slightly by a percentage difference of 1.48% from the HTTR fuel pin to the HTTR fuel block. This difference is consistent with the findings for the MHTGR-350 system, where the ^{235}U ($\bar{\nu}$) / ^{235}U ($\bar{\nu}$) contribution slightly increases by 1.67% from the fuel compact to the fuel block.

The ^{238}U (n,γ) / ^{238}U (n,γ) contribution decreases by 34.38% from the HTTR fuel pin to HTTR fuel block, this is consistent with the MHTGR-350 fuel compact and fuel block with the percentage difference being 30.39%.

Table 8-7 The top six contributors to uncertainty for the fuel compact and fuel block for the ENDF/B-VII.1 library

HTTR						
Nuclide-reaction pairs		Fuel Pin		Fuel Block		$\%diff$
		Rank	$\%\Delta\boldsymbol{k/k}$	**Rank**	$\%\Delta\boldsymbol{k/k}$	
^{235}U ($\bar{\nu}$)	^{235}U ($\bar{\nu}$)	1	0.3686	1	0.3741	1.48
^{238}U (n,γ)	^{238}U (n,γ)	2	0.2778	2	0.1964	34.38
^{235}U (n,γ)	^{235}U (n,γ)	3	0.2024	3	0.1853	8.88
c-graphite elastic	c-graphite elastic	4	0.1383	5	0.1193	32.10
^{235}U fission	^{235}U (n,γ)	5	0.1069	4	0.1198	11.34
^{235}U fission	^{235}U fission	6	0.0718	6	0.0972	30.09
MHTGR-350						
Nuclide-reaction pairs		Fuel Compact		Fuel Block		$\%diff$
		Rank	$\%\Delta\boldsymbol{k/k}$	**Rank**	$\%\Delta\boldsymbol{k/k}$	
^{235}U ($\bar{\boldsymbol{\nu}}$)	^{235}U ($\bar{\nu}$)	1	0.3511	1	0.3570	1.67
^{238}U (n,γ)	^{238}U (n,γ)	2	0.2694	2	0.1983	30.39
^{235}U (n,γ)	^{235}U (n, γ)	3	0.2278	3	0.1783	24.47
c-graphite elastic	c-graphite elastic	4	0.1458	4	0.1568	7.27
^{235}U fission	^{235}U (n, γ)	5	0.1011	5	0.1191	16.35
^{235}U fission	^{235}U fission	6	0.0683	6	0.1111	47.71

The ^{235}U (n,γ) / ^{235}U (n,γ) contribution decreases between HTTR fuel pin and HTTR fuel block by 8.88%, whilst in the MHTGR-350 the percentage difference was recorded to be 24.47%. The percentage difference is larger for the MHTGR-350 case, and this could be because the fuel enrichment is higher for the MHTGR-350 (15.5 wt%) than the HTTR (6.3 wt% enrichment).

From Figure 8-16 (a), it can be seen that the HTTR system has more graphite in the single fuel block than in the unit cell, which is the same for the MHTGR-350 (Figure 8-16 (b)). However, contrary to the MHTGR-350, the c-graphite elastic / c-graphite elastic contribution for the HTTR is now lower for the fuel block than the fuel pin at a percentage difference of 32.10%. Given that the enrichment of the uranium oxide in terms of ^{235}U is higher for the MHTGR-350 in comparison with the HTTR, the relative amount of ^{238}U would be higher in the HTTR system. It is therefore being shown that the interplay between the uranium and carbon number density ratio and the enrichment of the uranium influences the amount of the contributions of the various components to the uncertainty. However, other as yet undetermined factors are also most probably in play.

The ^{235}U fission / ^{235}U (n,γ) contribution increases by 11.34% for the HTTR system between the fuel pin and the fuel block. In the MHTGR-350, the percentage difference is 16.35%. ^{235}U fission / ^{235}U fission contribution increases by 30.09% from the HTTR fuel pin to the HTTR fuel block and increases by 47.71% between the MHTGR 350 fuel compact and block. Once again, these differences observed could be due to the interplay between the enrichment of uranium and the uranium and graphite number density ratio.

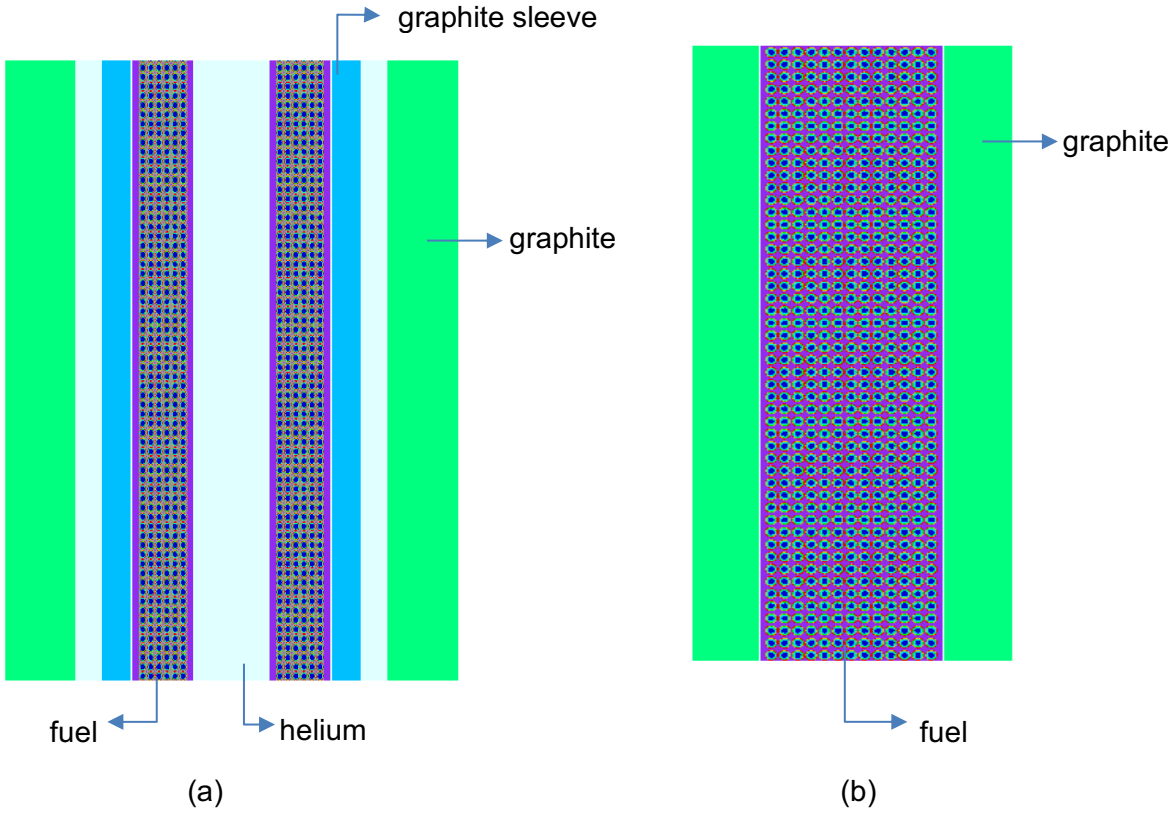

Figure 8-15 (a) Portion of the HTTR fuel pin and (b) MHTGR-350 fuel compact.

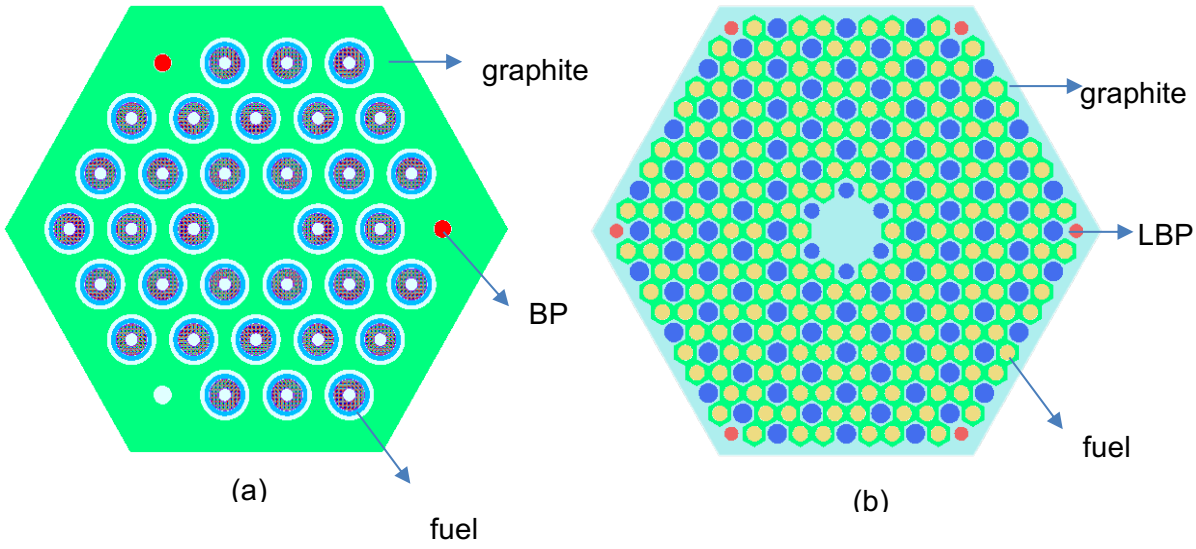

Figure 8-16 Cross sectional view of the (a) HTTR fuel block and (b) MHTGR-350 single fuel block.

8.6.2 HTTR Single fuel row UQ

As an intermediate model between the HTTR fuel block and the HTTR critical full core model, the UA is performed on an HTTR single fuel row. The third fuel row (i.e. fifth core layer) is chosen and is shown in Figure 8-17. The top and bottom planes are modelled as reflective planes. Control rods are also modelled, and due to the reflective planes at the top and bottom, the effect of the control rods on absorption will be greater than when modelled in the full core. The resulting k_{inf} value is 0.90697 (16).

The values of $\%\Delta k/k$ for the top 6 contributors to the uncertainty are recorded. The relative standard deviation ($\%\Delta k/k$) is 0.56106% and the corresponding Δk value is 509 pcm.

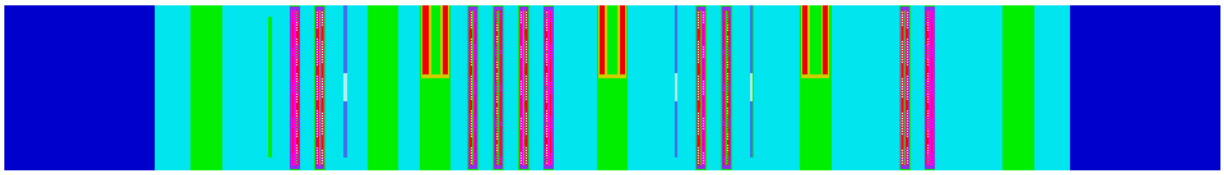

Figure 8-17 Third fuel row with control rods placed at the critical positions.

As shown in Table 8-8, the number 1 uncertainty contributor is ^{235}U ($\bar{\nu}$) / ^{235}U ($\bar{\nu}$), this is consistent with the fuel pin and fuel block in Section 8.6.1. The ^{235}U ($\bar{\nu}$) / ^{235}U ($\bar{\nu}$) contribution increased between the HTTR fuel pin and fuel block. It also increases from the fuel block to the single core layer.

Table 8-8 Top six uncertainty contributors for the fuel row of the HTTR full core benchmark model using ENDF/B-VII.1

Rank	**Nuclide-reaction pairs**		$\%\Delta \boldsymbol{k/k}$
1	^{235}U ($\bar{\nu}$)	^{235}U ($\bar{\nu}$)	0.37452
2	c-graphite elastic	c-graphite elastic	0.20340
3	c-graphite (n,γ)	c-graphite (n,γ)	0.18746
4	^{238}U (n,γ)	^{238}U (n,γ)	0.16258
5	^{235}U (n,γ)	^{235}U (n,γ)	0.15816
6	^{235}U fission	^{235}U fission	0.13312

The second contribution in Table 8-8 is c-graphite elastic / c-graphite elastic and the third contribution is c-graphite (n,γ) / c-graphite (n,γ). Compared to the HTTR fuel block uncertainty contributors in Table 8-7, the c-graphite elastic contribution is considerably higher for the core layer than it is for the fuel block. This is most probably due to the increase in the graphite of the system since the third fuel layer of the core also contains graphite blocks and the permanent reflector in addition to the fuel. This core layer has a control rod as shown in in Figure 8-17. The alloy cladding of the control rod also has carbon.

In Figure 8-18 the top uncertainty contributors are compared for the HTTR 3rd active fuel layer to the HTTR fuel block (Table 8-7). The $\%\Delta k/k$ values for the ^{235}U (n,γ) / ^{235}U (n,γ) contribution and for the ^{238}U (n,γ) / ^{238}U (n,γ) contribution are lower for the core layer than for the fuel block. Once again, these changes can be understood in terms of the change in the ratio of the number of isotopes of the uranium and carbon going from the fuel block to the active fuel layer of the core.

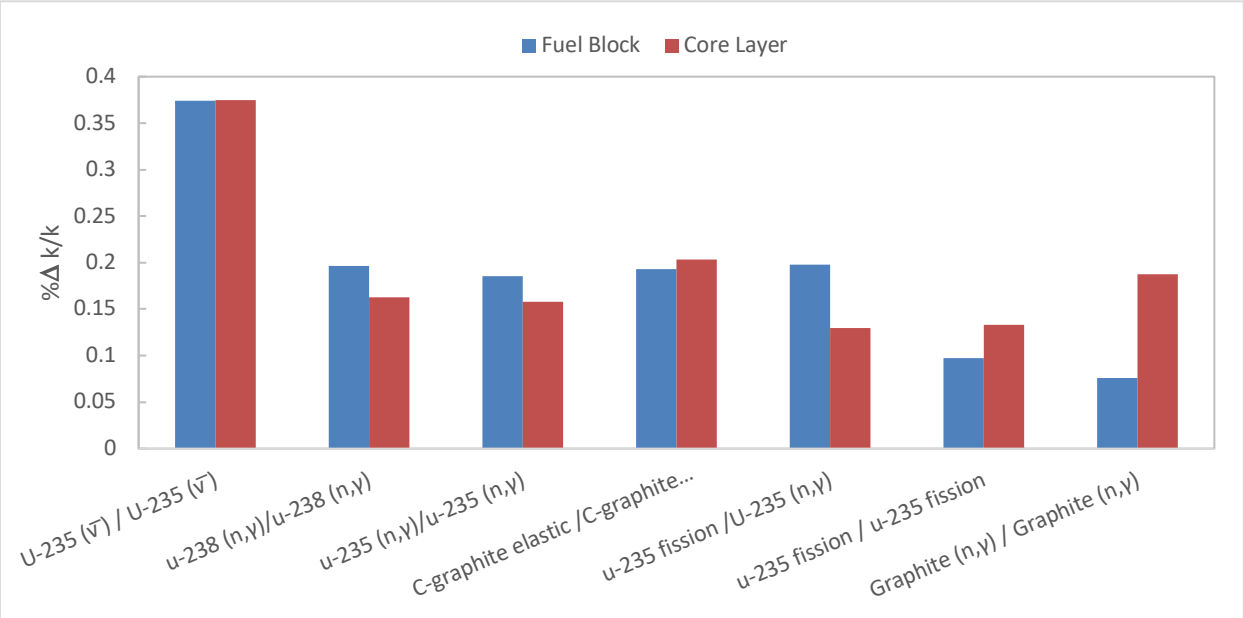

Figure 8-18 Top contributions to uncertainty for the HTTR fuel block and core layer.

8.7 Uncertainty quantification for the core models.

Three full core models are built using NWURCS based on the HTTR benchmark model, which are:

- the critical model;
- the subcritical model; and
- the supercritical model.

For the critical model, the control rods are placed as stipulated in HTTR-GCR-RESR-001. The uncertainty of the full core critical model is quantified for the two different nuclear data libraries. For the subcritical model, the control rods are placed 10 cm below the fuel. The subcritical and supercritical models are only executed using the ENDF/B-VII.1 library since the subcritical model with the ENDF/B-VII.0 library failed to execute. The supercritical model is defined by the removal of the control rods. The reader should note that this is not the benchmark definition of the super critical model defined in HTTR-GCR-RESR-001. The value of k_{eff} for the supercritical model using the ENDF/B-VII.1 library is 1.14972. The k_{eff} values for the critical and supercritical HTTR models were reported in Section 8.3.1.

8.7.1 Critical full core uncertainty quantification

The values of $\%\Delta k/k$ are shown in Table 8-9 for the three cores. The subcritical core has the highest value of $\%\Delta k/k$ and the supercritical model has the lowest value. This difference in the subcritical and supercritical models is likely due to the presence of the alloy material of the control rods. The difference, (calculated from Equation 5.12) between the $\%\Delta k/k$ of the critical and subcritical core is 0.07325 and the corresponding percentage difference (calculated from Equation 5.14) is 11.92%. The difference between the $\%\Delta k/k$ of the critical and supercritical core is 0.02102 and the corresponding percentage difference is 3.67%. The difference between the $\%\Delta k/k$ of the supercritical and subcritical core is 0.09427 and the corresponding percentage difference is 15.49%.

Table 8-9 Value of Δk and $\%\Delta k/k$, for the critical, subcritical and supercritical HTTR core.

Library	**System**	$\boldsymbol{\Delta k}$	$\boldsymbol{\%\Delta k/k}$
ENDF/B-VII.0	Critical	0.00587	0.57332
ENDF/B-VII.1	Critical	0.00590	0.58265
	Subcritical	0.00451	0.65590
	Supercritical	0.00646	0.56163

The difference (calculated from Equation 5.12) between the Δk values (in Table 8-9) of the supercritical and the subcritical model is 195 pcm. Again the difference is a result of the presence of the control rods. The ENDF/B-VII.0 and ENDF/B-VII.1 produce similar Δk and $\%\Delta k/k$ results for the critical HTTR core as shown in Table 8-10, with the ENDF/B-VII.0 results being slightly lower than the ENDF/B-VII.1. Furthermore, it should again be noted again that this difference of 3 pcm is well within the statistical uncertainty due to the Monte Carlo as modelled in this work.

The top six uncertainty contributors are compared for the critical model with two different libraries. This comparison is shown in Table 8-10. The top contributor in Table 8-10 to uncertainty is ^{235}U ($\bar{\nu}$) / U^{235} ($\bar{\nu}$) followed by c-graphite (n,γ) / c-graphite (n,γ). The order of the first 6 uncertainty contributors is consistent between ENDF/B-VII.0 and ENDF/B-VII.1. The differences between the two libraries are insignificant for the uranium nuclide-reaction pairs but are large for the c-graphite nuclide-reaction pairs. This is expected since the ENDF/B-VII.1 library has updated c-graphite capture cross sections.

Table 8-10 Top six uncertainty contributors for the ENDF/B-VII.0 and ENDF/B-VII.1 critical core model

Rank	**Nuclide-reaction pairs**		$\%\Delta k/k$		
			ENDF/B-VII.0	**ENDF/B-VII.1**	$\%diff$
1	^{235}U ($\bar{\nu}$)	^{235}U ($\bar{\nu}$)	0.37692	0.37680	0.03
2	c-graphite (n,γ)	c-graphite (n,γ)	0.24043	0.25649	6.46
3	^{238}U (n,γ)	^{238}U (n,γ)	0.17815	0.17798	0.01
4	c-graphite elastic	c-graphite elastic	0.16198	0.17035	5.04
5	^{235}U (n,γ)	^{235}U (n,γ)	0.16128	0.16027	0.63
6	^{235}U fission	^{235}U fission	0.13308	0.13418	0.82

The ENDF/B-VII.1 library causes an increase of 6.64% for c-graphite (n,γ) / c-graphite (n,γ) contribution when compared to the ENDF/B-VII.0 library. Whilst c-graphite elastic / c-graphite elastic increases by 5.04%. The contributors and their rank for graphite are isolated and are shown in Table 8-11. The percentage difference between the two libraries is calculated and shown in Table 8-11.

From Table 8-11, the largest percentage difference is seen for c-graphite (n,γ) / c-graphite (n,n'), which has a percentage difference of 41.48% between the two nuclear data libraries. However, c-graphite (n,γ) / c-graphite (n,n') only ranks 68th, therefore its contribution is of negligible importance. Large differences are also seen in the c-graphite (n,n') / c-graphite (n,n') contribution as well as c-graphite (n,γ) / c-graphite (n,γ) contribution with the differences being 8.03% and 6.46% respectively.

Table 8-11 Top graphite contributors to uncertainty for the ENDF/B-VII.0 and ENDF/B-VII.1 critical core model

Rank	**Nuclide-reaction pairs**		$\%\Delta k/k$		
			ENDF/B-VII.0	**ENDF/B-VII.1**	$\%diff$
2	c-graphite (n,γ)	c-graphite (n,γ)	0.24043	0.25649	6.46
4	c-graphite *elastic*	c-graphite *elastic*	0.16198	0.17035	5.04
9	c-graphite (n,n')	c-graphite (n,n')	0.31119	0.33723	8.03
11	c-graphite elastic	c-graphite (n,n')	-0.02869	-0.02787	2.89
15	c-graphite (n,α)	c-graphite (n,α)	0.007943	0.007830	1.46
21	c-graphite (n,α)	c-graphite (n,n')	0.004462	0.004556	2.07
68	c-graphite (n,γ)	c-graphite (n,n')	5.0423E-05	7.6809E-05	41.48

The sensitivity plots and their integrals are shown for c-graphite (n,n') and c-graphite (n,γ) in Figure 8-19 and Figure 8-20. The plots are shown for the ENDF/B-VII.0 and ENDF/B-VII.1 library. These plots show significant differences in the sensitivity profiles of c-graphite (n,γ) and c-graphite (n,n'). From Section 8.3.1, the k_{eff} difference between the two libraries is 1145 pcm and from Table 8-11. These differences are as a result of updates in the c-graphite (n,γ) and c-graphite (n,n') cross sections, which are shown in Figure 8-21 and Figure 8-22. The data used to produce Figure 8-21 and Figure 8-22 is taken from the IAEA Nuclear Data Services (*https://www-nds.iaea.org*). The data extracted from this site shows that the c-graphite (n,α) and c-graphite elastic cross sections have not been updated. However, the increase in the c-graphite elastic / c-graphite elastic contribution indicates that some aspect of the data could have been updated, possibly the covariance data.

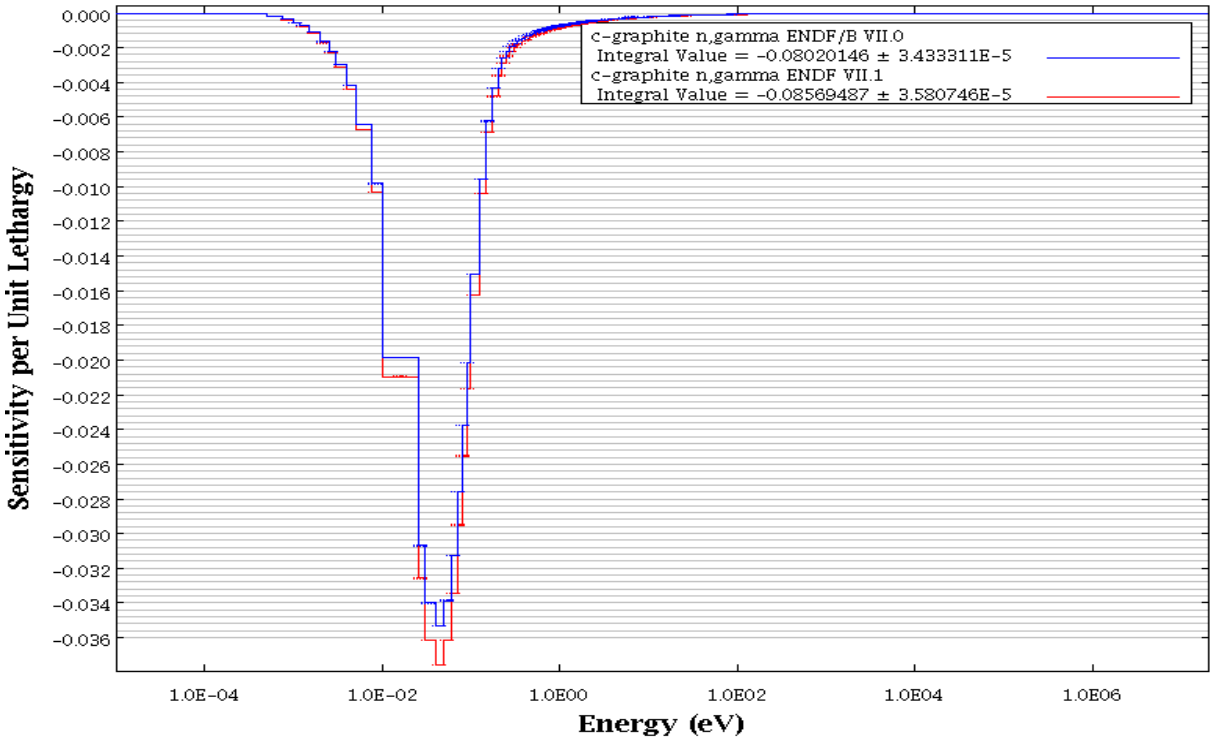

Figure 8-19 k_{eff} sensitivity profile for c-graphite (n, γ) for the ENDF/B-VII.0 and ENDF-VII.1.

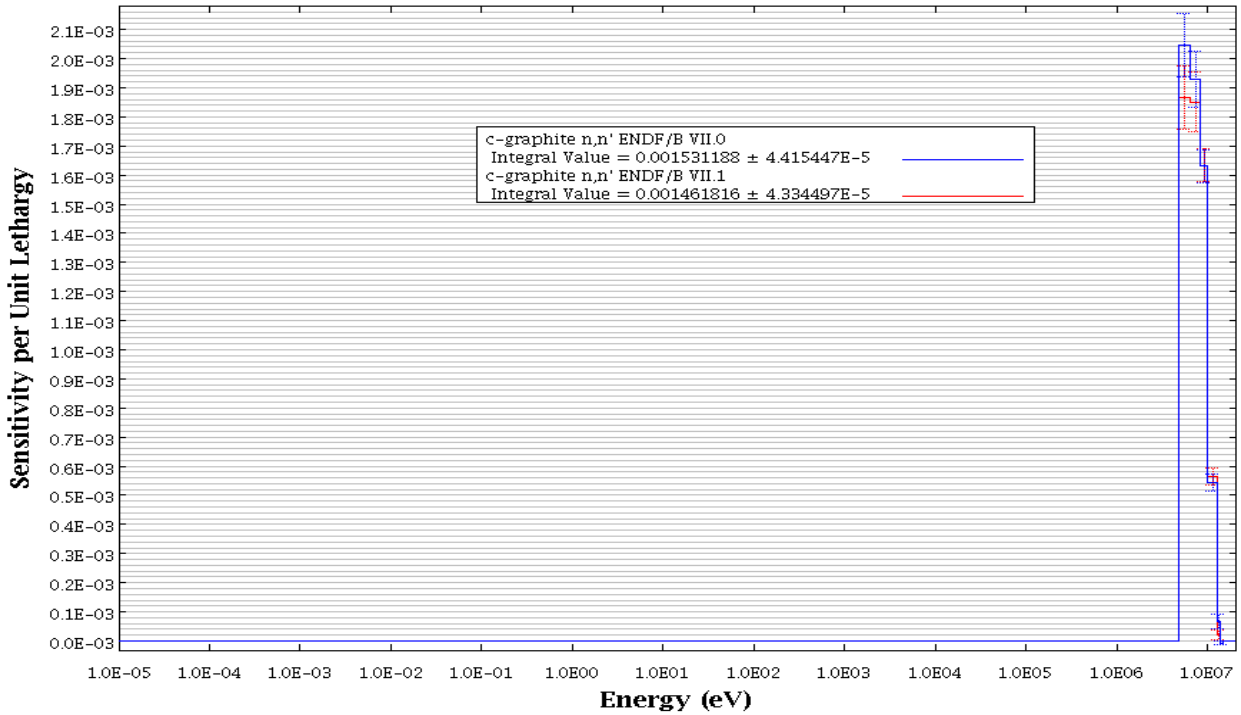

Figure 8-20 k_{eff} sensitivity profile for c-graphite (n, n') for the ENDF/B-VII.0 and ENDF-VII.1.

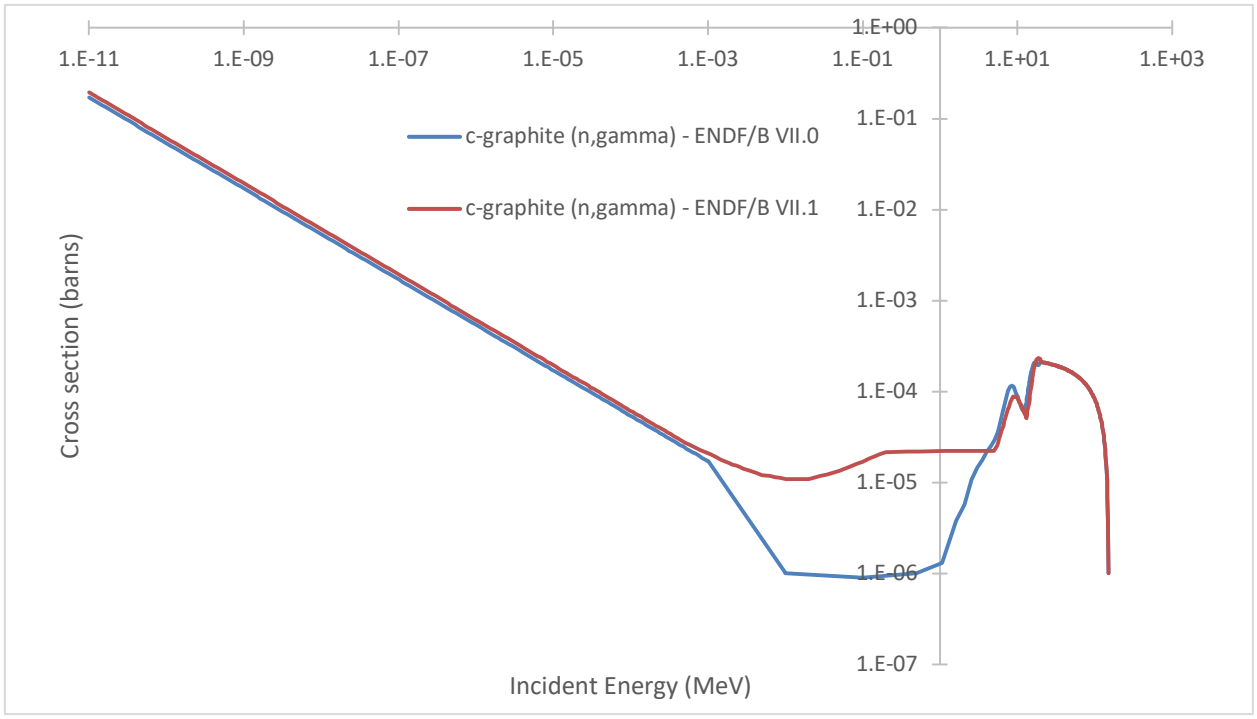

Figure 8-21 C-graphite (n, γ) cross section for the ENDF/B-VII.0 and ENDF/B-VII.1 library.

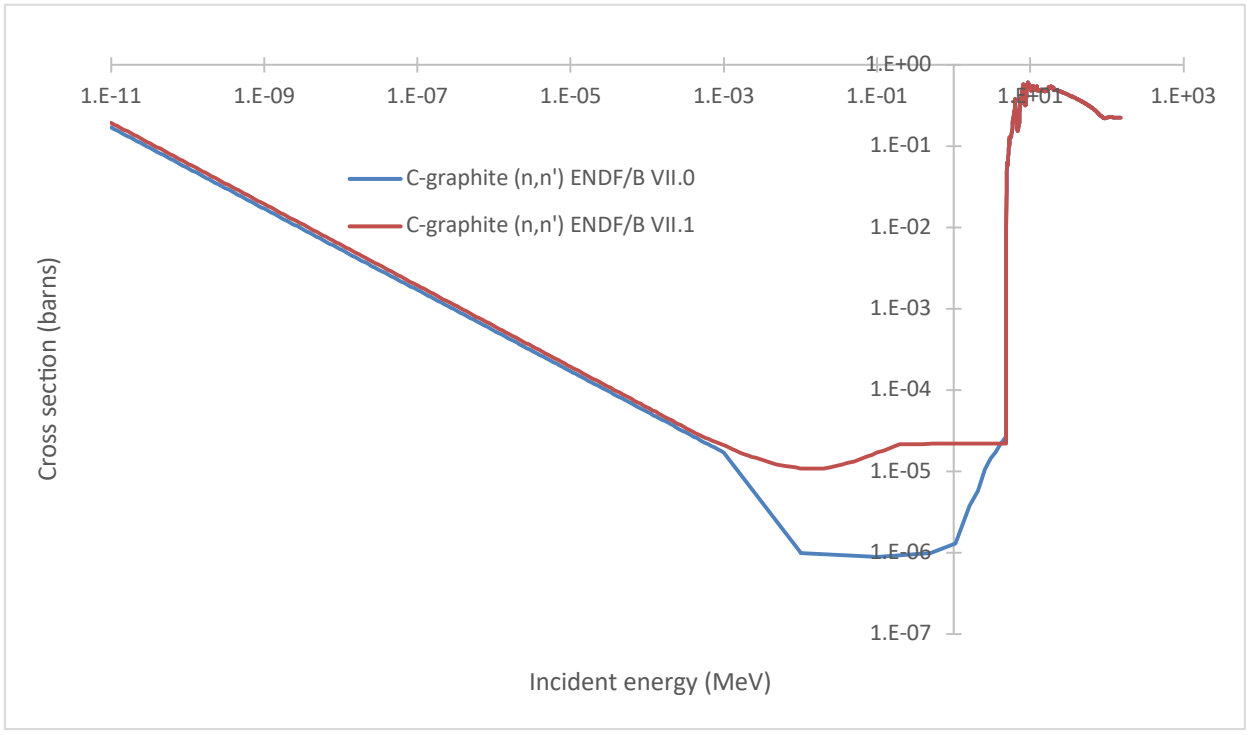

Figure 8-22 C-graphite (n, n') cross section for the ENDF/B-VII.0 and ENDF/B-VII.1 library.

8.7.2 Subcritical full core uncertainty quantification

Table 8-12 shows the highest uncertainty contributor to be c-graphite elastic / c-graphite elastic for the HTTR subcritical core model. All the previous results in Table 8-7, Table 8-8 and Table 8-10 showed ^{235}U ($\bar{\nu}$) as the top uncertainty contributor. In the critical HTTR core, the c-graphite elastic / c-graphite elastic contribution was 0.17035 (Table 8-10) whilst in the subcritical core the contribution is 0.40988. In the subcritical model, the c-graphite elastic contribution increases by a percentage difference of 82.5% compared to the critical model. This increase is most probably due to the presence of graphite in the alloy cladding of the control rods (see Figure 4.19 (b)).

When the control rods are not present, the control holes are filled with He, with a very low density. Introduction of the control rods therefore introduced a significant amount of graphite into the system. This effect of the graphite number density (in terms of the uranium number density) on the uncertainty contribution from the various contributors was also seen in Chapter 6 when the fuel pin was compared with the fuel block. Boron is also present, but the first uncertainty contributor associated with boron is ranked at the 17th position. It is ^{10}B (n,α) / ^{10}B (n,α) with a contribution of 7.5955E-03. The next contributor after this is ^{11}B elastic / ^{11}B elastic and it ranks 52th with a value of 8.9619E-04. However, it is noted that these contributors appear in the fuel block model (and single fuel row) as a result of the presence of boron in the BPs. Therefore, even with the control rods inserted in the HTTR full core model, boron does not play a significant role in the uncertainty contribution.

Table 8-12 Contributions to uncertainty for the full core subcritical HTTR

Library	**Rank**	**Nuclide-reaction pairs**		$\%\Delta k/k$
ENDF/B-VII.1	1	c-graphite elastic	c-graphite elastic	0.40998
	2	^{235}U ($\bar{\nu}$)	^{235}U ($\bar{\nu}$)	0.36933
	3	^{235}U (χ)	^{235}U (χ)	0.17103
	4	^{235}U (n,γ)	^{235}U (n,γ)	0.15010
	5	^{238}U (n,γ)	^{238}U (n,γ)	0.14799
	6	^{235}U fission	^{235}U fission	0.13662

In Table 8-10, the ^{235}U ($\bar{\nu}$) / ^{235}U ($\bar{\nu}$) contribution for the critical HTTR is 0.37680 whilst the ^{235}U ($\bar{\nu}$)/ ^{235}U ($\bar{\nu}$) contribution (shown in Table 8-12) for the subcritical HTTR is 0.36933. The percentage difference is 2%. Even with the presence of the control rods the value of the ^{235}U ($\bar{\nu}$)/ ^{235}U ($\bar{\nu}$) contribution is still unaffected.

The ^{235}U (χ) / ^{235}U (χ) contribution appears for the first time in the models analysed thus far, and it is present when the contribution from c-graphite seems to be strong. (χ is the fission neutron energy spectrum which was discussed in Section 2.1). This therefore cautions one in attempting to attribute the appearance of the contribution in terms of strength precisely to a given physical consideration. It also points out that more detailed analysis of the contributions is required, possibly in terms of the covariance data itself, and then in terms of the neutron transport phenomena and the manner in which they are mathematically represented. This would include the mathematical foundations for the uncertainty propagation analysis. In terms of the covariance data, one needs to realize that the data depends on many parameters, including energy, and therefore the analysis would not be straight forward. Therefore, given the experience gained in this study in terms of research hours required, such analyses are deemed to be beyond the scope of the work, and should be carried out as separate projects.

8.7.3 Supercritical full core uncertainty quantification

The top six contributors for the supercritical core model are shown in Table 8-13. The top contributor is the ^{235}U ($\bar{\nu}$) nuclide-reaction pair, as also seen in the critical model. The c-graphite elastic contribution is 0.15389 in Table 8-13. In Table 8-12 (subcritical model), the c-graphite elastic contribution is 0.40988. The percentage difference for the c-graphite elastic contribution between the subcritical and the supercritical HTTR core is 90.81%. In Table 8-10 (critical model), the c-graphite elastic contribution is 0.17035. The percentage difference for the c-graphite elastic contribution between the critical and the supercritical HTTR core contribution is 10.81%. The supercritical c-graphite elastic contribution is lower than the critical core and the subcritical core. In the supercritical model, the amount of c-graphite is further reduced (by virtue of the control rods being pulled out even further). The trend of the c-graphite elastic / c-graphite elastic uncertainty contribution is therefore clear to see. It increases from the supercritical to the critical and further increases to the subcritical, or in terms of the control rod, the c-graphite elastic / c-graphite elastic uncertainty contribution increases as the control rods move into the core. This trend in the uncertainty contribution is significant in the analysis of the uncertainty of the reactor calculations from the viewpoint of the amount of c-graphite present and also in terms of determining the uncertainty associated with the analysis of control rod movement.

The sensitivity profile for c-graphite elastic is shown in Figure 8-23 for the critical, subcritical and supercritical HTTR core. The supercritical core has the lowest sensitivity integral value for c-graphite elastic compared to the critical and subcritical core. The sensitivity integral for the supercritical HTTR core is 0.3094187. The subcritical core has the highest integral value, which is 0.8178804. The percentage difference between the subcritical and supercritical core integrals is 90.22%. The integral value for the critical core c-graphite elastic is 0.3420723. The percentage

difference between the critical and supercritical core integral values is 10.02%. It is also observed that the increase in the sensitivity is consistent over the entire energy range. This is visually clear when comparing the subcritical spectrum (red) with the other two.

Table 8-13 Top uncertainty contributors for the HTTR model with no control rods.

Library	Rank	Nuclide-reaction pairs		$\%\Delta k/k$
ENDF/B-VII.1	1	^{235}U $(\bar{\nu})$	^{235}U $(\bar{\nu})$	0.37576
	2	c-graphite (n,γ)	c-graphite (n,γ)	0.24523
	3	^{235}U (n,γ)	^{235}U (n,γ)	0.17457
	4	c-graphite elastic	c-graphite elastic	0.15389
	5	^{238}U (n,γ)	^{238}U (n,γ)	0.15067
	6	^{235}U fission	^{235}U fission	0.12607

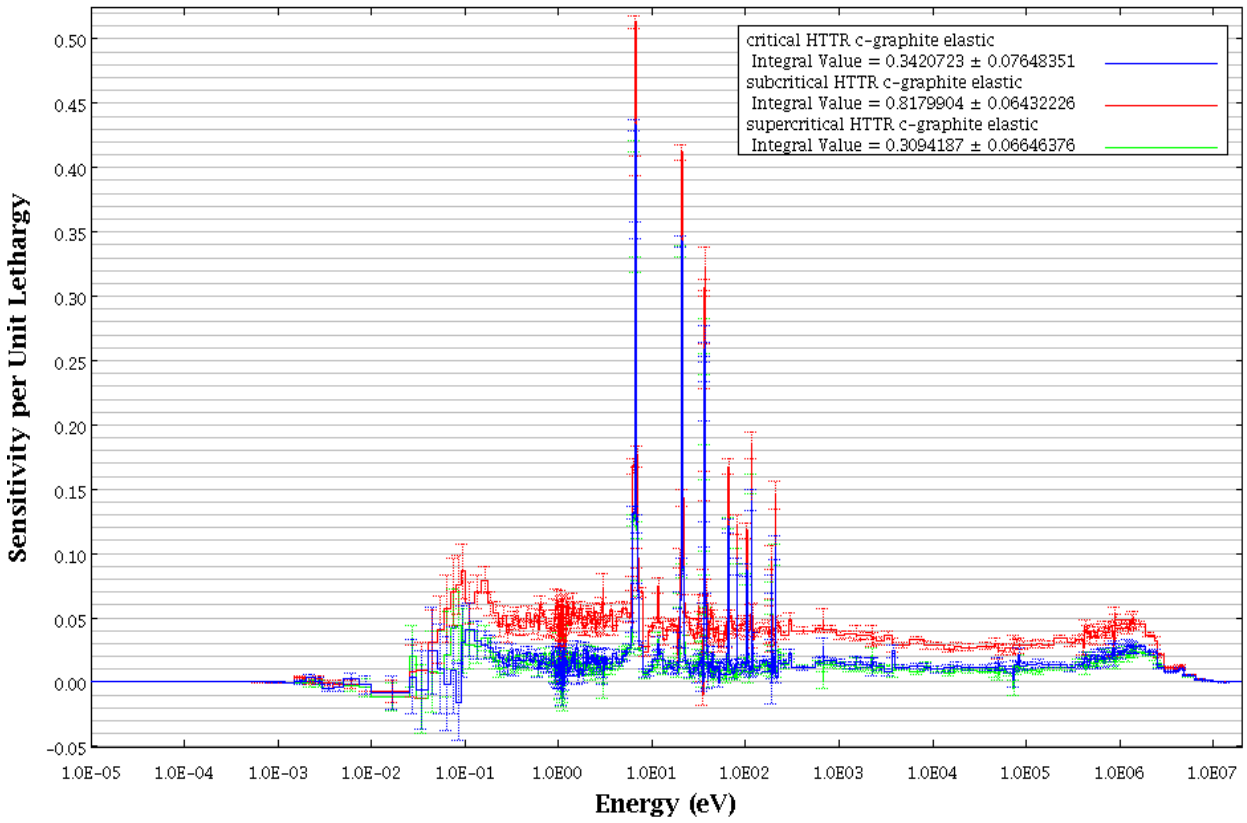

Figure 8-23 C-graphite elastic sensitivity profiles for the HTTR benchmark model.

8.7.4 Comparison of critical, subcritical and supercritical HTTR.

The $\%\Delta k/k$ value of the ^{235}U $(\bar{\nu})/$ ^{235}U $(\bar{\nu})$ contribution is 0.36 to 0.38 for all the HTTR systems. The value of the ^{235}U $(\bar{\nu})/$ ^{235}U $(\bar{\nu})$ contribution for the MHTGR fuel block and fuel compact is approximately 0.35. Bostelmann and Strydom (2017) also found that the ^{235}U $(\bar{\nu})/$ ^{235}U $(\bar{\nu})$ $\%\Delta k/k$ value to be 0.37 to 0.38 for the VHTRC fuel compact, fuel unit cell, fuel block and the full core. Hao et al (2018) reports the ^{235}U $(\bar{\nu})/$ ^{235}U $(\bar{\nu})$ contribution to be 0.3802 for the pebble-bed HTR-10 initial critical core model.

Naicker et al (2016) reported the ^{235}U $(\bar{\nu})$ / ^{235}U $(\bar{\nu})$ contribution to be approximately 0.27 for the homogeneous MHTGR-350 fuel compact using the ENDF/B-VII.0 library (44 group covariance library) and Bostelmann, Strydom et al (2016) reported a similar value for the ^{235}U $(\bar{\nu})$ contribution for the same system and same library.

Bostelmann and Strydom (2017) reported the VHTRC fuel compact ^{235}U $(\bar{\nu})$ contribution to be 0.29423 for the ENDF/B-VII.0 library (44 group covariance library) and 0.37308 for the ENDF/B-VII.1 (56 group covariance library). In this work there was no variation between the ^{235}U $(\bar{\nu})/$ ^{235}U $(\bar{\nu})$ contribution produced by the ENDF/B-VII.0 library and ENDF/B-VII.1 library since the 56 group covariance library was used for both libraries. The 56 group covariance library is the default in all SCALE 6.2 TSUNAMI calculations. Bostelmann and Strydom (2017) reported that there is an update in the ^{235}U $(\bar{\nu})$ covariance data. In the thermal region, the ^{235}U $(\bar{\nu})$ uncertainty was increased from 0.311 in the 44 group covariance library to 0.385 in the 56 group covariance library (Bostelmann and Strydom, 2017).

The ^{235}U $(\bar{\nu})/$ ^{235}U $(\bar{\nu})$ contribution is the highest contribution for almost all the HTTR systems with the exception of the subcritical model. In this model, the contribution of the c-graphite inelastic nuclide-reaction pair surpassed the ^{235}U $(\bar{\nu})/$ ^{235}U $(\bar{\nu})$. The presence of graphite in the control rod alloy cladding also has an effect on the c-graphite elastic contribution. However, the presence of the control rods also increases the contribution of ^{235}U (χ) / ^{235}U (χ) as seen in the subcritical model. ^{235}U (χ) / ^{235}U (χ) only appears in the top six contributors of the subcritical model. It ranks third.

The second dominant contribution in the critical and supercritical core is c-graphite (n,γ) / graphite (n,γ) whilst in the fuel block and fuel compact, the 2nd dominant contribution is ^{238}U $(n,\gamma)/$ ^{238}U (n,γ). This is as a result of the different isotopic number density ratios of uranium and graphite in fuel compact, fuel block and full core models.

8.8 NWURCS user experience

8.8.1 Advantages of using NWURCS

- NWURCS removed the task of assigning numbers for the units and arrays. Usually this is a simple task but for a complicated model such as the HTTR this can be a cumbersome process.
- The HTTR required 120 fuel blocks to be modelled. Using NWURCS made building and keeping track of the fuel blocks more manageable since each fuel block is written in its own file.
- NWURCS simplified moving the control rods up and down.

8.8.2 Disadvantages of NWURCS

- The calculation time of the NWURCS models is double that of the manually generated model.
- From a user perspective it took more time to build a NWURCS model than it would a manually generated model since the user still has to learn how to use NWURCS.
- NWURCS improved the manageability of building an HTTR input but did not improve the complexity of modelling the MHTGR-350. Further improvements are required to simplify input model generation for very complex systems if possible.
- Multigroup model generation capability is not as yet available.
- Because the HTTR is a very complex model, the output files were very large and they had to be split using a Fortran code so that they could be read using Notepad++, which is a Windows text editor. The output files were well over 1.0 gigabytes for the full core models.
- NWURCS cannot produce CE TSUNAMI inputs. So KENO-VI inputs are converted manually into CE TSUNAMI.

8.8.3 Issues with NWURCS v2.1

- The rods could not be placed at the subcritical position for the HTTR core. For the fuel block at the bottom layer of the core, the control rod hole does not extend through the entire length of the fuel block. The bottom of the block below the control rod hole must then be filled with non-movable graphite, and this is the origin of the computer bug. The code does work properly for control rod holes that extend through the entire length of the block.

- The material c-graphite is not programmed to the NWURCS's material specification so ^{12}C was selected. Once the input model has been generated by NWURCS then ^{12}C is changed manually.
- There is a bug with the reflector boundaries in the NWURCS generated input model, so boundaries have to be changed manually. However, if the user forgets to change this, the k_{inf} value becomes very low, and the error will be noticed and can be rectified.

8.8.4 Suggested improvements for the NWURCS input generator

Reduction of the size of the input file generated by NWURCS. Possible causes could be the duplication of surface definitions and the use of many lattice containing volumes for the compact instead of a single lattice. The duplication of surface definitions is illustrated in Figure 8-24. It can be seen that cylinder 10 and cylinder 30 are identical. The same applies to cylinder 40 and cylinder 50. In this case only cylinder 10 and cylinder 40 needed to be defined.

```
' ------------------------------------------------------------------------
unit 10
  cylinder   10   163.50000  58.00000   0.00000
  array   2   10  place  6  6  1   0.00000   0.00000   0.00000
  cylinder   30   163.50000  58.00000   0.00000
  cylinder   40   215.50000  58.00000   0.00000
  media       1  1   -30    40
  cylinder    50   215.50000  58.00000   0.00000
  boundary   50
' ------------------------------------------------------------------------
```

Figure 8-24 Example of NWURCS unit definition.

8.9 Chapter summary

- NWURCS v2.1 successfully modelled the critical HTTR benchmark model.
- The subcritical benchmark model could not be modelled sufficiently using NWURCS due to a coding bug.
- The parameters for $F^*(\vec{r})$ convergence were found to be standard for the MHTGR-350 and HTTR systems.
- Comparison of the HTTR and MHTGR-350 fuel blocks showed similar results for the top nuclide contributions to nuclear data uncertainty.
- The ENDF/B-VII.0 and ENDF/B-VII.1 showed significant differences in the graphite contributions.
- The critical and supercritical models produced comparable nuclear data uncertainties whilst the subcritical model produced different nuclear data uncertainties.

- The ^{235}U ($\bar{\nu}$) / ^{235}U ($\bar{\nu}$) contributor is the highest contributor for all HTTR systems apart from the subcritical model.
- In the subcritical model, the c-graphite elastic nuclide-reaction pair is the highest contributor to the nuclear data uncertainty.

CHAPTER 9: CONCLUSION AND RECOMMENDATIONS

This chapter concludes the research findings presented in this study and gives recommendations for future work. The double heterogeneity of the HTGR system requires specialised methods to model the HTGR accurately and quantify the uncertainty propagated due to nuclear data uncertainty. The MHTGR-350 is the chosen prismatic benchmark for the IAEA CRP on HTGR UAM. Uncertainty analysis methods and codes are applied to this benchmark. To validate the uncertainty results of the MHTGR-350 benchmark, an experimental reactor that is similar to the MHTGR-350 is chosen. In this work the HTTR was chosen and the neutronic similarity of these two systems can be assessed. This chapter begins by concluding the research findings from the MHTGR-350 system and proceeds to the research findings of the HTTR system uncertainty analysis. Their similarities are obtained in terms of nuclear data uncertainties and recommendations for future work are established. The MHTGR-350 system models were constructed manually whilst the HTTR system models were built using NWURCS. Thus the NWURCS capability to model HTGR systems is verified.

9.1 MHTGR-350 results

The MHTGR-350 systems studied are the heterogeneous fuel compact and a single heterogeneous fuel block. Uncertainties are propagated for these two systems. Prior to the propagation of nuclear data uncertainties, sensitivity studies coupled with convergence studies are performed. Convergence studies are required so that the results obtained are reliable, and the sensitivity studies leads to optimization of the models, which is also necessary in terms of time expenditure and other considerations. Therefore, the codes that perform uncertainty analysis, CE TSUNAMI and Sampler, must be converged and optimized. The uncertainty codes execute the transport codes (KENO-VI and Sampler), hence the transport codes are also optimized.

For the NEWT calculation of the heterogeneous fuel compact, a finer grid definition is required for the heterogeneous compact when compared to the homogeneous fuel compact. In the NEWT calculation of the fuel block, the local grids could not be refined to grids smaller than 4 x 4 and the response of $k_{\inf}$ to grid size variation is somewhat erratic. Utilising the partial unstructured CMFD acceleration allowed for further grid refinement whilst unstructured grid refinement caused NEWT to stop working at very fine grids. In terms of the uncertainty propagation, a total of 600 data perturbations in Sampler are found to be sufficient for the convergence of the relative standard deviation result and the convergence of the average multiplication factor.

In the CE treatment, modelling was assessed in terms of the packing and randomisation of the fuel TRISO particles. Jiggling the coated particles had no effect on the k_{inf} and also had no effect on the uncertainty propagated using nuclear data uncertainty.

Homogenization of the LBP causes a bias of more than 1500 pcm in the MG calculation when the CE calculation is taken as a reference case. This bias is as a result of a lack of self-shielding. Therefore, the modelling of the LBP was assessed. The LBP Trace method improves this bias by 1400 pcm. Homogenizing the LBP with a reduction in the boron concentration by 12% also produced a value of k_{inf} that is comparable to the CE model. All three LBP models produced nodal absorption and total cross sections that were close to each other in magnitude. This was because the number of LBP compacts defined in the single fuel block of the MHTGR-350 benchmark is only 6 (i.e. a small number). When the number of LBP compacts increased to 12, 24 and 48 then the differences between the nodal cross sections becomes more pronounced. The largest differences are seen at a BP compact number of 48. Homogenizing the LBP and reducing the boron concentration by 12% produced an uncertainty due to nuclear data uncertainties that was equivalent to the model with the doublehet LBP. However, it is still advisable to use the LBP Trace method, since the multiplication factor in the core calculation is expected to be different, depending on the model used for the LBP compacts.

The CLUTCH method in CE TSUNAMI-3D is chosen due to its capability to treat the double heterogeneity of the HTGR as well as its runtime performance and low memory usage. The accuracy of the CLUTCH method relies on the proper definition of the weighting function $F^*(\vec{r})$. $F^*(\vec{r})$ is specified in terms of spatial meshes and is converged before the sensitivity coefficients can be calculated. Convergence of $F^*(\vec{r})$ is performed on the MHTGR-350 fuel compact and the fuel block. A strategy to achieve convergence of $F^*(\vec{r})$ in CE TSUNAMI was found by changing the parameter *A* (number of skipped generations per voxel) and monitoring the output edits. The maximum converged value of *A* was found to be approximately 200 for all mesh definitions that were studied. Coarse mesh definitions are recommended since they score more tallies, converge quicker and require less histories. The convergence parameters were the same for both the fuel compact and single fuel block.

There is a several hundred pcm difference between MG and CE k_{inf} results for the fuel compact and block. Although there are considerably large differences between the transport calculations of the CE and MG models, Sampler/NEWT and CE TSUNAMI-3D produced very comparable results for the relative standard deviation of k_{eff} due to nuclear data uncertainties. Comparison of the top uncertainty contributors of the fuel compact and fuel block show expected behaviour in the nuclide-reaction pairs. The ^{235}U $(\bar{\nu})$ / ^{235}U $(\bar{\nu})$ is observed as the top contributor. The uranium contributions (i.e ^{235}U (n,γ) / ^{235}U (n,γ) and ^{238}U (n,γ) / ^{238}U (n,γ)) decrease from a fuel compact

to a fuel block. Only the ^{235}U ($\bar{\nu}$) / ^{235}U ($\bar{\nu}$) contribution is fairly unaffected by the change in the system. All the homogenized nodal cross sections for the fuel compact are considerably higher than the fuel block which is expected and are discussed in the text.

9.2 HTTR results

The current version of NWURCS cannot produce MG inputs for the HTGRs, hence validation could not be assessed in terms of the multigroup codes. NWURCs successfully modelled the HTTR benchmark model in CE. The k_{eff} results were in agreement with what was observed in literature.

The CE TSUNAMI convergence study was also applied to the HTTR fuel block and an active HTTR core layer. The $F^*(\vec{r})$ convergence parameters for the HTTR systems were found to be identical to the MHTGR-350 systems. It can therefore be assumed that the full core MHTGR-350 and HTTR full core models will converge at $A = 200$. The $F^*(\vec{r})$ convergence only has a spatial dependence, therefore one can expect that the parameters found in this work are applicable for all prismatic HTGR systems. It cannot be said with certainty that these parameters would be sufficient for other types of reactors.

Similarly to the MHTGR-350, ^{235}U($\bar{\nu}$) / ^{235}U($\bar{\nu}$) is the highest contribution in the HTTR fuel rod, block and core layer calculations and this value is fairly unaffected by the change in system. The top six contributions from the HTTR fuel pin and block are the same as the MHTGR-350 contributions thus indicating a neutronic similarity between the two systems.

The CE TSUNAMI analysis of the full core models using ENDF/B-VII.0 and ENDF/B-VII.1 shows small differences in the nuclear data uncertainty. The c-graphite (n,γ) / c-graphite (n,γ) contributions and c-graphite elastic / c-graphite elastic contributions increase significantly from ENDF/B-VII.0 to ENDF/B-VII.1. This is expected due to the updates in cross section data.

An insertion of control rods in the core model of the HTTR increases the c-graphite elastic / c-graphite elastic contribution. Fully inserting the control rod caused the ^{235}U (χ) / ^{235}U (χ) contributions to show up in the top contributions to uncertainty. Furthermore, the uncertainty due to the total nuclear data uncertainty increased significantly when compared to the critical and super critical model.

The IAEA CRP on HTGR UAM also identified two other experimental designs for validation, i.e. the VHTRC and the pebble-bed HTR-10. The VHTRC CE TSUNAMI uncertainty results reported by Bostelmann and Strydom (2017) showed similarities with the uncertainty results presented in this thesis. Although the HTR-10 is a pebble bed reactor it still compares favourably from a nuclear

data uncertainty point of view to the HTTR subcritical model, as the top contributions for the HTR-10 and the subcritical HTTR show the same behaviour.

9.3 Recommendations

A list of recommendations aimed at supplementing and continuing the current study is as follows:

- Completion of the randomization study of the packing of the coated particles in the compact.
- A random particle capability should be added to SCALE that will allow the user not only to randomise the CP TRISO particles, but also to randomise the LBP BISO particles in the MHTGR-350.
- The computer bug in NWURCs should be fixed so that the control rods can be moved without errors.
- Once NWURCS is able to build MG models, the nuclear data uncertainties can be propagated with Sampler for the HTTR analysis.
- MG TSUNAMI should be able to accommodate the doublehet function so that an MG analysis can be completed.
- Inconsistencies in the SCALE codes were found for KENO-VI convergence. This can be investigated in future work as well as the SAMS failure to compute some calculations.
- Generation of other collapsed constants such as the diffusion coefficients and subsequent nodal calculations using a code such as NESTLE are needed.
- Build a thermal hydraulic core model and couple the neutronic core model with the thermal hydraulic core model.
- Uncertainty propagation of the calculation defined in the previous bullet.
- Burnup studies including uncertainty propagation.

9.4 Closing remarks

This thesis succeeded in quantifying the uncertainty due to nuclear data for the MHTGR-350 heterogeneous fuel compact and fuel block. This was one of the objectives of the IAEA CRP on HTGR. The uncertainty results were successfully validated with the HTTR benchmark model. Furthermore, NWURCS was successfully verified for HTGR systems. Although a fairly comprehensive uncertainty and sensitivity study is presented in this work, there are still other aspects of uncertainty and sensitivity analysis that must be studied. Due to time and scope constraints, these aspects could not be included in this study. Hence the uncertainty and sensitivity analysis of the MHTGR-350 and HTTR can be studied further as listed in the recommendations.

BIBLIOGRAPHY

Ardakani, A. T., Ghofrani, M. B., & Ezzati, A. O. (2014). Stochastic arranging of CFPs in HTTR and criticality benchmark considering different modeling of CFPs. *Nuclear Engineering and Design,* 271, 348-351.

Ardakani, A. T., Ghofrani, M. B., & Ezzati, A. O. (2015). Comparative modeling of the stocahstic versus regular arrangement of TRISO particles in HTTR. *Progress in Nuclear Energy, 271*, 291-296.

Ball, S. J., Holcomb, D. E., & Cetiner, S. M. (2012). HTGR Measurements and Instrumentation Systems. ORNL/TM-2012/107.

Becker, B., Dagan, R., & Lohnert, G. (2009). Proof and implementation of the stochastic formula for ideal gas, energy dependent scattering kernel. *Annals of Nuclear Energy, 36*, 470–474.

Bess, J. D. (2010). Benchmark evaluation of the start-up core reactor physics measurements of the high temperature engineering test reactor. *PHYSOR 2010 – Adavances in Reactor Physics to Power the Nuclear Renaissance*. Pittsburgh, Pennsylvania, USA: American Nuclear Society.

Bess, J. D., & Fujimoto, N. (2014). Benchmark Evaluation of Start-Up and Zero-Power Measurements at the High-Temperature Engineering Test Reactor. *Nuclear Science and Engineering, 178*(3), 414-427.

Bess, J. D., Fujimoto, N., Dolphin, B. H., Snoj, L., & Zukeran, A. (2009). Evaluation of the Start-Up Core Physics Tests at Japan's High Temperature Engineering Test Reactor (Fully-Loaded Core). *HTTR-GCR-RESR-001*. INL/EXT-08-14767.

Bomboni, E., Cerullo, N., & Lomonaco, G. (2012). Simplified models for pebble-bed HTR core burn-up calculations with Monteburns 2.0. *Annals of Nuclear Energy, 40*, 72-83.

Bostelmann, F., Strydom, G., Reitsma, F. Ivanov, K., (2016). The IAEA coordinated research programme on HTGR uncertainity analysis: Phase I status and Ex I-1 prismatic reference results. *Nuclear Engineering and Design*, 77-88.

Bostelmann, F., Hammer, H. R., Ortensi, J., Strydom, G., & Velkov, K. (2016). Criticality calculations of the Very High Temperature Reactor Critical Assembly benchmark with Serpent and SCALE/KENO-VI. *Annals of Nuclear Energy,* 90, 343-352.

Bostelmann, F., & Strydom, G. (2017). Nuclear data uncertainity and sensitivity analysis of the VHTRC benchmark using SCALE. *Annals of Nuclear Energy, 110*, 317-329.

Brown, F. B. (2006, September 10-14). On the Use of Shannon Entropy of the Fission Distribution for Assessing Convergence of Monte Carlo Criticality Calculations. *PHYSOR-2006, ANS Topical Meeting on Reactor Physics*. Vancouver, BC, Canada

Brown, F. B., Martin, W. R., Ji, W., Conlin, J. L., & Lee, J. C. (2005). Stochastic Geometry and HTGR Modeling with MCNP5. *The Monte Carlo Method: Versatility Unbounded In A Dynamic Computing World*. American Nuclear Society.

Canuti, E., Petruzzi, A., Auria, E. D., & Kozlowski, T. (2012). Sensitivity Studies for the Exercise I-1 of the OECD/UAM Benchmark. Hindawi Publishing Corporation, Science and Technology Nuclear Installations.

Chiang, M.-H., Wang, J.-Y., Sheu, R.-J., & Liu, Y.-W. H. (2014). Evaluation of the HTTR criticality and burnup calculations with continous-energy and multigroup cross-sections. *Nuclear Engineering and Design*, 327-331.

Dahmani, M., & Kastanya, D. (2013). Use of Sensitivity and Uncertainty Analysis in Reactor Design Verification. Part 1: TSUNAMI analysis. *Annals of Nuclear Energy,* 60, 439-447.

Doc. No. 12-9051191-001. (2007). *NGNP with Hydrogen Production Preconceptual Design Studies Report*.

DOE-HDBK-1019/2-93. (1993, January). DOE Fundamentals Handbook. *Nuclear Physics and Reactor Physics Theory : Volume 2 of 2*. Washington, D.C: U.S. Department of Energy.

Dong, Z. (2016). Model-Free Coordinated Control for MHTGR-Based Nuclear Steam Supply Systems. *Energies 2016, 9*(1).

Duderstadt, J. J., & Hamilton, L. J. (1976). *Nuclear Reactor Analysis.* United States. Wiley.

Du Toit, M. H. (2017). Analysis of Specific Design Aspects of a Thorium-uranium fuelled European Pressrised Reactor. *Thesis submitted in fulfilment of the requirements for the degree Philosophae Doctor in Nuclear Enginnering at Potchefstroom Campus of the North-West University*. Potchefstroom, South Africa.

Du Toit, M. H., & Naicker, V. V. (2018). Developing a full core MCNP6 and RELAP5 model of the EPR using NWURCS. *Nuclear Science and Technology,* 3, 291-304.

Gehin, J., Jessee, M., Lee, D., Goluoglu, S., Ilas, G., Ilas, D., & Bowman, S. (2010). Development and validation of SCALE nuclear analysis methods for high temperature gas-cooled reactors. *Proceedings of HTR 2010*. Prague, Czech Republic: Paper 206.Goluoglu, S., & Williams, M. L. (2005). Modeling Doubly Heterogenous Systems in SCALE. 2005. *"Talk About Nuclear Differenty: A Good Story Untold"*. Washington, D.C: American Nuclear Society.

Goluoglu, S., Elam, K., Rearden, B. T., Broadhead, B. L., & Hopper, C. M. (2004). *Sensitivity Analysis Applied to the Validation of the B-10 Capture Reaction in Nuclear Fuel Casks.* Oak Ridge National Laboratory.

Goluoglu, S., & Williams, M. L. (2005, November). Modeling Doubly Heterogeneous Systems in SCALE. Washington, D.C: Submitted to American Nuclear Society 2005 Winter Meeting "Talk About Nuclear Differently: A Good Story Untold".

Gupta, C.K, (1989). *Materials in Nuclear Energy Applications* (Vol.1). CRC Press, Taylor and Francis group.

Hao, C., Chen, Y., Guo, J., Wang, L., & Li, F. (2018). Mechanism Analysis of the Contribution of Nuclear Data of the K-eff uncertainty in the pebble HTR. *Annals of Nuclear Energy,* 120, 857-868.

Hart, S. W., Maldonado, G. I., Goluoglu, S., & Rearden, B. (2013). Implementation of the Doppler broadening rejection correction in KENO. American Nuclear Society.

Herman, M., & Trkov, A. (2009). ENDF-6 Formats Manual. *Data Formats and Procedures for the Evaluated Nuclear Data File ENDF/B-VI and ENDF/B-VII*. Upton, NY: National Nuclear Data Center, Brookhaven National Laboratory.

Hicks, T. (2011). *Modular HTGR Safety Basis and Approach*. United States: INL/EXT-11-22708.

Ho, H. Q., Honda, Y., Goto, M., & Takada, S. (2017). Numerical investigation of the random arragement effect of coated fuel particles on the criticality of the HTTR fuel compact using MCNP6. *Annals of Nuclear Energy, 103*, 114-121.

Ho, H. Q., Honda, Y., Goto, M., & Takada, S. (2018). Investigation of Uncertainty caused by random arrangement of coated fuel particles in HTTR criticality calculations. *Annals of Nuclear Energy,* 112, 42-47.

IAEA-TECDOC-1382. (2003). Evaluation of high temperature gas cooled reactor performance: Benchmark analysis related to initial testing of the HTTR and HTR-10. Vienna, Austria.

Ilas, D., & Gehin, J. (2010). HTTR Fuel Block Simulations with SCALE. *PHYSOR 2010 – Advances in Reactor Physics to Power the Nuclear Renaissance*. Pittsburgh, Pennsylvania, USA.

Ilas, G., Ilas, D., Kelly, R. P., & Sunny, E. E. (2012). Validation of SCALE for High Temperature Gas- Cooled Reactor Analysis. NUREG/CR-7107 ORNL/TM-2011/161.

Ivanov, I., Avramova, M., Kamerow, S., Kodeli, I., Sartori, E., Ivanov, E., & Cabellos, O. (2013). *Benchmarks for Uncertainty Analysis in Modelling (UAM) for the Design, Operation and Safety Analysis of LWRs, Volume I: Specification and Support Data for Neutronics Cases (Phase I).* OECD NUCLEAR ENERGY AGENCY.

Iyoku, T., Ueta, S., Sumita, J., Umeda, M., & Ishihara, M. (2004). Design of Core Components. *Nuclear Engineering and Design, 233*, 71-79.

Ji, W., Liang, C., & Pusateri, E. N. (2014). Analytical Dancoff factor evaluations for reactor designs loaded with TRISO particle fuel. *Annals of Nuclear Energy,* 63, 665-673.

Kim, K. S., & DeHart, M. D. (2011). Unstructured partial- and net-current based coarse mesh finite difference acceleration applied to the extended step characteristics method in NEWT. *Annals of Nuclear Energy,* 38, 527-534.

Leppanen, J., & Dehart, M. (2009). HTGR Reactor Physics and Burnup Calculations Using the Serpent Monte Carlo Code. *Transactions of the American Nuclear Society*.

Lewis, E. E. (2008). *Fundamentals of Nuclear Reactor Physics.* San Diego, United States: Academic Press.

Lewis, E. E., & Miller, M. F. (1993). *Computational methods of neutron transport.* La Grange Park, Illinois: American Nuclear Society.

Loucks, D. P., & Van Beek, E. (2005). Water Resources Systems Planning and Management. *An Introduction to Methods, Models and Applications*. ISBN 92-3-103998-9.

Maratele, D. A. (2016). Uncertainty analysis of the fuel compact of the prismatic high temperature gas-cooled reactor test problem using SCALE 6.1. *Dissertation submitted in partial fulfillment of the requirements for the degree Master of Science in Nuclear Engineering at the Potchefstroom Campus of the North-West University*. South Africa.

Marshall, W. J., Rearden, B. T., & Jones, E. L. (2013). Validation of Criticality Safety Calculations with SCALE 6.2. United States: UT-Battelle, LLC under Contract No. DE-AC05-00OR22725.

McEwan, C. E. (2013). Covariance in Multigroup and Few-group Reactor Physics Uncertainity Calculations. *Open Access Dissertations and Theses*. Paper 8216.

Menzel, F., Sabudjian, G., & D'Auria, F. (2018). BEPU and licensing of nuclear power plants. *Best Estimate Plus Uncertainty International Conference (BEPU 2018).* Real Collegio, Lucca, Italy: ANS.

Montierth, L. M., Terry , W. K., & et al,. (2009). Evaluation of the initial critical configuration of the HTR-10 pebble-bed reactor. *International handbook of evaluated reactor physics benchmark experiments (IRPhE) Handbook. Nucl. Energy Agency*.

Montwedi, O. E. (2014). Neutronic Simulation of a European Pressurised Reactor. *Dissertation submitted in partial fulfilment of the requirements for the degree Master of Engineering at the Potchefstroom Campus of the North-West University*.

Naicker, V. V., Maratele, D. A., Reitsma, F., Bostelmann, F., & Strydom, G. (2016, May 1-5). Quantification of the SCALE 6.1 Eigenvalue Uncertainty due to Cross Section Uncertainties for Exercise I-1 of the IAEA CRP on HTGR Uncertainities. *PHYSOR*. Sun Valley, ID.

NEA. (2013). International Reactor Physics Experiment Evaluation (IRPhE) Project. *NEA/NSC/DOC, NEA No. 7140*.

NEA/NSC/R(2017)4. (2018). Nuclear Energy Agency Nuclear Science Committee NEA/NSC/R (2017) 4. *NEA Benchmark of the Modular High-Temperature Gas-Cooled Reactor-350 MW Core DesignVolumes I and II*. Organisation for Economic Co-operation and Development (OECD).

NESTLE,V5.2.1, (2003). Few-Group Neutron Diffusion Equation Solver Utilizing the Nodal Expansion Method for Eigenvalue, Adjoint, Fixed-Source Steady-State and Transient Problems. *Electric Power Research Center,* North Carolina State University.

Novotny, F., Matejkova, J., & Katovsky, K. (2016). Nuclear Data Generation Sensitivity Analysis for VVER Reactor Dynamic Benchmark. *17th International Scientific Conference on Electric Power Engineering (EPE).* Prague, Czech Republic.

Nyalunga, G., Naicker, V., & du Toit, M. (2016). Developing Skills for Neutronic Modelling of Nuclear Power Reactors in South Africa. *Journal of Energy*, *127, 64-67*

Ortensi, J., Cogliati, J. J., Pope, M. A., Bess, J. D., Ferrer, R. M., Bingham, A. A., & Ougouag, A. M. (2010). Deterministic Modeling of the High Temperature Test Reactor. *INL/EXT-10-18969*.

Perfetti, C. (2013). Continuous-Energy Eigenvalue Sensitivity Coefficient Calculations in TSUNAMI-3D. *International Conference on Mathematics and Computational Methods Applied to Nuclear Science & Engineering*. Sun Valley, Idaho, USA, May 5-9.

Perfetti, C. M. (2012). Advanced Monte Carlo Methods for Eigenvalue Sensitivity Coefficient Calculations. *A dissertation submitted in partial fulfillment of the requirements for the degree of Doctor of Philosophy (Nuclear Engineering and Radiological Sciences) in the University of Michigan*.

Perfetti, C. M., Rearden, B. T., & Martin, R. W. (2016). SCALE Continuous-Energy Eigen-value Sensitivity Coefficient Calcultaions . *Nuclear Science and Engineering, 182, 332-353*.

Pusa, M. (2012). Pertubation- Theory-Based Sensitivity and Uncertainty Analysis with CASMO-4. *Science and Technology of Installations*. doi:10.1155/2012/157029

Qin, W., Yang, K., Chen, J., & Cai, X. (2016). Dancoff factor analysis for pebble fluoride salt coooled high temperature reactor. *Progress in Nuclear Energy,* 88, 332-33.

Rearden, B. T., Jesee, M. A., & Eds, (2016). SCALE Code System, ORNL/TM-2005/39, Version 6.2.1. *Oak Ridge National Laboratory*. Oak Ridge, Tennessee.

Rearden, B. T., Petrie, L. M., Peplow, D. E., Bekar, K. B., Wiarda, D., Celik, C. & Marshall, W. J. (2015). Monte Carlo Capabilities of the SCALE code system. *Annals of Nuclear Energy, 82*, 130-141.

Reitsma, F., Ougouag, A. M., & Gougar, H. D. (2005). Investigation of the power peaking in the PBMR pebble-bed reactor. *Mathematics and Computation, Supercomputing, Reactor Physics and Nuclear and Biological Applications (M&C-2005)*. Palais des Papes, Avignon, France.

Salah, A. B., Kliem, S., Rohde, U., D'Auria, F., & Petruzzi, A. (2006). Uncertainty and sensitivity analyses of the Kozloduy pump trip test using coupled thermal–hydraulic 3D kinetics code. *Nuclear Engineering and Design,* 236, 1240–1255.

Salvatores, M., & Palmiotti, G. (2018). Production and use of nuclear parameter covariance data: an overview of challenging cross cutting scientific issues. EPJ *Nuclear Science & Technology, 4*(20).

Sanchez, R., Mao, L., & Santandera, S. (2002). Treatment of boundary conditions in trajectory-based transport methods. *Nuclear Science and Engineering,* 140, 23-25.

Shiozawa, S., Fujikawa, S., Iyoku, T., Kunitomi, K., & Tachibana, Y. (2004). Overview of HTTR Design Features. *Nuclear Engineering and Design, 233*, 11-21.

Sihlangu, S. F. (2016). A neutronic model of the PMR200 prismatic modular reactor using MCNP5. *Dissertation submitted in fulfilment of the requirements for the degree Magister Scientiae in Nuclear Engineering at the Potchefsroom Campus of the North-West University*.

Sihlangu, S. F., Naicker, V. V., Hou, J., & Reitsma, F. (2018). Uncertainty Quantification in the MHTGR-350 Fuel Compact and block using TSUNAMI-3D CLUTCH method and Sampler. *ANS Best Estimate Plus Uncertainty International Conference*. Real Collegio, Lucca, Italy, Lucca, Italy: American Nuclear Society, May 13-19.

Stacey, W. M. (2007). *Nuclear Reactor Physics* (Vol. Second edition). Weinheim: Wiley-VCH Verlag GMbH & Co. KGaA.

Strydom, G. (2012). *Uncertainty and Sensitivity Analyses of a Pebble Bed HTGR Loss of Cooling Event, 2013*. (K. Ivanov, Ed.) Idaho Falls, USA: Hindawi Publishing Corporation, Science and Technology of Nuclear Installations. doi:10.1155/2013/426356

Strydom, G., Bostelmann, F., & Yoon, S. (2015). Results for Phase 1 of the IAEA Coordinated Research Project on HTGR Uncertainties. Internation National Laboratory.

Sunny, E. E., Brown, F. B., Kiedrowski, B. C., & Martin, W. R. (2013). Temperature Effects of Resonance Scattering in Free Gas for Epithermal Neutrons. *LA-UR-11-04886*.

Taylor, J. R. (1997). *An Introduction to Error Analysis: The Study of Uncertainties in Physical Measurements* (Vol. Second Edition). University Science Books.

Teuchert, E., Haas, K. A., Rütten, H. J., Brockmann, H., Gerwin, H., Ohlig, U., & Scherer, W. (1994). V.S.O.P. Computer Code System for Reactor Physics and Fuel Cycle Simulation, *JUL-2897*. Forschungszentrum Jülich.

Thomas, S. (2011). The Pebble Bed Modular Reactor: An Orbituary. *Energy Policy, 39*(5).

Wang, M.-J., Sheu, R.-J., Peir, J.-J., & Liang, J.-H. (2014). Criticality calculations of the HTR-10 pebble-bed reactor with SCALE6/ CSAS6 and MCNP5. *Annals of Nuclear Energy,* 64,1-7.

Wiarda, D., Dunn, M. E., Green, N. M., Williams, M. L., Celik, C., & Petrie, L. M. (2016, April). AMPX-6: A Modular Code System for processing ENDF/B Evalualations. Prepared by Oak Ridge National Laboratory.

Williams, M. L., & Rearden, B. T. (2008). SCALE-6 Sensitivity/Uncertainty Methods and Covariance Data. *Nuclear Data Sheets, 109*(12), 2796-2800.

Zerovnik, G. (2012). Use of covariance matrices for estimating uncertainties in reactor calculations. Doctoral Dissertation submitted to the University of Ljubljana, Faculty of Mathematics and Physics, Department of Physics. Ljubljana.

Zhu, T., Vasiliev, A., Ferroukhi, H., Pautz, A., & Tarantola, S. (2015). NUSS-RF: Stochastic sampling-based tool for nuclear data sensitivity and uncertainty quantification. *Journal of Science and Technology, 52*, 1000-1007. doi:10.1080/00223131.2015.1040864

Zwermann, W., Aures, A., Gallner, L., Hannstein, V., Kryzkacz-Hausmann, B., Velkov, K., & Martinez, J. S. (2014). Nuclear Data Uncertainty and Sensitivity analysis with XSUSA for Fuel Assembly Depletion Calculations. *Nuclear Engineering and Technology, 46*(3), 343-352.